Universitätsmedizin Essen
Westdeutsches Tumorzentrum Essen
Translationale Neuroonkologie

westdeutsches tumorzentrum essen

dkfz.
Deutsches Konsortium für Translationale Krebsforschung
Partnerstandort Essen|Düsseldorf

Dissertation

zur

Erlangung des Doktorgrades

Dr. rer. nat.

der Fakultät für

Biologie

an der

Universität Duisburg-Essen

vorgelegt von

Vivien Ullrich

aus Essen

zum Thema

“Targeting clonally expanding drug-resistant tumor cells in recurrent glioblastoma”

14.06.2023

Die der vorliegenden Arbeit zugrunde liegenden Experimente wurden in der DKFZ-Abteilung für Translationale Neuroonkologie
am WTZ des Universitätsklinikum Essen durchgeführt.

1. Gutachter: Prof. Dr. Björn Scheffler

2. Gutachter: Prof. Dr. Verena Jendrossek

Vorsitzender des Prüfungsausschusses: Prof. Dr. Dr. Jürgen Becker

Tag der mündlichen Prüfung: 28. September 2023

Teilergebnisse der vorliegenden Arbeit wurden veröffentlicht in: /

In the context of this doctoral work, the following articles were published:

Kebir S, Ullrich V, Berger P, Dobersalske C, Langer S, Rauschenbach L, Trageser D, Till A, Lorbeer FK, Wieland A, Wilhelm-Buchstab T, Ahmad A, Fröhlich H, Cima I, Prasad S, Matschke J, Jendrossek V, Remke M, Grüner BM, Roesch A, Siveke JT, Herold-Mende C, Blau T, Keyvani K, van Landeghem FKH, Pietsch T, Felsberg J, Reifenberger G, Weller M, Sure U, Brüstle O, Simon M, Glas M, Scheffler B. A Sequential Targeting Strategy Interrupts AKT-Driven Subclone-Mediated Progression in Glioblastoma. Clin Cancer Res. 2023 Jan 17;29(2):488-500. doi: 10.1158/1078-0432.CCR-22-0611. PMID: 36239995; PMCID: PMC9843437.

Teilergebnisse der vorliegenden Arbeit wurden zu Veröffentlichung eingereicht: /

In the context of this doctoral work, the following articles were submitted:

Ullrich et al., in revision 2023

Teilergebnisse der vorliegenden Arbeit wurden als Erfindungsmeldung eingereicht:

Scheffler and Ullrich: „KDM5B predicts temozolomide-resistant subclones in glioblastoma / KDM5B-Companion" (DKFZ ref. P-1698) (Universität Duisburg-Essen ref. 23-713-Med)

Table of Contents

Summary

Glioblastoma, as the most common malignant brain tumor in adults, is characterized by the development of treatment resistance to the standard chemotherapy temozolomide (TMZ), leading to disease relapse and subsequently to high patient mortality. This work, conducted within the DFG-funded Clinical Research Unit 337 "Phenotypic Therapy and Immune Escape in Cancer", is based on the discovery of subclonal dynamics, that were detected in human patient tissue and in cellular and in vivo models of glioblastoma disease. As cellular models, short-term expanded, paired clinical cell samples of treatment-naive cells, extracted from the patient's primary tumor and the corresponding relapse cells were used. Relapse cells were obtained from the patient's clinical relapse or generated through serial *in vitro* TMZ exposure (experimental relapse). A rare treatment-naive ALDH1A1+ (Aldehyde Dehydrogenase 1 Family Member A1) cell population, subclonally enriches and acquires phosphorylated, active AKT (pAKT; phosphorylated protein kinase B) in the relapse, leading to increased resistance to TMZ. Based on the speculation that it is an early process in which cells phenotypically adapt to enable persistence under otherwise effective therapies (drug-tolerant persisters (DTPs)), cellular models for disease progression were developed to investigate early TMZ-induced responses of tumor cells. TMZ exposure resulted in a rapid increase in KDM5B^{high} cells, which were further characterized as slow-cycling, drug-tolerant cells, that present increased pAKT levels. The individual level of KDM5B expression in treatment-naive cells can predict the rare cellular identities, that newly arise as drug-resistant subclones after TMZ exposure. Thus, KDM5B was identified as a prospective indicator for the subclonal expansion of ALDH1A1+/pAKT+ cell populations and might be used in future biomarker-assisted clinical trials. If further developed, KDM5B could enable the prediction of patients responding to sequential subclone-specific targeting strategies already before TMZ-exposure. In this sequential targeting approach, one could take advantage of the TMZ-induced enrichment of resistant ALDH1A1+/pAKT+ subclones and subsequently target the enriched subclones in a second step via inhibition of pAKT. This "Enrich and Kill“ strategy could prolong patients survival.

Zusammenfassung

Das Glioblastom, der häufigste bösartige Gehirntumor des Erwachsenen, ist durch die Entwicklung einer Therapieresistenz gegen die Standard Chemotherapie Temozolomid (TMZ) gekennzeichnet, was zu einem Rückfall der Erkrankung, einem sogenannten Rezidiv, und daraufhin zu einer hohen Sterblichkeitsrate der Patienten führt. Diese Arbeit, die im Rahmen der DFG-geförderten Klinischen Forschergruppe 337 “Phenotypic Therapy and Immune Escape in Cancer” durchgeführt wurde, basiert auf der Entdeckung einer subklonalen Dynamik, die in humanem Patientengewebe, in zellulären und in vivo-Modellen des Glioblastoms nachgewiesen wurde. Für die zellulären Modelle wurden therapie-naive Zellen des Primärtumors des Patienten mit gepaarten Rezidivzellen verglichen, die entweder aus dem klinischen Rezidiv des Patienten stammten oder als experimentelles Rezidiv *in vitro* hergestellt wurden. Eine ALDH1A1+ Zellpopulation, die in therapie-naiven Tumoren nur selten zu finden war, sich aber in Rezidiven subklonal angereichert hatte, zeigte eine Zunahme von phosphoryliertem, aktiven AKT (pAKT), was zu einer erhöhten Resistenz gegenüber TMZ führte. Ausgehend von der Vermutung, dass es sich um einen frühen Prozess handelt, in dem Zellen phänotypisch so adaptiert werden, dass sie unter sonst wirksamen Therapien überleben und persistieren können, wurden zelluläre Modelle für Progressionsmechanismen entwickelt, um frühe TMZ-induzierte Reaktionen der Tumorzellen zu untersuchen. Eine TMZ-Exposition der Zellen führte zu einer rapiden Zunahme von KDM5B^{high} Zellen, die sich durch ein verlangsamtes Zellwachstum und ein erhöhtes pAKT Level auszeichneten, sowie eine verstärkte TMZ Toleranz aufwiesen. Das individuelle KDM5B Niveau in therapie-naiven Zellen ermöglichte die spezifische Vorhersage der anfänglich seltenen zellulären Identitäten, die unter TMZ-Exposition persistieren können und im Laufe der Progression expandieren und den Tumor dominieren. Somit wurde KDM5B als ein prädiktiver Faktor für die subklonale Expansion der ALDH1A1+/pAKT+ Zellen identifiziert und könnte als Biomarker in zukünftigen klinischen Studien verwendet werden, um vorherzusagen, welche Patienten auf eine auf spezifische Subklone ausgerichtete Therapiestrategie ansprechen werden. In dieser sequenziellen Therapie würde man eine „Enrich and Kill“ Strategie verfolgen und sich das TMZ-induzierte Anreichern der resistenten ALDH1A1+/pAKT+ Subklone zunutze machen. Die resistenten Subklone würden im Anschluss an die TMZ-Exposition in einem zweiten Schritt gezielt mittels pAKT Inhibition getroffen und so könnte das Überleben der Patienten verlängert werden.

1. Introduction

Traditionally, **glioblastoma**, the most common malignant brain cancer of the adult, is considered as a disease of **genetic evolution** – and **drug resistance** as its consequence. Yet, research of the last two decades increasingly appreciates dynamic cancer cell phenotypes that undergo cell state transitions under the influence of drug exposure and thus can escape from therapy without additional genetic aberrations. In this work, I interrogated drug-mediated, **adaptive plasticity** and early **tumor cell state transitions,** leading to treatment resistance in glioblastoma.

1.1. Glioblastoma characteristics and classification

Glioblastoma represents 45.2 % of all malignant central nervous system (CNS) tumors, with an incidence of approximately 3 cases per 100,000 persons. Although the isocitrate dehydrogenase (IDH)-wildtype diffuse astrocytic glioma occurs more frequently in older patients, it may present at any age, with men being more often affected than women (Ostrom et al., Neuro Oncol. 2019). It´s remarkable poor prognosis, with a median overall survival (mOS) of 15-18 months, confers the status of a highly malignant tumor with World Health Organization (WHO) grade IV (Weller et al., Nat Rev Clin Oncol. 2021). The current clinical gold standard therapy, the “Stupp-Scheme”, consist of surgical resection followed by concomitant chemoradiotherapy with the alkylating agent temozolomide (TMZ) and a maintenance therapy with TMZ (Stupp et al., N Engl J Med. 2005). Fatal relapse occurs inevitably, already during primary therapy. Upon recurrence, patients have a mOS of only 24–44 weeks (Reifenberger et al., Nat Rev Clin Oncol. 2017, Wen et al., Neuro Oncol. 2020). A better understanding of drug resistance in this uncurable brain tumor is clearly needed. Glioblastomas are characterized by a highly immunosuppressive environment, in which cells are able to suppress immune response through negative regulators, such as Programmed death-ligand 1 (PD-L1) or production of tumor-promoting cytokines as Transforming growth factor beta (TGF-ß) and Interleukin 10 (IL-10) (Brown et al., Br. J. Cancer 2018; Abedalthagafi et al., NPJ Precis. Oncol. 2018). Furthermore, glioblastomas immunosuppressive environment is characterized by activation of regulatory T cells and tumor-associated macrophages (Crane et al., Neuro Oncol. 2012; Wu et al., Neuro Oncol. 2010; McGranahan et al., Curr. Treat Options Oncol. 2019).

Traditionally, glioblastoma is considered as a genetic disease, harboring specific molecular features, which can evolve during the course of disease and contribute to tumor progression. Glioblastoma is one of the best characterized cancer entities with regard to its molecular landscape and distinct subtypes have been tried to assign. Most tumors are found to harbor alterations of the epidermal growth factor receptor (EGFR) and in common pathways, such as in the protein kinase B (Akt) pathway, e.g. phosphatidylinositol-3-kinase (PI3K) and phosphatase and tensin homolog (PTEN). Other common features are telomerase reverse transcriptase (TERT) promoter mutations or p53 mutations (Verhaak et al., Cancer Cell 2010). Using single-cell RNA-sequencing (RNA-seq) high intratumoral heterogeneity was identified, already at time of the primary diagnosis. Within each individual tumor high transcriptional diversity was detected, and furthermore, cells from one tumor were even spanning into the transcriptional profile of another tumor, revealing heterogeneous cell mixtures of individual identities (Patel et al., Science 2014). Consistent with the single cell-based RNA analyses it was reported that glioblastoma subclones, subsets of tumor cells within the population, present as hybrid states between different subtypes. The different subclones featured unique proliferation- and differentiation capabilities and could tolerate and respond differently to various drug treatments (Meyer et al., Proc Natl Acad Sci U S A 2015).

In order to stratify this inter- and intra-tumoral heterogeneous disease, Verhaak and others established a classification of molecular subtypes of glioblastomas, based on specific gene expression patterns into classic, mesenchymal, proneural, and neural. While the classic subtype presents chromosome 7 amplifications, including the EGFR locus, a loss of chromosome 10 and high expression of stem cell markers as notch and sonic hedgehog, the mesenchymal subtype contains highly expressed genes of the tumor necrosis factor super family NF-kB pathway and markers of epithelial-to-mesenchymal transition (EMT), as well as neurofibromatosis type 1 (NF1) mutations in most of the samples. Characteristics of the proneural tumors include alterations of platelet-derived growth factor receptor alpha (PDGFRA), whereas neural tumors are defined as tumors, that express specific neuron markers (Verhaak et al., Cancer Cell 2010). Furthermore, Capper et al. (Nature 2018) reported on an approach for DNA methylation-based tumor classification, based on DNA methylation analysis, fluorescence *in situ* hybridization and immunohistochemistry (Capper et al., Nature 2018). Via single-cell sequencing, Neftel et al. (Cell 2019) detected plasticity between 4 cellular states, the OPC-like state, in which they observed PDGFRA amplifications,

the NPC-like state, harboring cyclin-dependent kinase 4 (CDK4) amplifications, the AC-like state characterized by EGFR amplifications and the MES-like state, with NF1 alterations and involvement of immune cells. According to the authors each tumor seems to harbor a composition of different cellular states, that can transit into each other. When cells of a specific cellular state implanted into mice, they did not form a tumor of that single state, instead the cell state diversity of the primary tumor was re-established, recapitulating the tumors heterogeneity (Neftel et al., Cell 2019). Newest publications attempt to combine recent findings and defined 3 subgroups, which all have TERT promoter mutations. The proneural gene expression/receptor tyrosine kinase (RTK) I DNA methylation group, which is most common in younger patients, harbors amplifications of CDK4 and PDGFRA. In the classical gene expression/RTK II DNA methylation group amplifications of EGFR and homozygous loss of cyclin-dependent kinase inhibitor A and B (CDKN2A/B) can be detected. While the mesenchymal like subtype presents with a NF1 loss and increased infiltration of macrophages (reviewed in Wen et al., Neuro Oncol. 2020).

1.2. Conflicting models of tumor evolution

Tumor heterogeneity in general is thought to be a consequence of the clonal evolution of cancers. It is increasingly appreciated, that the genetic landscape evolves over time and especially in response to selective pressure conferred by therapy. For glioblastoma, evidence for conflicting models of branched and neutral evolution were reported. The branched evolution model states, that recurrences are derived from clones with different mutational profiles (Kim et al., Cancer Cell 2015; Wang et al., Nat. Genet. 2016), while in the neutral evolution model the tumor relapse is driven by oligoclonal populations, that were already present early in tumor development (Körber et al., Cancer Cell 2019; Klughammer et al., Nat. Med. 2018). Johnson et al. (Science 2014) already reported, that half of the initial tumor mutations were not detectable at the time of disease recurrence, confirming that therapy could act as a selective pressure and a “bottleneck” with underrepresented subpopulations being present in the primary tumor (Johnson et al., Science 2014). The underlying mechanism could be a combination of different models, as other investigators detected mutations exclusively of the initial glioblastoma or the recurrence, as well as shared mutations, that were detected in the initial and in the relapse tumor (Wang et al., Nat Genet 2016). Likewise, some scientists presented the idea of three possible models for the

development of drug resistance. Firstly, genetic changes might confer therapy resistance. Secondly, pre-existing inherently resistant cells could be found in many tumors. And lastly, it could be a combination of both (Meacham and Morrison, Nature 2013). Moreover, it was proposed, that local recurrences of glioblastomas might follow a linear evolution model with many mutations within the primary tumor, while a spatially distant relapse could present a branched or divergent evolution model with fewer initial mutations (Kim et al., Cancer Cell 2015). More recently fate mapping studies on DNA barcoded cell samples engrafted into patient-derived xenograft models of disease (PDX) confirmed that slow-cycling stem-like cells could undergo asymmetric cell divisions, generating rapidly dividing progenitors. Moreover, a rare drug-resistant 'outlier' clone, that was pre-existing in the untreated tumors and increased under TMZ treatment, was identified (Lan et al., Nature 2017).

Interestingly, analysis of tissue from paired patient cohorts, obtained before and after TMZ therapy, could not detect many TMZ-specific alterations. Rather, the mutations at the time of recurrence were found largely random. This coincides with the finding that cellular dynamics takes place under the pressure of TMZ allowing relapse subclones to originate from pre-existing rare subclones at primary disease (Barthel et al., Nature 2019; Körber et al., Cancer Cell 2019). As shown in Figure 1, the founder cell is considered to emerge years prior diagnosis, allowing several years of cancer evolution, where subclonal diversification takes place. The first-line treatment then reduces the number of tumor cell hierarchies, but oligoclonal expansion of some resistant subclones occurs towards recurrence of disease (Körber et al., Cancer Cell 2019).

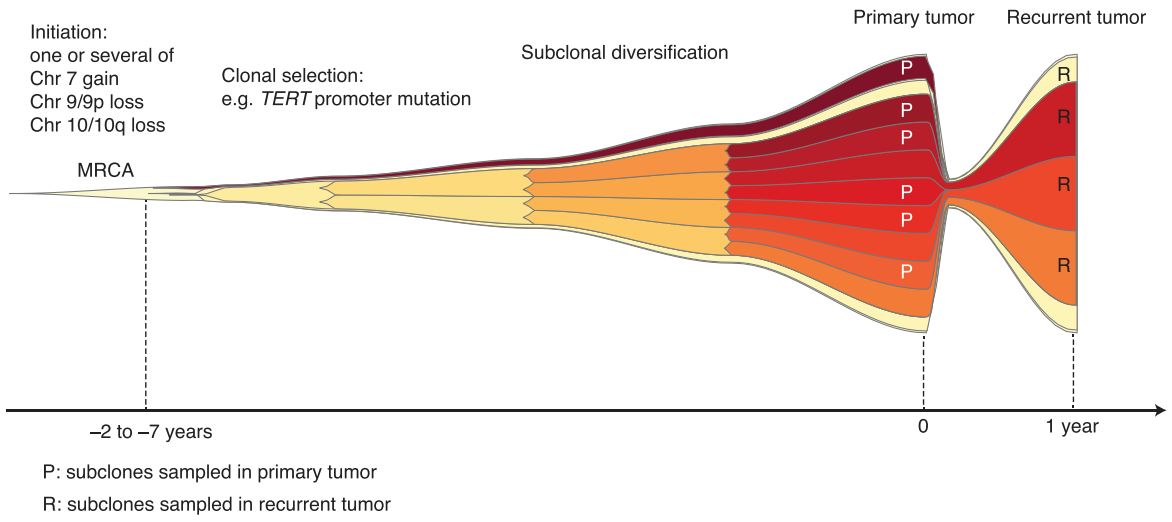

Figure 1: Subclonal dynamics under disease progression, including subclonal diversification during tumor evolution and oligoclonal expansion after therapy (from Körber et al., Cancer Cell 2019).

1.3. Treatment challenges and the development of drug resistance

Current treatment options, which fail to prevent tumor relapse, do not take into account a potential clonal expansion of co-existing tumor cell populations that harbor distinct drug resistance profiles. The standard of care treatment TMZ is a prodrug that is administered orally to patients, as it is able to penetrate the blood–brain barrier. Under physiological conditions TMZ is metabolized to 5-(3-methyltriazen-1-yl)imidazole-4-carboxamide (MTIC) that further converts into the active form methyldiazonium ion. Methyldiazonium ion adds its methyl group to purine bases of DNA, which leads to DNA damage in form of double-strand break, resulting in cell cycle arrest and apoptosis (as reviewed in Singh et al., Cancer Drug Resist 2021). As an alkylating agent that methylates DNA, TMZ can be counteracted by the DNA repair enzyme O(6)-methylguanine-DNA methyltransferase (MGMT), that is able to remove the added methylgroups. So that patients harboring MGMT promoter methylations, that result in decreased expression of the cellular repair protein, were reported to show a greater overall survival (Hegi et al., N Engl J Med. 2005; Hegi et al., J Clin Oncol. 2008). Beside MGMT and other DNA repair enzymes, aberrations of RTKs (Pearson et al., Signal Transduct Target Ther 2017), induction of autophagy as a protective mechanism (Sui et al., Cell Death Dis 2013) or even the production of extracellular vesicles, that carry propagating factors (D'Asti et al., Cell Mol Neurobiol. 2016), can lead to TMZ resistance.

Multiple molecularly targeted therapies that performed well in preclinical studies have failed in clinical phase III trials in humans (Shergalis et al., Pharmacol Rev. 2018). However, retrospective analysis, comparing patients treated with molecularly matched vs. unmatched targeted therapies in recurrent glioblastoma patients gave hints on increased progression-free survival (PFS) as well as mOS for patients treated with matched targeted therapies. The longest PFS could be achieved through combination of dabrafenib and trametinib for BRAF-V600E mutation harboring patients, while the worst results could be seen under Palbociclib for CDKN2A/B deleted patients. Other matched treatments were Pembrolizumab in case of PD-L1 expression, Eribulin for TERT promoter mutations, Cabozantinib for MET amplification, Lorlatinib in case of ALK rearrangements and Osimertinib for patients with EGFR mutations. Overall this lead to a mOS of 13 months when a matched therapy was administered compared to a mOS of 4.3 months in patients receiving an unmatched therapy (Lazaridis et al., J Cancer Res Clin Oncol. 2022). In the field of immunotherapy, no new therapeutic

options have been approved, despite preclinical promise. The prevailing view is that all efforts were impeded by the glioblastoma immunosuppressive tumor microenvironment (Wang et al., Front Genet. 2021). In a clinical trial the addition of tumor-treating fields (TTFields) during adjuvant TMZ was shown to significantly extend mOS by a median of 4.9 months in a subgroup of patients. TTFields, a loco-regional treatment, are low-intensity, intermediate frequency, alternating electric fields administered via transducer arrays attached to the shaved scalp. It is believed that their administration leads to disruption of the mitotic spindle formation, which induces mitotic arrest, stops cell division and initiates apoptosis (Stupp et al, JAMA 2015; Stupp et a., JAMA 2017). In relapse TTFields are discussed to confer longer survival following disease progression (Post-progression survival (PPS)) to patients with a PTEN mutated recurrent glioblastoma (Dono et al., J Neurooncol. 2021).

There is no standard of care after glioblastoma relapse, several treatment options may be considered that is the surgical resection of the relapse tumor, temozolomide re-challenge, addition of nitrosoureas to the treatment schedule such as lomustine, the vascular endothelial growth factor (VEGF) antibody bevacizumab (Wick et al., N Engl J Med 2017), or other chemotherapeutic agents such as carboplatin or etoposide (NCCN Clinical Practice Guidelines in Oncology, Central Nervus System Cancers 2019). None of these options have been shown to prolong survival significantly and to prevent glioblastoma's high mortality in randomized trials. The effect of multimodal therapies were discussed already in 2015 (Scorsetti et al., BMC Cancer 2015). An identification of subclone-specific drug combinations could be considered. It was suggested that a closer investigation of the relapse tumor is necessary to find effective therapies (Wang et al., Nat Genet. 2016; Johnson et al., Science 2014). However, conduction of secondary surgery at relapse is not always possible, so that the tumor´s characteristics after treatment cannot be determined to decide for a secondary treatment option.

This is why my lab historically aimed at identifying cues involved in treatment-mediated clonal selection. If the respective subclonal dynamics could be predicted already at the time of the primary disease, one could deplete of the predicted dominant subclone at disease relapse without the need to study surgically inaccessible relapse tissue. In one of the previous publications of our group, Reinartz et al. (Clin Cancer Res 2017) conducted a proof-of-principal study, generating over 30 single cell-derived subclones from five clinical glioblastoma cases using cloning cylinders or the limiting

dilution technique. Investigation of sublones from the same parental cells showed that they display distinct morphological characteristics, that they are genetically different and even differ in their tumorigenic potential, thus also reflecting functional intra-tumoral heterogeneity. The upper panel of Figure 2 displays phase contrast pictures of representative subclones in cell culture. The lower panel depicts hematoxylin and eosin (H&E) staining, further emphasizing the distinct tumor cell morphologies, particularly multinucleated giant cells, after orthotopic xenografting (PDX). The cells of CL2 cells were not tumorigenic in the patient derived xenografts.

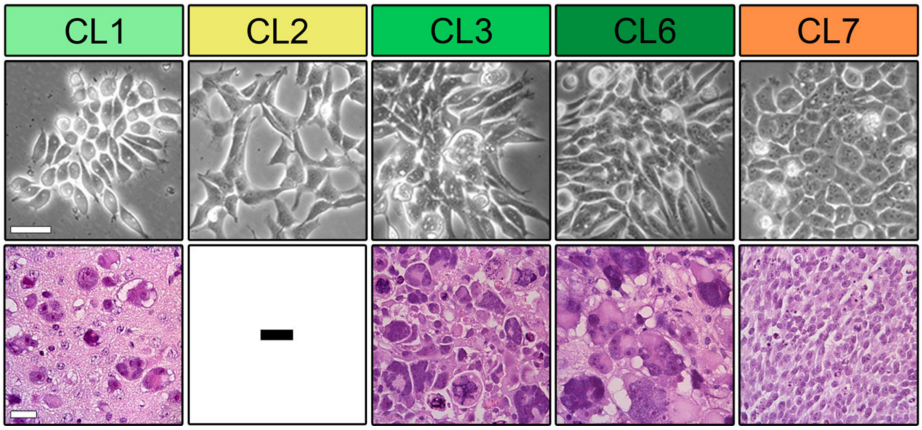

Figure 2: Single cell-derived subclones from clinical glioblastoma cases display distinct morphological characteristics and tumorigenic potential (from Reinartz et al., Clin Cancer Res 2017).

In addition, clone-by-clone differences in the sensitivity to clinical-grade drugs and compounds became apparent. Specific compounds eradicate specific tumor subpopulations, while others remain, leading to drug-specific effects onto the subclonal composition of the tumor. The obtained drug-profiles could be used to forecast treatment-induced clonal population shifts in vitro (Figure 3). This led to the conclusion that heterogenous glioblastoma could potentially be driven towards enrichment of a specific subclone under first-line treatment. While the enrichment could be predicted, one could determine a rationale for the choice of a 2nd line treatment in a sequential targeting approach (Enrich and Kill Strategy) (Reinartz et al., Clin Cancer Res 2017).

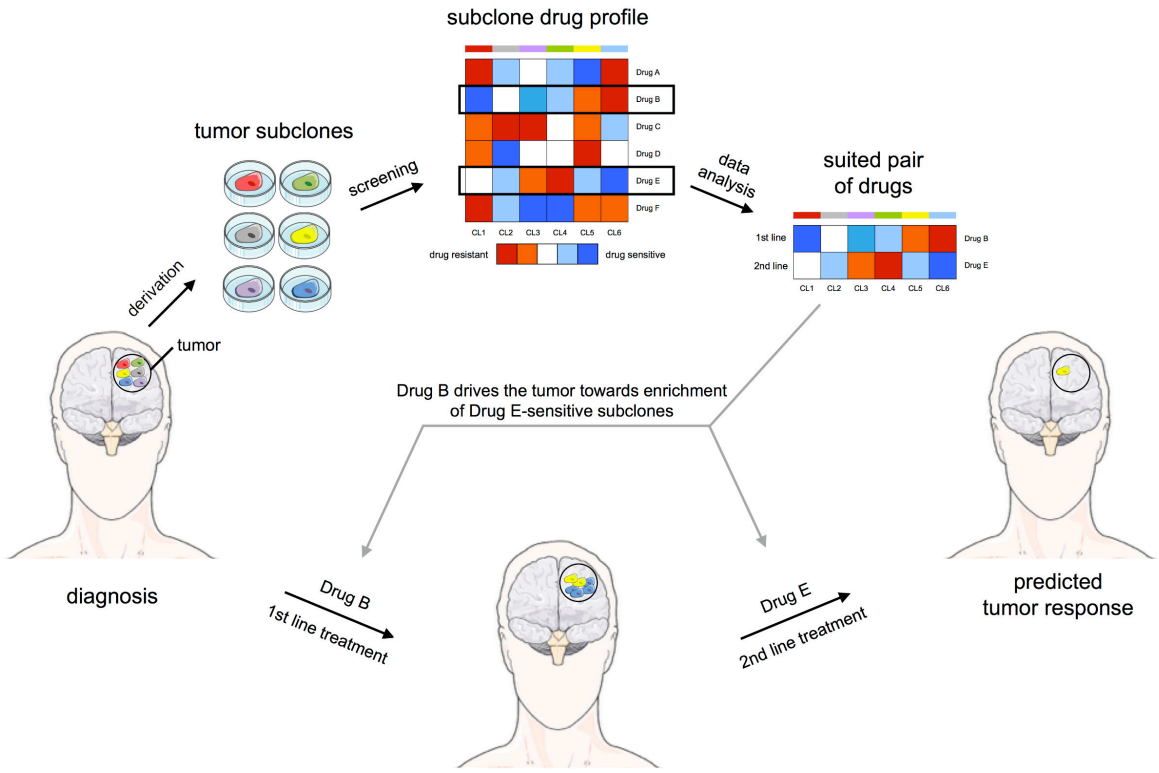

Figure 3: Predicting population dynamics for 2nd line treatment decisions through subclone profiling (from Reinartz et al., Clin Cancer Res 2017).

1.4. Adaptive plasticity and dynamic cellular state transitions

Glioblastoma research has focused on hierarchies of cancer stem cell (CSC) as a major source of treatment resistance (Chen et al., Nature 2012; Lan et al., Nature 2017). In the past, the CSC model considered a hierarchical organization of tumors, in which only a small population of cells were intrinsically resistant and tumorigenic. CSCs would harbor self-renewal capacities and could generate more differentiated progeny, compared to the bulk of the tumor cells (Shibue and Weinberg, Nat Rev Clin Oncol. 2017). Glioblastoma stem cells (GSCs) were therefore described to exhibit self-renewal potential, to propagate tumors and to give rise to rapidly dividing, more differentiated tumor cells (Singh et al., Cancer Res. 2003; Lathia et al., Genes Dev. 2015). Upon therapeutic pressure, GSCs were shown to adapt phenotypically and convert from a proliferative state to a quiescent state with slowed proliferation and stem-like properties, before they produce populations of highly proliferative cells, which repopulate the tumor (Chen et al., Nature 2012). Nowadays, it is increasingly appreciated that cell states may not be definitive, but dynamic. DNA methylation changes in single-cell multi-omics data revealed that cells can dedifferentiate into stem-like cell states, indicating bidirectional cell state transitions (Chaligne et al., Nat

Genet. 2021). Emerging data suggests that GSCs not represent a clonal entity or a discrete singular cell type with distinct properties, but rather a plastic cell state, with fluid cellular phenotypes, that most glioblastoma cells can adopt. Highly adaptable populations were reported to be capable of transient plasticity that takes place in response to therapeutic pressure (as reviewed in Gimple et al., Nat Rev Cancer 2022). Recently, phenotypic plasticity was even recognized as an additional general hallmark of cancer (Hanahan, Cancer Discov. 2022).

As further research on glioblastomas subclonal dynamics and cellular adaptions to therapeutic pressure is needed, we wanted to extend on the approach of a clinical setting in my thesis, by investigating paired tissue and cell samples from the naive glioblastoma status at primary disease (^{naive}cells), in comparison to the corresponding post-therapeutic status of the same glioblastoma patient at disease recurrence (^{cR}cells). In addition, experimental relapse cells ($^{TMZ→eR}$cells) were used, that were established by serial *in vitro* exposure of TMZ to naive patient cell samples every other day for 16 days. Only 10-20% of the original ^{naive}cells survived the drug, and stayed non-proliferative for 3-6 weeks, until clonally expanding populations emerged, referred to as experimental relapse cells ($^{TMZ→eR}$cells) (Figure 4; Kebir et al., Clin Cancer Res. 2023).

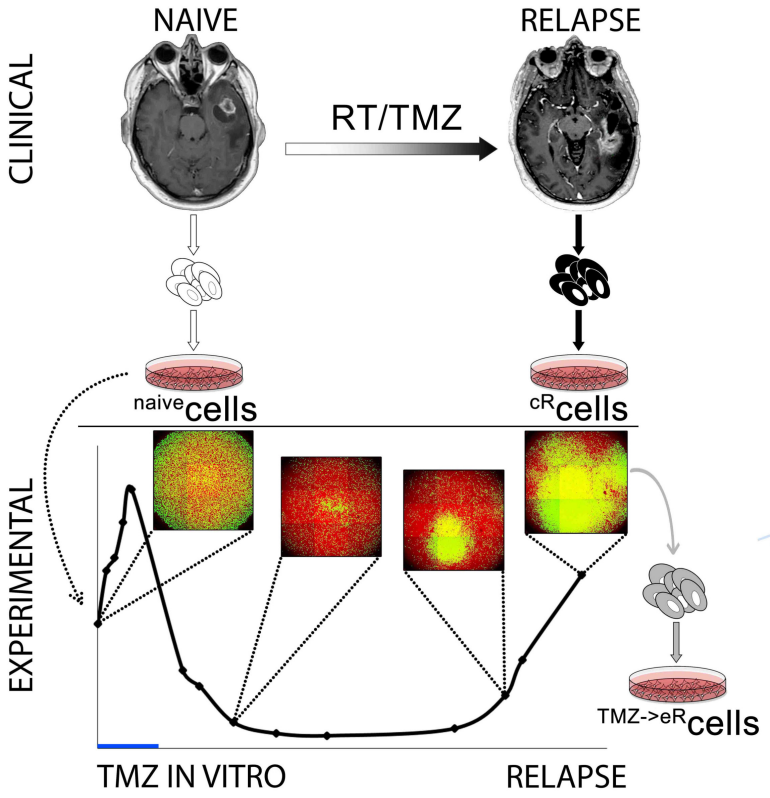

Figure 4: Collection of primary cell samples from surgically extracted treatment-naive, and paired clinical relapse (cR) tumor tissue; experimental relapse (TMZ→eR) cells gained by in vitro exposure to

TMZ (500 µM) every other day for 16 days (blue bar), regrowth 3-6 weeks later monitored by software-based cell recognition (from Kebir et al., Clin Cancer Res. 2023)

Survival of drug-tolerant, but non-proliferative cells after treatment exposure followed by clonal expansion of $^{TMZ \rightarrow eR}$cells observed in this experimental relapse model resembled the behavior of drug-tolerant persisters (DTPs) in lung adenocarcinoma or melanoma models. In these models, dynamic adaptions to therapeutic pressure change the tumor cells phenotype in a reversible manner, keeping them viable, but not proliferative, leading to the development of subpopulations, which persist under therapy (reviewed in Shen et al., Cell 2020).

Originally, Sharma et al. referred to a small fraction of viable cells, that survived from a lung adenocarcinoma cell line after chemotherapy as drug tolerant persisters (DTPs). These cells maintain in a drug-tolerant, but quiescent and slow-cycling state. However, DTPs can acquire drug resistance and resume proliferation again, which are then referred to as drug tolerant expanded persisters (DTEP) (Sharma et al., Cell 2010). Beside slowed proliferation the DTP state is reported to be related to adaptions in cell metabolism, transition from an epithelial towards a mesenchymal cell state, immune cell suppression and changes in the chromatin state performed via epigenetic regulation (Shen et al., Cell 2020).

Epigenetic regulation can lead to substantial variations among subpopulations and allows tumor cells to adapt to therapeutic pressure spontaneously (Marine et al. Nat Rev Cancer 2020). The human chromatin is organized wrapped around histone proteins, consisting of an octamer of the subunits H2A, H2B, H3 und H4. The subunits N-terminal ends can be modified, e.g., by methylation, acetylation, ubiquitylation or phosphorylation (Strahl and Allis, Nature 2000). Post-translational modifications on histones, that regulate gene expression, can be performed and eliminated via antagonizing writer and erasers enzymes. For example, methylgroups are added by methyltransferases and taken away by histone demethylases (Rea et al., Nature 2000). The modifications can alter the accessibility of the chromatin, by induction of chromatin structure changes between the transcription-active euchromatin and the tightly packed heterochromatin. Depending on the specific modification location, chromatin remodeling can either provoke positively or negatively regulated gene transcription. Attachment of Histone 3 lysine 4 (H3K4) methylation to gene promoters and enhancers activates transcription (Li et al., Nature 2016), whereas other trimethylations as of H3K9 or H3K27 are often associated with closed heterochromatic regions and less DNA accessibility (Barski et al., Cell 2007).

Sharma and colleagues, who defined the DTP model for cancer, reported, that the establishment of the DTP state depends on the histone demethylase KDM5A. Knockdown of KDM5A, which would remove H3K4 methylations, reduced the amount of DTEPs after cisplatin treatment, whereas expression of the same decreased the cell´s drug sensitivity (Sharma et al., Cell 2010). By now, the requirement of KDM family members for the survival of DTPs has been studied in multiple cancers. In melanoma another member of the KDM family, namely the H3K4 demethylase KDM5B, was shown to be highly expressed in a dynamic subpopulation of slow-cycling melanoma cells, that harbor cancer stem cell-like features and enable tumor growth (Roesch et al., Cell 2010).

KDM5B was initially discovered as an upregulated gene in breast cancer and was shown to repress tumor suppressor genes, like Breast cancer type 1 (BRCA1) (Yamane et al., Mol. Cell 2007). Later it was shown that KDM5B leads to a closed chromatin structure, leading to transcriptomic heterogeneity and consequently a higher risk of drug-resistance in breast cancer (Hinohara et al., Cancer Cell 2018). By now KDM5B has been reported as an oncogene in various cancer entities, including colorectal cancer (Ohta et al., Int. J. Oncol. 2013), hepatocellular carcinoma (Tang et al., Oncotarget 2015), gastric cancer (Wang et al., Am. J. Cancer Res. 2015), oral cancer (Facompre et al. Cancer Res. 2016), acute lymphoblastic leukemia (Huang et al., Eur. Rev. Med. Pharmacol. Sci. 2018), NSCLC (Kuo et al., Clin. Epigenetics 2018), Ewing sarcoma (Chen et al., Cell Death Dis. 2022) and esophageal squamous cell carcinoma (Wang et al., J. Radiat. Res. 2022).

In glioblastoma, a drug-tolerant, persister-like state has been discovered, similar to the one in melanoma, but characterized by upregulation of the H3K27 demethylase KDM6A (Liau et al., Cell Stem Cell 2017). However, the described effects were observed in response to Receptor Tyrosine Kinase (RTK) inhibitor treatment. Immediate changes of epigenetic regulators under exposure of TMZ, as the gold standard care for glioblastoma, have not been studied yet. Therefore, we investigated if members of the KDM family could play a role in mediating subclonal enrichment upon TMZ, representing an example for adaptive plasticity driving tumor progression.

1.5. Aims and experimental approaches of this thesis

We and others consider that under primary therapy subclonal dynamics take place, driven by dominant subclones, which can either be resistant or sensitive to the treatment. Beside the dynamic subclones, the tumor harbors cells that play a minor role at this point of disease, a static bystander pool of clones. However, under therapeutic pressure the dominant pool is reduced and newly arising subclones, which have been underrepresented before, arise from the bystander pool. As a consequence, the subclonal composition at relapse is differing from the subclonal composition at naive, leading to a totally different disease (Figure 5; Ullrich et al., in revision 2023).

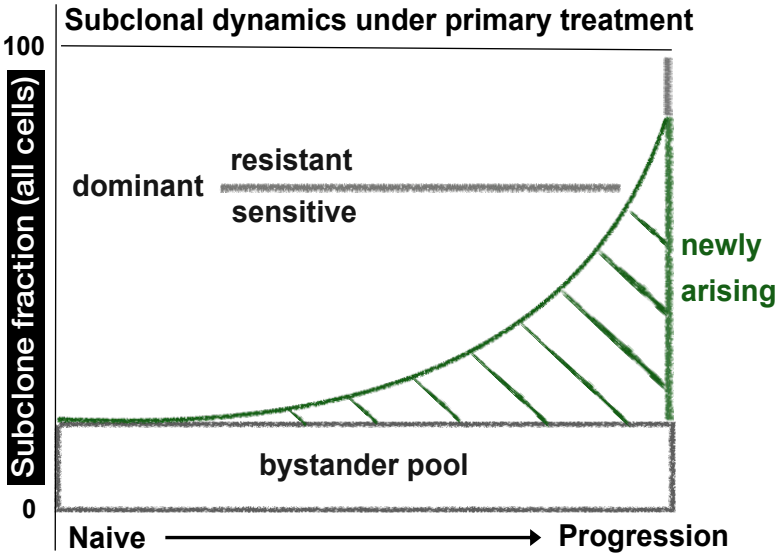

Figure 5: Scheme portraying subclonal dynamics under primary treatment; at disease relapse dominant subclones are reduced and previously rare identities newly arise from bystander pool leading to a change in subclonal composition (from Ullrich et al., in revision 2023).

Understanding the subclonal dynamics and phenotypic cell state transitions under the influence of TMZ, could help to develop strategies, on how to interfere with disease-driving cellular hierarchies along their clinical course. In this thesis, I aimed to investigate, if the specific subclones are traceable, which mechanisms underly the drug resistance and if an interference with the progression is possible. My objective was to enable the prediction of newly arising subclones, which appeared undetectable in the naive tumor, but could expand in response to primary therapy conferring treatment resistance and tumor progression. A main goal was to use this project's translational potential to advance treatment options in future clinical trials and to reduce mortality among glioblastoma patients.

To accomplish the aims of this thesis, I utilized non-immortalized, short-term expanded primary patient cells accessible for controlled experimentation through expansion in vitro. In our lab, we developed culturing methods, which allow preserving the patient specific traits outside of the human organism. Specifically, the phenotypic and genetic characteristics remain stable in single cells from tumor tissue extraction to at least culture passage 20, if they are kept under stem cell-favoring adherent culture conditions (Reinartz et al., Clin Cancer Res 2017). I took advantage of this protocol to study drug-induced subclonal cellular dynamics. By comparing paired patient samples derived from pre- vs. post-treatment on gene expression and on protein levels, I identified TMZ-mediated enrichment of subclones and validated their presence by flow cytometric analyses. I then manipulated targets of these cells, via siRNA-mediated knockdown or pharmacological inhibition, and I characterized the downstream effects on the level of cellular clonogenicity, self-renewal potential, cellular viability, proliferation, and, apoptosis. Based on the obtained data, I developed sequential targeting strategies. Using a fluorescent reporter construct (Roesch et al., Cell 2010), which I stably integrated into clinical cell samples, I observed the rapid TMZ-mediated increase of an epigenetic regulator. Finally, I adopted a DNA-barcoding technology (Bhang et al., Nat. Med. 2015) to monitor immediate subclonal population dynamics in response to TMZ. This allowed the prediction of expansive potential in rare, pre-existing subclones under the influence of TMZ exposure, which then take on an active role as drug-resistant glioblastoma cell population during tumor progression.

2. Results

The following data was published in Kebir et al., Clin Cancer Res. 2023.

2.1. TMZ-induced enrichment of ALDH1A1+ subclones

Former lab members used paired, treatment-naive and (experimental or clinical) relapse cell samples of n=7 glioblastoma patients as a discovery cohort, gene expression microarray analysis revealed eight differentially expressed genes involved in TMZ resistance. The most pronounced upregulated gene in the relapse cell samples was Aldehyde Dehydrogenase 1 Family Member A1 (ALDH1A1), which could be validated on publicly available RNA sequencing data of paired glioblastoma (GLASS cohort, Barthel et al., Nature 2019).

The expression of ALDH1A1 could be confirmed by immunohistochemistry in a validation cohort consisting of paired formalin-fixed paraffin-embedded (FFPE) tissue from n=38 glioblastoma patients, which received either radiotherapy (RT)-only or radiotherapy combined with TMZ (RT/TMZ) as initial treatment after surgical resection. The naive patient tissue displayed rare ALDH1A1+ cells, whereas subclonal-like clusters of ALDH1A1+ cells were enriched in RT/TMZ-relapse tissue, but not in relapse tissue of patients treated with RT-only.

Via ALDEFLUOR-based quantification, a fluorescent reagent system that is used to identify cells expressing high levels of the enzyme ALDH, former lab members could already verify increased ALDH positive cell fractions among experimental relapse cells from serial in vitro TMZ exposure (resulting in $^{TMZ \rightarrow eR}$BN46), but not upon serial in vitro exposure to ionizing irradiation (resulting in $^{RT \rightarrow eR}$BN46) (Kebir et al., Clin Cancer Res. 2023).

As the used ALDEFLUOR-assay detects the conversion of the substrates by all members of the ALDH family, in this work a more specific detection via an FITC-coupled antibody against the ALDH1A1 isoform via flow cytometry was performed, in order to validate the previous data. Antibody-based flow cytometric analyses of patient cells were performed as described in Methods chapter “5.5.4. Flow cytometric analysis”. A naive sample of patient BN46 (^{naive}BN46) was compared to experimental relapse cells, derived from ^{naive}BN46 cells by serial exposure to ionizing irradiation ($^{RT \rightarrow eR}$BN46), and additionally, through serial exposure to TMZ (500 µM) ($^{TMZ \rightarrow eR}$BN46).

The samples were analyzed for their ALDH1A1 expression levels by determining the mean fluorescence intensity (MFI) of the ALDH1A1 antibody-labeled cells.

The exemplary stacked FACS histograms for ^{naive}BN46 cells and $^{TMZ→eR}$BN46 cells in Figure 6 (left) demonstrate an increase of the antibodies fluorescence intensity, evident as a marked right-shift of the Alexa-Fluor 488 peak in the $^{TMZ→eR}$BN46 cells but not in the $^{RT→eR}$BN46 compared to ^{naive}BN46. This finding supported the idea that TMZ mediated the increase of ALDH1A1 expression. To determine the ALDH1A1 expression the MFI was normalized to the corresponding isotype control using the formula (MFI(ALDH1A1)-MFI(Isotype))/MFI(Isotype) multiplied by 100. The ALDH1A1 expression (normalized MFI) increased from ^{naive}BN46 to $^{TMZ→eR}$BN46 with a mean fold change (mFC) of 37.0 ((mean(relapse)-mean(naive))/mean(naive)). As opposed to this, the ALDH1A1 expression did not increase in $^{RT→eR}$BN46 cell samples (Figure 6 right plot).

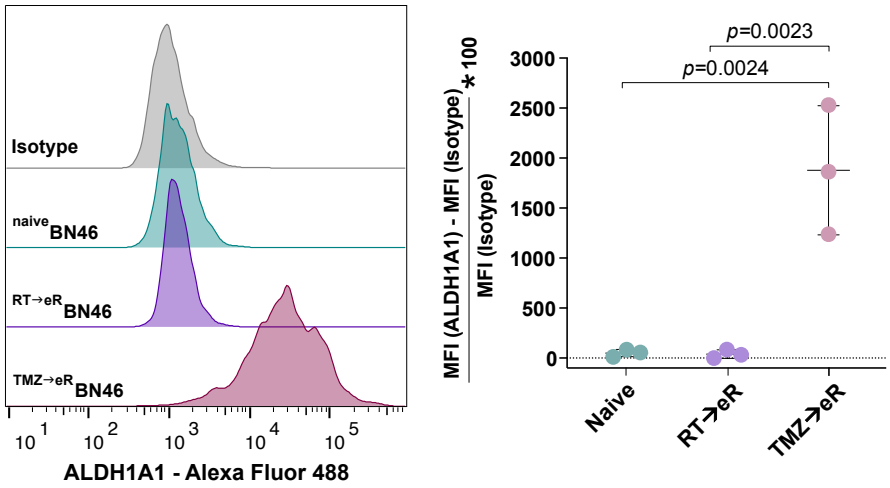

Figure 6: Left: "Histograms represent ALDH1A1 flow cytometry data from naive vs. experimental relapse BN46 cells." Isotype control shown in gray; Right: "Dotplot shows ALDH1A1 mean fluorescence intensity (MFI) in paired BN46 treatment-naive vs. experimental relapse conditions (in vitro exposure to TMZ (TMZ→eR) or irradiation (RT→eR)). Data are normalized to isotype control, mean ± SD. p values calculated by Kruskal-Wallis test with Dunn's post-hoc test" (adapted from Kebir et al., Clin Cancer Res 2023).

When comparing the ALDH1A1 expression, detected via the MFI, in paired treatment-naive vs. clinical relapse cell samples (BN91, BN118, BN123, BN132), a strong increase was observed in four out of four clinical relapse cell samples, depicted in purple, compared to the paired treatment-naive cell samples, shown in petrol (Figure 7 Upper panel). After normalization to the corresponding isotype controls, shown in grey, the most pronounced significant increase of ALDH1A1 expression (normalized

MFI) was observed in patient cell samples ^{cR}BN91 with a mFC of 84.0 compared to naive cell samples. Cell samples of BN118 displayed a significant increase with a mFC of 32.3. In cell samples from BN123 and BN132 the increase of the normalized MFI was not statistically significant, but presented the same trend: ^{cR}BN123 cell samples exhibited the least increase with a mFC of 0.9 and ^{cR}BN132 cell samples increased with a mFC of 2.2 (Figure 7 Lower panel).

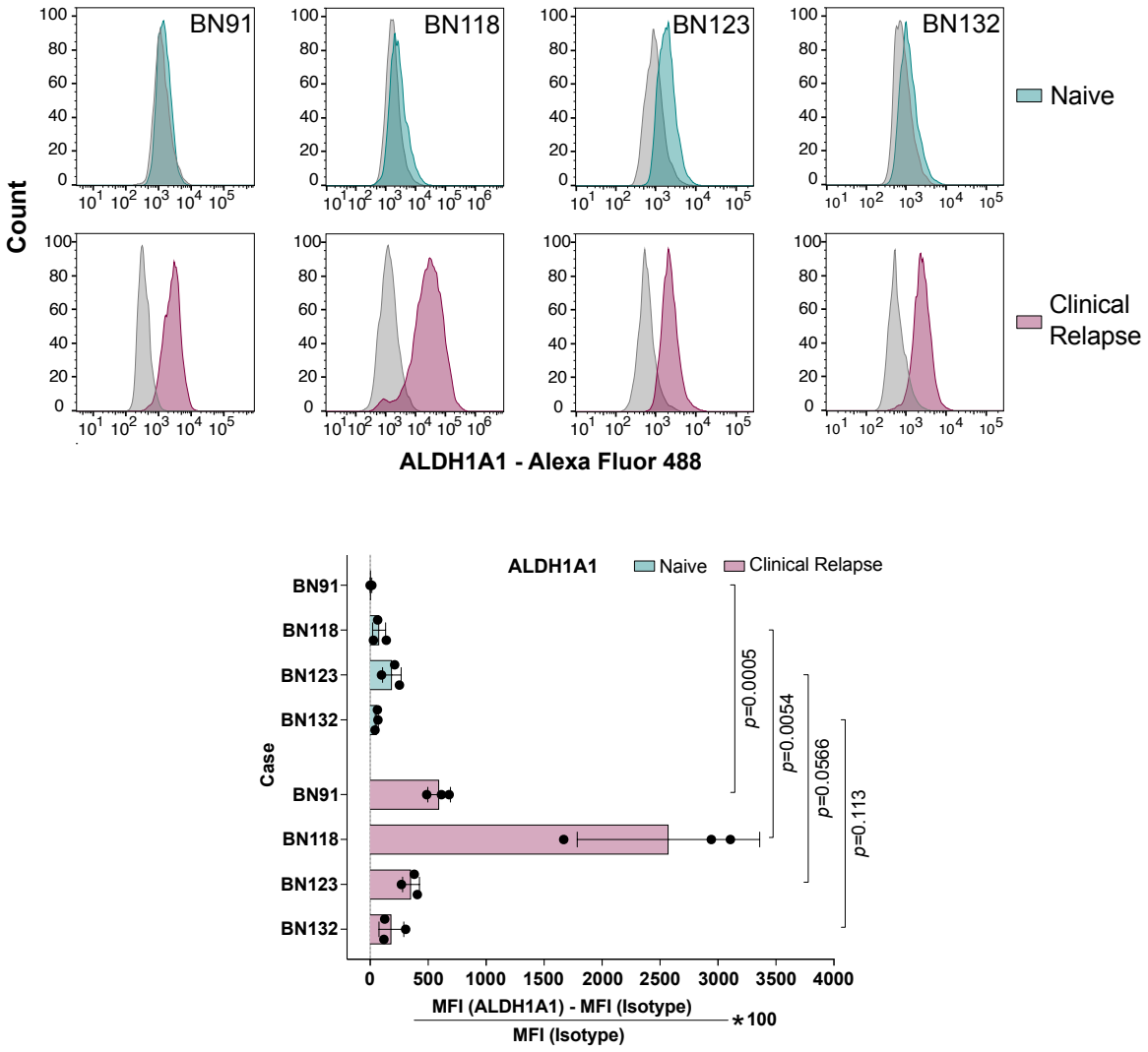

Figure 7: Upper Panel: "Flow cytometry histograms showing ALDH1A1 expression in the paired treatment-naive vs. clinical relapse patient samples quantified in" the bar charts (lower panel). Isotype controls shown in gray; Lower panel: " Bar chart represents ALDH1A1 mean fluorescence intensities (MFI) normalized to isotype control in paired treatment-naive vs. clinical relapse patient cell samples measured by flow cytometry. Mean ± SD. p values obtained by pairwise comparisons using Wilcoxon´s test, adjusted for multiple testing" (adapted from Kebir et al., Clin Cancer Res 2023).

2.2. Clonogenicity and self-renewal under the influence of knockdown or overexpression of ALDH1A1

Former lab members demonstrated that pharmacological inhibition of ALDH with diethylaminobenzaldehyde (DEAB) or knockdown of ALDH1A1 expression using short-hairpin RNA (shRNA) could delay recurrent growth of patient cells after TMZ-exposure. By contrast, ALDH1A1 overexpressing cells recovered earlier from TMZ exposure than corresponding naive cells transduced with green fluorescent protein (GFP) instead. However, when co-cultures of ALDH1A1-overexpressing (ALDH1A1 Ovx) and GFP-control cells (GFP Ctrl) were exposed to TMZ, their initial drug response kinetics was similar. This suggested that treatment-naive patient cells were not inherently resistant to TMZ (Kebir et al., Clin Cancer Res. 2023).

To confirm this observation and to extend the functional characterization, a limiting dilution analysis (LDA) was conducted, where ALDH1A1 overexpressing (ALDH1A1 Ovx) and shRNA-mediated ALDH1A1 knockdown (shALDH1A1) cells, generated from ^{naive}BN46 cells, were analyzed for their ability to expand clonally. Prior to conducting the experiments, stability and extent of ALDH1A1 overexpression and ALDH1A1 knockdown, respectively, were verified using qPCR (see Methods, chapter “5.5.3. Quantitative polymerase chain reaction (qPCR)”). ALDH1A1 gene expression was increased by 50-fold in the ALDH1A1 Ovx cells compared to the GFP Ctrl cells, while ALDH1A1 gene expression was decreased by 0.75 fold (75%) in shALDH1A1 cells compared to shNT control cells (Supplementary Figure 1).

For each of the experimental conditions, 0.5 cells/well were seeded in 96-well plates. The number of clones per plate and the number of cells per monoclonal colony were assessed using an automated cell imager after 16 days. Also, the estimated doubling time was calculated, considering an exponential cell growth (see Methods, chapter “5.5.6. Limiting dilution analysis” for further details). shALDH1A1 cells showed less clones per plate (shALDH1A1 = 1.6±1 vs shNT = 2.4±1; not significant) and less cells per colony (shALDH1A1 = 15.5±7 vs. shNT = 22.9±5; not significant) compared to the shNT control cells. The estimated doubling times were non significantly higher with a mean of 4.4±1 days per cell division in shALDH1A1 cells compared to a mean of 3.6±0.2 days per cell division in the shNT control cells. ALDH1A1 Ovx cells exhibited the same number of clones per plate (ALDH1A1 Ovx = 2±2 vs. GFP Ctrl = 2±2 ; not significant) but more cells per colony (ALDH1A1 Ovx = 26.9±6 vs. GFP Ctrl = 23.3±7;

not significant). The estimated doubling times were not significantly lower with a mean of 3.4±0.2 days per cell division in ALDH1A1 Ovx cells compared to a mean of 3.6±0.3 days per cell division in the GFP Ctrl cells. To conclude, neither ALDH1A1 knockdown nor ALDH1A1 overexpression did significantly influence the ability of treatment-naive cells to form monoclonal populations (Figure 8).

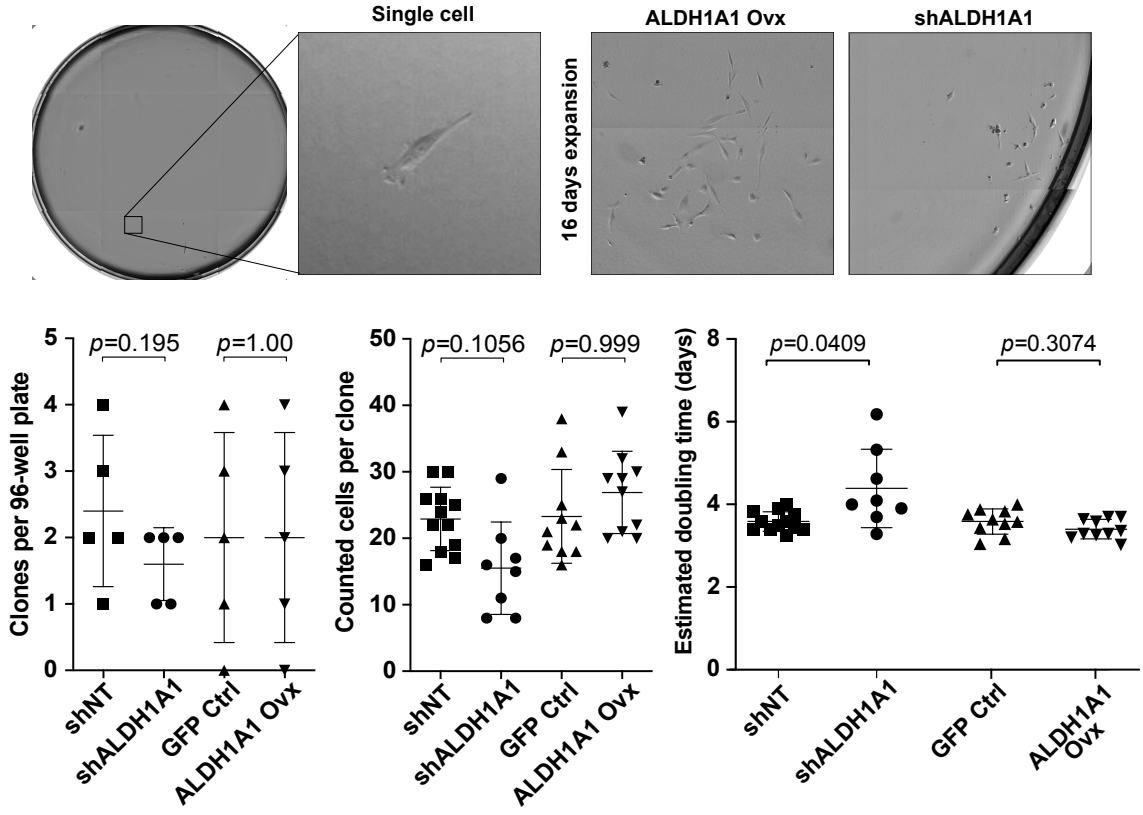

Figure 8: "Limiting Dilution Assay evaluating clonal expansion of individually plated naiveBN46 shALDH1A1 and naiveBN46 ALDH1A1 Ovx cells and their respective controls". Upper panel: "Brightfield image of BN46 cells in 96-well plates during monitoring by software-based cell recognition in the limiting dilution assay (NyOne®). An exemplary single cell/well is shown at one day post seeding; representative monoclonal colonies of ALDH1A1-knockdown (sh) and -overexpressing (Ovx) cells at day 16 after seeding". Lower panel: left dotplot = counted clones per 96-well plate, middle dotplot = counted cells per clone, right dotplot = estimated doubling time; for all three dotplots data shown as mean ± SD; Left and middle dotplot: p values obtained by pairwise comparisons using Wilcoxon test, adjusted for multiple testing; Right dotplot: P values calculated by Kruskal-Wallis test with Dunn's post-hoc test" (adapted from Kebir et al., Clin Cancer Res 2023).

Following the LDA, neurosphere assays were carried out to analyze the clonogenic and self-renewal capacities of ^{naive}BN46 ALDH1A1 Ovx cells and ^{naive}BN46 shALDH1A1 cells (see Methods, chapter "5.5.7. Neurosphere assay"). It is widely accepted that in the assay, the frequency of 1º neurospheres indicates clonogenic capacity, while the fold change of 1º vs. 2º neurospheres can be regarded as an estimation of their self-renewal capacity. Furthermore, immunofluorescence (IF)

analysis of the 2º neurospheres can indicate (multi)potency when glial and neuronal cells coincide (glial fibrillary acidic protein (GFAP) = glial cells, β3-tubulin = neuronal cells). The fraction of neurosphere-forming cells per well was determined via automated cell imaging 12 days after seeding.

Comparable to the LDA no significant difference could be detected after ALDH1A1 knockdown or ALDH1A1 overexpression. shALDH1A1 cells exhibited a lower fraction of neurosphere-forming cells with 0.9±0.05 % compared to 1.4±0.04 % in the shNT cells (not significant), whereas ALDH1A1 Ovx cells showed slightly higher 1.7±0.03 % of neurosphere forming cells compared to 1.5±0.07 % in the GFP Ctrl cells (not significant). The self-renewal capacity was not significantly changed with a fold change from the 1º to the 2º generation of neurospheres, of 2.12 in the ALDH1A1 Ovx cells compared to 2.15 in the GFP Ctrl cells and 2.67 in the shALDH1A1 cells compared to 2.31 in the shNT control cells. IF analysis of all the analyzed 2º neurospheres revealed coinciding GFAP- and β3-tubulin-expressing cells (Figure 9).

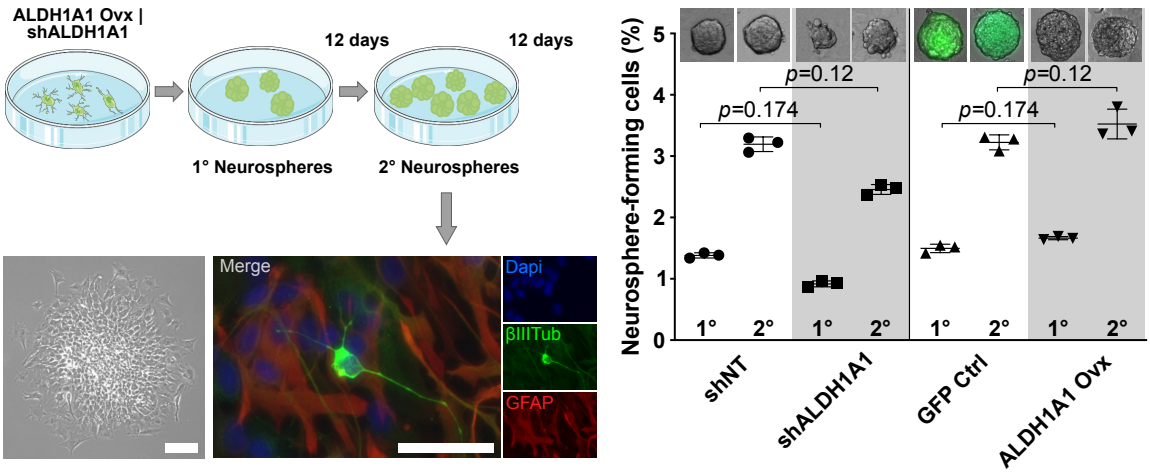

Figure 9: "Neurosphere assay evaluating 1° and 2° neurosphere generation of naiveBN46 shALDH1A1 and naiveBN46 ALDH1A1 Ovx cells and their respective controls; Cartoon describes the neurosphere experiments. Phase contrast microscopic appearance of plated 2° neurosphere and respective immunofluorescence visualization of antibody labeling on neurosphere-derived cells. Neuronal phenotype, β3-tubulin (β3-tub); glial phenotypes, glial fibrillary acidic protein (GFAP). Nuclei exposed with DAPI. Scale bars: left: 100 µM, right: 50 µM"; Right: "Dotplot shows estimation of neurosphere-forming cell frequencies from counting generated neurospheres 12 days after seeding of cells. Upper insets: Phase contrast appearance of respective neurospheres"; "mean ± SD. p values obtained by pairwise comparisons using Wilcoxon's test, adjusted for multiple testing" (adapted from Kebir et al., Clin Cancer Res 2023).

Our data obtained in ^{naive}BN46 cell samples suggested that neither ALDH1A1 knockdown nor ALDH1A1 overexpression significantly impact the cells clonogenicity, self-renewal capacities and multipotency, at least in ^{naive}cell samples. Speculating that ALDH1A1 positive cells might alter only after exposure to TMZ, the neurosphere assay

was repeated in paired patient cell samples BN46 (^{naive} vs. $^{TMZ→eR}$) as well as BN118 and BN123 (^{naive} vs. ^{cR}). To ensure knockdown of ALDH1A1 during the initial neurosphere-forming period the paired cell samples were treated four days prior neurosphere seeding with a small interfering RNA (siRNA) pool against ALDH1A1 (siALDH1A1) or a non-targeting pool (siNT), that served as a control. During neurosphere seeding, an additional siRNA transfection was performed, as shown in the Cartoon (Figure 10) (see Methods, chapter "5.5.7. Neurosphere assay"). The efficiency of siRNA-based ALDH1A1 knockdown was verified using qPCR (see Methods, chapter "5.5.3. Quantitative polymerase chain reaction (qPCR)") in ^{naive}BN46, ^{naive}BN118 and ^{cR}BN118 cells before the experiment was conducted. In siALDH1A1 cells ALDH1A1 gene expression was reduced by 0.67 fold (^{naive}BN46), 0,95 fold (^{naive}BN118) and 0,92 fold (^{cR}BN118) compared to the siNT control (Supplementary Figure 2).

For the neurosphere assay, the number of neurosphere-forming cells within the siALDH1A1 cell samples was measured in the first as well as in the second generation and normalized to the corresponding siNT control cells. Whereas the fraction of neurosphere-forming ^{naive}cells was nearly unchanged after siALDH1A1 knockdown, the ^{cR}cell samples (^{cR}BN118 and ^{cR}BN123) exhibited a decrease of neurosphere-forming cells of 70±4 % in the first and 69±7 % in the second generation compared to siNT control ^{cR}cells (Figure 10 left bar chart). In $^{TMZ→eR}$BN46 a reduction of neurosphere-forming cells by 48±2 % in the first generation and by 56±7 % in the second generation could be displayed after siALDH1A1 compared to siNT (Figure 10 right bar chart). So that in three out of three relapse cell samples (^{cR} and $^{TMZ→eR}$) an effect of the ALDH1A1 knockdown on the cell´s clonogenicity was exposed, while no significant reduction in the cell´s clonogenicity could be detected after ALDH1A1 knockdown in three out of three ^{naive}cell samples.

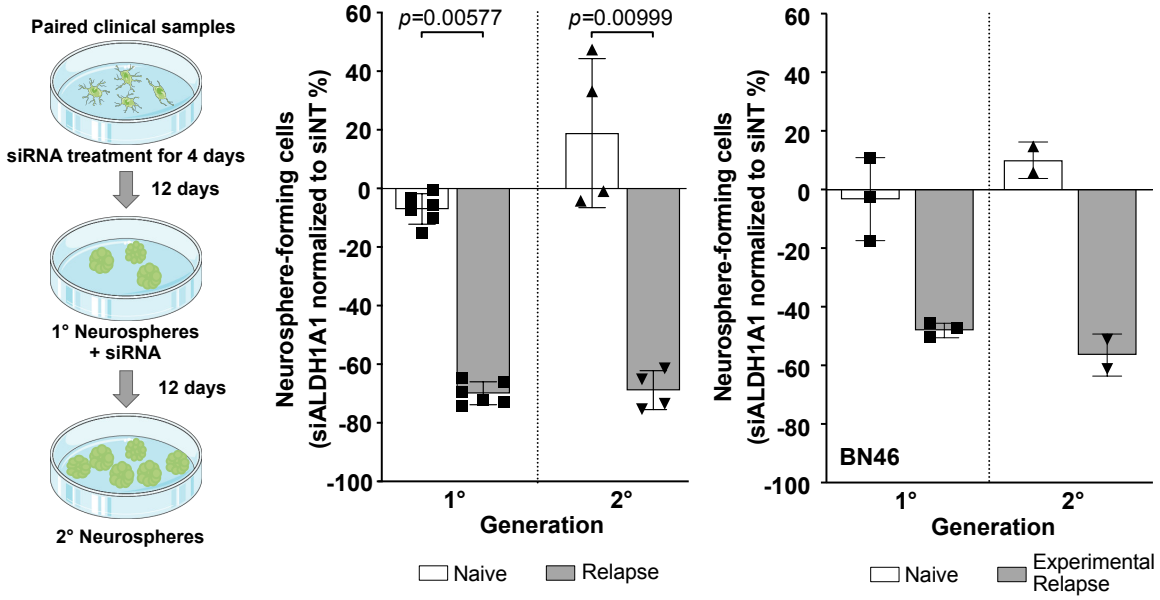

Figure 10: "Cartoon illustrating course of neurosphere experiments, applying treatment-naive and paired experimental and clinical relapse patient cells". Left bar chart: "Neurosphere assay of ALDH1A1 siRNA and non-targeting control (siNT) of paired treatment- naive vs. clinical relapse cell samples (BN118, BN123). Individual data points represent triplicates (1°) and duplicates (2°) per case. Results normalized to siNT and shown as mean ± SD. p values obtained by pairwise comparisons using Wilcoxon's test, adjusted for multiple testing". Right bar chart: "paired treatment-naive vs. experimental relapse (TMZ→eR) BN46 cells. Data as mean ± SD" (adapted from Kebir et al., Clin Cancer Res 2023).

2.3. Acquisition of pAKT in ALDH1A1+ subclones

Former lab members conducted a gene set enrichment analysis (GSEA) of paired patient cell samples, which exposed that the PI3K/AKT pathway is more frequently enriched in the relapse samples. This could be confirmed by Western blot analysis in which elevated ALDH1A1 protein levels, as well as elevated levels of phosphorylated protein kinase B (pAKT) (Ser473) and its downstream target phosphorylated glycogen synthase kinase-3 beta (pGSK3ß) were detected in relapse cell samples compared to the paired treatment-naive cell samples. The negative regulator of pAKT, phosphatase and tensin homolog (PTEN) showed a strongly decreased abundance in relapse cell samples (Kebir et al., Clin Cancer Res. 2023).

Using flow cytometry, an increase of AKT phosphorylation at Ser473 (called ´pAKT´ later on) was confirmed in $^{TMZ→eR}$BN46 cell samples compared to ^{naive}BN46, detected via a PE-coupled antibody against pAKT (Ser473). The antibody-based flow cytometric analyses of patient cell samples were performed as described in Methods chapter "5.5.4. Flow cytometric analysis". Exemplary stacked FACS histograms for ^{naive}BN46 cells and $^{TMZ→eR}$BN46 cells are shown. Compared to the isotype controls,

shown in grey, the fluorescent intensity of the PE antibody signal, was increased in the $^{TMZ→eR}$BN46 cell sample, depicted in purple, compared to the ^{naive}BN46 cell sample, presented in petrol (Figure 11 left). The samples were analyzed for their pAKT levels by determining the mean fluorescence intensity (MFI) of the antibody-labeled cells. The MFI was normalized to the corresponding isotype control using a similar formula, as for the antibody-based ALDH1A1 detection: (MFI(pAKT)-MFI(Isotype))/MFI(Isotype) multiplied by 100. The pAKT expression (normalized MFI) increased from ^{naive}BN46 to $^{TMZ→eR}$BN46 with a mean fold change (mFC) of 1.1 ((mean(relapse)-mean(naive))/mean(naive)) (Figure 11 right plot).

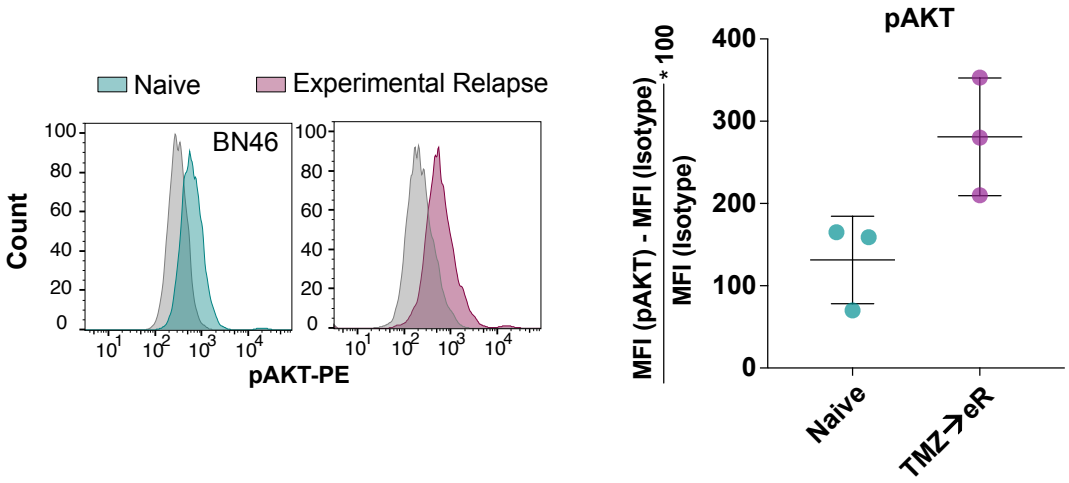

Figure 11: Left: "Flow cytometry histograms of pAKT(Ser473)" Right: "quantification of data derived from treatment-naive and paired experimental relapse (TMZ→eR) BN46 cells. Data represent mean fluorescence intensities (MFI), ± SD, normalized to isotype control (gray)" (adapted from Kebir et al., Clin Cancer Res 2023).

Comparable to the $^{TMZ→eR}$cells, a significant increase of pAKT expression, detected via the MFI, could be observed in four out of four clinical relapse cell samples (BN91, BN118, BN123, BN132), depicted in purple, compared to the paired treatment-naive cell samples, shown in petrol (Figure 12 Upper panel). After normalization to the corresponding isotype controls, shown in grey, pAKT expression differences were observed between the different patient cases in the ^{naive}cell samples. ^{naive}BN118 presented the highest pAKT expression (MFI normalized to isotype = 289.33). In ^{naive}BN91 cell samples and ^{naive}BN132 cell samples, no fluorescence intensity compared to the isotype control could be determined, corresponding to no detectable pAKT expression via the pAKT antibody-labeling. In the paired ^{cR}cell samples the normalized MFI increased to 504.7 in ^{cR}BN91 and to 245.7 in ^{cR}BN132 (significant increase compared to ^{naive}cells). In ^{cR}BN118 cell samples the normalized MFI increased significantly compared to ^{naive}BN118 cell samples with a mFC of 2.1 and in

^{cR}BN123 cell samples compared to ^{naive}BN123 cell samples with a mFC of 19.0 (Figure 12).

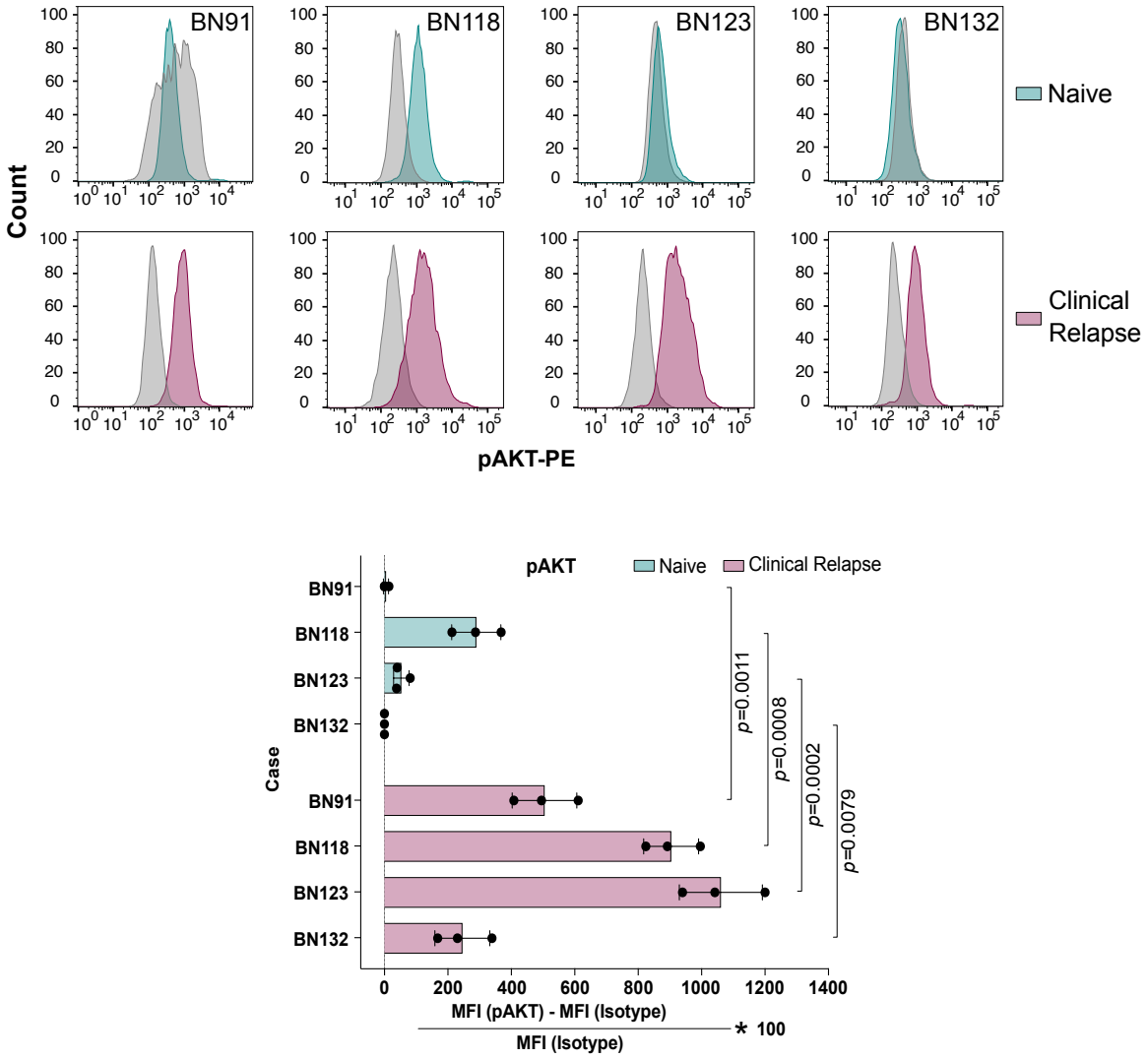

Figure 12: Upper panel: "Flow cytometry histograms depicting pAKT (Ser473) expression in the paired treatment-naive vs. clinical relapse patient samples quantified in" the bar charts (lower panel). Isotype controls shown in gray; Lower panel: "Bar chart represents pAKT (Ser473) MFI normalized to isotype control in paired treatment-naive vs. clinical relapse patient cell samples measured by flow cytometry. Mean ± SD. p values obtained by pairwise comparisons using Wilcoxon´s test, adjusted for multiple testing" (adapted from Kebir et al., Clin Cancer Res 2023).

Co-expression of antibody-labeled ALDH1A1 and pAKT was analyzed using flow cytometry. ALDH1A1 was detected using a FITC-coupled ALDH1A1 antibody and measured in the Alexa-Fluor 488 channel and pAKT was detected using a PE-coupled antibody in the PE channel. The co-labeling exhibited low fractions of cells that were positive for ALDH1A1 (Alexa Fluor 488) and positive for pAKT (PE) within the ^{naive}cell samples. To evaluate the mFC of ALDH1A1+/pAKT+ cells between the ^{naive}cell samples and the ^{cR} or $^{TMZ→eR}$cell samples, the gating for each ^{naive}cell sample was set

to a fraction of 5 % double-positive (Alexa Fluor 488+/PE+) cells within the total cell population and was then applied to the corresponding relapse sample (see Methods, chapter “5.5.4. Flow cytometric analysis”).

^{naive}BN46 cells were compared with the corresponding experimental relapse specimens of patient BN46 ($^{RT→eR}$ and $^{TMZ→eR}$). In the $^{RT→eR}$BN46 cell sample the fraction of co-expressing cells was decreased compared to the ^{naive}BN46 cell sample, while in the $^{TMZ→eR}$BN46 cells the fraction of ALDH1A1+/pAKT+ double positive cells was increased compared to the ^{naive}BN46 cell sample with a mFC of 3.1 (Figure 13).

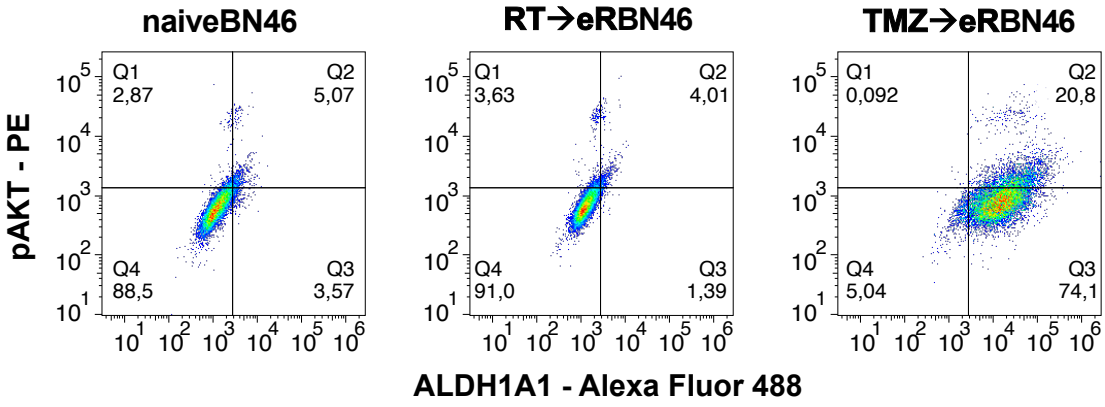

Figure 13: “Flow cytometry profiles of ALDH1A1/pAKT (Ser473)-labeled, paired treatment-naive vs. experimental relapse conditions of BN46 cells (in vitro exposure to TMZ (TMZ→eR) or irradiation (RT→eR))” (adapted from Kebir et al., Clin Cancer Res 2023).

In three out of four clinical relapse cell samples (BN91, BN118, BN123, BN132) the increase of ALDH1A1/pAKT (Alexa Fluor 488/PE) double positive cells was significant. ^{cR}BN118 cell samples displayed the highest fraction of ALDH1A1+/pAKT+ among all cells (44.83 %; significant), which represents a mFC of 7.9 compared to the respective ^{naive}BN118 cell samples. In ^{cR}BN91 cell samples a mFC of 3.8 (24.27 %; significant) and in ^{cR}BN123 cell samples a mFC of 2.8 was detected (18.87 %; significant) compared to the respective ^{naive}cell samples. For the ^{cR}BN132 cell samples, a mFC of 3.8 was measured (24.27 %), which was not significant, but showed the same trend of an increase of ALDH1A1/pAKT double positive cells in the ^{cR}cell samples (Figure 14).

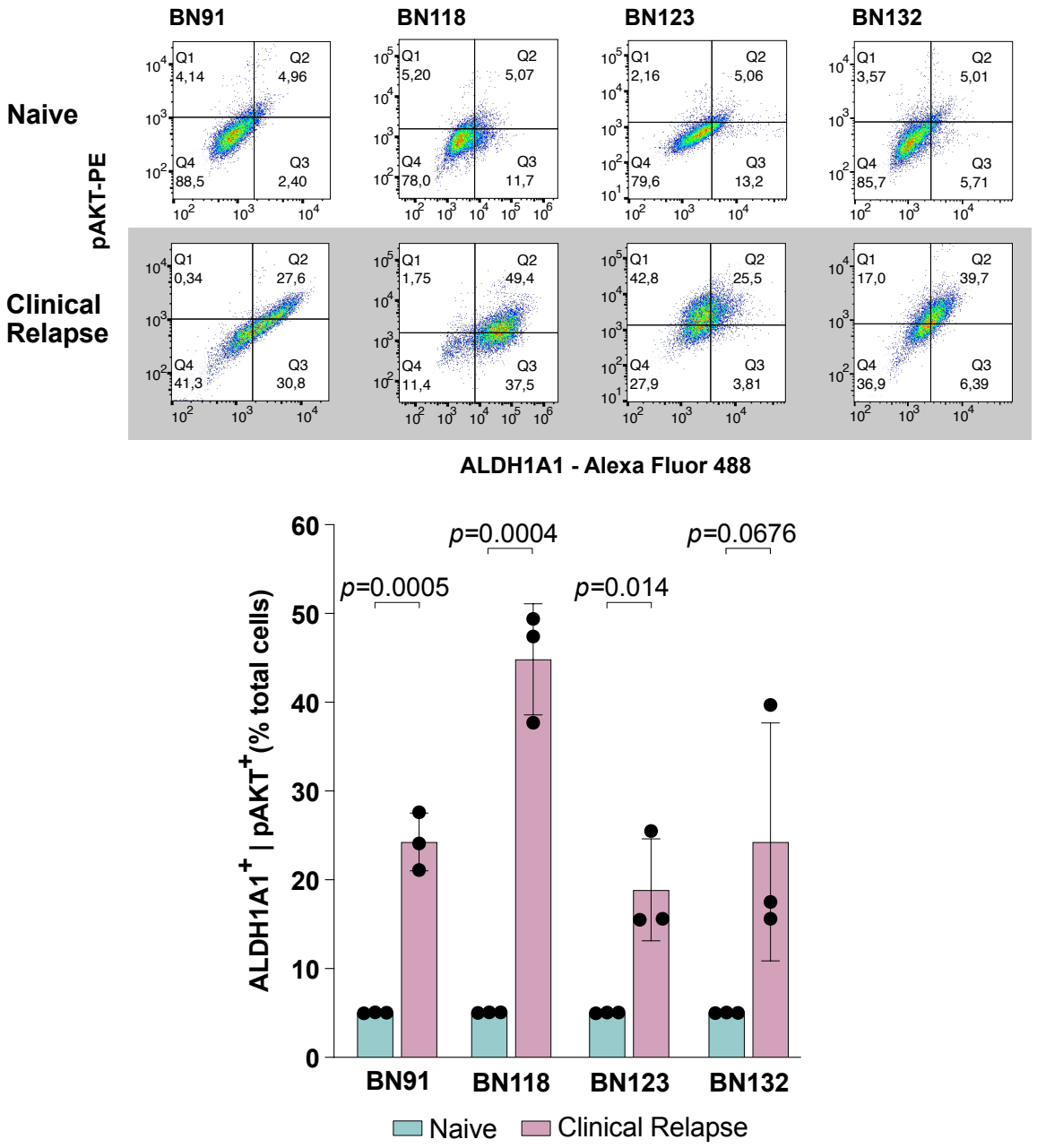

Figure 14: Upper panel: "Flow cytometry profiles of ALDH1A1/pAKT (Ser473)-labeled, paired treatment-naive vs. clinical relapse cell samples"; Lower panel: "Bar chart showing percent ALDH1A1/pAKT (Ser473) co-expressing cells as determined by flow cytometry in paired samples (treatment-naive vs. clinical relapse). Data shown as mean ± SD, p values calculated using a Kruskal–Wallis test followed by Dunn´s post-hoc test" (adapted from Kebir et al., Clin Cancer Res 2023).

Other members of the lab confirmed the increase of ALDH1A1+ cells in clinical glioblastoma relapse tissue and also established a morphological correlation to ALDH1A1/pAKT co-expressing cells *in situ*. In naive tissue, rare ALDH1A1+ cells were detected, while accumulation of ALDH1A1+ cells, co-expressing pAKT occurred in patient relapse tissue as well as in PDX models of disease upon TMZ exposure (Kebir et al., Clin Cancer Res. 2023).

2.4. Targeting ALDH1A1+/pAKT+ cells

To test for strategies targeting the relapse-enriched subclones, paired cell samples of case BN46 (^{naive}BN46 vs. $^{TMZ→eR}$BN46) were exposed to TMZ (500 µM every other day) and their course of cellular confluence was analyzed under TMZ treatment. A set of Dimethyl sulfoxide (DMSO) (0.5 %) treated samples were added to preclude influence of the solvent. The cell confluence was measured using an automated cell imager (see Methods, chapter "5.5.1 Cell Confluence measurement"). The relative cell confluence was computed by normalizing each data point to the respective value of cell confluence on day 0. ^{naive}BN46 cells were sensitive to TMZ, noticeable by a strong decrease in cell confluence to 27 % after a 16 day-exposure of the drug, while TMZ pre-exposed $^{TMZ→eR}$BN46 samples had higher degrees of resistance to TMZ revealing a cellular confluency of 83 % at day 16 of the experiment (Figure 15).

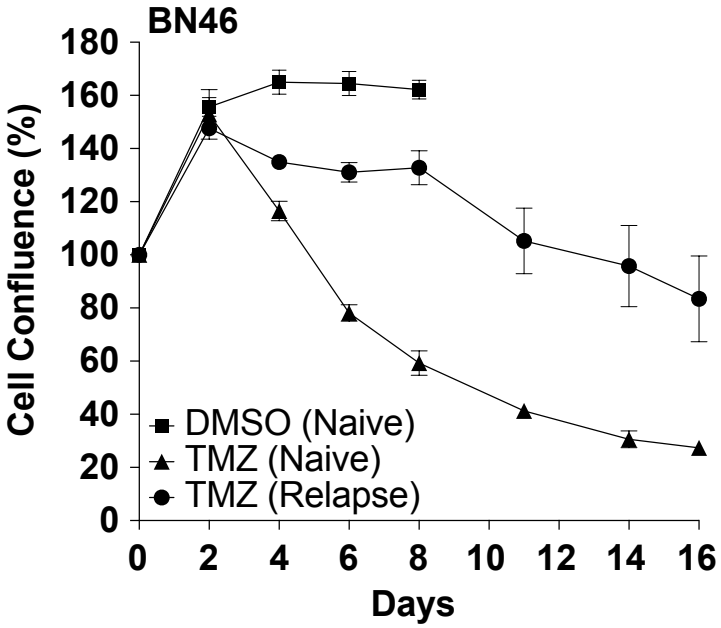

Figure 15: "Graph shows percent in vitro cell confluence of paired naive vs. experimental relapse cells (BN46) treated with control DMSO (0.05%) vs. 500 µM TMZ (software-based cell recognition, NyOne®). Data shown as mean ± SD of n=3 technical replicates". (adapted from Kebir et al., Clin Cancer Res. 2023).

As ALDH1A1/pAKT double positive cells were increased in all relapse cell samples, the specific subpopulation was targeted via inhibiting AKT, thereby indirectly targeting ALDH1A1+ cells. The allosteric inhibitor MK2206, that inhibits phosphorylation of AKT (Janku et al., Nat Rev Clin Oncol 2018), was used. Comparable to the experimental setup in Figure 16, the course of cellular confluence was measured under the influence of TMZ (500 µM) vs. TMZ (500 µM) + MK2206 (5 µM) (every other day), for 8 days *in vitro*. Each measured data point was normalized

to the corresponding DMSO control (0.5 %) value, to preclude influence of the solvent. Application of TMZ reduced the cell confluence of ^{naive}cell samples by 83.3±0.8 % (^{naive}BN46), 66.4±2 % (^{naive}BN118) and 62±7 % (^{naive}BN132) at the endpoint of the measurement (Figure 17). By contrast, relapse samples responded less to TMZ application, i.e., by a decrease of 31.3±3 % ($^{TMZ→eR}$BN46), 2.7±16 % (^{cR}BN118), 22.8±7 % (^{cR}BN123) and 47.2±4 % (^{cR}BN132). When combined TMZ and MK2206 were applied to ^{naive}cell samples no significant additive-negative effect on the cell confluence was detected compared the TMZ-only schedule after a 8 day-exposure of the drugs. In contrast, in relapse cell samples, the cell confluence significantly decreased upon combinatorial treatment with TMZ and MK2206 by additional 38.5±1.8 % ($^{TMZ→eR}$BN46), 55.7±14 % (^{cR}BN118), 30.7±8 % (^{cR}BN123) and 44.1±4 % (^{cR}BN132) compared to the TMZ-only schedule (Figure 16).

To conclude inhibiting phosphorylation of AKT using MK2206 in combination with TMZ reverted the increased levels of TMZ resistance in experimental ($^{TMZ→eR}$BN46) and clinical (^{cR}BN118, ^{cR}BN123, ^{cR}BN132) relapse cells. On the contrary in ^{naive}cell samples the administration of MK2206 in addition to TMZ did not reduce the cell confluence compared to the TMZ-only schedule.

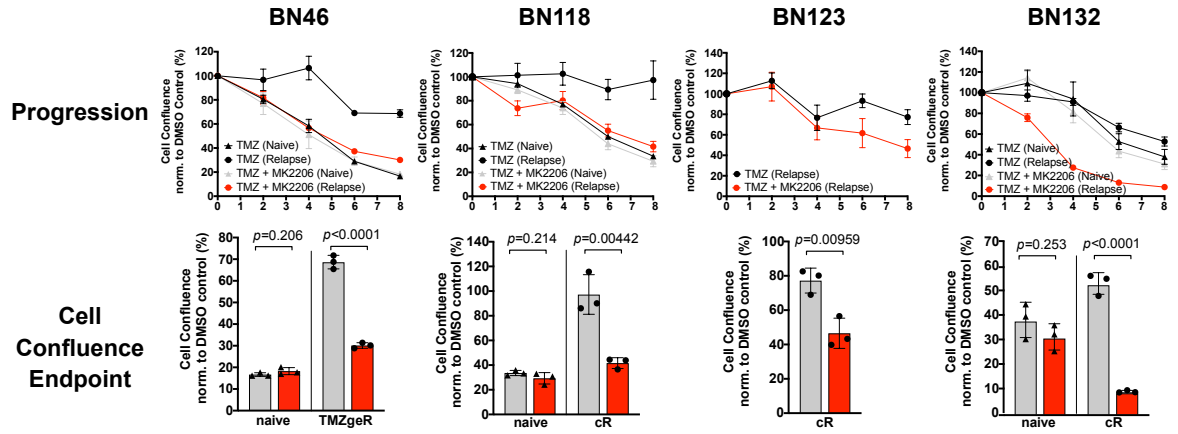

Figure 16: Upper panel, "diagrams: in vitro cell confluence dynamics of paired treatment naive vs. TMZ-related experimental (TMZ→eR; BN46) or clinical (RT/TMZ; BN118, BN123, BN132) relapse patient cells. Monitoring of cell confluence by software-based cell recognition."; „treated with TMZ (500 µM) vs. TMZ (500 µM) + MK2206 (5 µM). Data normalized to DMSO-control and shown as mean ± SD, n=3 technical replicates"; Lower panel, graphs: NyOne-readout results from the indicated cases; Cell Confluence on day 8. "Data as mean ± SD. p values calculated by pairwise Wilcoxon rank-sum test followed by multiple testing correction using Benjamini-Hochberg method". (adapted from Kebir et al., Clin Cancer Res 2023).

After additional 2 days, at day 10 of the treatment scheme (TMZ (500 µM) vs. TMZ (500 µM) + MK2206 (5 µM); given every other day), the cell viability was investigated via AlamarBlue™ assay (see Methods, chapter "5.5.2. Cell viability

assessment"). In ^{naive}cell samples the cell viability was reduced by 62.3±2 % (^{naive}BN46), 59.3±3 % (^{naive}BN118) and 77.3±5 % (^{naive}BN132) through TMZ-only, compared to the DMSO control (0.5 %). In relapse cell samples TMZ-only reduced the cell viability, i.e., by a decrease of 11,5±4 % ($^{TMZ→eR}$BN46), 0±3 % (^{cR}BN118), 8.7±13 % (^{cR}BN123) and 50.4±3 % (^{cR}BN132).

When MK2206 was administered in combination with TMZ no significant additive effect on the cell viability was detectable in ^{naive}cell samples (^{naive}BN46, ^{naive}BN118, ^{naive}BN132). In contrast in relapse cell samples the combinatorial treatment TMZ+MK2206 decreased the cell viability significantly by additional 40.6±7 % ($^{TMZ→eR}$BN46), 52.1±4 % (^{cR}BN118), 67.9±18 % (^{cR}BN123) and 48.7±3 % (^{cR}BN132) compared to TMZ-only (Figure 17).

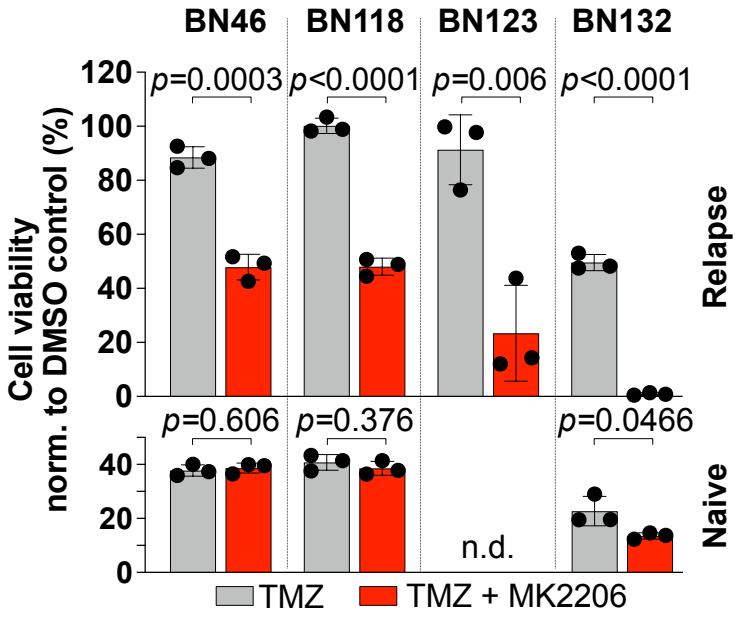

Figure 17: "Bar plots show cell viability readouts on day 10 (alamarBlueTM) for samples described in" Fig 16. "Data were normalized to DMSO-control and shown as mean ± SD of n=3 replicates. p values calculated by one-way ANOVA followed by Tukey´s post-hoc test." (adapted from Kebir et al., Clin Cancer Res 2023).

Other members of the lab furthermore examined ALDH1A1/Ki67 co-expression in PDX tumors of a mouse model, as a proliferative index. The number of Ki67 positive ALDH1A1+ cells increased after TMZ treatment and decreased when TMZ was combined with MK2206 (Kebir et al., Clin Cancer Res. 2023).

To reveal the induction of apoptotic processes the active caspase-3 levels were determined after the combined application of MK2206 and TMZ to ^{cR} and $^{TMZ→eR}$cell samples (Caspase assay as described in Methods, chapter "5.5.4. Flow cytometric

analysis"). Samples were studied at day 10 of the treatment schedule (TMZ (500 µM) vs. TMZ (500 µM) + MK2206 (5 µM); every other day). The exemplary histograms stacked in Figure 18 (left) demonstrate the fluorescence intensity of the antibody labeling, corresponding to the active caspase-3 level. TMZ leads to an increased active caspase-3 level in ^{naive}cells (turquoise histogram) compared to the DMSO control (0.5 %) (grey histogram). The exposure of relapse cell samples to the TMZ-only schedule (blue histogram) did not increase active caspase-3 levels significantly compared to the DMSO control. The addition of TMZ+MK2206 to relapse cell samples (red histogram), lead to significantly higher levels of active caspase-3. The pro-apoptotic effect of TMZ+MK2206 addition to the relapse cell samples was even exceeding the effect observed in TMZ treated ^{naive}cell samples (turquoise histogram).

The relative active caspase-3 levels, presented in Figure 18 (right bar chart) were examined by normalization of flow cytometrically determined MFIs for the indicated treatments to the DMSO control (0.5 %). In $^{TMZ→eR}$BN46 cells the relative active caspase-3 level was increased with a mFC of 3.5 through addition of TMZ+MK2206 compared to TMZ-only (51.4 % vs. 232.7 %). The relative active caspase-3 level was increased with a mFC of 1.8 in ^{cR}BN118 (44.5 % vs. 125.7 %), 2.1 in ^{cR}BN123 (71.9 % vs. 225.1 %) and 10.3 in ^{cR}BN132 (51.9 % vs. 585.5 %) upon TMZ+MK2206 compared to TMZ-only. The data confirm, that TMZ+MK2206 can induce apoptotic processes in ^{cR} and $^{TMZ→eR}$cell samples and can revert their increased TMZ-resistance.

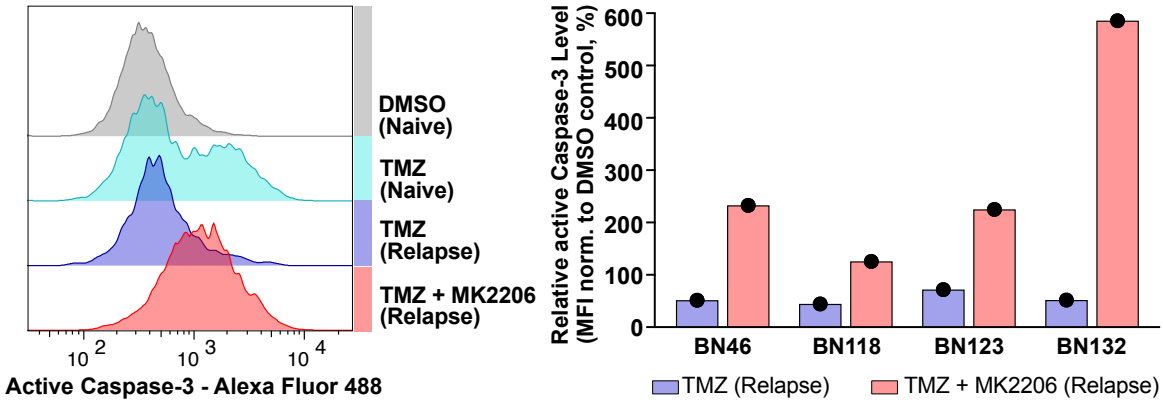

Figure 18: Left: "Histograms represent active caspase-3 flow cytometry data from naïve vs. experimental relapse BN46 cells treated with DMSO, TMZ, and TMZ + MK2206." Right: "Bar plot represents MFI of active caspase-3 measured by flow cytometry on day 10 of exposure to TMZ (500 µM) vs. TMZ (500 µM) + MK2206 (5 µM). Data from unicate analysis of samples representing experimental (RT→eR; BN46) or clinical (RT/TMZ; BN118, BN123, BN132) relapse status, normalized to DMSO control." (adapted from Kebir et al., Clin Cancer Res 2023).

In addition, co-labeling of ALDH1A1 and active caspase-3 was performed in the same patients (BN46, BN118, BN123, BN132), displayed in Figure 19. In the DMSO-treated control, 12.3±5 % of all ALDH1A1+ cells were positive for active caspase-3, while upon TMZ exposure of ^{naive}cell samples 74.8±13 % of all ALDH1A1+ cells were positive for active caspase-3. Whereas, in the corresponding ^{cR} and $^{TMZ→eR}$cell samples only 33.8±23 % of all ALDH1A1+ cells were positive for active caspase-3. However, when the relapse cells were exposed to TMZ+MK2206, 92.9±2 % of all ALDH1A1+ cells were positive for active caspase-3, indicating that the pAKT inhibition seems to induce apoptotic processes specifically in ALDH1A1+ cells.

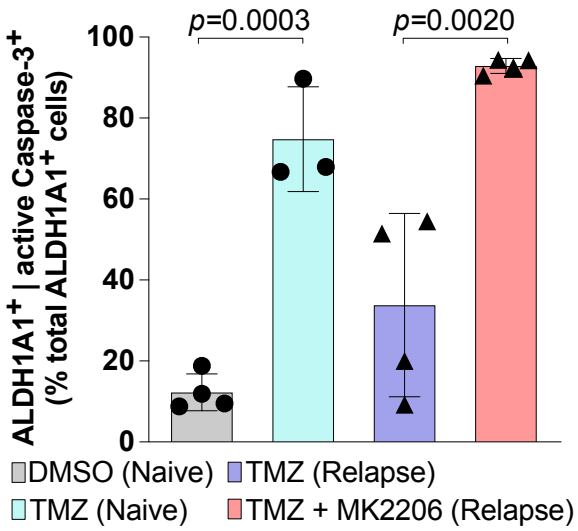

Figure 19: "Bar plot representing percent ALDH1A1+/active caspase-3+ double positive cells measured by flow cytometry at day 10, n=4 samples " (sample IDs were described in Fig 19), "results shown as mean ± SD, p values calculated using the Kruskal–Wallis test followed by Dunn´s post hoc test." (adapted from Kebir et al., Clin Cancer Res 2023).

Finally, as described in Kebir et al. (Clin Cancer Res. 2023), former lab members tested different timings of sequential targeting strategies. When MK2206 was applied subsequently to TMZ exposure the clonal expansion was inhibited *in vitro*, on the contrary the MK2206-only schedule had no effect on proliferation of ^{naive}cells. The findings of the *in vitro* sequential treatment experiments could be confirmed in *in vivo* experiments. In xenografts, MK2206 monotherapy did not confer any survival benefit. Furthermore, the combination of MK2206 with TMZ within the first two weeks, could not extend survival, while a delayed addition of MK2206 during weeks 4-5 of TMZ exposure schedules conferred a more than two-fold survival benefit over TMZ-monotherapy (Kebir et al., Clin Cancer Res. 2023).

To summarize, it was confirmed that TMZ-based treatment schemes lead to the enrichment of rare ALDH1A1 expressing subclones, which then expand clonally and potentially drive progression as TMZ resistant ALDH1A1+/pAKT+ subclones. ALDH1A1 knockdown and ALDH1A1 overexpression influenced clonogenicity in relapse cell samples, but not in treatment-naive cell samples. Moreover, it was shown that the inhibition of AKT phosphorylation, could target specifically the ALDH1A1+/pAKT+ subclones, leading to an overall reduction of cell confluence and cellular viability and an increase of apoptotic processes, especially in the ALDH1A1+ target cells.

The following data was partly submitted as Ullrich et al., in revision 2023.

2.5. Correlation of treatment-naive KDM5B levels with elevated ALDH1A1 at relapse

To establish a hypothesis on the mechanistic link for the acquisition of AKT phosphorylation in ALDH1A1+ cells under primary TMZ exposure, follow-up investigation used qPCR data of pre- vs. post-treatment (^{naïve} vs. $^{TMZ→eR}$ or ^{cR}) patient cell samples derived from n=8 individuals (BN46, BN78, BN91, BN118, BN123, BN132). A quantitative assessment of ALDH1A1 gene expression was performed by applying the 2-ΔCT method and normalization to the housekeeper gene ribosomal protein L37a (RPL37A) (Figure 20) (see Methods, chapter “5.5.3. Quantitative polymerase chain reaction (qPCR)”). The resulting data on ALDH1A1 gene expression matched the data on protein level, obtained by flow cytometry (compare Figure 6 and Figure 7). The relative *ALDH1A1* expression was low in all ^{naive}cell samples with a mean relative expression of 1.6±1.2 ($^{TMZ→eR}$BN46), 0.1±0.1 ($^{TMZ→eR}$BN78), 0.01±0 (^{cR}91), 1.2±0.1 (^{cR}BN118), 6±3 (^{cR}123) and 0.7±0.2 (^{cR}132). In contrast the relative *ALDH1A1* expression was increased in all ^{cR} and $^{TMZ→eR}$cell samples. The extent of the *ALDH1A1* increase differed between the patient cases, comparable to the data obtained in flow cytometric analyses. The relapse cell samples presented a mean relative *ALDH1A1* expression of 40.1±6 ($^{TMZ→eR}$BN46), 2.5±2 ($^{TMZ→eR}$BN78), 22.8±10 (^{cR}91), 61.8±8 (^{cR}BN118), 14.4±7 (^{cR}123) and 10.2±2 (^{cR}132) (Figure 20).

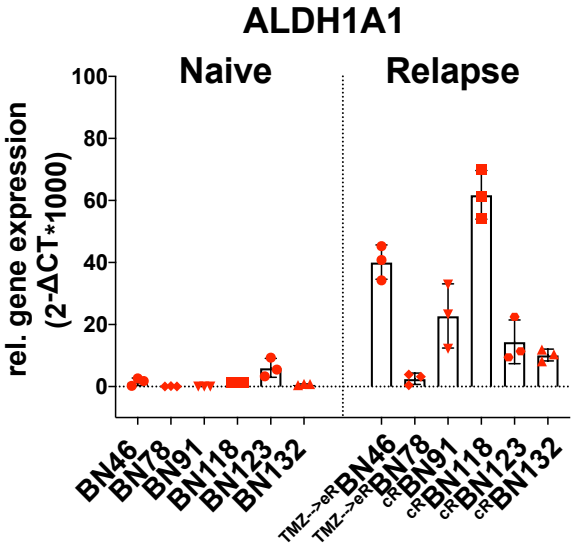

Figure 20: "Relative ALDH1A1 gene expression detected using qPCR. Results of n=6 paired patient samples (IDs indicated). Data shown in triplicate as mean ± SD." (adapted from Ullrich et al., in revision 2023).

To reveal a potential relationship of *ALDH1A1* expression in the treatment-naive vs. the relapse cell samples, the R squared coefficient of determination (square of the Pearson correlation coefficient) was analyzed. The higher the R-squared value, the better the model fits the data (see Methods, chapter "5.5.3. Quantitative polymerase chain reaction (qPCR)"). However, there was no correlation as revealed by the broad distribution of data points outside the regression line and the low R^2 level of 0.0017 (Figure 21 left). This led to the conclusion that the enrichment of ALDH1A1 under the influence of TMZ cannot be predicted by determining the extent of *ALDH1A1* expression beforehand, in the treatment-naive cell samples.

As subclonal enrichment can be caused by drug-induced epigenetic regulation and subsequent adaptive plasticity in selected cells of a tumor bulk (see Chapter "1.4. Adaptive plasticity and dynamic cellular state transitions"), epigenetic regulators of the KDM family were investigated. The histone-demethylases KDM5A and KDM6A were already described as epigenetic inducers in non-small cell lung cancer (NSCLC) (Sharma et al., 2010) and in glioblastoma (Liau et al., Cell Stem Cell 2017), respectively. However, expression levels of *KDM5A and KDM6A* in treatment-naive cell samples also did not correlate with increasing *ALDH1A1* expression in the paired relapse cell samples, as presented by the broad distribution of data points and the low R^2 values of 0.00256 and 0.0589 (Figure 21 middle and right panel).

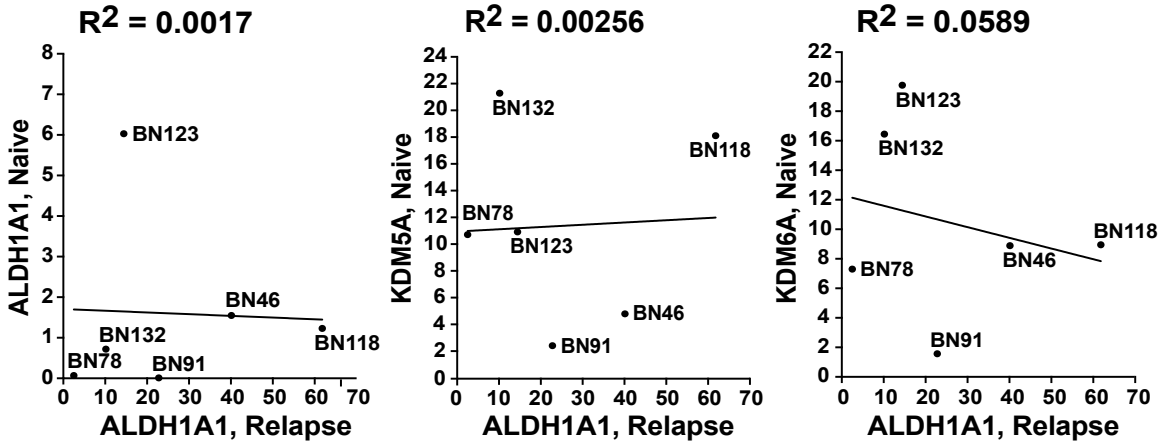

Figure 21: "Graphs depict personalized qPCR-based gene expression values of short-term expanded pairs of patient cell samples. Patient IDs indicated. Mean of triplicate. R2, Pearson coefficient of determination. Treatment-naive expression levels of" ALDH1A1 (Left), KDM5A (Middle), KDM6A (Right), "were correlated with the ALDH1A1 levels of respective relapse samples." (adapted from Ullrich et al., in revision 2023)

As neither KDM5A nor KDM6A correlated with elevated *ALDH1A1* in ^{cR} and $^{TMZ\rightarrow eR}$cell samples, the histone-demethylase KDM5B, which was published as a marker for DTPs e.g. in melanoma was investigated (Roesch et al., Cell 2010; see Chapter "1.4. Adaptive plasticity and dynamic cellular state transitions").

The relative expression of *KDM5B* did not significantly change between paired ^{naive}cell samples and ^{cR} and $^{TMZ\rightarrow eR}$cell samples, with a mean(relapse)/mean(naive) of 0.9 (^{naive}BN46 vs. $^{TMZ\rightarrow eR}$BN46), 0,8 (^{naive}BN78 vs.$^{TMZ\rightarrow eR}$BN78), 0.8 (^{naive}BN91 vs. ^{cR}BN91), 1,2 (^{naive}BN118 vs. ^{cR}BN118), 0.57 (^{naive}BN123 vs. ^{cR}BN123) and 1.1 (^{naive}BN132 vs. ^{cR}BN132) (Figure 22). This is contrary to *ALDH1A1*, which levels were strongly increased in ^{cR} and $^{TMZ\rightarrow eR}$cell samples (compare Figure 20).

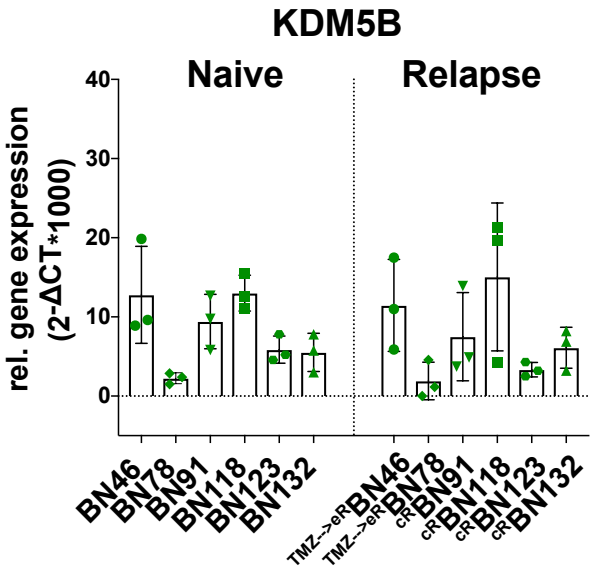

Figure 22: "Relative KDM5B gene expression detected using qPCR. Results of n=6 paired patient samples (IDs indicated). Data shown in triplicate as mean ± SD." (adapted from Ullrich et al., in revision 2023).

As the patient IDs of the relapse cell samples, which exhibited the highest values for ALDH1A1 gene expression were equal to the patient IDs of ^{naive}cell samples, which exhibited the highest values for KDM5B gene expression (Figure 23 left), a correlation analysis of KDM5B in ^{naive}cell samples with ALDH1A1 in ^{cR} and $^{TMZ→eR}$cell samples was performed. Indeed, higher *KDM5B* expression in ^{naive}cells significantly correlated with elevated *ALDH1A1* expression in the paired ^{cR} or $^{TMZ→eR}$cells, as shown by the data points fitting the regression line and the R^2 value of 0.8598. The data indicates that KDM5B in treatment-naive cell samples could be a predictive factor for ALDH1A1 enrichment in the relapse cell samples (Figure 23 right plot).

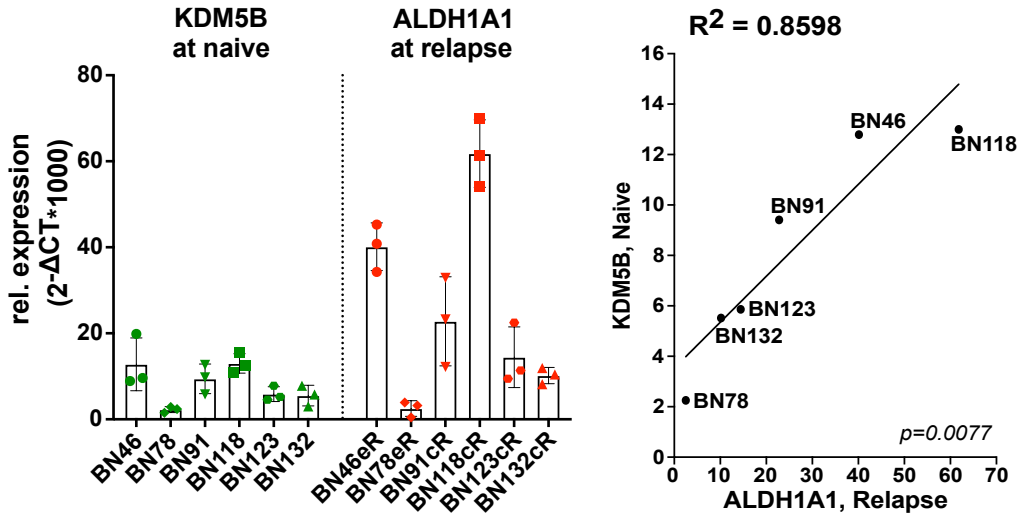

Figure 23: Left: Comparison of relative KDM5B gene expression at naive with ALDH1A1 gene expression at relapse, detected using qPCR. Right: "Graphs depict personalized qPCR-based gene expression values of short-term expanded pairs of patient cell samples. Patient IDs indicated. Mean of

triplicate. R2, Pearson coefficient of determination. Treatment-naive expression levels of KDM5B were correlated with the ALDH1A1 levels of respective relapse samples." (adapted from Ullrich et al., in revision 2023).

2.6. TMZ triggers dynamics of KDM5B expression

To study KDM5B not only at specific timepoints under therapeutic pressure, but rather to follow its dynamics throughout TMZ treatment schemes, a stably integrated reporter construct, that was published earlier (Roesch et al., Cell 2010), was applied into our patient cells via lentiviral transduction. The construct consists of an Enhanced green fluorescent protein (EGFP) reporter, inserted behind and controlled by a human KDM5B promoter, allowing the indirect monitoring of KDM5B expression via detection of EGFP (scheme of construct shown in Figure 24).

After lentivirus production in Human Embryonic Kidney 293T (HEK293T) cells using the pLU-JARID1Bprom-EGFP-BLAST vector, the target cells (n=4 naive and n=2 relapse cell samples), were transduced and the successful transduction was confirmed via flow cytometry (Supplementary Figure 3 and 4). Thereafter, transduced cells were selected using blasticidin and successful selection to 100% construct-carrying cells was confirmed using flow cytometry (Supplementary Figures 3 and 4). Procedures for the stable integration of the reporter construct are described in detail in Methods chapter "5.3 KDM5B-promoter-EGFP-reporter construct cells". From here on, the various transduced, patient-derived treatment-naive cells are indicated as ^{naive}BN46$^{KDM5B\text{-}EGFP}$, ^{naive}BN118$^{KDM5B\text{-}EGFP}$, ^{naive}E049$^{KDM5B\text{-}EGFP}$, ^{naive}E056$^{KDM5B\text{-}EGFP}$, and the respectively paired transduced relapse cell samples as $^{TMZ\rightarrow eR}$BN46$^{KDM5B\text{-}EGFP}$, ^{cR}BN118$^{KDM5B\text{-}EGFP}$. Figure 24 shows the fluorescence-/phase- contrast appearance of the transduced cell samples ^{naive}BN46$^{KDM5B\text{-}EGFP}$ (left) and ^{naive}E049$^{KDM5B\text{-}EGFP}$ (right).

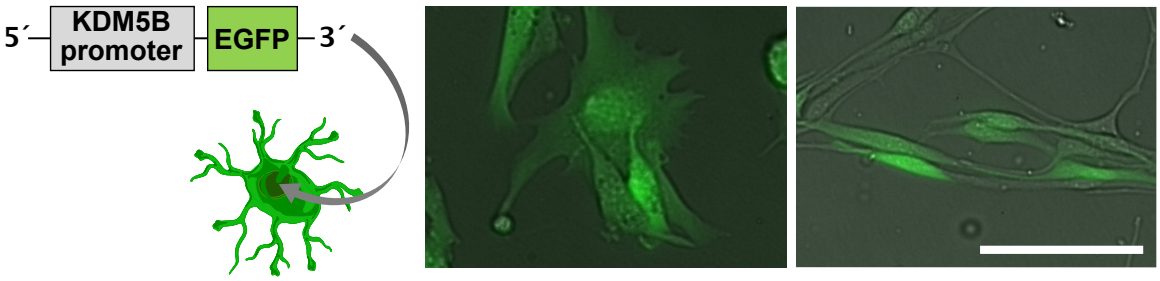

Figure 24: "Phase contrast appearance and vital EGFP fluorescence of representative patient cell" samples (Left: ^{naive}BN46; Right: ^{naive}E049) "transduced with KDM5B promoter-EGFP reporter construct as indicated by the cartoon (pLU-JARID1Bprom-EGFP-BLAST, provided by " Roesch et al., Cell 2010), "Scale bar, 100µM." (adapted from Ullrich et al., in revision 2023).

After stable integration of the KDM5B-promoter-EGFP-reporter construct, the KDM5B-EGFP intensity was measured by software-based cell recognition over 16 day TMZ exposure in ^{naive}BN46$^{KDM5B\text{-}EGFP}$ and ^{naive}BN118$^{KDM5B\text{-}EGFP}$ as well as in the respective paired relapse samples $^{TMZ\rightarrow eR}$BN46$^{KDM5B\text{-}EGFP}$ and ^{cR}BN118$^{KDM5B\text{-}EGFP}$. The cells were treated every other day with 300 µM, 600 µM and 1 mM TMZ or the corresponding DMSO controls. DMSO did not induce an increase in the KDM5B-EGFP intensity, indicating the KDM5B expression. A concentration-dependent increase of the KDM5B-EGFP intensity was observed in ^{naive}BN46$^{KDM5B\text{-}EGFP}$ and ^{naive}BN118$^{KDM5B\text{-}EGFP}$ cells. At the endpoint of 16 days the KDM5B-EGFP intensity increased to 253.3 % (BN46$^{KDM5B\text{-}EGFP}$) and 603.2 % (^{naive}BN118$^{KDM5B\text{-}EGFP}$) upon 600 µM TMZ, respectively 527.4 % (BN46$^{KDM5B\text{-}EGFP}$) and 1480.1 % (^{naive}BN118$^{KDM5B\text{-}EGFP}$) upon 1 mM TMZ. In contrast in the paired relapse cell samples the KDM5B-EGFP intensity increased to 112.6 % ($^{TMZ\rightarrow eR}$BN46$^{KDM5B\text{-}EGFP}$) and 114.3 % (^{cR}BN118$^{KDM5B\text{-}EGFP}$) upon 600 µM TMZ at the endpoint of 16 days. The concentration of 1 mM was not applied to the relapse cell samples. 300 µM TMZ did not lead to an increase in the ^{naive} as well as in ^{cR} and $^{TMZ\rightarrow eR}$cell samples (Figure 25).

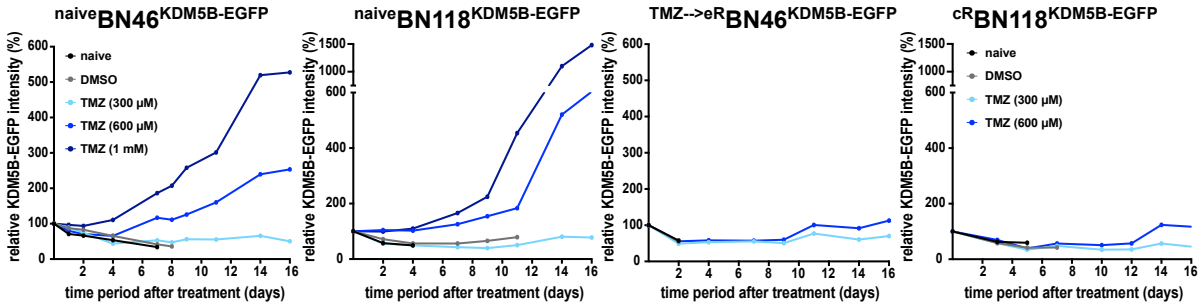

Figure 25: Monitoring of relative KDM5B-EGFP-intensity using software-based cell recognition (NyOne®) under TMZ (300 µM, 600 µM or 1mM) or under control DMSO (0.05%) exposure for 16 days; naive construct-bearing patient cells (^{naive}BN46KDM5B-EGFP and ^{naive}BN118 KDM5B-EGFP) and relapse construct-bearing patient cells ($^{TMZ\rightarrow eR}$BN46KDM5B-EGFP and ^{cR}BN118KDM5B-EGFP).

As a second readout parameter flow cytometric readout by determination of the mean fluorescence intensity (MFI) as well as investigation of the subpopulation of top 5 % KDM5B-EGFP fluorescence reporter intensity, describing the KDM5B^{high} cells, was performed. The specific threshold of 5 % was based on the gating strategy applied by Roesch et al. (Cell 2010), who confirmed via sorting of the top 5 % KDM5B-EGFP fluorescence reporter intensity that these cells display KDM5B^{high} cells on RNA and protein level. The gating strategy incorporated selection of the top 5 % KDM5B-EGFP reporter cell counts in the treatment-naive cell sample, and subsequent use of the gate

as an analytical threshold for all other samples of the experiment, so that the relative number of cells that reached the reference fluorescence intensity was scored (see Methods, chapter “5.5.4. Flow cytometric analysis”).

Following the same protocol as for the experimental relapse model, established in our lab to generate $^{TMZ→eR}$cells (see Figure 4 and chapter “1.4. Adaptive plasticity and dynamic cellular state transitions”), the cells were treated with TMZ for 16 days every other day before TMZ was withdrawn. During this long-term TMZ-on/-off treatment scheme, samples were taken for flow cytometric fluorescence measurement at the treatment-naive state (before the first TMZ treatment was applied), at the endpoint of the TMZ treatment (day 16) and at the timepoints 1 day after withdrawal (day 17), 2 days after withdrawal (day 18), 1 week after withdrawal (day 23), 3 weeks after withdrawal (day 37) and 4 weeks after withdrawal (day 44).

Exemplary histograms of the long-term experiment in ^{naive}BN46$^{KDM5B\text{-}EGFP}$ cells are presented in Figure 26, also illustrating the gating strategy. Until day 23 the whole population shifts to the right towards higher EGFP intensity, resulting in an increased fraction of cells laying within the KDM5B^{high} subpopulation gate (45.8 % on day 23). In the day 37 cell sample the fraction of KDM5B^{high} cells is decreased again to 40 % and in the day 44 cell sample the relative numbers decreased further to 14.4 % KDM5B^{high} cells.

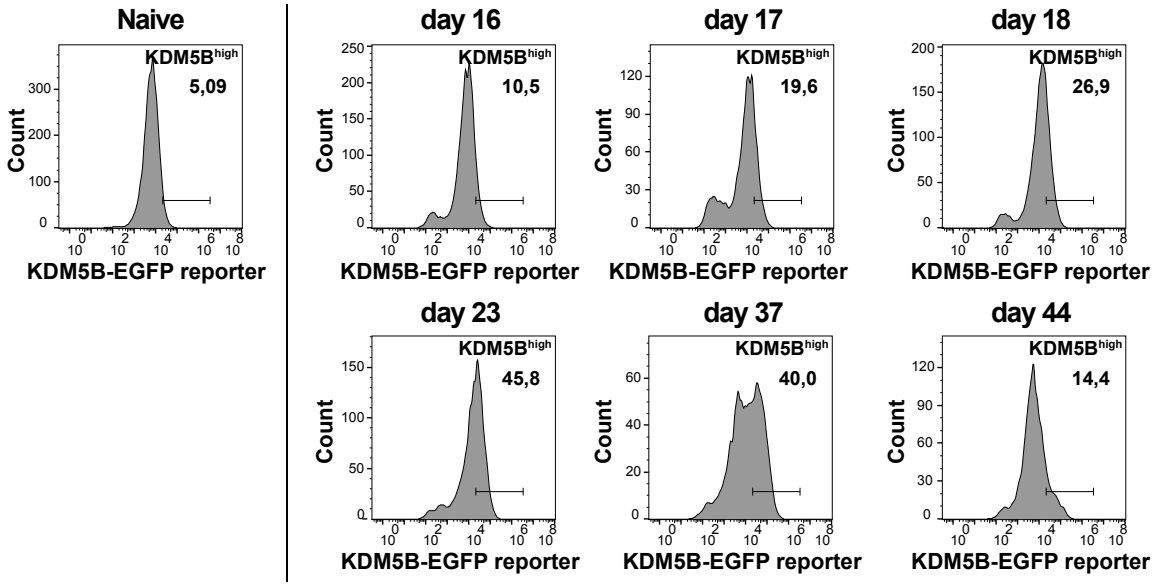

Figure 26: “Flow cytometry histograms (patient sample ^{naive}BN46$^{KDM5B\text{-}EGFP}$) at naive stage (gated for KDM5B^{high}) and during TMZ (500µM)-on/-off schedule. Time points as indicated.” (adapted from Ullrich et al., in revision 2023).

The fraction of KDM5B^{high} cells of all the treated ^{naive}BN46$^{KDM5B\text{-}EGFP}$ cell samples were normalized to the naive sample and plotted in Figure 27. Following 16 days TMZ exposure the relative number of KDM5B^{high} cells doubled (106 % compared to the treatment-naive sample). Whereas 1 day after withdrawal the increase was at 285.1 % and 2 days after withdrawal at 428.5 % of the naive cell sample (5-fold increase). 1 week after withdrawal the curve peaked at 800 %, signifying a 9-fold increase compared to the naive cell sample. Between the first and the third week after withdrawal the values were decreasing again, leading to 182.9 % (increase normalized to the naive sample) on day 44 of the long-term TMZ-on/-off scheme (Figure 27).

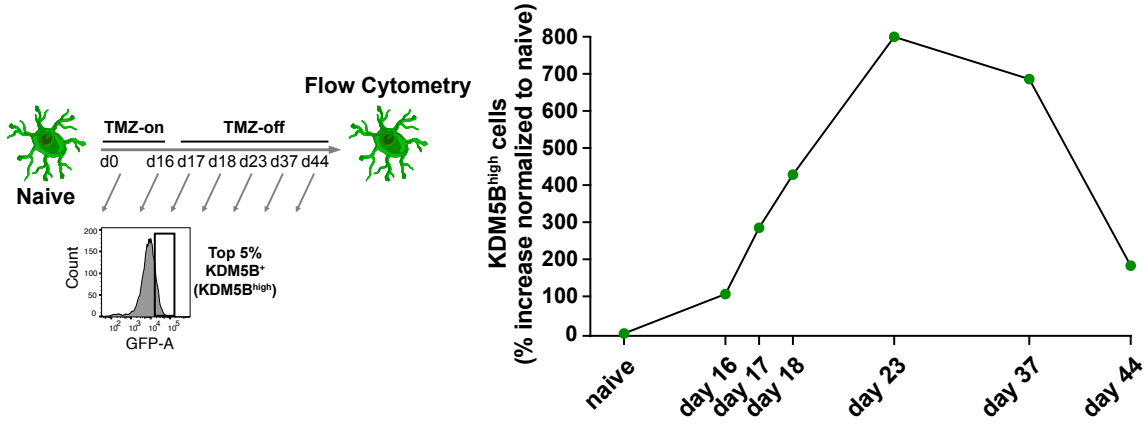

Figure 27: "Graph plotting flow cytometry data obtained from KDM5B^{high} subpopulations of reporter construct-transduced, naive BN46KDM5B-EGFP patient cells. Time points and TMZ (500µM)-on/-off schedule as indicated. Data represent the percent increase of KDM5B^{high} cells (relative number of cells that reached the set fluorescence threshold), normalized to the naive time point" (adapted from Ullrich et al., in revision 2023).

The long-term treatment, as presented in Figure 27 (16 days (500 µM) TMZ-on phase followed by TMZ-off phase) was repeated with genetically unmodified patient cells (BN46, BN91, BN118, BN123, BN132). *KDM5B* expression was validated using qPCR analysis from the bulk of ^{naive}cell samples. Samples were taken at the treatment-naive timepoint, as well as at the timepoint marked by the peak of KDM5B^{high} cells in the long-term experiment (day 23; see Figure 27), and after the non-proliferative period, when clonal expansion of $^{TMZ\rightarrow eR}$cells had taken place (day 80). The *KDM5B* expression was calculated by $2^{-\Delta CT}$*1000 and shown relative to the housekeeper *RPL37A*. *KDM5B* expression did not significantly differ between the ^{naive}cell samples and the samples on day 80, but was increased significantly in samples on day 23 compared to the ^{naive}cell samples (mFC = 1.9) (Figure 28).

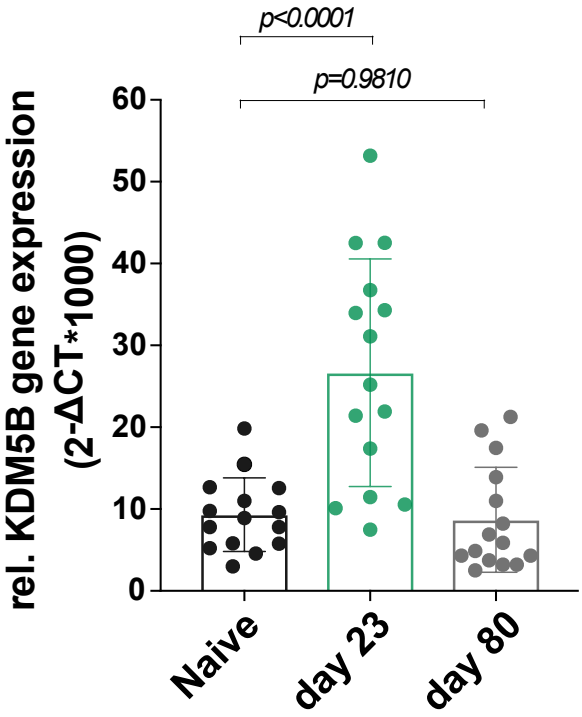

Figure 28: "Relative KDM5B gene expression measured via qPCR at the indicated time points of the experiment. Results from n=5 patient samples (BN46, BN91, BN118, BN123, BN132), presented in triplicate, as mean ± SD. P value by one-way analysis of variance (ANOVA) with Tukey post-hoc test for multiple comparison." (adapted from Ullrich et al., in revision 2023).

In the long-term experiment, a strong increase of KDM5B could be observed, that took place rapidly, within a few days after TMZ withdrawal and was transiently regulated. As described in chapter "1.4. Adaptive plasticity and dynamic cellular state transitions" epigenetic regulation and plasticity through histone demethylases is known to take place as an early response mechanism after therapeutic pressure. Therefore, controlled, short-term *in vitro* models, termed short-term in the following, were used. The short-term experiment comprised condensed TMZ-on/-off schemes. TMZ (500 µM) was administered for 2 days (TMZ-on) before being withdrawn for a TMZ-off phase of additional 3 days, in the 4 naive (^{naive}BN46$^{KDM5B\text{-}EGFP}$, ^{naive}BN118$^{KDM5B\text{-}EGFP}$, ^{naive}E049$^{KDM5B\text{-}EGFP}$, ^{naive}E056$^{KDM5B\text{-}EGFP}$) and the 2 relapse ($^{TMZ\rightarrow eR}$BN46$^{KDM5B\text{-}EGFP}$, ^{cR}BN118$^{KDM5B\text{-}EGFP}$) patient samples. A set of DMSO (0.5 %) treated control cell samples was included, in order to preclude influence of the solvent. Samples for flow cytometric investigation were taken on experimental days 2, 3, 4, and 5 of the TMZ-on/-off scheme. Other TMZ-on/-off schemes were tested, in which TMZ exposure was given for a shorter period (1 day TMZ-on + 1/2/3 days TMZ-off) or a longer period (3 days TMZ-on + 1/2/3 days TMZ-off), both leading to less abundant increases of KDM5B^{high} cells than with the TMZ-on/-off schemes described above (Supplementary Figure 5).

Exemplary histograms for ^{naive}BN118$^{KDM5B\text{-}EGFP}$cells under the short-term TMZ-on/-off schemes (2 days TMZ-on (500 µM) + 3 days TMZ-off) are presented in Figure 29, also illustrating the gating strategy. As similarly described for Figure 26, the gating strategy included the selection of the top 5 % KDM5B-EGFP cells, representing the KDM5B^{high} cells, in the DMSO (0.5 %) control. The gate was applied as an analytical threshold to the samples day 2, 3, 4 and 5 of the TMZ-on/-off schemes, to score the relative number of cells that reach the reference fluorescence intensity (see Methods, chapter “5.5.4. Flow cytometric analysis”).

The EGFP fluorescence peak shifts towards higher KDM5B-EGFP reporter signals. The fraction of cells laying within the KDM5B^{high} subpopulation gate increase to 10.3 % on day 2. On day 3 the fraction of cells laying in the KDM5B^{high} gate increased to 15.5 %, on day 4 to 24,9 % and on day 5 to 34,9 %.

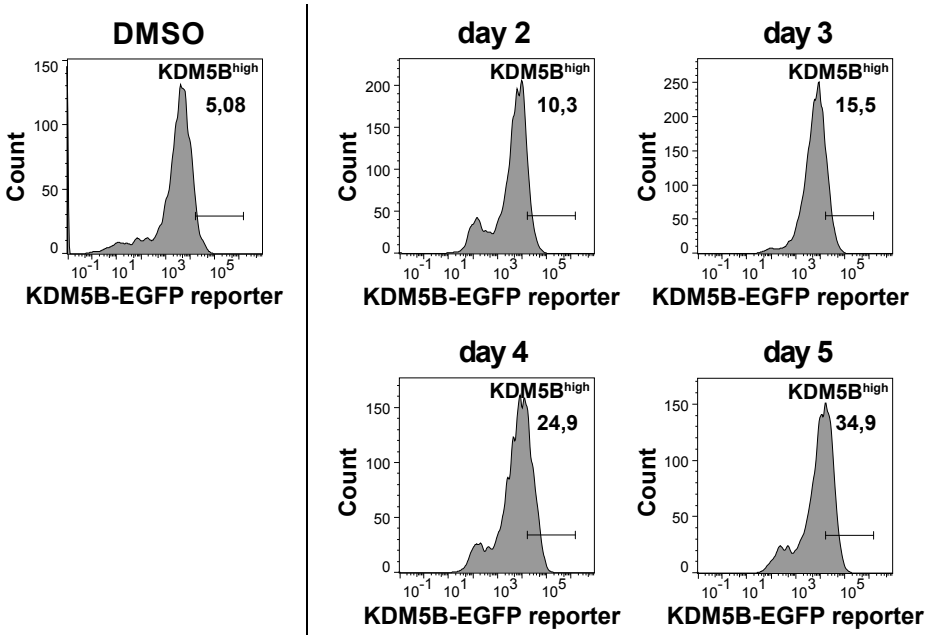

Figure 29: “Representative Flow cytometry histograms (patient sample BN118KDM5B-EGFP) after DMSO (0.5%) exposure (gated for KDM5B^{high}), or under the influence of TMZ (500µM)-on/-off schedule. Time points as indicated” (adapted from Ullrich et al., in revision 2023).

The MFI values as well as the fraction of KDM5B^{high} cells (compare exemplary histograms in Figure 29) for each indicated time point were normalized to the corresponding DMSO control (0.5 %). The left panel of Figure 30 shows the normalized increase of KDM5B expression in all cells, detected through the MFI, and the right panel shows the increase of the frequency of KDM5B^{high} cells. The TMZ-induced increase of KDM5B is more pronounced in the KDM5B^{high} subpopulation but is mirrored in the MFI of all cells. In addition the effect was more distinct in treatment-

naive cell samples than in TMZ pre-exposed relapse patient cell samples ($^{TMZ→eR}$ and ^{cR}). In naive cell samples (^{naive}BN46$^{KDM5B\text{-}EGFP}$, ^{naive}BN118$^{KDM5B\text{-}EGFP}$, ^{naive}E049$^{KDM5B\text{-}EGFP}$, ^{naive}E056$^{KDM5B\text{-}EGFP}$) the MFI was increased significantly by a factor of 1.6 (59.91±17 %) on day 5 of the TMZ-on/-off schemes, while in relapse cell samples ($^{TMZ→eR}$BN46$^{KDM5B\text{-}EGFP}$, ^{cR}BN118$^{KDM5B\text{-}EGFP}$) the MFI increased by a factor of 1.3 (32.8±16 %). For the relative numbers of KDM5B^{high} cells a similar difference between naive and relapse cell samples is detected. In naive cell samples the relative number of KDM5B^{high} cells increased by a factor of 3.2 (223.47±76 %) on day 5 of the TMZ-on/-off schemes compared to a factor of 2.3 (133.6±49 %) in relapse cell samples, presenting early TMZ effects on KDM5B dynamics (Figure 30).

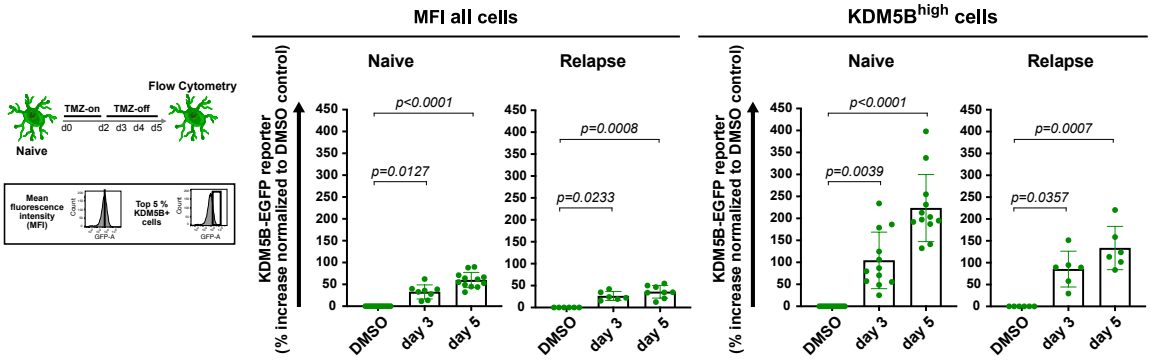

Figure 30: Increase of KDM5B in reporter construct-carrying naive (^{naive}BN46$^{KDM5B\text{-}EGFP}$, ^{naive}BN118$^{KDM5B\text{-}EGFP}$, ^{naive}E049$^{KDM5B\text{-}EGFP}$, naiveE056$^{KDM5B\text{-}EGFP}$) and 2 respective relapse ($^{TMZ→eR}$BN46$^{KDM5B\text{-}EGFP}$, ^{cR}BN118$^{KDM5B\text{-}EGFP}$) patient cell samples; Left bar plots: increase of MFI (mean fluorescence intensity of KDM5B-EGFP reporter); Right bar plots: increase of KDM5B^{high} subpopulations (top 5% KDM5B-EGFP reporter cells); for both bar plots: "Time points and TMZ (500µM) -on/-off schedule as indicated. Values normalized to corresponding (0.5%) DMSO controls and shown as mean ± SD. P values calculated using Kruskal-Wallis test with Dunn's post-hoc test." (adapted from Ullrich et al., in revision 2023).

To validate that the observed KDM5B increase is representing an early TMZ-mediated effect and is not caused by the stable integration of the construct and the indirect detection through the EGFP-reporter, antibody-based flow cytometric analysis were performed. Genetically unmodified ^{naive}BN46 and ^{naive}BN118 cells were treated either with DMSO (0.5 %) or according to the short-term TMZ-on/-off scheme (TMZ-on (500 µM) for 2 days followed by 2 or 3 days TMZ-off). Samples were taken at the indicated time points, fixed and permeabilized before an unconjugated antibody against KDM5B and a secondary PE-labeled antibody were added, as described in Methods chapter "5.5.4. Flow cytometric analysis". The MFI was increased, indicating KDM5B expression, exactly as observed with the reporter construct (Figure 31).

In conclusion, a TMZ-dependent KDM5B-induction could be observed, that is mostly evident in the KDM5B^{high} subpopulation. It is a rapid post-TMZ effect, transiently regulated, with the strongest outcome shortly after TMZ withdrawal. Lastly, the effect is more evident in treatment-naive than in relapse cells of glioblastoma patients.

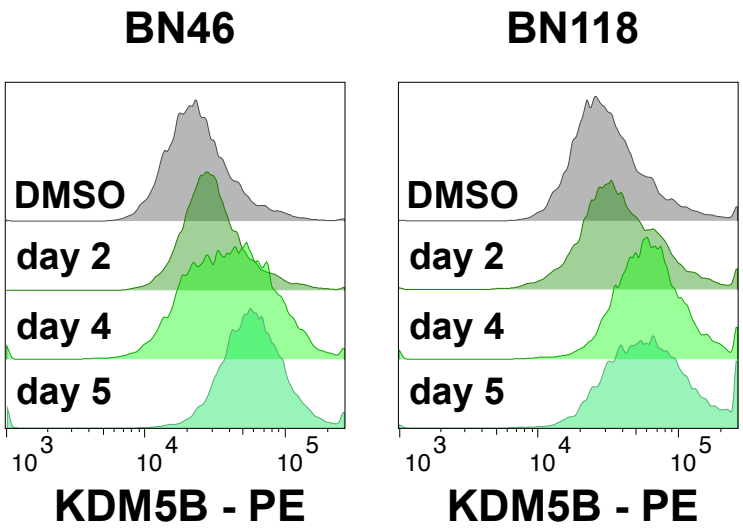

Figure 31: "Flow cytometry histograms display antibody-exposed KDM5B in non-transduced patient cells (IDs indicated) after DMSO (0.5%) exposure, or under the influence of TMZ (500µM)-on/-off schedule. Time points as indicated." (adapted from Ullrich et al., in revision 2023).

2.7. KDM5B^{high} slow-cycling DTP-like cells

To investigate the viability of the KDM5B^{high} cell subpopulations in the experimental TMZ-on/-off scheme, the 7-aminoactinmycin-D (7-AAD) assay was used in ^{naive}BN46$^{KDM5B\text{-}EGFP}$ and ^{naive}BN118$^{KDM5B\text{-}EGFP}$ cells (see Methods, chapter "5.5.4. Flow cytometric analysis"). The cells were treated either with DMSO (0.5 %) or according to the short-term TMZ-on/-off scheme (2 days TMZ-on (500 µM) + 3 days TMZ-off). The 7-AAD dye is excluded from viable cells, but labels non-viable cells. Respective flow cytometry gates and signals are shown in Figure 32 (left). On day 5 of the TMZ-on/-off scheme 1.2±1 % of the KDM5B^{high} cells were positive for 7-AAD (non-viable), while up to 19 % (mean = 14±5 %) of the KDM5B^{low} cells were positive for 7-AAD. This finding illustrates that KDM5B^{high} cells are more viable than KDM5B^{low} cells after exposure to TMZ (Figure 32 right bar chart).

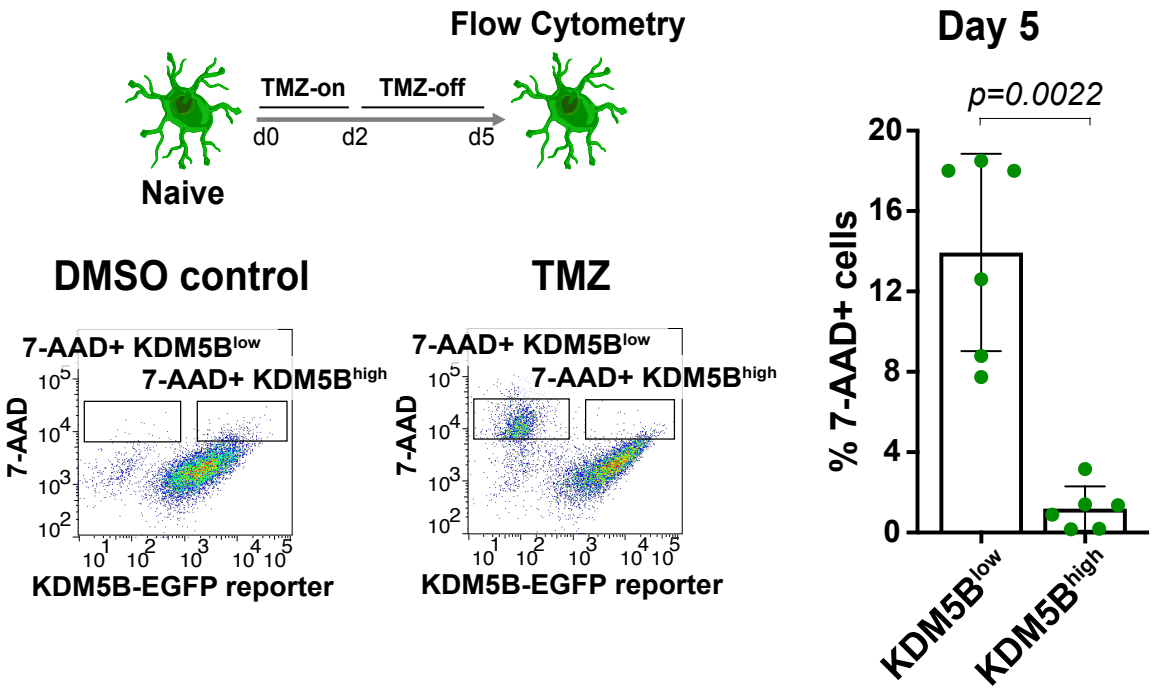

Figure 32: 7-AAD-viability assay. Left: Representative flow cytometry plots (BN46$^{KDM5B\text{-}EGFP}$), TMZ (500µM)-on/-off schedule and (0.5%) DMSO-control., Right: "Bar plot indicating 7-AAD+ cell frequencies in KDM5B^{high} vs. KDM5B^{low} subpopulations of construct-bearing naive BN46$^{KDM5B\text{-}EGFP}$ and naive BN118$^{KDM5B\text{-}EGFP}$ patient cell samples. Triplicate data, obtained by flow cytometry after TMZ (500µM)-on/-off schedule as indicated, shown as mean ± SD. P value by Wilcoxon rank sum test (gated)." (adapted from Ullrich et al., in revision 2023).

Then the CellTrace™ assay was implemented to further study ^{naive}BN46$^{KDM5B\text{-}EGFP}$ and ^{naive}BN118$^{KDM5B\text{-}EGFP}$ cells. The cells were treated either with DMSO (0.5 %) or according to the short-term TMZ-on/-off scheme (2 days TMZ-on (500 µM) + 3 days TMZ-off). Staining with the CellTrace™ Far Red dye enables distinguishing of slow-cycling cells from moderate cycling or cycling cells. The dye is diluted upon each cell division, so that cycling cells are characterized by decreased fluorescent intensity of the CellTrace™ dye, whereas moderate or slow-cycling cells show a higher fluorescent intensity (see Methods, chapter "5.5.4. Flow cytometric analysis"). In each of the fluorescent peaks, CellTrace^{low}=cycling, CellTrace^{medium}=moderate cycling, and CellTrace^{high}=slow-cycling cells, were determined by MFI-based flow cytometry (Figure 33 left). Slow-cycling cells displayed a 7-times higher EGFP fluorescence intensity in ^{naive}BN46$^{KDM5B\text{-}EGFP}$ cells, or respectively 3,1-times higher MFI levels in ^{naive}BN118$^{KDM5B\text{-}EGFP}$ cells than the cycling cells, revealing a lower proliferative capacity of KDM5B^{high} cells on day 5 of the TMZ-on/-off scheme (Figure 33 right bar chart).

To summarize, the findings reveal that high levels of KDM5B are expressed in slow-cycling, drug-tolerant cells, and rapidly increase upon TMZ exposure schedules.

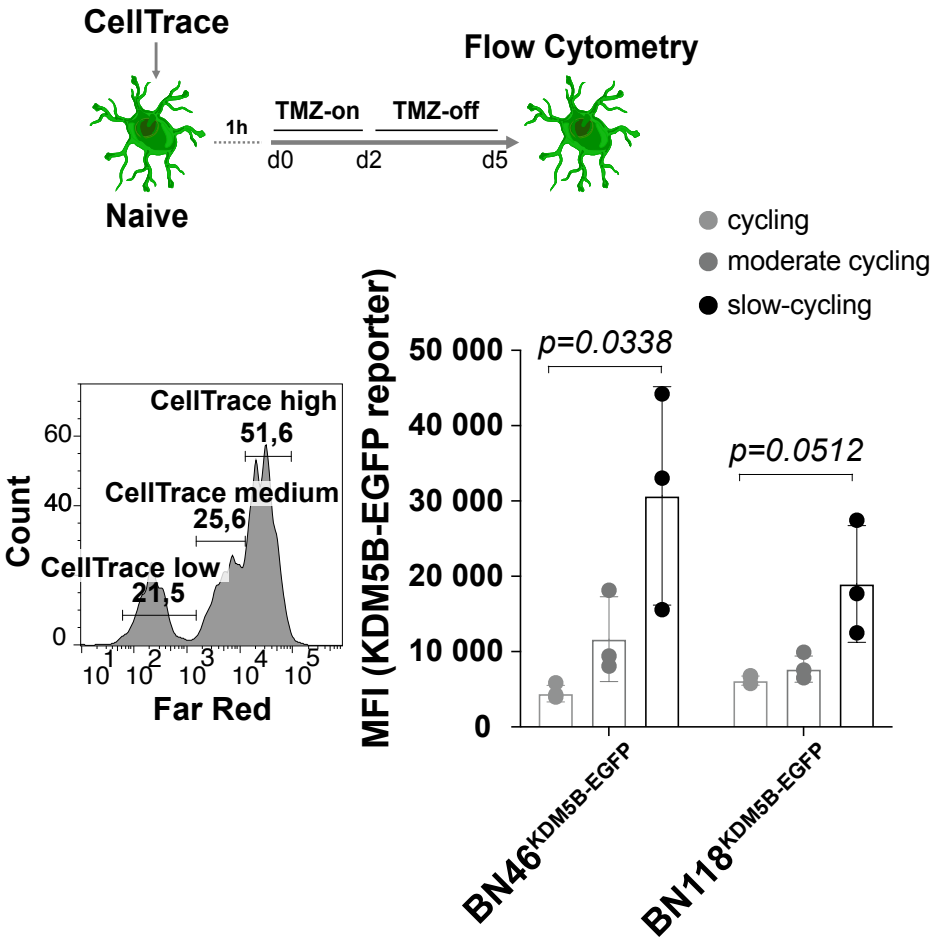

Figure 33: CellTrace™ experiment. Left: "Histogram of Far Red peaks revealing high, moderate, and slow-cycling subpopulations by flow cytometry (representative case, naive BN118$^{KDM5B\text{-}EGFP}$)"; Right: "Bar chart representing mean fluorescence intensity (MFI) of KDM5B-EGFP reporter for each Far Red peak. Triplicate data as mean ± SD. P values by Kruskal-Wallis test." (adapted from Ullrich et al., in revision 2023).

2.8. KDM5B^{high} cells co-express ALDH1A1 and pAKT

For all further experiments genetically unmodified clinical cell samples were used.

The functional properties of KDM5B^{high} cells upon TMZ exposure and the positive correlation of *KDM5B* expression in treatment-naive cells with paired expression levels of *ALDH1A1* in relapse cell samples suggested a unique connection.

Potential KDM5B/ALDH1A1 co-expression was investigated via flow cytometry in ^{naive}BN46 and ^{naive}BN118 cell samples. The cells were treated either with DMSO (0.5 %) or according to the short-term TMZ-on/-off scheme (2 days TMZ-on (500 µM) + 3 days TMZ-off). A combination of a FITC-labeled ALDH1A1 antibody, detected in the Alexa Fluor 488 channel, and an unlabeled KDM5B antibody with a Alexa Fluor 555

secondary antibody, detected in the PE channel was applied (see Methods, chapter "5.5.4. Flow cytometric analysis"). In the DMSO control sample the gate of KDM5B+/ALDH1A1+ cells was set to 5 % and subsequently applied to the corresponding samples of the TMZ-on/-off scheme. Exemplary flow cytometry profiles of ^{naive}BN118 cells are shown in Figure 34 (left). On day 2, KDM5B/ALDH1A1 co-expression was increased by a factor of 1.6, compared to the gated DMSO control (8.2±0.8 % KDM5B+/ALDH1A1+ cells among all cells). On day 5, the KDM5B/ALDH1A1 co-expression was increased significantly by a factor of 3 compared to the gated DMSO control (14.5±2.6 % KDM5B+/ALDH1A1+ cells among all cells) (see Figure 34 right bar chart).

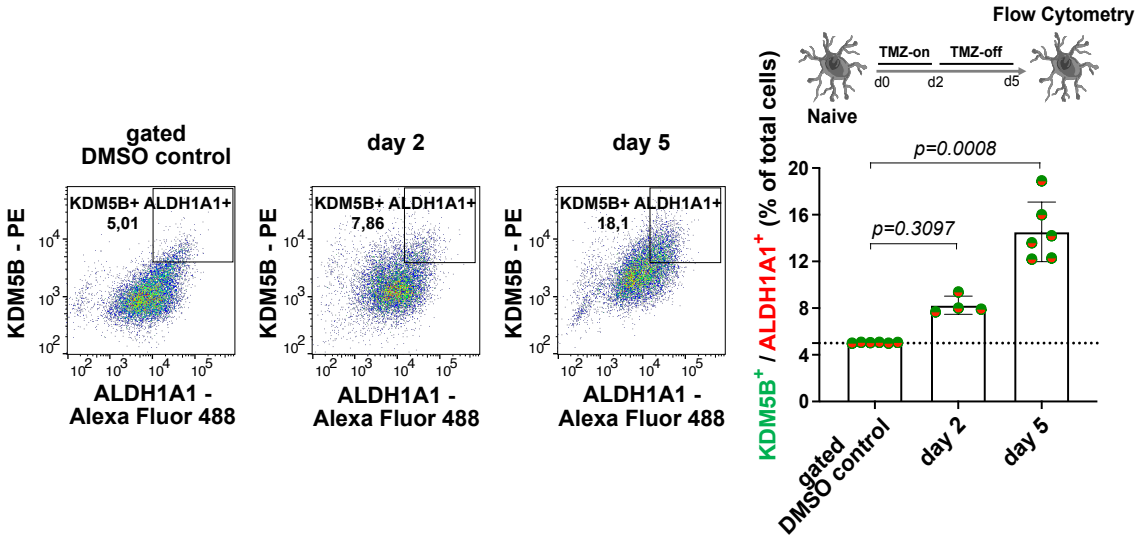

Figure 34: Left: "Representative flow cytometry profiles of ALDH1A1- and KDM5B-labeled cells from patient sample BN118. Analysis performed after exposure to 0.5% DMSO (gated as a control to 5%), or under the influence of a TMZ (500µM)-on/-off schedule. Time points as indicated."; Right: "Bar chart showing frequency of co-expressing cells at the indicated time points of the treatment scheme: TMZ-on, exposure to 500µM TMZ; TMZ-off, no drug. Flow cytometry analysis, in duplicate/triplicate on sample IDs BN46, BN118; presented as mean ±SD. P values obtained by Kruskal Wallis with Dunn's post-hoc test." (adapted from Ullrich et al., in revision 2023).

To reveal a potential connection between KDM5B expression and the phosphorylation of AKT, antibody-based flow cytometric analyses of pAKT (Ser473), using an Alexa Fluor 488-labeled antibody, were performed in ^{naive}BN46 and ^{naive}BN118 cells. Again the cells were treated with DMSO (0.5 %) or following the short-term TMZ-on/-off scheme (2 days TMZ-on (500 µM) + 3 days TMZ-off). Exemplary histograms for the DMSO control vs. TMZ-exposed cell samples on day 5 are shown in Figure 35 (Left). pAKT MFIs increased significantly from 1064±155 (0.5% DMSO) to 1725±195 (TMZ) on day 5 of the experimental scheme, corresponding to a significant increase by a factor of 1.6 in the overall cell population (Figure 35 right bar chart).

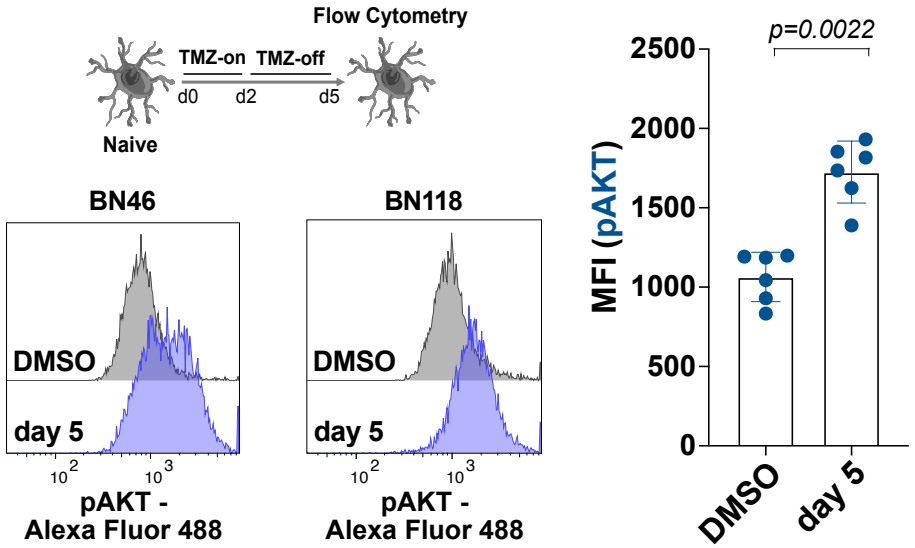

Figure 35: Left: "Representative flow cytometry histograms exposing pAKT (Ser473)-labeled patient cells (IDs indicated) after DMSO (0.5%) exposure, or at the end point of TMZ (500µM)-on/-off schedule."; Right: "Bar chart depicting flow cytometry MFI data obtained from two naive patient samples (BN46, BN118). Treatment scheme as indicated, comprised of TMZ (500µM)-on/-off periods vs. 0.5% DMSO-control. Data obtained on day 5 in triplicate, shown as mean ± SD. P values calculated by Mann-Whitney test." (adapted from Ullrich et al., in revision 2023).

Potential KDM5B/pAKT co-expression was analyzed using flow cytometry. Again ^{naive}BN46 and ^{naive}BN118 cell samples were treated either with DMSO (0.5 %) or the short-term TMZ-on/-off scheme (2 days TMZ-on (500 µM) + 3 days TMZ-off). Alexa Fluor 488-labeled pAKT antibody was combined with the unlabeled KDM5B antibody and the Alexa Fluor 555 secondary antibody, detected in the PE channel (see Methods, chapter "5.5.4. Flow cytometric analysis"). As described for the KDM5B/ALDH1A1 co-expression (compare Figure 34) a gate was set for the DMSO control (5 % KDM5B+/pAKT+ cells) and applied to day 2 and day 5 of the TMZ-on/-off scheme. The exemplary flow cytometry plots in Figure 36 (left) present the gating strategy in ^{naive}BN118 cell samples. The frequency of KDM5B/pAKT co-expressing cells as percentage of all cells is depicted in Figure 36 (right bar chart). On day 2 the frequency of KDM5B+/pAKT+ cells among all cells increased by a factor of 2 (10±2 % KDM5B+/pAKT+ cells among all cells). On day 5 frequency of KDM5B+/pAKT+ cells increased significantly by a factor of 3.3 (16.3±3 % KDM5B+/pAKT+ cells among all cells).

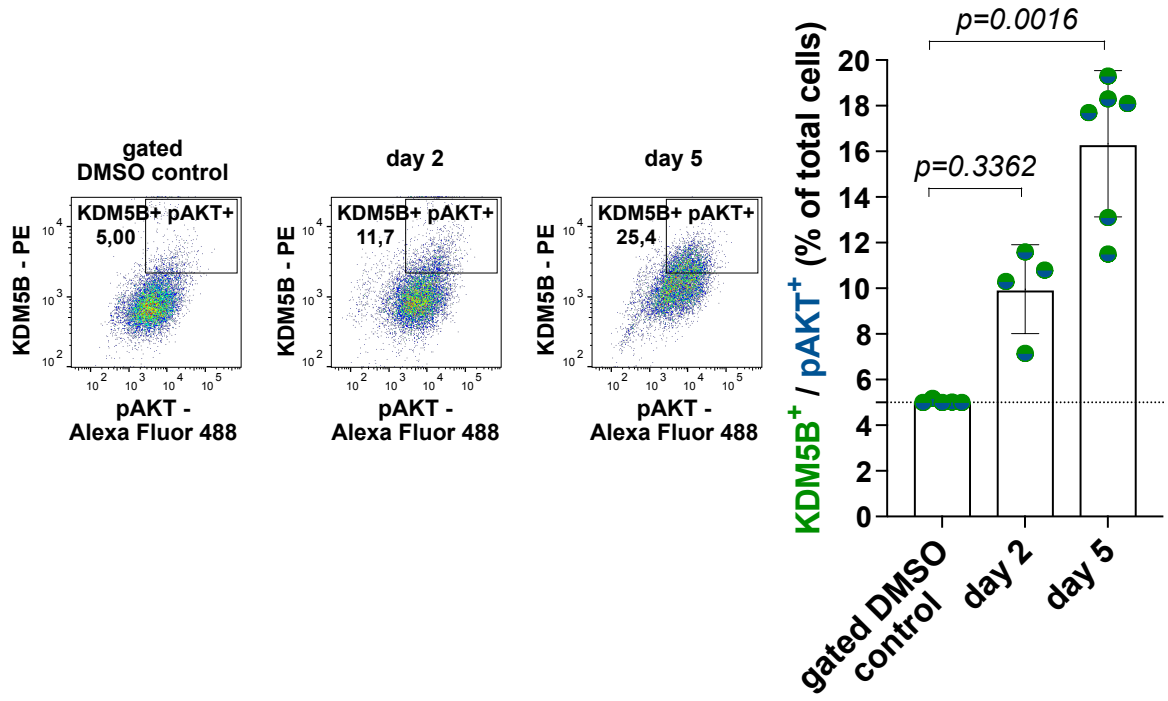

Figure 36: Left: "Representative flow cytometry profiles of pAKT (Ser473)/ KDM5B-labeled patient sample BN118, after DMSO (0.5%) exposure (gated as a control to 5%), or under the influence of TMZ (500µM)-on/-off schedule. Time points as indicated."; Right: "Bar chart showing percentage of co-expressing cells, determined by flow cytometry from two naive patient samples (BN46, BN118) at days 2 and 5 of the assay. Duplicate or triplicate data as mean ± SD. P values by Kruskal Wallis with Dunn's post-hoc test." (adapted from Ullrich et al., in revision 2023).

2.9. KDM5B expression levels affect the PI3K/AKT pathway

Consequently, the downstream effects of siRNA-based knockdown of KDM5B were evaluated, particularly attending pAKT and pathway-related targets. KDM5B knockdown efficiency was revealed on day 6 in the range of 75 and 88 % reduction via qPCR in four treatment-naive patient cell samples (BN46, BN118, E049 and E056; Supplementary Figure 6). The effect of a siRNA pool against KDM5B (siKDM5B) or a non-targeting pool (siNT) on KDM5B and on pAKT was evaluated via flow cytometry using pAKT (Alexa Fluor 488) and KDM5B (secondary antibody = PE channel) antibodies. The MFI of the siKDM5B cell samples was normalized to the siNT cell samples using the following formula: (MFI(siKDM5B)-MFI(siNT))/MFI(siNT) multiplied by 100.

The normalized MFI of KDM5B was reduced by 82.71±7 % (Figure 37 right bar chart). Along with the changes in KDM5B, a peak shift of pAKT takes place upon siKDM5B for 6 days compared to siNT, as evident in the exemplary histograms in the inlay of Figure 38 (left). After normalization, the pAKT was reduced by 23.1±12 % in

siKDM5B cell samples, pointing towards an inhibition of AKT activity through KDM5B knockdown (Figure 37 right bar chart).

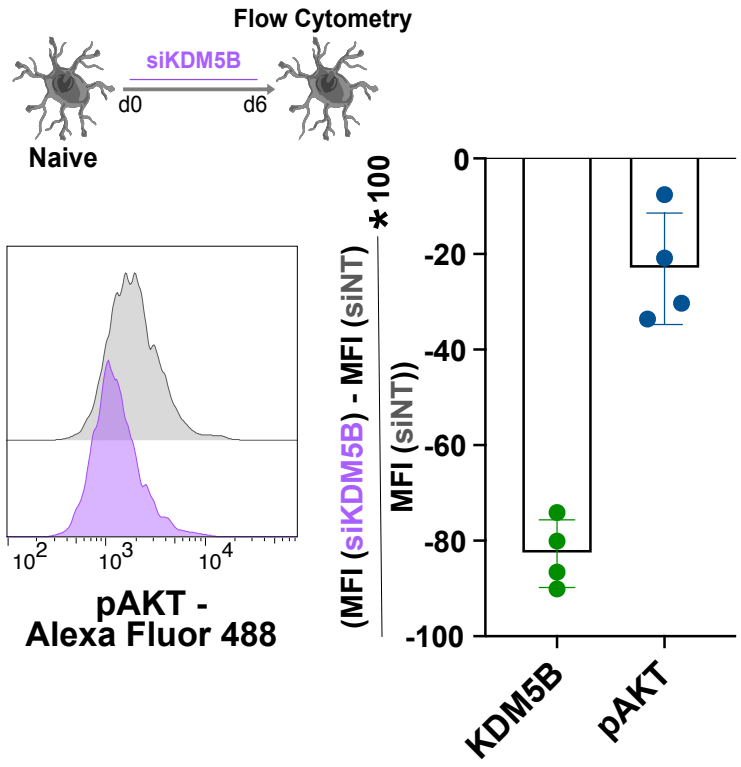

Figure 37: "Flow cytometry evaluation on day 6 of siRNA-mediated KDM5B knockdown in naive patient samples BN46, BN118, E49, and E56. Left: exemplary histograms (BN118; purple, siRNA; gray, siNT). Right: bar chart presenting respective MFI values of KDM5B and pAKT (Ser473) in the experiment. Data normalized to corresponding siNT control." (adapted from Ullrich et al., in revision 2023).

The potential downstream effects of KDM5B knockdown on pAKT and other pathway-related targets was next investigated by Western blot analysis. Total protein of siRNA/siNT-treated cell samples was extracted after 6 days as described in the Methods chapter "5.5.5. Protein expression studies". Protein levels of pAKT, phosphorylated glycogen synthase kinase-3 beta (pGSK3ß), pmTOR (phosphorylated mammalian target of rapamycin), Cyclin D3, and phosphatase and tensin homolog (PTEN) were determined.

Knockdown of KDM5B resulted in a strong decline of KDM5B protein abundance in the Western blots. Similarly, the protein levels of pAKT and its downstream targets pGSK3ß and Cyclin D3 were strongly reduced. pmTOR showed a less strong decline. In contrast to this, adverse effects could be detected in pAKT´s negative regulator PTEN, where protein levels were increased after KDM5B knockdown (Figure 38, left; ^{naive}BN118). Protein abundance for ^{naive}BN46, ^{naive}BN118, ^{naive}E049 and ^{naive}E056 siRNA/siNT-treated cell samples was quantified using the

Image Lab™ software and normalized to the ß-actin loading control. The relative protein levels after KDM5B knockdown was determined as a percentage of siNT (Figure 39, right). Knockdown of KDM5B reduced pAKT by 63± %, which was an even stronger effect than detected via flow cytometry. The pAKT downstream targets pGSK3ß, pmTOR, and Cyclin D3 also showed a strongly decreased abundance (pGSK3ß = -52± %, pmTOR = -51± %, Cyclin D3 = -37± %) in three respectively four analyzed patient samples (Figure 38 right).

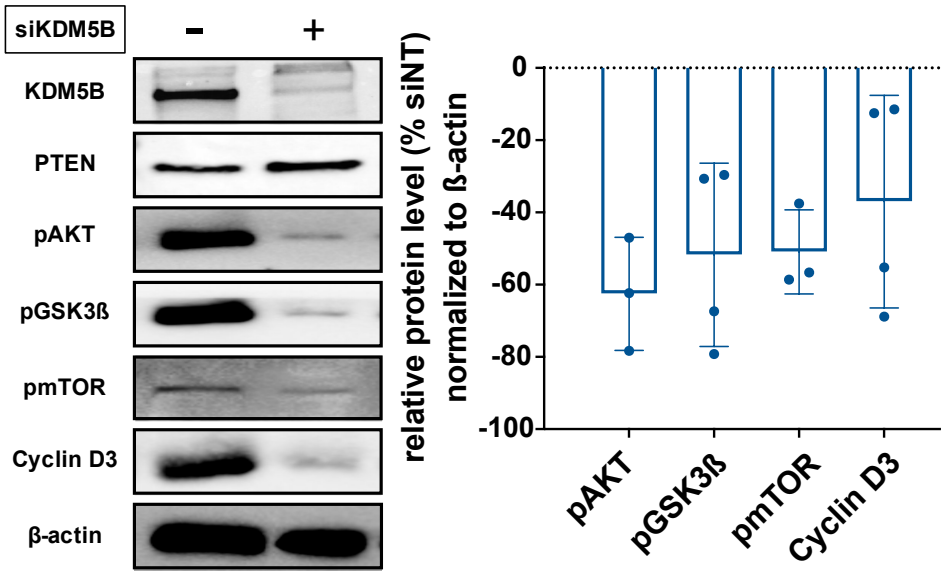

Figure 38: Left: "Protein expression patterns of AKT-PTEN pathway genes subsequent to" siKDM5B or the respective siNT control; "Western blot analysis of naive BN118 cells."; Right: "Quantification of Western blot data for the indicated targets. Data as mean ± SD, derived from n=3-4 naive patient samples (BN46, BN118, E049, E056)." (adapted from Ullrich et al., in revision 2023).

To confirm the increase of PTEN protein levels additional Western blots of siRNA/siNT-treated ^{naive}BN46, ^{naive}BN118 cell samples were performed. After quantification using the Image Lab™ software and normalization to the ß-actin loading control, relative protein levels were determined for siKDM5B cell samples as a percentage of siNT. KDM5B showed a strongly decreased abundance of 51.9±20 % (^{naive}BN46), and 67.3±12 % (^{naive}BN118) after knockdown. At the same time PTEN was increased by 23.6±12 % (^{naive}BN46) and by 47.3±23 % (^{naive}BN118) in siKDM5B compared to siNT cell samples.

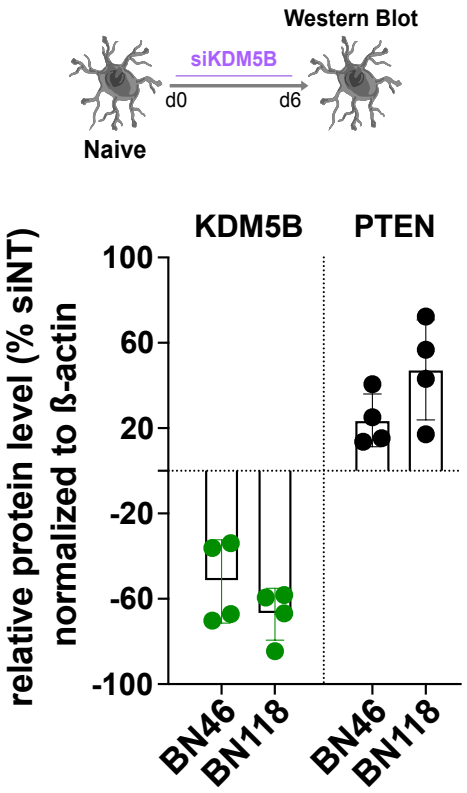

Figure 39: "Quantification data derived from quadruplicate Western Blot analysis of naive patient samples BN46 and BN118. Treatment scheme as indicated. Data normalized as indicated and presented as mean ± SD." (adapted from Ullrich et al., in revision 2023).

These data suggested that PTEN was a key (downstream) target of KDM5B, and thus, a rescue experiment was conducted involving three experimental conditions and 4 patient cell samples (^{naive}BN46, ^{naive}BN118, ^{naive}E049 and ^{naive}E056). The first condition was a siRNA-based KDM5B knockdown alone over a period of 6 days, the second condition was siRNA-based KDM5B knockdown for 6 days followed by TMZ exposure for 3 days, and the third condition was a TMZ exposure for 3 days followed by a siRNA-based KDM5B knockdown for 6 days. After each of these experimental paths, a cell viability readout was performed using the AlamarBlue™ assay (see Methods, chapter "5.5.2. Cell viability assessment"). Subsequently to the readout, SF1670, a specific small molecule PTEN inhibitor (Rosivatz et al., ACS Chem Biol 2006) (10nM) was added to each experimental path for 24 hours, before an additional cell viability readout was performed.

In the first condition (siKDM5B alone) the cell viability was reduced by 38±7 % (^{naive}BN46), 29.2±11 % (^{naive}BN118), 25.9±5 % (^{naive}E049) and 26.9±6 % (^{naive}E056). In the second condition (siKDM5B→TMZ) a decrease in cellular viability by 52.1±13 % (^{naive}BN46), 40.7±13 % (^{naive}BN118), 31.5±5 % (^{naive}E049) and 38.1±15 % (^{naive}E056) can be detected.

The siKDM5B knockdown exhibited the most pronounced effect, when administered sequential to TMZ exposure (third condition = TMZ→siKDM5B), which reduced cell viability by 90±0.6 % (^{naive}BN46), 75±8 % (^{naive}BN118), 71.5±5 % (^{naive}E049) and 76±9 % (^{naive}E056). For all three conditions, the reduction in cell viability could be reversed by the post-hoc supply of PTEN Inhibitor SF1670 (Figure 40).

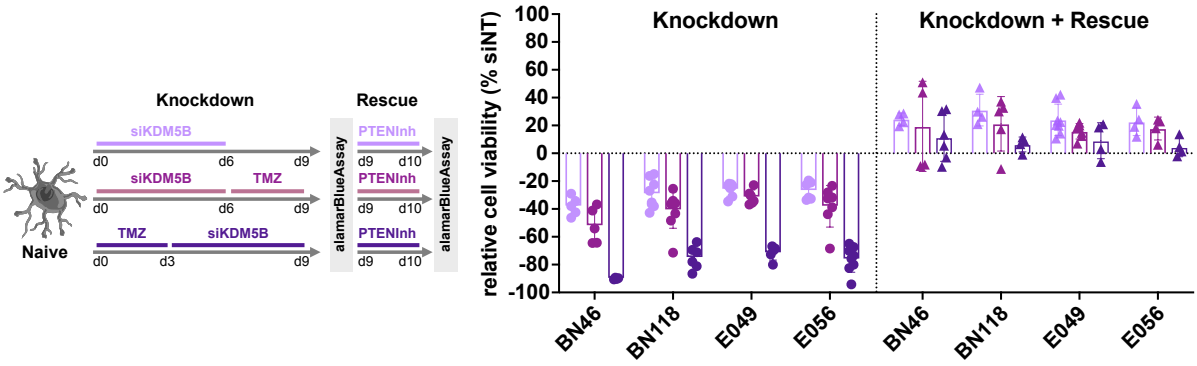

Figure 40: "siKDM5B-knockdown/PTEN inhibitor-rescue experiment. Cartoon illustrates series of experiments conducted with naive patient samples BN46, BN118, E049, and E056. Bar plots present alamarBlueTM readout data, normalized to the corresponding siNT-controls and shown as mean ± SD. PTEN inhibition (PTENInh) by SF1670 (10nM for 24h)." (adapted from Ullrich et al., in revision 2023).

Based on the obtained data, one could speculate that KDM5B inhibited PTEN expression, which activates the AKT pathway and consequently increases cellular viability. If KDM5B is knocked down, the cellular viability could be reduced, because KDM5B is not longer inhibiting the expression of PTEN. The subsequent addition of a PTEN inhibitor would then lead to the acquirement of pAKT and an increase in cellular viability.

Because KDM5B is known to regulate expression of specific targets by impeding the accessibility of their promoters via H3K4-demethylation (see chapter "1.4. Adaptive plasticity and dynamic cellular state transitions"), it was tempting to speculate that KDM5B could directly act on *PTEN* via its demethylating activity. Consequently, Chromatin Immunoprecipitation Sequencing (CHIP-seq) was performed on patient samples ^{naive}BN46 and ^{naive}BN118 using antibodies directed against the H3K4trimethylation sites (see Methods, chapter "5.7. Chromatin Immunoprecipitation Sequencing (CHIP-Seq)"). Experiments involved treatment with siKDM5B or the corresponding siNT for 6 days before the CHIP-seq was conducted. In addition to the H3K4trimethylation antibody, positive (Histone H3) and negative (Normal Rabbit Immunoglobulin G (IgG)) antibody controls were added. The Histone H3 antibody is expected to bind to multiple DNA regions, so that, e.g., the

housekeeping gene RPL30 should be enriched as a control. The antibody against normal Rabbit IgG is not supposed to be specific and consequently no or less accumulation of the RPL30 gene is expected, enabling assessment of non-specific binding. The successful CHIP was validated using qPCR with primers for the ribosomal housekeeper gene RPL30 in the positive and negative antibody control samples (Supplementary Figure 7).

Bioinformatic analysis was performed (by Diagenode Epigenomic Services) and specific gene loci of selected members of the PI3K pathway were investigated. The resulting peaks in the *PTEN* region as well as in *AKT 1*, *AKT 2* and *AKT 3*, *PIK3CA* and *mTOR* are visualized in Figure 41. No significant differences were detected between the peaks of the siKDM5B samples and the peaks of the corresponding siNT control samples, at least in the two patient cell samples tested (^{naive}BN46 and ^{naive}BN118). Thus, the data did not support a direct suppression of the *PTEN* promoter or of promoter regions of the investigated AKT pathway genes through KDM5Bs demethylating activity.

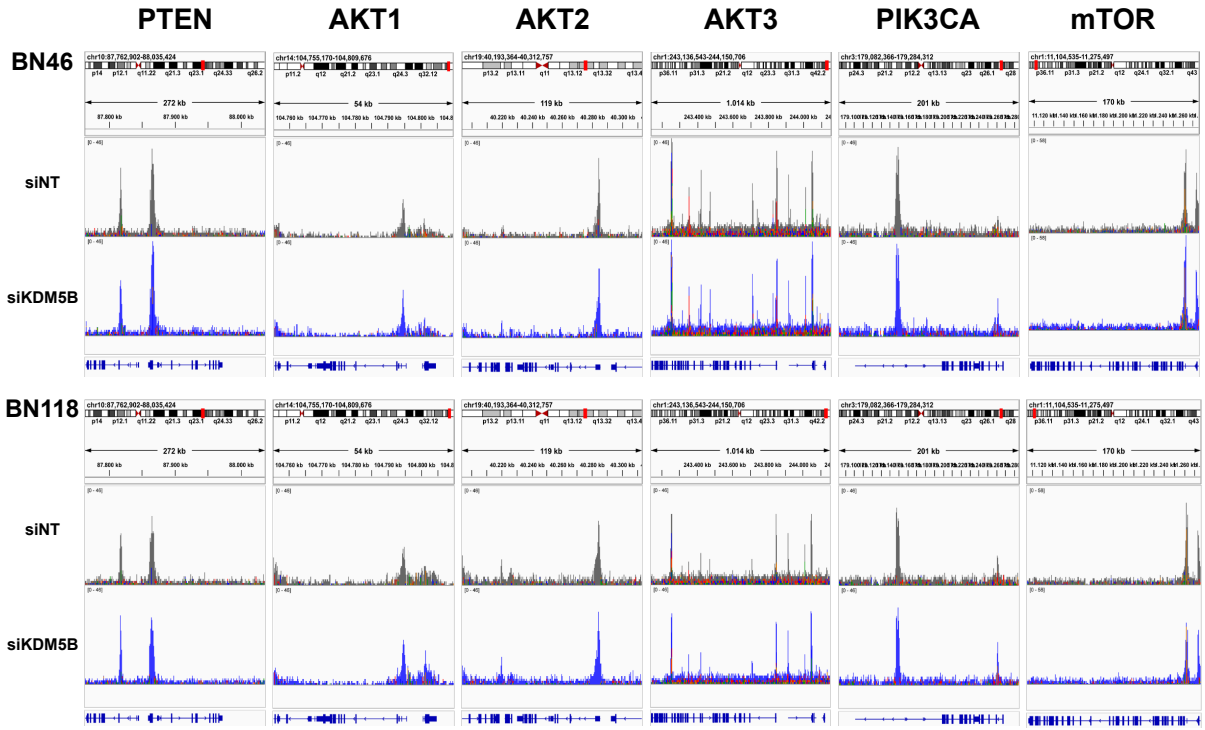

Figure 41: "Chromatin Immunoprecipitation Sequencing (ChIP-Seq) analysis using an anti-H3K4trimethylation antibody in n=2 patient samples (IDs indicated). Snapshots of IGV-software interface exposing the signal intensities of histone mark modification H3K4me3 at the specific gene loci (genes as indicated). Data from siRNA-mediated KDM5B knockdown and corresponding siNT control samples are presented." (adapted from Ullrich et al., in revision 2023).

2.10. Effects of KDM5B inhibition on apoptosis, cellular viability and proliferation

To nevertheless validate that siRNA-based KDM5B knockdown (siKDM5B) induces increased TMZ sensitivity, interference assays were conducted to analyze effects on apoptotic processes.

Before the apoptosis assays were conducted the capability of siKDM5B to reverse the TMZ-induced KDM5B increase was confirmed in ^{naive}BN118 cell samples. After a 4 days TMZ-on→2-days TMZ-off scheme, either siKDM5B or siNT was added to the cells. Flow cytometric readouts were performed after 6 days siKDM5B or siNT. In Figure 42 (left) exemplary histograms of ^{naive}BN118 cells are presented. Through TMZ-only the KDM5B MFI increased by 59.5±3 % (compared to naive). The subsequent addition of siKDM5B reduced the KDM5B MFI by 40.3±31 % compared to the naive cell samples. The increase of KDM5B was not only reversed to the level of ^{naive}cell samples but in some replicates KDM5B even reduced further than in ^{naive}cell samples (Figure 42 right bar chart).

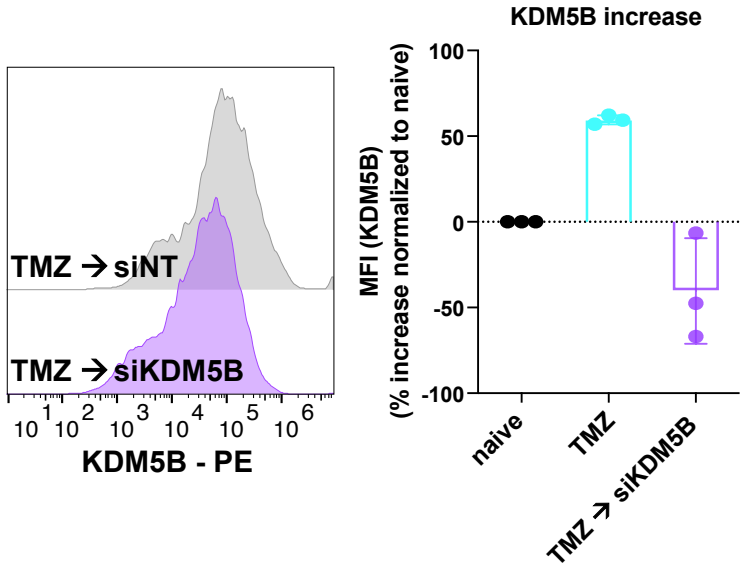

Figure 42: Left: Exemplary flow cytometry histograms of KDM5B-labeled BN118 cells six days after siRNA-mediated knockdown (pink) and respective siNT control (gray), following a TMZ-on/-off scheme; Right: Bar chart depicting the percental increase in the MFI normalized to naive after siRNA-mediated knockdown of KDM5B in naive glioblastoma patient sample BN118 (TMZ 500µM); results in triplicates as mean ± SD.

To investigate the effect of the sequential treatment strategy (4 days TMZ-on → 2-days TMZ-off → 6 days siKDM5B) on induction of apoptotic processes an antibody-labeling for active caspase-3 and readout of the MFIs via flow cytometry was performed (see Methods chapter “5.5.4. Flow cytometric analysis”). The MFI of active

caspase-3 was increased significantly in naiveBN118 cell samples upon siKDM5B subsequent to TMZ exposure (mFC = 0,42) compared to siNT subsequent to TMZ exposure (Figure 43).

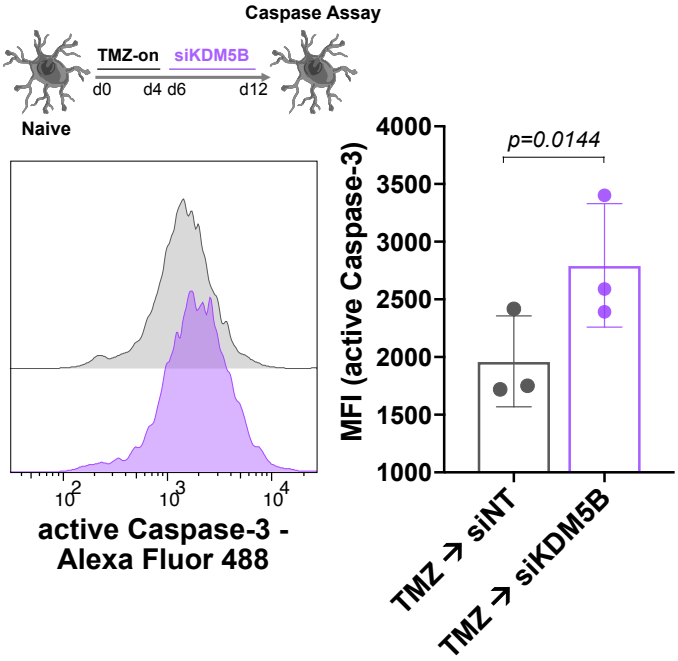

Figure 43: "Caspase assay subsequent to indicated treatment scheme." Left: Exemplary histogram representing shift of active Caspase-3 peaks through siRNA-mediated knockdown of KDM5B in TMZ (500µM) pretreated naive glioblastoma patient cells (BN118); Right: "Bar chart depicting MFI data of active caspase-3. Flow cytometry analysis of patient cell sample BN118 according to indicated treatment scheme. Data in triplicate as mean ± SD. P value by paired t-test." (adapted from Ullrich et al., in revision 2023).

Assuming that the minor TMZ-induced increase of KDM5B in relapse cells (compare Figure 30), would influence the effect of the siKDM5B knockdown on apoptotic processes, the MFI assessment for active caspase-3 was repeated in cRBN118 cell samples. The addition of siKDM5B after TMZ exposure did not reveal a significant effect on the active caspase-3 MFI in cRBN118 cell samples (Supplementary Figure 8).

To estimate potential pharmacological targeting strategies, the pan-KDM5 inhibitor CPI-455 (Fu et al., Eur J Med Chem. 2020) was applied to naiveBN118 cell samples at a concentration of 12µM for 6 days after an initial TMZ-treatment scheme (4 days TMZ-on + 2 days TMZ-off). As a control naiveBN118 cell samples were exposed to CPI-455 (12µM) for 6 days after an initial DMSO (0.5 %)-treatment scheme (4 days DMSO-on + 2 days DMSO-off). In addition naiveBN118 cell samples were exposed to

single treatments of TMZ-only or DMSO (0.5 %)-only for 12 days. The active caspase-3 antibody MFIs were determined by flow cytometry as a readout parameter.

The TMZ-only schedule induced a 2.4-fold increase of active caspase-3 MFI compared to the DMSO-only schedule. TMZ→CPI-455 induced a 3.2-fold increase compared to DMSO→CPI-455. Consequently, the subsequent addition of CPI-455 had an additive effect on active caspase-3 levels (TMZ→CPI-455 vs. TMZ-only = 1.64-fold). Without pre-exposure to TMZ, the CPI-455 exhibited a less pronounced additive effect on caspase-3 levels (DMSO→CPI-455 vs. DMSO-only = 1.2-fold) (Figure 44).

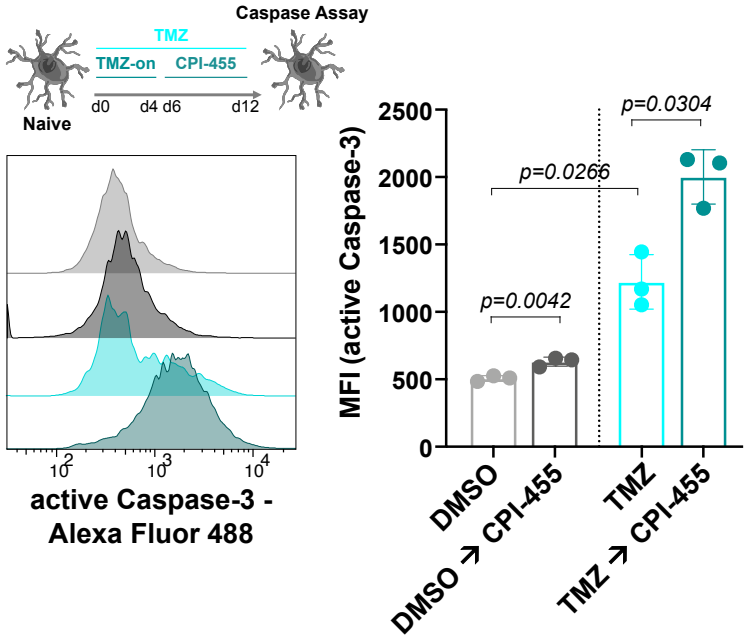

Figure 44: "Caspase assay subsequent to indicated treatment schemes, involving TMZ (500µM), CPI455 (12µM), or DMSO (0.5%). Left: Exemplary histograms, respectively color-coded. Bar chart depicting MFI data of active caspase-3. Flow cytometry analysis of patient cell sample BN118. Triplicate, data as mean ± SD. P values by paired t-test." (adapted from Ullrich et al., in revision 2023).

As CPI-455 increases apoptotic caspase-3 levels the effect of CPI-455 on cellular viability was evaluated after 12 days of single- or combinatorial treatment schemes (compare Figure 44). An AlamarBlue™ assay was performed (see Methods, chapter "5.5.2. Cell viability assessment") in cell samples of ^{naive}BN46 and ^{naive}BN118 that were either treated with single treatments of DMSO (0.5 %)-only, TMZ-only, CPI-455-only, the concurrent addition of CPI-455+TMZ or the combinatorial sequences of CPI-455→TMZ and TMZ→CPI-455. The detected cell viability values were normalized to the corresponding DMSO controls and presented in Figure 45.

The cell viability was decreased by 51.9±5 % through the TMZ-only schedule, while CPI-455-only decreased cell viability by 7.1±0.9 %. The combinatorial sequence

of CPI-455→TMZ decreased the cell viability by 14.6±4 %. Concurrent CPI-455 and TMZ addition decreased the cell viability significantly compared to TMZ with a decrease of 65.4±3 % (1.3-fold more decreased than TMZ-only). The strongest reduction of 79.2±2 % could be noticed upon the combinatorial sequence of TMZ→CPI-455, resulting in a 1.5-fold stronger decrease than with the TMZ-only schedule. (Figure 45).

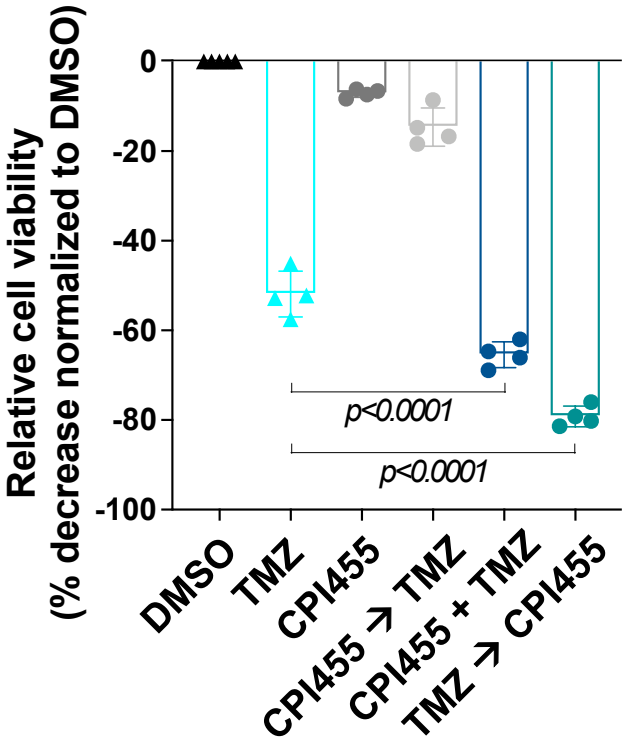

Figure 45: "12-day assays of indicated single- and combinatorial drug treatments, involving TMZ (500µM), CPI455 (12µM), or DMSO (0.5%). Bar plots represent alamarBlueTM cell viability readouts on naive patient samples BN46, and BN118, normalized to the DMSO-control. Duplicate analysis, data as mean ± SD. P values calculated by Kruskal-Wallis test with multiple comparison." (adapted from Ullrich et al., in revision 2023).

CPI-455 increases apoptotic caspase-3 levels leading to reduced cellular viability, which was then corroborated using automated imaging of cell confluence as a second readout parameter (see Methods, chapter "5.5.1 Cell Confluence measurement"). In the experiment, DMSO (0.5%), TMZ (500µM) and CPI-455 (12µM) were applied in single- or combinatorial treatment schemes to the patient cell samples, and the relative cell confluence was computed by normalizing data to the respective value of cell confluence on day 0.

In ^{naive}BN46 patient cells, TMZ-only reduced the relative cell confluence to 56±7 %, while CPI-455-only did not decrease the cell confluence (relative confluency on day 10 = 152±20 %). Similarly, the combinatorial sequence of CPI-455→TMZ did not lead to a reduction in cell confluence, with a relative cellular confluency of 107±18 % on day

10. The concurrent addition of CPI-455 and TMZ reduced relative cellular confluency compared to TMZ-only (relative confluency on day 10 = 39.9±6 %). The most pronounced effect could be measured under combinatorial sequence of TMZ→CPI-455, which decreased the relative cell confluence to 25.7±6 % on day 10 (Figure 46).

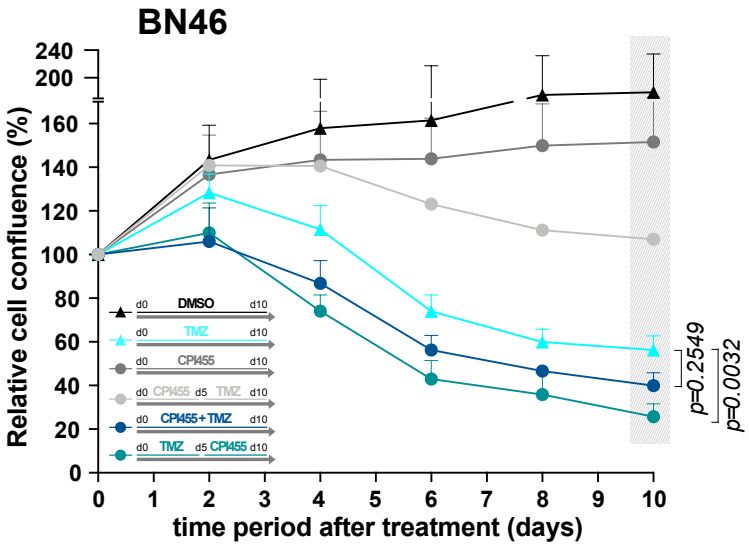

Figure 46: Graph shows percent in vitro cell confluence (monitored by software-based cell recognition, NyOne®) of a naive patient sample (BN46) treated with either control DMSO (0.05%), 500 µM TMZ-only, 12 µM CPI455-only or combinational or sequential TMZ and CPI455 treatment schemes, treatment was performed every other day; cell confluence is presented relative to day 0; data shown are mean ± SD of n=3-5 technical replicates. P values calculated using a Kruskal–Wallis test with multiple comparison.

In ^{naive}BN118 cell samples, TMZ-only reduced the relative cell confluence to 29.4±12 %, while the CPI-455-only schedule was overgrown on day 4. The combinatorial sequence of CPI-455→TMZ reduced the cell confluence to 52.9±10 % on day 10, showing a less distinct effect than the TMZ-only schedule. The concurrent CPI-455 and TMZ exposure reduced the relative cellular confluency compared to TMZ-only with 20.9±3 % at day 10. The most pronounced effect could be detected upon the combinatorial sequence of TMZ→CPI-455, with a reduction of the relative cell confluence to 9.9±6 % on day 10 (Figure 46).

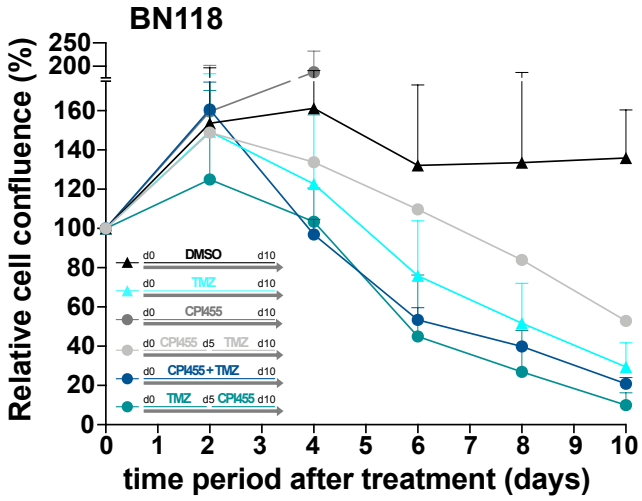

Figure 47: Graph shows percent in vitro cell confluence (monitored by software-based cell recognition, NyOne®) of a naive patient sample (BN118) treated with either control DMSO (0.05%), 500 µM TMZ-only, 12 µM CPI455-only or combinational or sequential TMZ and CPI455 treatment schemes, treatment was performed every other day; cell confluence is presented relative to day 0; data shown are mean ± SD of n=3-5 technical replicates.

As similarly seen in $^{TMZ\rightarrow eR}$BN46 cell samples (compare Figure 15) TMZ-only did not decrease the cell confluence of ^{cR}BN118 cell samples (relative confluency on day 10 = 123.1±2 %). No additive effect on the relative cell confluence was detected in ^{cR}BN118 cell samples after the combinatorial sequence of TMZ→CPI-455 (relative confluency on day 10 = 125.9±9 %), confirming the observation that TMZ exposure followed by KDM5B knockdown did not lead to an increase in active caspase-3 levels in ^{cR}BN118 (compare Supplementary Figure 8)

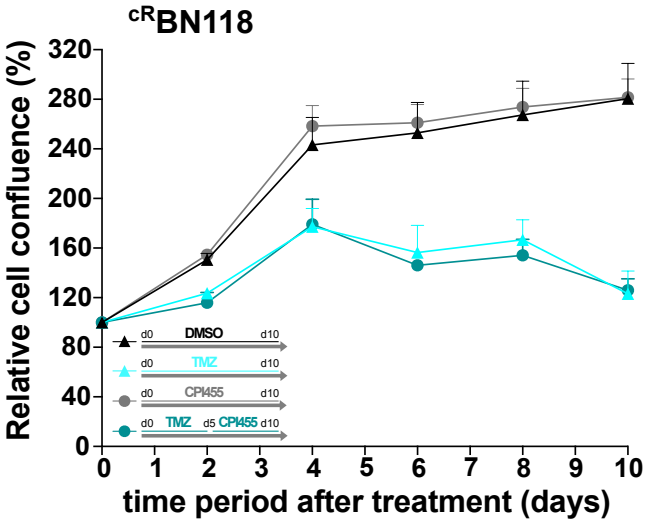

Figure 48: Graph shows percent in vitro cell confluence (monitored by software-based cell recognition, NyOne®) of a clinical relapse patient sample (cRBN118) treated with either control DMSO (0.05%), 500 µM TMZ-only, 12 µM CPI455-only or sequential TMZ and CPI455 treatment, treatment was performed every other day; cell confluence is presented relative to day 0; data shown are mean ± SD of n=3 technical replicates.

Overall, the obtained data demonstrate, that the sequential treatment scheme of preliminary standard of care TMZ exposure followed by KDM5B inhibition leads to an increase in apoptosis and consequently a decrease of cellular viability and cell confluence.

To observe if KDM5B inhibition impedes clonal expansion of $^{TMZ\rightarrow eR}$cells a long-term experiment was performed using ^{naive}BN118 cells (see Figure 4 and chapter “1.4. Adaptive plasticity and dynamic cellular state transitions”). The cells were exposed to TMZ every other day for 16 days before TMZ was withdrawn. After a 3-day TMZ withdrawal (TMZ-off phase) CPI-455 was applied every other day for 8 days or 16 days. The relative cell confluence was obtained by normalization of the data to the respective values of the cell confluence on day 0.

The addition of CPI-455 to DMSO pre-treated cells did not decrease cell confluence compared to DMSO-only. Serial exposure to TMZ led to a reduction of relative cell confluence to 11.5±1 %. Then a non-proliferative period of 24 days can be observed. At day 40 the quiescent cells started to proliferate. The cell confluence raised again to 119.3±6 % at the end of the observation period (day 56). In contrast, KDM5B inhibition subsequent to TMZ exposure could prevent or delay expansion of $^{TMZ\rightarrow eR}$cells, at least until the end of the observation phase. The cell confluence was lower than 10 % until the end of the observation period (day 56) (TMZ→WD 7 days→Cpd46 8 days = 2.4±0.4 %; TMZ→WD 7 days→Cpd46 16 days = 2±0.2 %) (Figure 49).

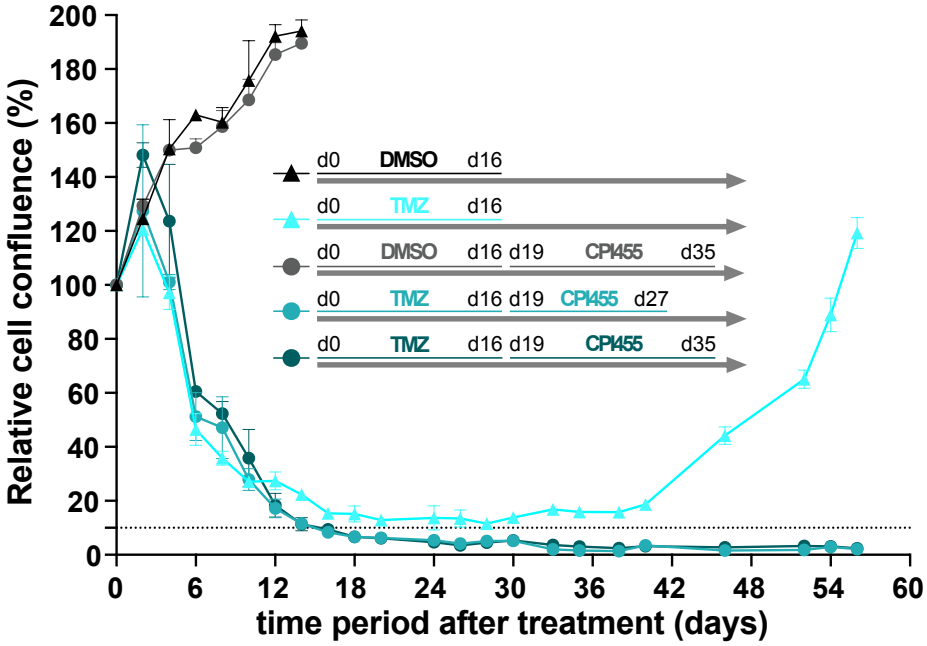

Figure 49: Graph shows long term observation of percent in vitro cell confluence (monitored by software-based cell recognition, NyOne®) of naive patient cells (BN118) under sequential treatment schemes; DMSO (0.05%), TMZ (500µM) and CPI455 (12µM) were given every other day; cell confluence is presented relative to day 0; data shown are mean ± SD of n=2 technical replicates.

Taken together the sequential treatment with CPI-455 subsequent to TMZ increased apoptotic processes compared to TMZ-only, reduced cell viability and cell confluence compared to TMZ-only and could delay the expansion of $^{TMZ\rightarrow eR}$cells, that was observed with TMZ-only.

To further understand the expansion of $^{TMZ\rightarrow eR}$cells an additional long-term treatment was perfomed using the fast proliferating glioblastoma cell line LN229. The LN229 cells were treated with different TMZ-concentrations (250 µM, 500 µM, 750 µM, and 1mM) every other day for 16 days. The relative cell confluence was obtained by normalization of the data to the respective values of the cell confluence on day 0.

The expansion dynamics of $^{TMZ\rightarrow eR}$cells differed between the replicates. The quiescent cells did not overcome their non-proliferative state and started to expand at once ($^{TMZ\rightarrow eR}$cells) in all replicates. A classification according to turning points, from the non-proliferative state phase (DTP-like) to the expansion phase, into fast (cheetah), moderate (meerkat) and slow (sloth) expanding $^{TMZ\rightarrow eR}$cells was performed. In the following the $^{TMZ\rightarrow eR}$cells will be called DTEPs. The turning point of cheetahs was day 29±3, the turning point of meerkats was day 49±6, and the turning point of sloths was day 107±13. The division into replicates with different turning points was independent of the TMZ concentration that was administered (Figure 50).

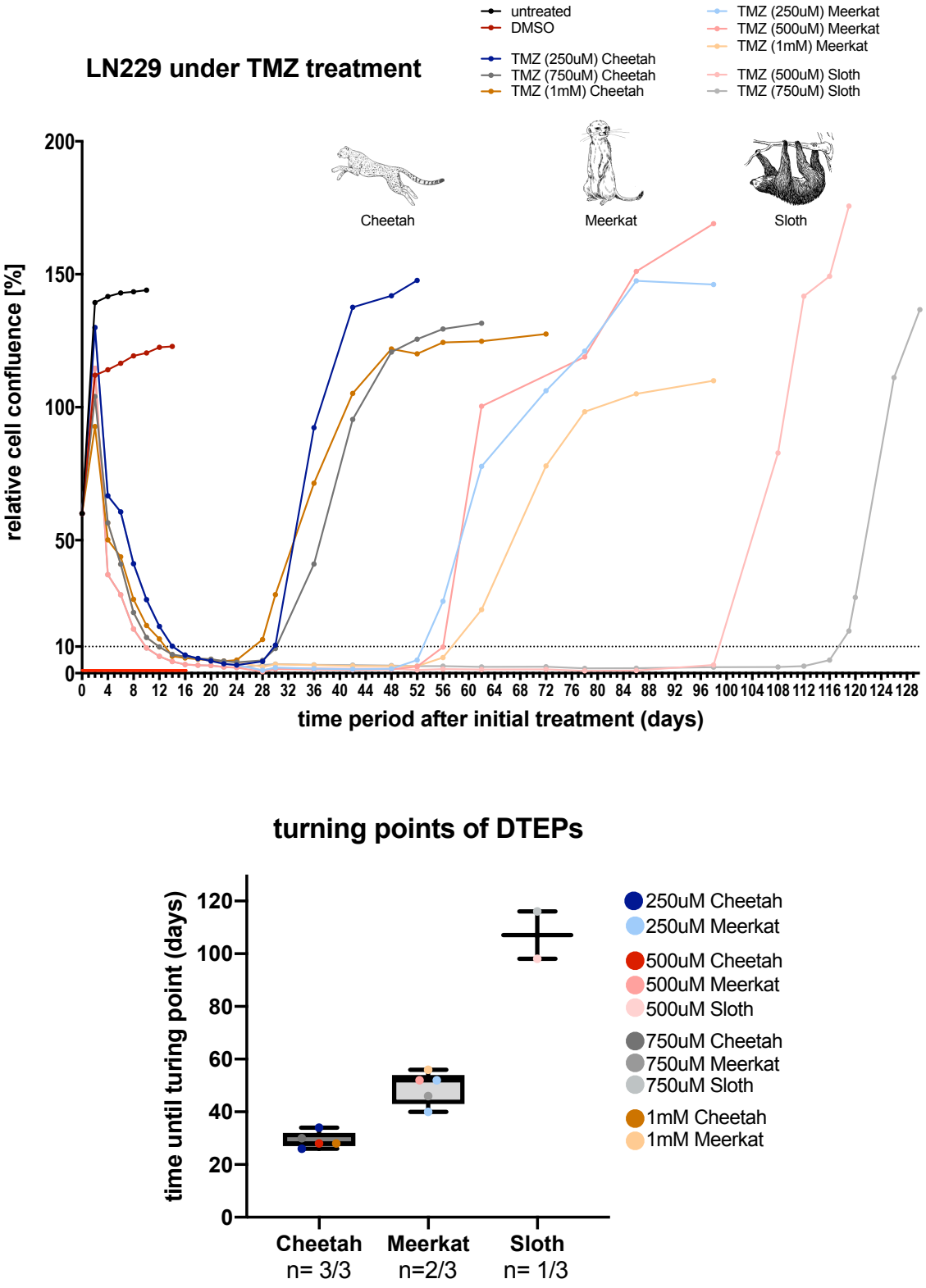

Figure 50: Upper panel: percent in vitro cell confluence (monitored by software-based cell recognition, NyOne®) of cell line LN229 during and after 16 days TMZ exposure, observation time: 130 days; TMZ concentrations indicated; cell confluence is presented relative to day 0; n=1; Lower panel: turning points of LN229 DTEPs in cheetah, meerkat and sloth samples after exposure to the indicated TMZ concentrations, n=3

2.11. Monitoring of subclonal dynamics and newly arising subclones via DNA-Barcoding

To further investigate subclonal dynamics under the influence of TMZ exposure, DNA barcoding technology was used as a model system. Individual ^{naive}cell samples (^{naive}BN46 and ^{naive}BN118) were labeled with unique DNA sequences, to trace them under TMZ treatment until the expansion of $^{TMZ→eR}$cells.

Using ClonTracer, an established DNA-Barcoding System (Bhang et al., Nat. Med. 2015), the mapping of subclonal populations and their dynamics over time can be accomplished. In the established experimental assays, barcoding enables the assessment of relationships between treatment-naive cells and their TMZ-resistant progeny. The experimental methodology is described in Methods chapter “5.6. DNA Barcoding” in detail. The lenti-viral pool was produced in HEK293T cells (Supplementary Figure 9).

For the transduction of ^{naive}BN118 and ^{naive}BN46 patient cells via lentiviral infection, a frequency of 10-30 % barcoded cells was aimed, to ensure a transduction efficiency of one barcode per cell. The transduction efficiency was analyzed via flow cytometric detection of the fluorescent marker RFP, that was included in the barcoding plasmid (Supplementary Figure 10 and 11). Antibiotic selection of the transduced cells enriched a pool of nearly 100% RPF+ cells (confirmed using flow cytometry, Supplementary Figure 12), that incorporated the barcode.

Subsequently, the *Pre-pool* contained one million individually labeled cells, each with a unique DNA barcode. The sample was expanded under controlled conditions in vitro for 3 passages to generate n=8 replicates (Naive). The ^{naive}cells were then exposed to DMSO (0.5%) as a control (^{DMSO}CTRL) or to TMZ (500 µM) every other day for 16 days. About 10 % drug-tolerant persister cells survived (DTPs; Supplementary Figure 12). After the quiescent phase of 3-4 weeks, the cells began to expand as $^{TMZ→eR}$cells. In the following the $^{TMZ→eR}$cells will be called DTEPs (n=4). Samples were taken from each timepoint. An overview of the experimental workflow is illustrated in Figure 51. The DNA of all collected samples was isolated, the barcode region was PCR amplified and purified via gelelectrophoresis (Supplementary Figure 16) and the bands were cut out for gel extraction and subsequent next generation sequencing (NGS).

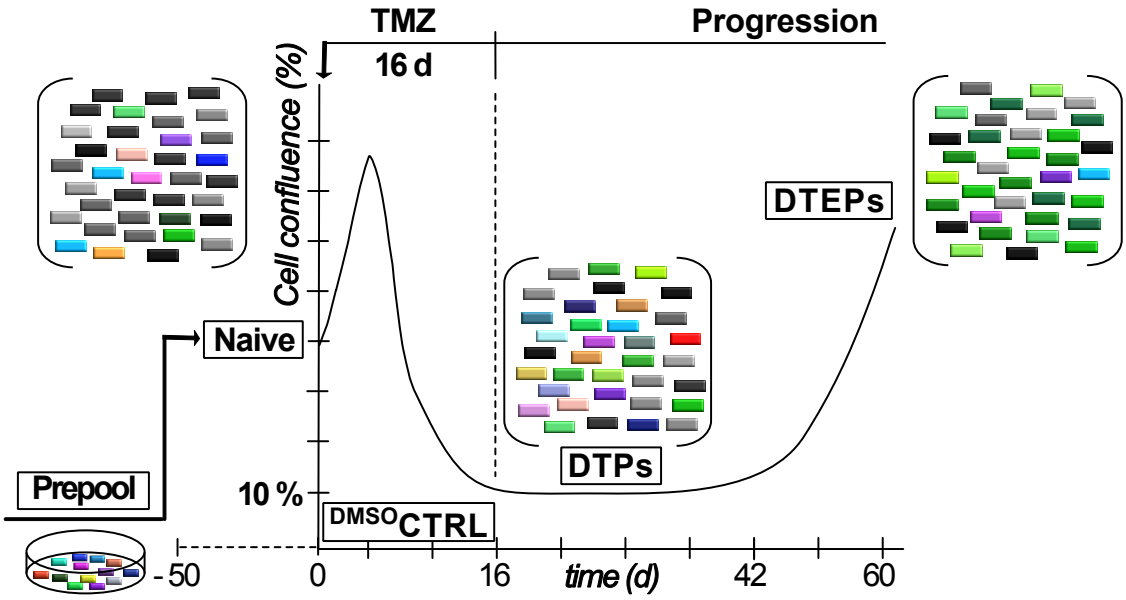

Figure 51: "Cartoon illustrating the experimental barcoding setup. Naive BN46 and BN118 patient cells were provided with the ClonTracer barcoding construct" (Bhang et al., Nat Med.2015), "exposed to 500µM TMZ or 0.5% DMSO, and analyzed by NGS at the indicated time points. Drug-tolerant persister cells (DTPs), drug-tolerant expanded persister cells (DTEPs)." (adapted from Ullrich et al., in revision 2023).

DTEPs emerged between day 40 and day 60 of the experimental workflow. Fast expanding DTEPs could be distinguished from slow expanding DTEPs as well via microscopical observation of the arising $^{TMZ \rightarrow eR}$subclones, as fast expanding DTEPs harbored less microscopically visible, diverse subclones than slow expanding DTEPs (Figure 52 and Supplementary Figure 14 and 15).

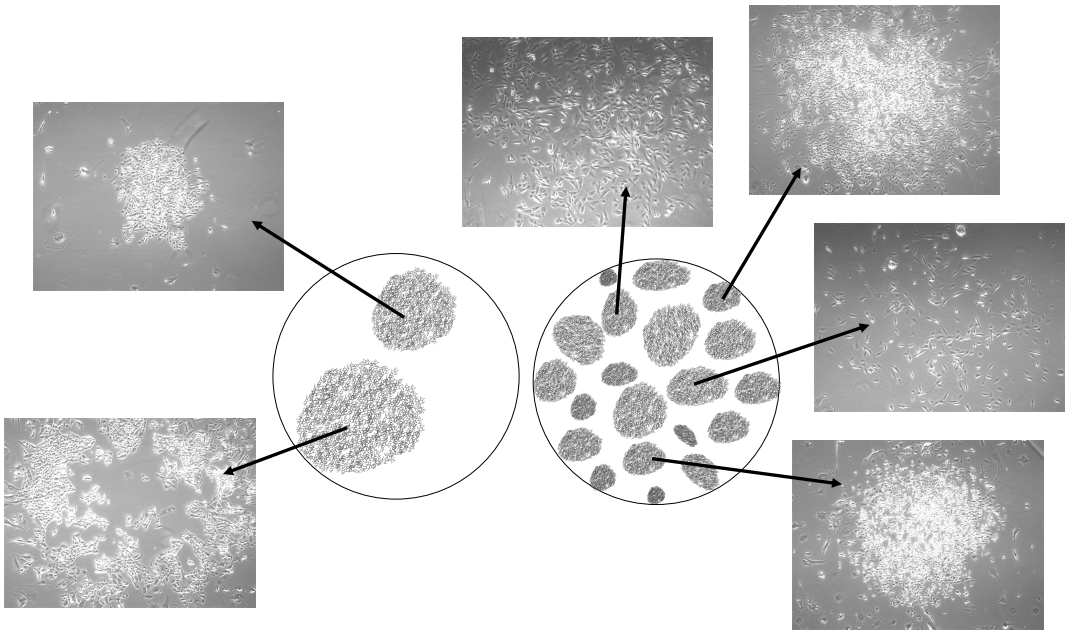

Figure 52: Illustration of microscopically diverse DTEP subclones. Left: fast DTEPs; Right: slow DTEPs.

Bioinformatic pipeline analysis detected the frequency of barcode identities (BCIs), that were detectable in NGS. At the time of barcoding cellular heterogeneity is expected to underly in a treatment-naive population. The number of identified BCIs in the different samples is shown in Figure 55 for both patients. The number of BCIs, that could be identified in the Prepool sample was strongly reduced below 0.3% in the Naive sample, while the number of undetectable BCIs was strongly increased during the in vitro expansion phase, in which the 8 replicates were generated (Prepool-BCIs = 106 ±11,313 vs. Naive-BCIs = 2,900±3,343). Through TMZ exposure a re-emergence of >250,000 BCIs (DTP-BCIs = 259,886±346,177), decreased again after the expansion of $^{TMZ\rightarrow eR}$cells (DTEP-BCIs = 6,613±5,964) (Figure 55).

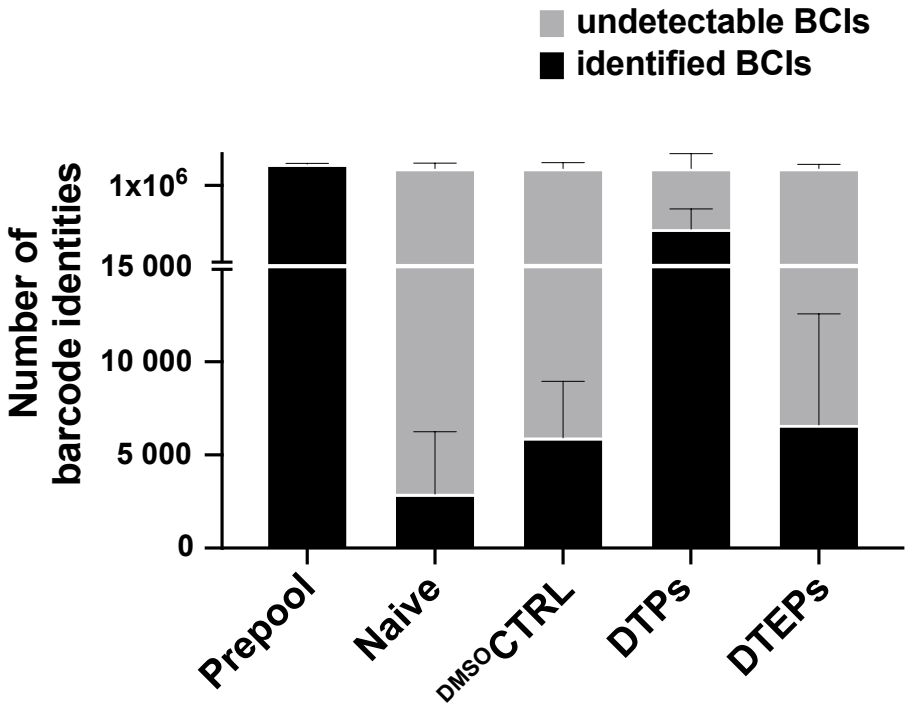

Figure 53: "NGS-based quantification of detectable barcode identities (BCIs) […] Bar charts representing ratios of identifiable vs. undetectable BCIs at the indicated experimental stages. Data points from naive patient samples BN46 and BN118, presented as mean ± SD." (adapted from Ullrich et al., in revision 2023).

As a next step the composition of the top 50 BCIs of the $^{TMZ\rightarrow eR}$ timepoint (in the following called DTEP) throughout disease progression was investigated. The stacked plot in Figure 56 displays the top 50 DTEP BCIs, for each time point in ^{naive}BN118. The plot is stacked to 100 % and is sorted according to the frequency of the BCIs in the DTEP samples (bioinformatic analysis by Igor Cima). The analysis as a stacked plot revealed, that dominant BCIs either disappeared (sensitive = colorful) or survived (resistant = grayscale) upon TMZ treatment, while newly arising BCIs emerged in

DTEP samples (newly arising = greenscale). The newly arising BCIs, which have been underrepresented in the Naive sample and have been uncovered upon TMZ treatment, were the most abundant BCIs in the DTEP samples (Figure 54).

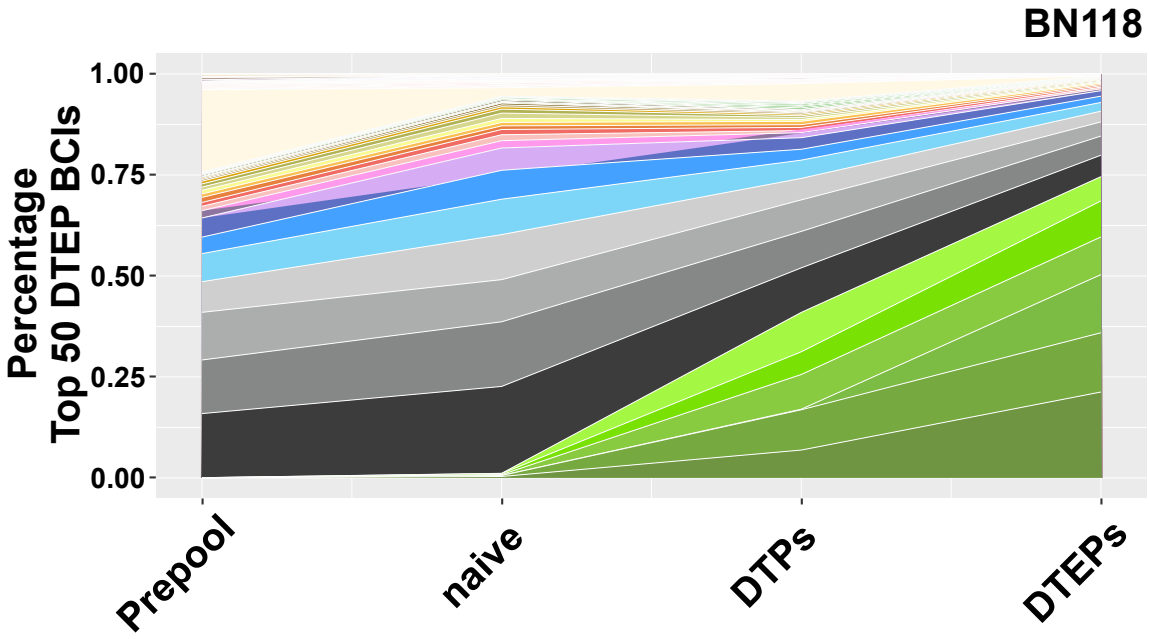

Figure 54: "Subclonal dynamics […], visualized as a stacked plot […] " (patient sample BN118). " […] Data represent the relative frequencies of the top 50 BCIs, as defined at the DTEP-stage, displayed for each stage of the experiments."; "Note: green-scale, newly arising BCIs under TMZ exposure vs. gray-scale, dominant BCIs at the Naive stage of the experiment. […]." (adapted from Ullrich et al., in revision 2023).

The results were confirmed in ^{naive}BN46 cell samples. The DTEP samples were mainly composed of the newly arising BCIs. However, in comparison to ^{naive}BN118 the newly arising BCIs in ^{naive}BN46 were still underrepresented in the DTP samples. The drug-sensitive dominant subclones (colorful) were reduced upon TMZ exposure, as observed in ^{naive}BN118. Regarding the BCIs that survived (resistant = grayscale) upon TMZ exposure another difference can be detected between the two patient cell samples. In ^{naive}BN46 only one BCI was detected, that was the most represented BCI in the Naive and DTP samples and stayed the most represented BCI in the DTEP samples (see Figure 56 Lower panel). For better visualization of the other BCIs this dominant resistant BCI (black) was left out of the stacked plot analysis, as it does not seem to play a role in the treatment-induced dynamics (Figure 55).

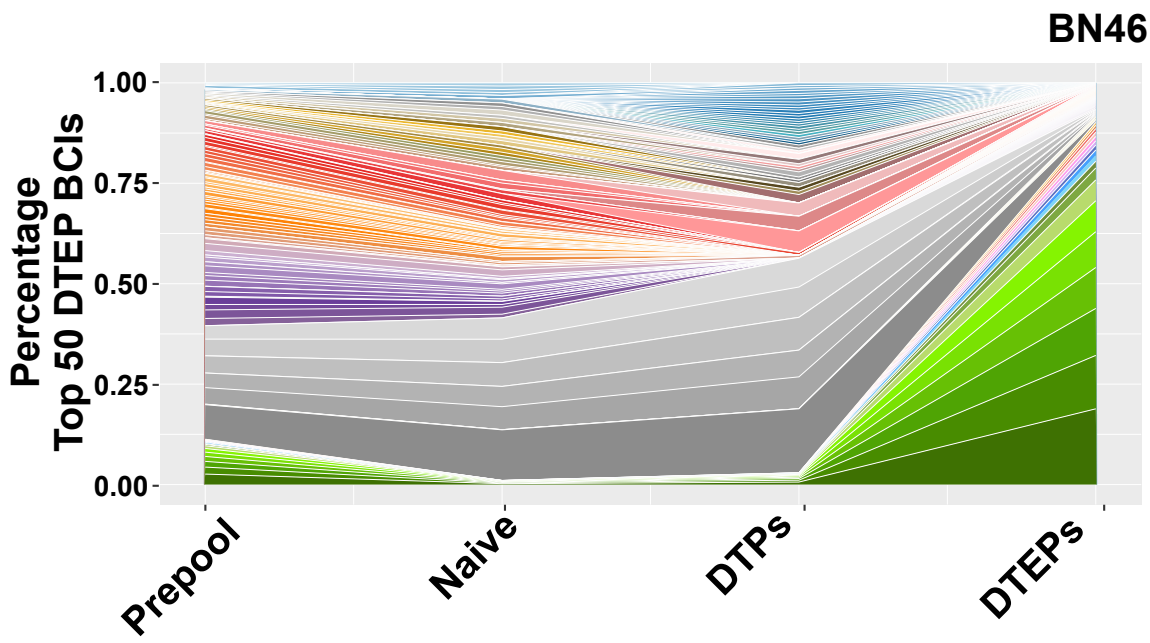

Figure 55: "Subclonal dynamics, visualized as a stacked plot (patient sample BN46). Data represent the relative frequencies of the top 50 BCIs, as defined at the DTEP-stage, displayed for each stage of the experiment."; "Note: green-scale, newly arising BCIs under TMZ exposure vs. gray-scale, dominant BCIs at the Naive stage of the experiment. […] "; "For better visualization of lower-ranked barcode fractions, the #1 dominant resistant clone, which is overrepresented in every sample […]" (see Fig 57)," […] is excluded from this graph." (adapted from Ullrich et al., in revision 2023).

As a following step the relative abundance for the top barcodes were plotted in bubble plots (bioinformatic analysis by Anna Baginska). All barcodes that had a relative abundance of at least 1 % were plotted and the size of the circles represents their relative abundance. The barcodes were visualized sorted following their abundance in DTEP samples. Figure 56 displays the data of patient BN118 (upper panel) and the data of patient BN46 (lower panel) separately. The relative abundance of each of the top BCIs shows that the DTEP samples were mainly composed of newly arising BCIs, that were underrepresented in the Naive sample and from some BCIs, that were dominant already in the Naive samples (resistant). The DTEP samples of patient BN118 were mainly composed of 4 resistant and 6 newly arising BCIs. The 6 newly arising BCIs have collectively outnumbered the originally dominant BCIs, as they represented 70% of the DTEPs in ^{naive}BN118. ^{naive}BN46 encompassed one dominant resistant (black), as already described before and 9 newly arising BCIs under the top ones. The 9 newly arising BCIs presented 55% of the DTEPs. Moreover the bubble plot of patient BN46 samples revealed, that the dominant resistant BCI, indeed stays the most prominent one, even if its abundance is reduced upon TMZ treatment compared to the Naive sample (Figure 56).

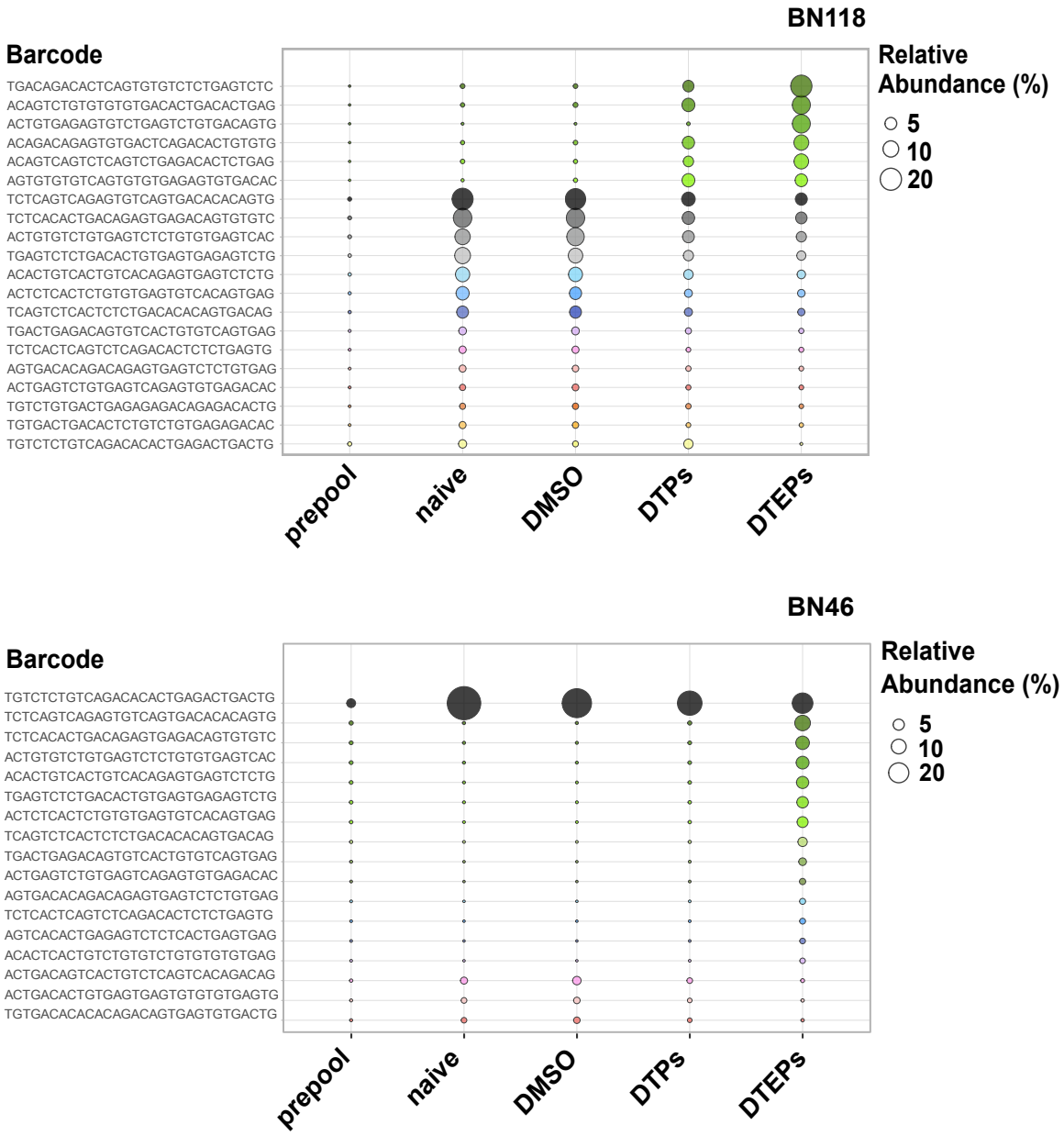

Figure 56: "Subclonal dynamics […], visualized as a bubble plot. Data represent relative barcode abundances, barcode identity as specified, at the indicated time points of the experiments. Barcodes of at least 1% relative abundance shown."; "Note: green-scale, newly arising BCIs under TMZ exposure vs. gray-scale, dominant BCIs at the Naive stage of the experiment. […]" Upper Panel: Patient sample BN118 shown; Lower Panel: Patient sample BN46 shown. (adapted from Ullrich et al., in revision 2023).

2.12. Enrichment of KDM5B^{high} cells allows prediction of newly arising subclones

To further characterize the subclonal dynamics, the 10 most prominent DTEP-BCIs were identified and allocated to ranking positions along the different stages of the experimental course (Top-ranked DTEP BCIs). In the samples of ^{naive}BN118 the dominant BCIs of the Naive sample (ranking positions 1 to 4) were at ranking positions 7 to 10 in the DTEP samples. The newly arising BCIs were underrepresented in the

Naive sample (ranking positions 20, 22, 25, 27, 85, 213), while in the DTEP samples the newly arising BCIs accumulated in the top 10 ranked list (ranking positions 1 to 6) (Figure 7 left plot). In the samples of ^{naive}BN46 the assignment of exact ranking positions elucidates, that the same dominant (black) BCI stayed at ranking position 1 in all samples, as discussed before. In DTEP samples the newly arising BCIs accumulated in the top 10 ranked list (ranking positions 2 to 10). The newly arising BCIs were underrepresented in the Naive sample (ranking positions 42, 73, 125, 227, 288 and between 547 and 2404) (Figure 57 right plot).

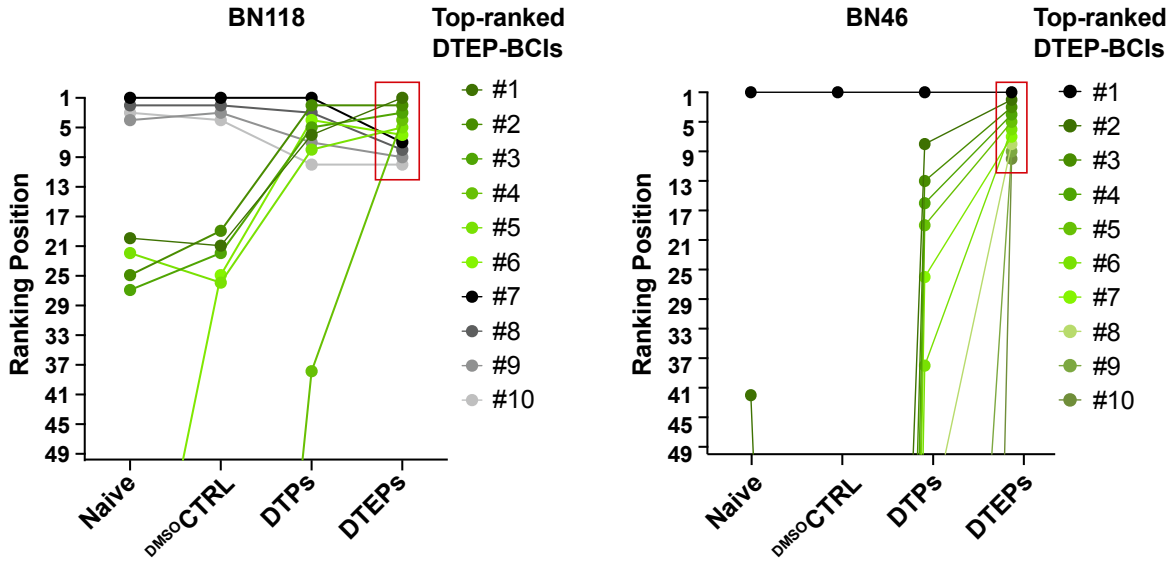

Figure 57: "Subclonal dynamics […], visualized as a ranked plot. Data represent individual ranking position of the top 10 BCIs, as defined at the DTEP-stage, displayed for each stage of the experiments."; "Note: green-scale, newly arising BCIs under TMZ exposure vs. gray-scale, dominant BCIs at the naive stage of the experiment. […] "; Left: Patient sample BN118 shown; Right: Patient sample BN46 shown. (adapted from Ullrich et al., in revision 2023).

The gene expression of KDM5B and ALDH1A1 in barcoded Naive samples was compared with the gene expression of KDM5B and ALDH1A1 in the barcoded DTEPs ($^{TMZ→eR}$cells), using qPCR (Figure 58). The *KDM5B* expression levels appear unchanged in naive vs. post-TMZ samples (Mean DTEP/mean naive: BN46 = 1.1; BN118 = 1.0), similar as shown for not barcoded ^{naive}cells vs. ^{cR}cells or $^{TMZ→eR}$cells earlier via qPCR (compare Figure 22). Whereas, *ALDH1A1* gene expression was upregulated in the barcoded DTEPs compared to the naive samples (Mean DTEP/mean naive: BN46 = 30.2; BN118 = 43.4) similar as shown for not barcoded ^{naive}cells vs. ^{cR}cells or $^{TMZ→eR}$cells earlier via qPCR (compare Figure 20).

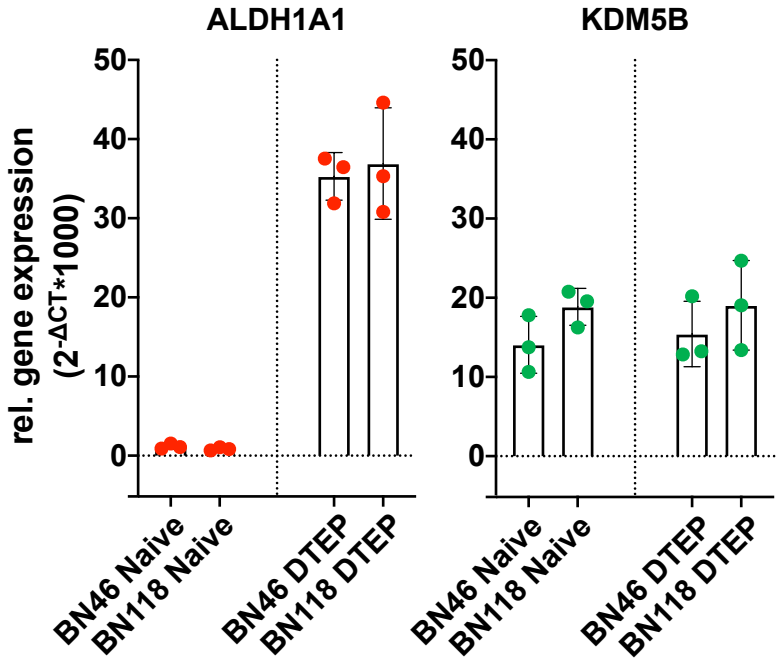

Figure 58: "Relative gene expression detected using qPCR, at the Naive vs. DTEP stage of the DNA Barcoding experiment. Patient IDs indicated. Data shown in triplicate as mean ± SD." (adapted from Ullrich et al., in revision 2023).

Based on the observations that KDM5B expression in ^{naive}cell samples could predict elevated ALDH1A1 in ^{cR} and $^{TMZ→eR}$ cell samples, KDM5B could potentially be a predictive factor for subclonal expansion. A population of KDM5B^{high} cellular identities was sorted-out from the barcoded heterogeneous samples at the Naive stage using a KDM5B antibody (top 5 % highest fluorescent intensity = KDM5B^{high} cells) (see Methods, chapter "5.6.5. Sample preparation and sequencing of barcoded patient cells" in detail) and was included in the DNA-barcoding analysis for ^{naive}BN46 and ^{naive}BN118. After sequencing and bioinformatic analysis, BCI composition of the sorted (KDM5B^{high}) as well as of the unsorted samples (Naive, DMSO, DTPs, DTEPs) was determined to follow the course of the KDM5B^{high} cellular identities (Figure 59).

The KDM5B^{high} population was mainly composed of the newly arising BCIs, and not of the BCIs, which were dominant in the Naive sample. The newly arising BCIs were determined with a fraction of 24.77 % in the KDM5B sorted sample of ^{naive}BN118 and 9.33 % in the KDM5B sorted sample of ^{naive}BN46. The BCIs, which were dominant in the Naive sample showed a fraction of 5,6 % in the KDM5B sorted sample of ^{naive}BN118 and could not be detected in the KDM5B sorted sample of ^{naive}BN46. This implies, that sorting for KDM5B seemed to resemble or mirror the composition of the Top-ranked DTEP BCIs, rather than the Naive sample, it was sorted from (Figure 59).

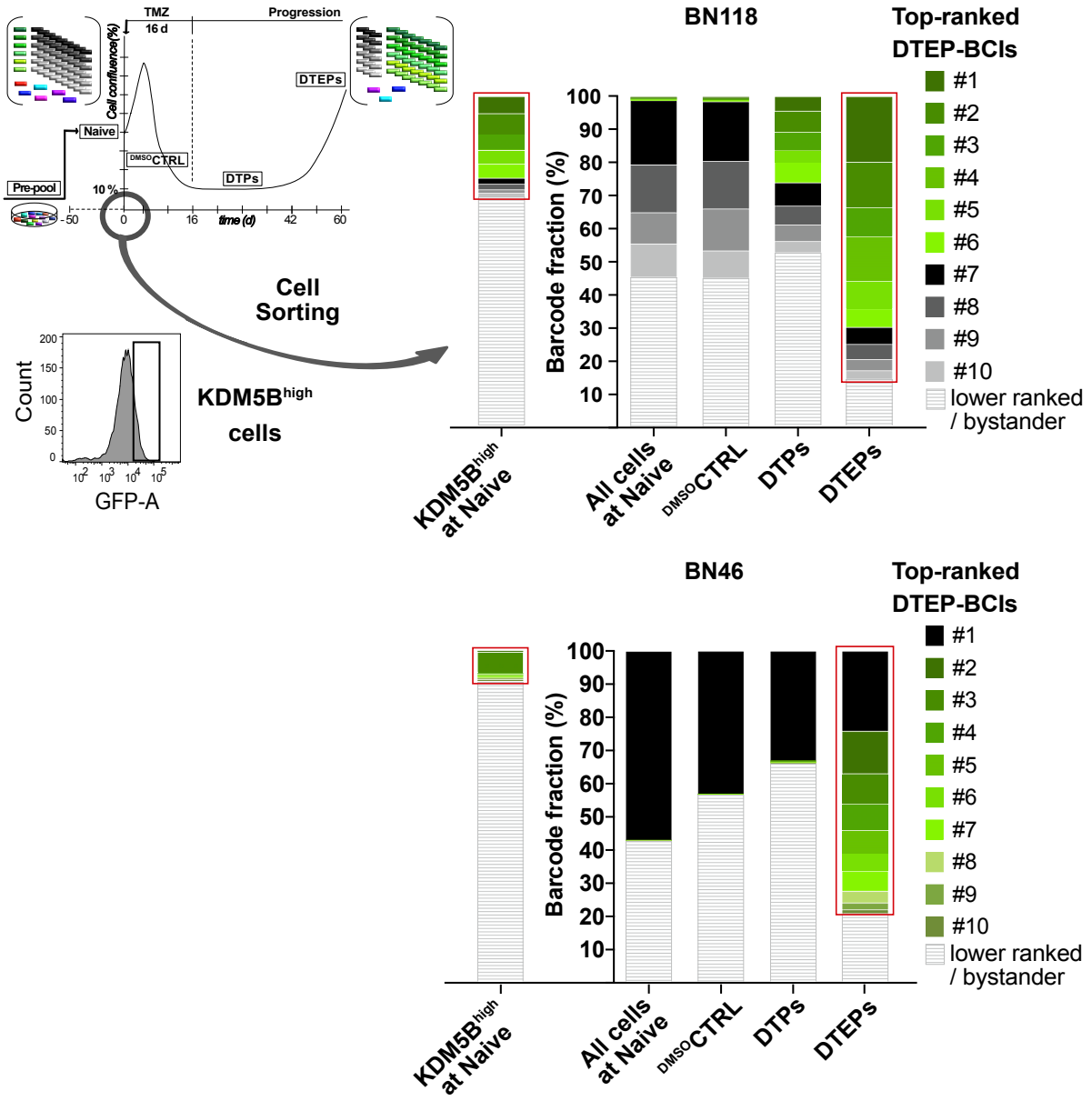

Figure 59: "Sorting experiment. Cartoon illustrating cell sorting of KDM5B^{high} barcoded cells at the Naive stage of the experiment. Subclonal dynamics and top DTEPs can be predicted; visualized as a slice plot (red boxes). Data represent ranking position of the top 10 BCIs, as defined at the DTEP-stage, color-coded for identity and displayed in relative abundance for each stage of the experiment. Abundance of lower-ranked thousands of bystander identities in white."; Upper panel: Patient sample BN118 shown; Lower Panel: Patient sample BN46 shown. (adapted from Ullrich et al., in revision 2023).

The Top-ranked DTEP BCIs were identified and allocated to ranking positions along the different stages of the experimental course. In ^{naive}BN118 (left plot) 9 of the Top-ranked DTEP BCIs were detected at ranking positions between 2 and 12 in the KDM5B sorted sample. In ^{naive}BN46 (right plot) all 9 newly arising barcodes were detected at ranking positions between 1 and 15. The dominant resistant barcode (black) could not be identified in the KDM5B sorted sample.

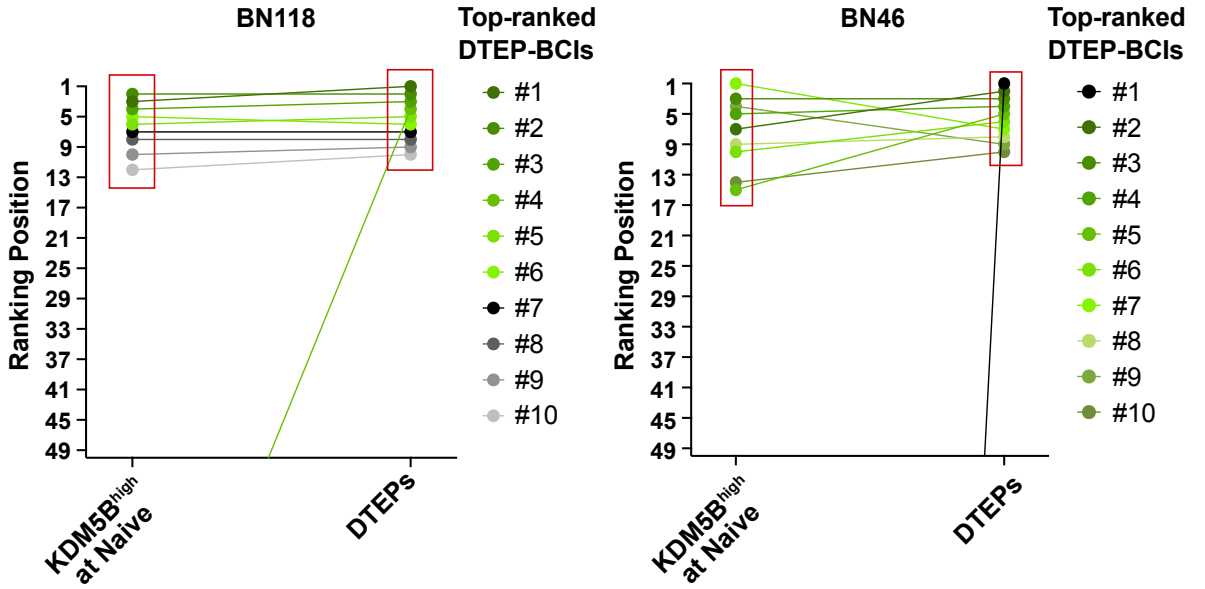

Figure 60: "Subclonal dynamics and top DTEPs can be predicted; visualized as a ranked plot (red boxes). Data represent individual ranking positions of the top 10 BCIs, as defined at the DTEP-stage, color-coded for identity and displayed as ranking positions at the DTEP stage and for the Naive-sorted KDM5B^{high} cells. Note the similarity of ranking positions among the individual BCIs at both time points."; Left: Patient sample BN118 shown; Right: Patient sample BN46 shown. (adapted from Ullrich et al., in revision 2023).

Taken together, the analysis reveals, that 9 out of 10 Top-ranked DTEP BCIs were traceable in the top-ranked BCIs of the sample sorted for KDM5B^{high} cells. Sorting for the KDM5B^{high} subpopulation, and as a consequence high levels of KDM5B itself, enables prediction of the newly arising subclones that will accumulate as $^{TMZ→eR}$cells in the relapse.

To conclude, high individual KDM5B levels in treatment-naive cells correlated with elevated ALDH1A1 in relapse cells, revealing KDM5B as a prospective indicator of subclonal expansion. This was confirmed by the DNA Barcoding combined with sorting for KDM5B^{high} cells, that enabled the identification of newly arising barcodes before the cells were exposed to TMZ. The predictability of adaptive plasticity was accessible in the patient-cell based assays that allowed us to study the dynamics of KDM5B-driven effects. Consequently, we established a suitable cellular model, in which KDM5B-driven adaptive plasticity was elucidated in the context of the subclonal expansion of ALDH1A1+/pAKT+ TMZ-resistant cells towards disease relapse.

3. Discussion

To summarize, in glioblastoma recurrence is unavoidable, leading to a 5-year overall survival estimate of only 3-8 % (Reifenberger et al., Nat Rev Clin Oncol. 2017; Wen et al., Neuro Oncol. 2020). The drug resistance, contributing to glioblastomas poor prognosis, is thought to be orchestrated by a variety of distinct mechanisms. For example, resistance was discussed to be driven by stem-like tumor-propagating cells (Chen et al., Nature 2012), to be developed through a selective process during therapy (Johnson et al., Science 2014), to be mediated by pre-existing cellular traits (Lan et al., Nature 2017), or to be conferred by adaptive mechanisms of highly plastic cells (Gimple et al., Nat Rev Cancer 2022). Our lab has shown in the past that glioblastoma tissue contains subclones of varying drug sensitivities and that application of drugs in a therapeutic effort may actually induce shifts in the subclonal composition of the tumor that can be predicted (Reinartz et al., Clin Cancer Res 2017).

In this work, a major effort was undertaken to understand whether a particular type of tumor subclone mediates dynamic population shifts along the clinical course from primary disease to relapse. Interestingly, the subclonal accumulation of ALDH1A1 positive cells in glioblastoma relapse tissue and -cells occurred in response to TMZ-based (single or combinatorial) treatment schedules, and not under radiotherapy (RT) alone. Therefore, this project started under the assumption that TMZ induced treatment resistance in rare ALDH1A1+ cells, which then become resistant and progress to a dominant hierarchy under the further influence of TMZ exposure. To study mechanisms that underly this peculiar form of adaptive plasticity and subsequent subclonal dynamics, it was relied on the use of clinical cell samples. The cohort of investigated samples consisted of paired treatment-naive cells from newly diagnosed glioblastoma, and from clinical relapse ($^{TMZ\rightarrow cR}$) of the same individual. Also, "*in vitro* relapsed", experimental relapse cell samples were used that were generated by serial TMZ exposure ($^{TMZ\rightarrow eR}$) or by repeated ionizing radiation ($^{RT\rightarrow eR}$) of naive cells.

Increased ALDH1A1-expressing cell populations as well as increased phosphorylation-based activation of AKT (pAKT) could be identified in ^{cR}cell and $^{TMZ\rightarrow eR}$cell samples compared to ^{naive}cell samples. Moreover, a strong TMZ-dependent increase of ALDH1A1/pAKT double-positive cells could be detected in ^{cR}cell and $^{TMZ\rightarrow eR}$cell samples compared to ^{naive}cell samples, as well as in tissue of a TMZ-exposed PDX mouse model and in relapse tissue of RT/TMZ-treated patients. Upon

ALDH1A1 knockdown or ALDH1A1 overexpression in ^{naive}cell samples no difference in the cell´s ability to form monoclonal colonies could be noted and the cell´s clonogenicity, self-renewal capacity and multi-potency was not changed significantly, contradicting an intrinsic TMZ resistance at least in ^{naive}cell samples. Knockdown of ALDH1A1 in ^{cR}cell and $^{TMZ→eR}$cell samples affected clonogenicity, self-renewal capacity and multi-potency, pointing towards the acquisition of alterations in relapse cell samples. Upon combinatorial treatment with TMZ and MK2206, a clinical-grade allosteric AKT inhibitor, additive-negative effects on cell confluence and cell viability compared to TMZ alone were observed in ^{cR}cell and $^{TMZ→eR}$cell samples, but not in ^{naive}cell samples. Use of MK2206 in combination with TMZ is capable of inducing apoptotic processes, not only in all ^{cR}cells or $^{TMZ→eR}$cells in general, but even specifically in almost 100% of ALDH1A1+ cells. The addition of MK2206 subsequent to TMZ could prevent experimental relapse ($^{TMZ→eR}$) *in vitro* and could even prolong survival of xenografts significantly (Kebir et al., Clin Cancer Res. 2023).

In Figure 61 the selection of ALDH1A1+ subclones from the heterogeneous cellular composition of the treatment-naive tumor through TMZ-based treatment schemes is illustrated. The subclonally enriched cells, acquire changes in phosphorylated, consequently active, AKT, that confers increased TMZ resistance. To follow up on this, the early stages of the process were investigated to decipher the early response mechanism to TMZ exposure that potentially drives the subclonal dynamic towards the development of drug resistance (Figure 61).

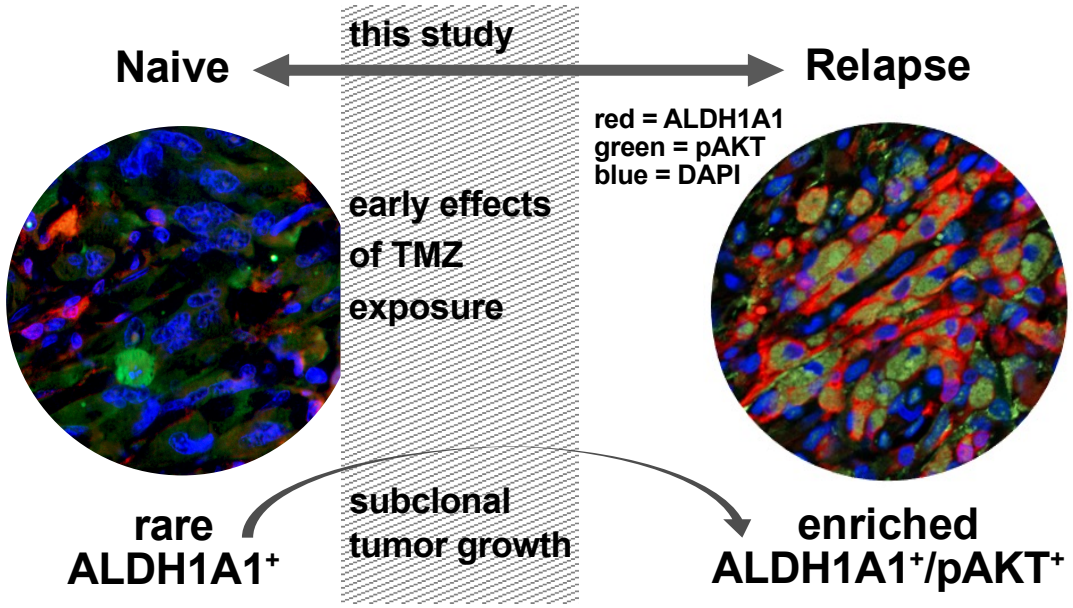

Figure 61: Cartoon illustrating the rationale of the project: The subclonally enriched ALDH1A1+/pAKT+ cells in disease relapse were discovered in the first part of the project. In the second part the focus

lays on the early effects of TMZ exposure potentially driving the subclonal tumor growth. Representative immunofluorescent stainings (performed by P.Berger and C.Dobersalske) of ALDH1A1 and pAKT in paired patient tissue, before (treatment-naive) and after clinical RT/TMZ therapy (relapse) (adapted from Ullrich et al., in revision 2023).

In a comparative approach using paired patient samples (^{naive} and ^{cR} or $^{TMZ→eR}$) *ALDH1A1* expression in treatment-naive cell samples could not predict enrichment of *ALDH1A1* in relapse cell samples, whereas *KDM5B* expression in treatment-naive cell samples could predict elevated *ALDH1A1* in the relapse cell samples. Using a stably integrated a KDM5B-EGFP reporter construct (Roesch et al., Cell 2010) in paired patient cell samples a rapid increase of KDM5B^{high} cells upon TMZ-on/-off treatment schemes could be detected. The effect was more pronounced in ^{naive}cell samples compared to ^{cR}cells or $^{TMZ→eR}$cells, pointing towards an early response mechanism during disease progression. Further analyses characterized KDM5B^{high} cells as a viable population, that survives under the influence of TMZ, but has a less proliferative capacity with slow-cycling cells. KDM5B/ALDH1A1 as well as KDM5B/pAKT co-expression was increased upon TMZ-on/-off schemes. In addition to that, siRNA-mediated knockdown of KDM5B was accompanied by a decrease of pAKT. Further, knockdown of KDM5B affected pAKT´s downstream targets pGSK3ß, pmTOR and Cyclin D3, while pAKT´s negative regulator PTEN was increased upon KDM5B knockdown. Reduction in cell viability conferred via KDM5B knockdown, could be reversed by the addition of a PTEN Inhibitor. However, no changes in the H3K4trimethylation on PTEN or on different players of the PI3K/AKT pathway could be detected upon KDM5B knockdown. Nevertheless, when siRNA-mediated knockdown of KDM5B or pharmacological inhibition of KDM5B was applied after TMZ exposure, a strong induction of apoptotic processes, as well as a decrease in cell confluence and cell viability could be detected compared to TMZ alone. In the DNA Barcoding analysis. TMZ exposure reduced dominant barcode identities (BCIs) within the primary tumor, at the same time favoring expansion of previously underrepresented cellular identities towards the expansion of $^{TMZ→eR}$cells, leading to a change in the composition of cellular identities. Even if thousands of underrepresented BCIs were uncovered upon the therapeutic pressure of TMZ, only few began to expand as newly arising $^{TMZ→eR}$cell hierarchies. The top-ranked BCIs of a KDM5B^{high} sorted sample, almost mirrored the top-ranked BCIs of the $^{TMZ→eR}$cells, suggesting that newly arising subpopulations under the influence of TMZ exposure could already be pre-determined in ^{naive}cell samples. To conclude, we identified KDM5B as a potential prospective indicator for subclonal expansion.

The data obtained in this thesis raises a number of interesting questions.

In the past attempts were made to characterize the glioblastoma in detail to enable strategies for personalized targeted therapies. The idea is to eradicate tumor cells by interfering with specific target molecules or pathways, known to be important for survival of the tumor cells (Al-Lazikani et al., Nat Biotechnol. 2012). Immunotherapies and targeted therapies are rapidly evolving in a variety of cancer entities, while in the treatment of glioblastoma limited progress has been made and the standard of care chemotherapeutic TMZ, alongside surgical resection and radiotherapy, has mostly remained unchanged since decades ("Stupp-Scheme") (Stupp et al., N Engl J Med. 2005) and is still the best option for patients. The treatment-scheme was just adjusted by the addition of TTFields in a subgroup of patients (Stupp et al, JAMA 2015; Stupp et a., JAMA 2017).

Originally, chemotherapies were developed long time ago from chemical weapons used in war. In 1942 soldiers showed lymphoid hypoplasia through the toxin nitrogen mustard that was used as a gas in the first world war. After injection of compounds that were closely related to nitrogen mustard, tumor regression was observed in a non-hodgkin lymphoma patient at least for a few weeks (Gilman et al., Science 1946; Gilman et al., Am. J. Surg. 1963). During this time the higher vulnerability of tumors than of healthy tissue to toxins was discovered but could not be explained yet. In 1948 an analogue to folic acid, a vitamin that was shown to induce proliferation of acute lymphoblastic leukaemia (ALL) cells in children, was synthesized and lead to short periods of ALL remission (Chabner et al., Nat Rev Cancer. 2005). Only 8 years later the same analogue, called methotrexate, was shown to cure the first solid cancer in humans, a choriocarcinoma (Li et al., N. Engl. J. Med. 1958). Methotrexate was the first drug for which drug resistance was studied (Curt et al., Cancer Treat. Rep. 1984). Moreover, it was the first drug in which pharmacokinetic analysis and the identification of patients harboring a risk of toxicity was performed (Stoller et al., N. Engl. J. Med. 1977), paving the way for all following studies on chemotherapeutics and the development of drug resistance.

Surprisingly, in this thesis work an unspecific chemotherapy induces the subclonal enrichment of a distinct cell population, the ALDH1A1+/pAKT+ cell population. Therefore, the question emerges if this cell population has stem cell potential. Cancer stem cells are considered as a small subpopulation of cells with the

potential to self-renew and the ability to perform multilineage differentiation and to build a tumor (Singh et al., Cancer Res. 2003; Shibue and Weinberg, Nat Rev Clin Oncol. 2017). Due to their believed high intrinsic resistance levels to chemotherapeutic agents and to radiotherapy exposure, they have been made responsible for tumor relapse (Liu et al., Mol Cancer 2006; Bao et al., Nature 2006). Indeed, ALDH1A1 has been suggested as a marker for cancer stem cells (Yue et al., Front Oncol 2022) and it was already established that the abundance of ALDH1A1+ cells correlated with malignancy and overall survival in glioma (Schafer et al., Neuro Oncol 2012).

Surprisingly, in this work the NSA und LDA assays showed no evidence for inherent resistance in ^{naive}cell samples. In addition, TMZ exposure alone was sufficient to induce apoptotic processes in 3/4 of all naive ALDH1A1+ cells, which confirms that ALDH1A1 cells are not inherently resistant. The data indicates that ALDH1A1 alone was not able to modulate or confer stem cell capacities to ^{naive}cells, but it could act as a marker of cells, which acquire resistance-conferring alterations later on. The amount of caspase-3 positive ALDH1A1+ cells after TMZ exposure was strongly reduced in ^{cR}cells and $^{TMZ\rightarrow eR}$cells, confirming the acquisition of resistance-conferring changes during disease progression.

Even if the distinct cell population was not intrinsically resistant, it was able to clonally expand anyway, as the DNA Barcoding experiments showed. DNA Barcoding is a tool, that allows the modelling of tumor evolution. In this lineage tracing method, individual cells are uniquely labeled with DNA sequences, that are stably integrated into the genome of the target cell and are then stably given to its progeny, so that a permanent tracing of cells is possible. This allows tracking and reconstruction of clonal lineages and to follow individual subpopulations in a dynamic heterogeneous cell pool over time. Bhang and colleagues were able to track the fate of more than 1 Million individual non-small cell lung cancer cells, using the in vitro-generated barcode library with more than 10^7 unique barcodes, called ClonTracer (Bhang et al., Nat. Med. 2015). The application of the ClonTracer System to the clinical glioblastoma cell samples in this thesis revealed that the expansion of ^{naive}cells *in vitro* was already driven by few dominant driver subclones, as the clonal diversity was reduced without therapeutic pressure. During the *in vitro* expansion to obtain the replicates for the experiment the detectable BCIs dropped below 0.3%.

In general, the DNA Barcoding experiment allowed to answer two questions: The first question was if resistance to TMZ exposure is rather an intrinsic resistance

via pre-existing drug-resistant cells or an acquired resistance. The second question the DNA Barcoding experiment allowed to answer was how many subclones build up the experimental relapse ($^{TMZ→eR}$) after the quiescent period.

Regarding the first question, it was reported earlier that glioblastoma fate mapping studies using DNA barcoding systems in PDX models revealed a potential expansion of pre-existing, drug-resistant stem-like cells (Lan et al., 2017). In the barcoding experiment performed in this thesis, cellular identities (detected through barcode identities (BCIs)) that were underrepresented in the ^{naive}cell population were expanding in the $^{TMZ→eR}$cell population. If the BCIs, that are expanding in the $^{TMZ→eR}$cell population would have been distinct between the independent replicates, treatment induced mutagenesis might have promoted the ability to clonally expand. However, the data obtained in this thesis exhibited, that the same BCIs are dominant in all $^{TMZ→eR}$cell replicates, suggesting pre-existing, inherently resistant clones that arise under TMZ exposure.

Regarding the second question, the DNA Barcoding experiment enables to determine the number of unique barcodes, presenting a quantitative measure for the number of clones the population originated from (clonal origins). In addition to that, the counts per unique barcode are a readout of the relative abundance of each clone, indicating clonal selection processes and proliferative capacities of subclones. As sensitivity to treatment varies within the tumor, TMZ was expected to lead to the eradication of drug-sensitive clones. Indeed, under TMZ exposure the dominant pool of detectable BCIs was reduced. But on top of this, the therapeutic pressures uncovered underrepresented subclones, leading to a heterogeneous population composed of diverse BCIs, that tolerated the drug, but stayed non-proliferative (DTP-like). The heterogeneity of detectable BCIs was reduced again when the cells exit the quiescent phase (DTP-like) and transit to $^{TMZ→eR}$cells (DTEP-like). Just a few cells regained proliferative capacity and expanded as $^{TMZ→eR}$cells. The newly arising clones, that were underrepresented in the ^{naive}cell population, made up 1/2 to nearly 3/4 of the $^{TMZ→eR}$cell population, indicating that very few cells from an original crowd of a million are responsible for creating the tumor bulk at disease progression.

Previously, low genetic intra-tumor heterogeneity was reported to be associated with a favorable prognosis in leukemia (Landau et al. Cell. 2013), as well as in head and neck cancer (Mroz et al., PLoS Med. 2015). Similarly Andor et al (Nat Med. 2016) confirmed using exome sequences from TCGA tumors that a clonal diversity of more

than 2 clones with >10% frequency is associated with increased mortality. Association between clone number and survival was especially observed in low-grade glioma and glioblastoma. However, they described as well that diversification to more than four clones reduced the risk. A potential reason they discussed, was the balance between benefits vs. costs of genomic instability for the tumor. In addition, they discussed the fact that high numbers of clones could draw the attention of more immune-cells and have an increased possibility to generate inviable daughter cells (Andor et al., Nat Med. 2016).

The DNA Barcoding in this thesis exhibited that distinct previously underrepresented cellular identities are responsible for driving subclonal expansion in response to TMZ. However, the exact number of subclones cannot ultimately be determined. In the described barcoding experiments the technical difficulty of the uniquely barcoding of cells underlies. The method is based on the assumption that the addition of 1 million unique barcodes to a specific cell number of 10 million cells with an efficiency of 10 % results in a statistical distribution of one barcode per cell. However, this assumption cannot be confirmed. Therefore, the number of newly arising BCIs does not necessarily represent the number of newly arising subclones, as two BCIs could potentially mark the same subclone.

Confirming the data of this thesis that indicated that enrichment of pre-existing cellular identities repopulates the $^{TMZ \rightarrow eR}$, it was reported lately that limited genetic evolution could be observed between primary disease and glioblastoma relapse. Data obtained from large, paired patient cohorts revealed that most driver mutations are acquired prior to initial diagnosis. The mutational patterns between treatment-naive and relapse tumors were similar and not many TMZ-specific mutations were detected in the relapse tumors. Rather oligoclonal expansion of pre-existing subclones takes place (Barthel et al., Nature 2019; Draaisma et al., J Clin Oncol 2020; Körber et al., Cancer Cell 2019).

It was tempting to consider that the process is a non-genetic mechanism of resistance. Feasible would be the resilience of ALDH1A1 cells that are not inherently resistant but adapt to the exogenous pressure of TMZ exposure. The term resilience stands for a flexibility and capacity of cancer cells to anticipate and cope with intrinsic or exogenous pressure and to recover from it. Resilience can be conferred through mechanisms on the phenotypic level and the so-called adaptive plasticity. Adaptive plasticity is the starting point for changes of a heterogeneous tumor population to adapt

under exogenous pressure, e.g., therapeutic pressure and enables cells to proliferate in the presence of the same. The capability to proliferate in the presence of therapeutic pressure would fit to ALDH1A1 as a cancer stem cell marker. However, lately the idea of a more dynamic glioma stem cell model is discussed, that includes transient plasticity, adaptivity and conversion between stem and non-stem cells, as reviewed by Gimple et al. (Nat Rev Cancer 2022). The idea is that small subsets of cancer cells seem to be tolerant to the drug and give rise to resistant colonies, resembling the behavior of drug-tolerant persisters (DTPs). Slow-cycling DTP cell states were reported to be able to survive/persist, while the majority of cells is more sensitive to the treatment (Sharma et al. Cell 2010; Roesch et al. Cell 2010; Shen et al., Cell 2020). The epigenetic regulator KDM5B, was described to be a marker for the small subpopulation of slow-cycling DTPs and to regulate therapeutic resistance (Roesch et al., Cell 2010).

In this thesis work, the increase KDM5B^{high} cells was much more pronounced in response to TMZ withdrawal (TMZ-off phase) than throughout TMZ treatment (TMZ-on phase), peaked after 1 week and constantly decreased thereafter. KDM5B levels were strongly increased within quiescent DTP-like cells after TMZ-on/-off schemes, but are decreased again after *in vitro* expansion of $^{TMZ→eR}$cells to a level comparable to naive cells. The data indicates that KDM5B is TMZ-dependent but perpetuates even without continuous therapeutic pressure. Moreover, the data indicates that KDM5B is transiently regulated, as similarly described in other cancer entities. However, in other cancer entities histone demethylases as KDM5B were described to confer a reversible DTP state. Upon withdrawal of drugs the cells are reported to revert to drug sensitivity, so that their progeny is often sensitive to rechallenge with the initial drug (Ramirez et al., 2016; Shen et al., 2019).

In comparison to this the generated $^{TMZ→eR}$cells are not in reversible state and continue to maintain resistance upon TMZ-withdrawal and TMZ-rechallenge, in an extent similar to clinically obtained ^{cR}cells, so that the $^{TMZ→eR}$cells differ from the described DTP→DTEP transition. It might be speculated, that through the slow cell division rate the cell gains time to adapt in an unreversible manner.

This was similarly described in other cancer entities. Circumscribed populations of cancer cells were reported to be able to evade anti-cancer drugs by entering the reversible persister state, until additional mechanisms of resistance can take place (Hata et al., Nat Med 2016; Marine et al., Nat Rev Cancer 2020; Ramirez et al., Nat Commun 2016; Shaffer et al., Nature 2017). The cells can acquire mutations and

evolve into a resistant phenotype, despite of their initially decreased proliferation rate. For example, Hata et al., (Nat Med 2016) described that in NSCLC patients T790M EGFR mutated clones did not only derive from the selection of pre-existing mutation carrying clones, but also from initially T790M-negative DTPs, that subsequently de novo acquired the resistance-conferring mutation (Hata et al., Nat Med 2016). Ramirez et al., (Nat Commun 2016) tested the response to a panel of 560 anticancer compounds in combination with erlotinib in lung cancer cells. Using sequencing they could identify, e.g., MET amplifications or MAPK pathway mutations, just to name two acquired resistance mechanisms. However, they could not answer if persister states that acquire different resistance mechanisms later on, differ from the persister states that do not (Ramirez et al., Nat Commun 2016). Shaffer et al., (Nature 2017) reported how transient effects allow initial resistance, so that a small subpopulation tolerates the drug until some cells develop a stably resistant state through cellular reprogramming via activation of new signaling pathways (Shaffer et al., Nature 2017). This is supported by the findings that non-genetic resistance can be stable, for example in acute myeloid leukaemia (Ding et al. Nature 2012) or breast cancer (Kim et al., Cell 2018), where no genetic cause for drug resistance of tumors could be found. Marine et al. (Nat Rev Cancer 2020) differed between the phoenix cell state, that adapted to the initial therapy by transcriptional and metabolic reprogramming and is no longer sensitive to rechallenge and the transient drug-tolerant persister cell state, which cells are sensitive to rechallenge with the initial therapy (Marine et al., Nat Rev Cancer 2020).

The dynamics of this process cannot be investigated by comparison of the starting vs. the end point of the course, as the unchanged KDM5B gene expression levels between the ^{naive} and ^{cR} or $^{TMZ\rightarrow eR}$ cell samples elucidate. Nevertheless, the overlap of high individual treatment-naive *KDM5B* levels with elevated *ALDH1A1* levels in relapse cell samples, lead to the hypothesis that the subclonal enrichment of ALDH1A1+/pAKT+ cells could be initiated through KDM5B early in disease progression. The hypothesis emerged, that KDM5B might play a role in the acquisition of pAKT in the enriched ALDH1A1+ subpopulation. Indeed, in ^{naive}cells KDM5B/ALDH1A1 co-expression, as well as KDM5B/pAKT co-expression was detected. Previously it has been shown in oral cancer, utilizing the same construct as used in this thesis, that KDM5B^{high} cells (Top 5% EGFP) expressed high levels of the stem cell marker as ALDH1A1. shRNA-mediated knockdown of KDM5B decreased

ALDH1A1 mRNA levels, as well as ALDH activity in ALDEFLUOR assays, whereas KDM5B overexpression increased ALDH1A1 mRNA levels and sphere formation capacity. Moreover, they even described that KDM5B upregulation promoted phosphorylation of pAKT and its downstream target GSK3ß, determined via western blotting. Additionally, AKT activation increased KDM5B as well, representing a feed forward loop of increasing AKT activation in oral cancer (Facompre et al., Cancer Res. 2016; Facompre et al., Oncotarget. 2017).

The AKT pathway was extensively studied in the past. Class IA phosphoinositide 3-kinase (PI3K) enzymes are known to catalyze the conversion of the membrane lipid phosphatidylinositol-4,5-bisphosphate (PI (4,5)P2) to the second messenger PI(3,4,5)P3 (PIP3). This phospholipid provokes regulation of various downstream effectors including AKT. AKT are serine/threonine kinases with the isoforms AKT1, AKT2, AKT3. The active, phosphorylated form of AKT (pAKT), regulates cell growth, metabolism, survival and proliferation. pAKT acts on various downstream substrates, leading for example to the phosphorylation of GSK3ß or mTOR. The serine-threonine kinase mTOR forms the two cellular complexes, mTOR complex 1 (mTORC1) and mTOR complex 2 (mTORC2). AKT activation results in the activation of mTORC1, that itself is involved in a negative feedback loop that prevents the overactivation of AKT (Manning and Toker, Cell 2017). Further, it is known, that activation of AKT is antagonized by the tumor suppressor PTEN, through converting PIP3, that regulates phosphorylation of AKT, back to PI(4,5)P2 (Thorpe et al., Nat. Rev. Cancer 2015).

Interestingly, in this thesis, the negative regulator of pAKT PTEN was, opposed to the other pathway-related proteins, increased after KDM5B knockdown, arguing for a KDM5B-mediated suppression of PTEN. As KDM5B is known to play a role in transcriptional repression by removing methyl groups from H3K4 at gene promoters, CHIP-Sequencing was performed to detect histone binding sites of KDM5B indirectly via observing changes in H3K4trimethylation. If a specific gene region would have been co-precipitated with the H3K4trimethylation antibody, it would have indicated a potential demethylating activity of KDM5B at this region. However, the Chip-seq analysis for H3K4me3 could not detect a significant demethylation activity on players of the pathway, so that the aberrant AKT signaling could not be confirmed to be epigenetically regulated, at least at the regions tested.

Nevertheless, this uncertainty could be addresses by sorting for the distinct cell subsets of $KDM5B^{high}$ cells and $KDM5B^{low}$ cells (via KDM5B antibody-labeling or

EGFP-reporter construct) and compare the differences in the H3K4trimethylation between the two cell subsets using CHIP-seq analyses. It might be that a demethylating activity of KDM5B is most pronounced in the KDM5B^{high} subpopulation and therefore not detectable when an unsorted bulk CHIP samples is sequenced. So that an epigenetically regulated mechanism of action could still be a reasonable explanation. This hypothesis is underlined by the comparison of the increase of the MFI vs. the increase of KDM5B^{high}cells. The measured increase of KDM5B was more distinct in the KDM5B^{high} subpopulation, than in the whole population (MFI), leading to the conclusion, that TMZ induces an increase of KDM5B^{high} cells, which is mirrored in the endogenous KDM5B levels of the whole population.

Multiple studies in other cancer entities showed, that KDM5B can regulate the PI3K/pAKT pathway. In hepatocellular carcinoma cells the PI3K/AKT pathway is directly induced by direct binding of KDM5B to the *PTEN* promoter and suppression of *PTEN* via its H3K4 demethylase activity (Tang et al., Oncotarget 2015).

In prostate cancer, a direct binding of KDM5B to the *PIK3CA* promoter is detected, but the regulation of *PIK3CA* through KDM5B is described to take place in a demethylase activity-independent manner. Similar to our data, no significant difference in the amount of H3K4me3 at the PIK3CA promoter could be detected after KDM5B knockout via H3K4me3-ChIP analysis (Li et al., Cancer Res. 2020). A possible explanation for the unchanged methylation levels would be, that besides its demethylase-activity, KDM5B was reported to influence multiple pathways through demethylase-activity-independent mechanism. KDM5B is known to be able to suppress in a demethylase activity-independent manner the retroelement expression and to recruit methyltransferase SETDB1 (SET domain bifurcated histone lysine methyltransferase 1) in melanoma (Zhang et al., Nature 2021). Further, KDM5B was shown to perform repression of cryptic intragenic transcription (Xie et al., EMBO J. 2011), while silencing KDM5B lead to spreading of H3K4 methylation to enhancer boundaries (Kidder et al., Genome Biol. 2014).

In addition to the demethylase-activity-independent mechanisms, KDM5B was reported to control genomic instability, by recruitment of BRCA1 and Ku7, two major players of non-homologous end joining and homologous recombination, during repair of double strand breaks (Li et al., Proc Natl Acad Sci U S A. 2014). Moreover, it was reported to promote progression of the cell cycle through increasing levels of Cyclin D1 (Mitra et al., J. Biol. Chem. 2011), via regulating p15 and p27 (Wang et al., J Exp

Clin Cancer Res. 2016) or via downregulation of p21 (Dai et al., Biochem Biophys Res Commun. 2014).

The analysis of double-strand break repair related proteins and cell cycle-related proteins in KDM5B^{high} cells or after RNA interference of KDM5B, could shed light on a potential evolvement in glioblastoma patient cell samples.

In addition to this, KDM5B was shown to interact with other chromatin regulators as Polycomb Repressive Complex 2 (PRC2) (Zhang et al., J Cell Biochem. 2014) and the Nucleosome Remodeling and Deacetylase complex (NuRD) as well as the H3K4me1/2-specific demethylase LSD1 (Li et al., Cancer Res. 2011). Using pull-down experiments, the interaction of KDM5B with other chromatin regulators could be investigated in glioblastoma patient cell samples.

Alternative pathways that were reported to be involved in KDM5Bs activity in other cancer entities were e.g. via the tyrosine-protein kinase c-Met in non-small cell lung cancer (Kuo et al., Clin Epigenetics 2018), via p16/Ink4a, an inhibitor of the G1-phase transition of the cell cycle, in colorectal cancer (Ohta et al., Int J Oncol 2013), via the Wnt/β-catenin signalling pathway in colorectal cancer (Huang et al., Cell Commun Signal 2020) or by reduction of expression of tumor suppressor FBXW7, leading to blocked degradation and accumulation of Cyclin E1 in Ewing sarcoma (Chen at al., Cell Death Dis 2022).

To clarify potential KDM5B-mediated changes in these pathways for our glioblastoma patient cells, KDM5B knockdown via RNA interference followed by readout methods as Western blotting or flow cytometry could be performed. Moreover, CHIP-seq analysis could be repeated in cell subsets of KDM5B^{high} vs. KDM5B^{low} cells, as described above, to check for methylation-based changes in these potentially involved signaling pathways.

Several potential mechanisms that could serve as explanations of the effect of KDM5B knockdown on the PI3K pathway are illustrated in Figure 62. Further investigation of the underlying cellular mechanisms is required and even pleiotropic effects could be considered.

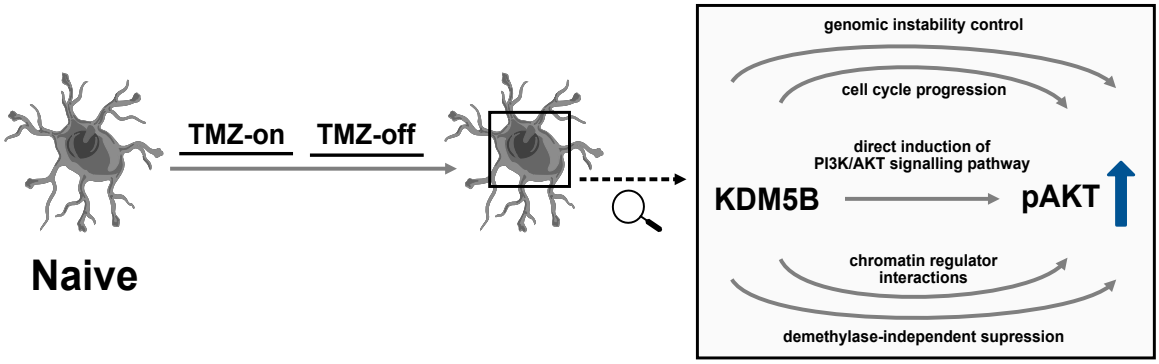

Figure 62: Cartoon illustrating potential mechanisms how TMZ-induced KDM5B could epigenetically regulate pAKT. KDM5B could directly induce the PI3K/AKT pathway by its demethylating function or indirectly via genomic instability control, regulation of cell cycle progression, interaction with other chromatin regulators or via demethylation-independent suppression mechanisms (adapted from Ullrich et al., in revision 2023).

The main interest of this work was the therapeutic possibilities of the subclonal enrichment, particularly because very limited number of clinical options are available after TMZ resistance at disease relapse. The overarching goal of translational research is the implementation of basic concepts and preclinical rationale into the clinic. An important aim is to develop biomarkers and to conduct innovative clinical trials to counteract drug resistance and the development of tumor relapse. In clinical trials, targeted agents have thus far failed to improve the outcome.

In this work, pharmacological inhibition and knockdown of KDM5B could increase the cells sensitivity to TMZ on the level of apoptosis, cellular viability and cell confluence. Expansion of $^{TMZ \rightarrow eR}$cells after TMZ withdrawal was delayed by KDM5B inhibition. This data fits to earlier publications, showing that overexpression of KDM5B led to cell proliferation and increased tumorigenicity *in vivo*. Additionally higher KDM5B expression correlated with shorter survival in patients (Dai et al., Biochem. Biophys. Res. Commun. 2014; Fang et al., Int. J. Mol. Med. 2016). However, KDM5B might not be appliable as a promising target for a combinatorial therapeutic approach in glioblastoma, as KDM5B levels seem to be dynamically regulated upon TMZ, that could adapt again upon inhibition of KDM5B and could even be compensated by other epigenetic regulators. Even though it is discussed, that targeting plasticity may improve treatment efficacy, the drug development for a “moving target” still has to deal with remarkable challenges (Yabo et al., Neuro Oncol. 2022).

The inhibition of KDM5B would probably not lead to a successful depletion of the tumor. Instead of ALDH1A1+/pAKT+ cells another subclone might be enriched from the heterogenous subclonal pool, that needs to be characterized thereupon.

The detection of enriched ALDH1A1+/pAKT+ cells in relapse patient tissue, led us approach potential targeting strategies. Most inhibitors broadly inhibit all ALDH isoforms, conferring severe side effects and high toxicity as for example disulfiram (De Sousa, Springer, Singapore 2019) and ALDH1A1 isoform-specific inhibitors are still developed (Yue et al., Front Oncol 2022). Moreover, ALDH1A1 is expressed in the adult brain (Anderson et al., Brain Res 2011), posing an additional difficulty for drug development with little side effects, especially on the brain. So that an indirect inhibition of the double positive target cells via targeting pAKT was aimed.

AKT is known to suppress apoptosis and to protect cancer cells from apoptosis, through different signaling cascades including the pro-apoptotic Bcl-2-family member BAD or proteins, that are involved in the mitochondrial pathway of apoptosis as, e.g., Caspase-9 (Franke et al., Oncogene. 2003). Targeting the RTK-PI3K-AKT-mTOR pathway is an ongoing matter in neurooncological trials (Colardo et al., Int J Mol Sci 2021). Interfering with the RTK-PI3K-AKT-mTOR signaling is investigated in clinical neurooncology trials already (Colardo et al., Int J Mol Sci 2021). However, AKT inhibitors as, e.g., perifosine were observed to be ineffective as monotherapy in glioblastoma relapse (Kaley et al., J Neurooncol. 2019). Nevertheless, the combination of the AKT inhibitor perifosine, ineffective as a monotherapy, with the mTOR inhibitor temsirolimus was considered for patients with a glioblastoma relapse (Kaley et al., Ann Clin Transl Neurol. 2020).

Combinatorial therapies were approached the first time in the late 1960s, were the combination of the chemotherapeutics nitrogen mustard, vincristine, procarbazine and prednisone, the so-called MOPP regimen, was applied to cure patients with Hodgkin's lymphoma and non-Hodgkin's lymphoma (Moxley et al., Cancer Res. 1967; Devita et. al., Ann. Intern. Med. 1970). Rational combinatorial drug therapies have to be designed on the basis of intratumor genetic heterogeneity, but it needs to be considered if the administration of combinatorial agents or administration in a sequential manner is more promising (Al-Lazikani et al., Nat Biotechnol. 2012). For example, in patients with 1p/19q non-co-deleted anaplastic glioma sequential TMZ schedules had an impact on survival benefit, whereas concomitant schedules did not (van den Bent et al., Lancet Oncol. 2021).

In this work, upon combinatorial treatment with TMZ and MK2206, a clinical-grade allosteric AKT inhibitor, active Caspase-3 was observed in almost 100% of ALDH1A1+ cells, indicating, that pAKT-inhibition by MK2206 enables the indirect, but highly specific targeting of ALDH1A1+ subclones. As a consequence, the addition of TMZ+MK2206 impaires cell viability and cell confluence, reverting the TMZ resistance of relapse cells to a level normally observed in naive cells.

Based on the obtained data a rational targeting strategy was established first in vitro and later *in vivo*. Concomitant schedules (TMZ + drug of interest) and sequential treatments, either with the drug of interest before or after the standard of care (drug of interest → TMZ vs. TMZ → drug of interest) may have to be considered. Expansion of subclones under therapeutic pressure, as we observed in this thesis, could present the need for sequential treatment as described already in Reinartz et al., (Clin Cancer Res 2017), who showed that timing of sequential schemes may affect the dynamics of intra-tumoral subclones. Early addition of MK2206 did not confer any survival benefit, which can be explained by the low amount of phosphorylated AKT at naive and the late appearance of ALDH1A1+/pAKT+ subclones, emphasizing the importance of the chronological sequence. This work demonstrates at the example of ALDH1A1+/pAKT+ subclones, that as soon as subclones accumulate, well-timed sequential treatment seems to be more effective than a concurrent combinational strategy. The successful elongation of survival in mice using sequential treatment with TMZ followed by MK2206 (Kebir et al., Clin Cancer Res. 2023), exposes pAKT inhibition as a promising second-line treatment for glioblastoma therapy.

Taken together, a potential conclusion from the data of this thesis is that sequential targeting approaches should be tested in future clinical trials. Those could involve an initial TMZ exposure, leading to enrichment of specific ALDH1A1+/pAKT+ subclones, which could then be targeted in the subsequent stages of disease progression via inhibition of pAKT in a second line therapy, to avoid AKT-mediated subclonal progression and drug resistance (Figure 63). This approach fits to the pre-clinically developed “Enrich and Kill” strategy, involving the enrichment of a particular subclone from the heterogenous tumor through the first-line therapy and in a second step the rational targeting and depletion of this particular subclone in a second-line therapy (see Figure 3; Reinartz et al., Clin Cancer Res 2017).

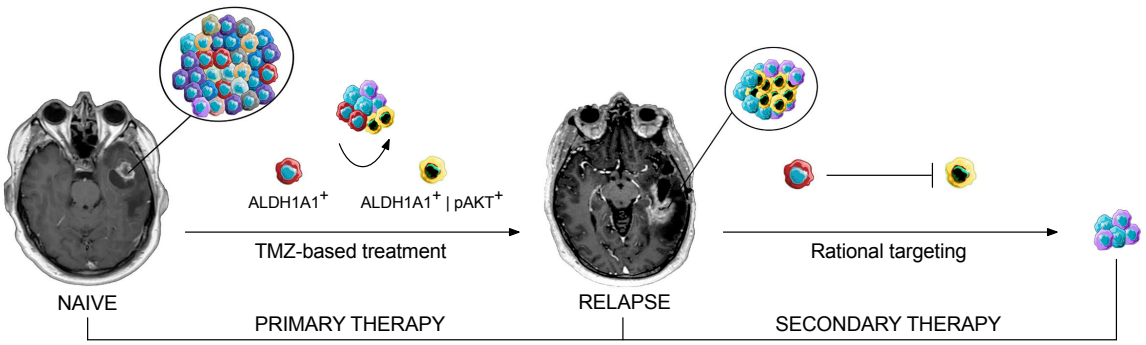

Figure 63: Enrich and kill as a sequential targeting strategy: TMZ-based primary therapy mediates enrichment of ALDH1A1+/pAKT+ subclones, that can then be targeted in a secondary therapy (from Kebir et al., Clin Cancer Res. 2023).

If the second-line treatment is applied to early, an alternative subclone could be enriched and the "Enrich and Kill" Strategy would not be applicable. The underlying phenomenon could be a TMZ-mediated AKT pathway dependency of the tumor. Cancer cells can be addicted to the activation of specific oncogenes or the loss of specific tumor suppressor genes. Weinstein (Science. 2002; and Cancer Res. 2008) described the concept of oncogene addiction, the dependency of cancer cells on specific genes or pathways for the maintenance of malignancy and survival. Weinstein and Joe (Cancer Res. 2008) called oncogene addiction, the "Achilles' heel" of tumors, however cancers can escape from a specific oncogene addiction by induction of bypass pathways (Weinstein, Science. 2002; Weinstein and Joe, Cancer Res. 2008)

For application in future clinical trials aiming to target pAKT in a second-line therapy, the content of the ALDH1A1+/pAKT+ target population should be determined before administration of the treatment. The flow cytometry data demonstrated that the pAKT enrichment strongly differs between different patient cell samples.

The prediction of subclonal enrichment is needed, especially in patients in which the ability to access serial tumor samples is missing, so that no biomaterial of the relapse tumor is available for diagnostic purposes. Therefore, an important aspect of this work is predictability.

In the paired clinical cell samples high individual KDM5B expression levels in treatment-naive cell samples correlated with enriched ALDH1A1 in relapse cell samples, suggesting that high KDM5B levels in treatment-naive cells are related to the propensity for clonal expansion of ALDH1A1+ cells under TMZ. Moreover, sorting for KDM5B^{high} barcoded cells, could exhibit the rare clones that expand under therapeutic

pressure. The newly arising subclones, that were underrepresented and therefore undetectable in the bulk of ^{naive}cell samples, were prospectively identified in the KDM5B^{high} sample. The data indicates that the KDM5B levels measured in vital, treatment-naive glioblastoma cells may indicate the identity of newly arising subclones under the influence of therapeutic TMZ. Particularly, the dynamics of KDM5B^{high} cells could serve as an indicator for the TMZ-driven enrichment of ALDH1A1+/pAKT+ subclones. To optimize the efficiency of sequential treatments, one may have to consider the extent of potential founder populations for drug-induced subclonal enrichment. A respective threshold level would have to be established to implement KDM5B^{high} cell populations as a biomarker in future clinical trials aiming to sequentially treat pAKT-dependent subclones, e.g., with MK2206 at disease relapse.

Before short-term vital cell-based assays are used as companion diagnostic, initial steps of biomarker development are preceding. Clinical assays must be developed and validated and screening studies have to be performed, as described similarly for the development of early detection biomarkers (Pepe et al., J Natl Cancer Inst. 2001). The chosen detection assay is required to be sensitive and specific as well as standardized in order to generate reliable and robust results (Wu and Qu, Chem Soc Rev 2015), that can be used for stratification of patients.

Currently, the O(6)-methylguanine-DNA methyltransferase (MGMT) promoter methylation status is considered as the only prognostic and predictive marker for better treatment response of TMZ-based chemotherapy in glioblastoma patients (Weller et al., Nat Rev Clin Oncol 2021). The dynamics of KDM5B^{high} cells used as a biomarker would be a valuable alternative and could specifically prospectively indicate the expansion of the targetable ALDH1A1+/pAKT+ subclones in the relapse.

Limitations of the work and outlook

A big issue in glioblastoma research is the intratumor heterogeneity and the heterogeneity of tumors across patients. It is a clear advantage of modern cell culture technology to be able to maintain this diversity ex vivo for prolonged periods of time (Reinartz et al., Clin Cancer Res 2017). However, the data generated in this study does not fully represent the cellular complexity of glioblastomas. It would be important to investigate the tumor in its full complexity, because dissociated single cells alone cannot comprehensively model the cell-cell interactions, the immune cell repertoire, or the diverse environmental interactions in the various niches of the tumor tissue. Moreover, it is important to consider that glioblastomas show a diffusely infiltrative and invasive behavior. Surgical resection cannot safely remove the entire tumor from the brain, so that the resected patient cells, used in experimental work, and residual tumor cells, remaining in the brain, can display different characteristics (Glas et al., Ann Neurol. 2010).

When a therapeutic agent is driven from pre-clinical exploitation into pilot studies in patients, the limitation of blood brain barrier permeability occurs, as insufficient penetration leads to limited therapeutic efficiency (Arvanitis et al., Nat Rev Cancer. 2020). In addition, drug-induced side effects can contribute to clinically unmanageable toxicities. In drug repurposing strategies cancer entities are treated with agents that were initially approved for other indications. This leads to a faster and cheaper process of drug development and clinical validation and helps avoiding severe and unexpected side effects (Bertolini et al., Nat Rev Clin Oncol. 2015; Corsello et al., Nat Cancer 2020; Zhang et al. Sig Transduct Target Ther. 2020). To transfer the sequential TMZ→compound regimens, that were established in clinical cell samples and PDX models of disease, to the clinical practice, the appropriate timing and duration of treatments needs to be studied in future clinical trials.

Regarding adaptive plasticity it has to be taken in consideration, that very few publications questioned, if cellular plasticity might potentially be triggered artificially even in short-term cell cultures. In literature it was argued that if the tissue microenvironment is missing dedifferentiation takes place and cells can acquire stem-like characteristics under in vitro culturing conditions (Gupta et al., Cell Stem Cell 2019). An example would be the acquired stem-like characteristics observed in mammary epithelial cells after short-term culture (Chaffer et al., Proc. Natl. Acad. Sci.

U. S. A 2011; Keller et al., Proc. Natl. Acad. Sci. U. S. A 2012). Moreover, epigenetic changes were reported to be caused artificially. Cell culture provoked changes in the chromatin structure, hetero- and euchromatin conformation was reorganized and DNA methylation changes were observed to take place, resembling an epigenetic drift (Chandra, T. et al. Cell Rep. 2015; Criscione et al. Sci. Adv. 2016; Franzen et al. Commun Biol 2021).

In future metabolic processes, as, e.g., oxidative phosphorylation, could be determined in paired glioblastoma samples, as KDM5B was described to strongly effect the cells metabolism, e.g. in melanoma (Roesch et al., Cancer Cell 2013; Vogel et al., J. Investig. Dermatol. 2019). Metabolic gene signatures could be investigated after molecular or pharmacological interference with KDM5B. Other studies presented evidence that persister cells are able to hijack the microenvironment (Shen et al., Cell 2020). Consequently, studying the impact of KDM5B on the microenvironment could be of potential interest for glioblastoma as well.

In the field increasing interest lays on using contemporary techniques, especially on single-cell-based technologies (Rambow et al., Cell 2018) and computational algorithms (Burkhardt et al., Cancer Discov 2022; Chowell et al., Cancer Res 2018; Tarabichi et al., Nat Methods 2021. Such cutting-edge techniques could be used to decipher cancer plasticity and to study subclonal composition and evolution of tumor populations.

The data obtained in this thesis indicated that expanding $^{TMZ \rightarrow eR}$populations could be classified regarding their turning points into fast (*cheetah*), moderate (*meerkat*) and slow (*sloth*) expanding $^{TMZ \rightarrow eR}$populations. It could be speculated that the quiescent persister state ensures initial drug tolerance, allowing a small subpopulation of tumor cells to survive drug exposure, until additional adaptions, e.g., reversible changes on a phenotypic level or even permanent mutations, enables some cells to proliferate and expand as. $^{TMZ \rightarrow eR}$cells, as described in the literature (e.g. Ramirez et al., Nat Commun 2016). Ramirez and colleagues (Nat Commun 2016) claimed the high diversity of heterogeneous mechanisms of drug-resistance the persister cells can acquire. In melanoma PDX models of disease, distinct timing in the onset of drug responses to a combination of BRAF and MEK inhibitors were detected. In some PDXs tumor regrowth was observed after a short time, reflecting intrinsic resistance, while in other PDXs tumor regrowth started after long periods of drug

tolerance, reflecting acquired resistance. Pre-existing resistant subclones were detected in the first group and *de novo* acquired genetic alterations were detected in the second group (Marin-Bejar et al., Cancer Cell 2021). DNA-Sequencing, CHIP-Sequencing and RNA-Sequencing of the distinct groups of $^{TMZ \rightarrow eR}$populations (cheetahs, meerkats, sloth) would enable to investigate potential genetic, epigenetic and transcriptomic differences, that would give a hint on the underlying resistance mechanism.

In this work a sample of KDM5B^{high} cells was sorted out of the heterogenous barcoded population and analyzed separately. During the last years barcoding techniques were established to extract additional information on specific cellular hierarchies. For example, Umkehrer and colleagues developed a technique called CaTCH, which enables to not only track, but as well to isolate specific single clones in a heterogenous population. Specifically designed single-guide RNAs are used that are complementary to the clone of interest and enable fluorescence-activated cell sorting-based isolation of the clone of interest via GFP (Umkehrer et al., Nat. Biotechnol. 2021). In future a clonal tracing combined with subsequent single cell RNA sequencing could be performed in the clinical glioblastoma cell samples using a construct, designed by cooperation partners. In contrast to Umkehrer et al., (Nat. Biotechnol. 2021), the isolation of interesting subclones is not needed to study their characteristics. Instead, the barcodes are translated into the mRNA, allowing integration of RNA sequencing information for each individual barcoded cell (Dujardin et al, in progress; Grüner lab). Furthermore, barcoding could serve for individual predictions on TMZ-induced subclonal progression and on the composition of tumor tissue at disease relapse. Treatment-naive tumor cells isolated from patient tissue (Lee et al., Cancer Cell 2006, Reinartz et al., Clin Cancer Res 2017), as well as “organoids”, “bioengineered tissue models” or “tumor fragment platforms” could present useful tools to predict such drug responses and subclonal dynamics (Drost and Clevers, Nat Rev Cancer 2018; Sood et al., Nat Commun 2019; Voabil et al., Nat Med 2021). A potential follow-up study could comprise lineage tracing using barcoding in patient-derived explants, which are vital surgically extracted pieces of patient tissue, that are maintained *ex vivo* (technique by C.Dobersalske, Scheffler lab). This approach could allow immediate treatment decisions in a translational context and a co-clinical setting.

Taken together, this work intended to enlighten the process of adaptive plasticity that was hypothesized to underly the subclonal expansion of rare ALDH1A1+ cells within the bulk of treatment-naive tumor cells only when exposed to TMZ as a standard treatment of primary care. Under the continued influence of TMZ, these cells acquire resistance, which could explain the subclonal enrichment of ALDH1A1+/pAKT+ cells in the relapsed tumor tissue of glioblastoma patients. This work took advantage of the fact that the phenomenon of subclonal enrichment can be similarly observed in animal models of disease and in short-term *in vitro* assays when using patient-derived cell samples. Drug-tolerant, slow-cycling KDM5B^{high} cells are enriched as an early response to TMZ and the individual level of KDM5B in treatment-naive samples serves as a prospective indicator for subclonal expansion of ALDH1A1+/pAKT+ cells. These findings can be translated into biomarker-assisted sequential “Enrich and Kill” strategies in future clinical trials and might prolong survival in glioblastoma patients.

4. References

Abedalthagafi M, Barakeh D, Foshay KM. Immunogenetics of glioblastoma: the future of personalized patient management. NPJ Precis Oncol. 2018 Dec 4;2:27. doi: 10.1038/s41698-018-0070-1. PMID: 30534602; PMCID: PMC6279755.

Al-Lazikani B, Banerji U, Workman P. Combinatorial drug therapy for cancer in the post-genomic era. Nat Biotechnol. 2012 Jul 10;30(7):679-92. doi: 10.1038/nbt.2284. PMID: 22781697.

Anderson DW, Schray RC, Duester G, Schneider JS. Functional significance of aldehyde dehydrogenase ALDH1A1 to the nigrostriatal dopamine system. Brain Res. 2011 Aug 23;1408:81-7. doi: 10.1016/j.brainres.2011.06.051. Epub 2011 Jun 26. PMID: 21784415; PMCID: PMC3995134.

Andor N, Graham TA, Jansen M, Xia LC, Aktipis CA, Petritsch C, Ji HP, Maley CC. Pan-cancer analysis of the extent and consequences of intratumor heterogeneity. Nat Med. 2016 Jan;22(1):105-13. doi: 10.1038/nm.3984. Epub 2015 Nov 30. PMID: 26618723; PMCID: PMC4830693.

Arvanitis CD, Ferraro GB, Jain RK. The blood-brain barrier and blood-tumour barrier in brain tumours and metastases. Nat Rev Cancer. 2020 Jan;20(1):26-41. doi: 10.1038/s41568-019-0205-x. Epub 2019 Oct 10. PMID: 31601988; PMCID: PMC8246629.

Bao S, Wu Q, McLendon RE, Hao Y, Shi Q, Hjelmeland AB, Dewhirst MW, Bigner DD, Rich JN. Glioma stem cells promote radioresistance by preferential activation of the DNA damage response. Nature. 2006 Dec 7;444(7120):756-60. doi: 10.1038/nature05236. Epub 2006 Oct 18. PMID: 17051156.

Barski A, Cuddapah S, Cui K, Roh TY, Schones DE, Wang Z, Wei G, Chepelev I, Zhao K. High-resolution profiling of histone methylations in the human genome. Cell. 2007 May 18;129(4):823-37. doi: 10.1016/j.cell.2007.05.009. PMID: 17512414.

Barthel FP, Johnson KC, Varn FS, Moskalik AD, Tanner G, Kocakavuk E, Anderson KJ, Abiola O, Aldape K, Alfaro KD, Alpar D, Amin SB, Ashley DM, Bandopadhayay P, Barnholtz-Sloan JS, Beroukhim R, Bock C, Brastianos PK, Brat DJ, Brodbelt AR, Bruns AF, Bulsara KR, Chakrabarty A, Chakravarti A, Chuang JH, Claus EB, Cochran EJ, Connelly J, Costello JF, Finocchiaro G, Fletcher MN, French PJ, Gan HK, Gilbert MR, Gould PV, Grimmer MR, Iavarone A, Ismail A, Jenkinson MD, Khasraw M, Kim H, Kouwenhoven MCM, LaViolette PS, Li M, Lichter P, Ligon KL, Lowman AK, Malta TM, Mazor T, McDonald KL, Molinaro AM, Nam DH, Nayyar N, Ng HK, Ngan CY, Niclou SP, Niers JM, Noushmehr H, Noorbakhsh J, Ormond DR, Park CK, Poisson LM, Rabadan R, Radlwimmer B, Rao G, Reifenberger G, Sa JK, Schuster M, Shaw BL, Short SC, Smitt PAS, Sloan AE, Smits M, Suzuki H, Tabatabai G, Van Meir EG, Watts C, Weller M, Wesseling P, Westerman BA, Widhalm G, Woehrer A, Yung WKA, Zadeh G, Huse JT, De Groot JF, Stead LF, Verhaak RGW; GLASS Consortium. Longitudinal molecular trajectories of diffuse glioma in adults. Nature. 2019 Dec;576(7785):112-120. doi: 10.1038/s41586-019-1775-1. Epub 2019 Nov 20. PMID: 31748746; PMCID: PMC6897368.

Bertolini F, Sukhatme VP, Bouche G. Drug repurposing in oncology--patient and health systems opportunities. Nat Rev Clin Oncol. 2015 Dec;12(12):732-42. doi: 10.1038/nrclinonc.2015.169. Epub 2015 Oct 20. PMID: 26483297.

Bhang HE, Ruddy DA, Krishnamurthy Radhakrishna V, Caushi JX, Zhao R, Hims MM, Singh AP, Kao I, Rakiec D, Shaw P, Balak M, Raza A, Ackley E, Keen N, Schlabach MR, Palmer M, Leary RJ, Chiang DY, Sellers WR, Michor F, Cooke VG, Korn JM, Stegmeier F. Studying clonal dynamics in response to cancer therapy using high-complexity barcoding. Nat Med. 2015 May;21(5):440-8. doi: 10.1038/nm.3841. Epub 2015 Apr 13. PMID: 25849130.

Brennan CW, Verhaak RG, McKenna A, Campos B, Noushmehr H, Salama SR, Zheng S, Chakravarty D, Sanborn JZ, Berman SH, Beroukhim R, Bernard B, Wu CJ, Genovese G, Shmulevich I, Barnholtz-Sloan J, Zou L, Vegesna R, Shukla SA, Ciriello G, Yung WK, Zhang W, Sougnez C, Mikkelsen T, Aldape K, Bigner DD, Van Meir EG, Prados M, Sloan A, Black KL, Eschbacher J, Finocchiaro G, Friedman W, Andrews DW, Guha A, Iacocca M, O'Neill BP, Foltz G, Myers J, Weisenberger DJ, Penny R, Kucherlapati R, Perou CM, Hayes DN, Gibbs R, Marra M, Mills GB, Lander E, Spellman P, Wilson R, Sander C, Weinstein J, Meyerson M, Gabriel S, Laird PW, Haussler D, Getz G, Chin L; TCGA Research Network. The somatic genomic landscape of glioblastoma. Cell. 2013 Oct 10;155(2):462-77. doi: 10.1016/j.cell.2013.09.034. Erratum in: Cell. 2014 Apr 24;157(3):753. PMID: 24120142; PMCID: PMC3910500.

Brown NF, Carter TJ, Ottaviani D, Mulholland P. Harnessing the immune system in glioblastoma. Br J Cancer. 2018 Nov;119(10):1171-1181. doi: 10.1038/s41416-018-0258-8. Epub 2018 Nov 5. PMID: 30393372; PMCID: PMC6251037.

Burkhardt DB, San Juan BP, Lock JG, Krishnaswamy S, Chaffer CL. Mapping Phenotypic Plasticity upon the Cancer Cell State Landscape Using Manifold Learning. Cancer Discov. 2022 Aug 5;12(8):1847-1859. doi: 10.1158/2159-8290.CD-21-0282. PMID: 35736000; PMCID: PMC9353259.

Cancer Genome Atlas Research Network. Comprehensive genomic characterization defines human glioblastoma genes and core pathways. Nature. 2008 Oct 23;455(7216):1061-8. doi: 10.1038/nature07385. Epub 2008 Sep 4. Erratum in: Nature. 2013 Feb 28;494(7438):506. PMID: 18772890; PMCID: PMC2671642.

Capper D, Jones DTW, Sill M, Hovestadt V, Schrimpf D, Sturm D, Koelsche C, Sahm F, Chavez L, Reuss DE, Kratz A, Wefers AK, Huang K, Pajtler KW, Schweizer L, Stichel D, Olar A, Engel NW, Lindenberg K, Harter PN, Braczynski AK, Plate KH, Dohmen H, Garvalov BK, Coras R, Hölsken A, Hewer E, Bewerunge-Hudler M, Schick M, Fischer R, Beschorner R, Schittenhelm J, Staszewski O, Wani K, Varlet P, Pages M, Temming P, Lohmann D, Selt F, Witt H, Milde T, Witt O, Aronica E, Giangaspero F, Rushing E, Scheurlen W, Geisenberger C, Rodriguez FJ, Becker A, Preusser M, Haberler C, Bjerkvig R, Cryan J, Farrell M, Deckert M, Hench J, Frank S, Serrano J, Kannan K, Tsirigos A, Brück W, Hofer S, Brehmer S, Seiz-Rosenhagen M, Hänggi D, Hans V, Rozsnoki S, Hansford JR, Kohlhof P, Kristensen BW, Lechner M, Lopes B, Mawrin C, Ketter R, Kulozik A, Khatib Z, Heppner F, Koch A, Jouvet A, Keohane C, Mühleisen H, Mueller W, Pohl U, Prinz M, Benner A, Zapatka M, Gottardo NG, Driever PH, Kramm CM, Müller HL, Rutkowski S, von Hoff K, Frühwald

MC, Gnekow A, Fleischhack G, Tippelt S, Calaminus G, Monoranu CM, Perry A, Jones C, Jacques TS, Radlwimmer B, Gessi M, Pietsch T, Schramm J, Schackert G, Westphal M, Reifenberger G, Wesseling P, Weller M, Collins VP, Blümcke I, Bendszus M, Debus J, Huang A, Jabado N, Northcott PA, Paulus W, Gajjar A, Robinson GW, Taylor MD, Jaunmuktane Z, Ryzhova M, Platten M, Unterberg A, Wick W, Karajannis MA, Mittelbronn M, Acker T, Hartmann C, Aldape K, Schüller U, Buslei R, Lichter P, Kool M, Herold-Mende C, Ellison DW, Hasselblatt M, Snuderl M, Brandner S, Korshunov A, von Deimling A, Pfister SM. DNA methylation-based classification of central nervous system tumours. Nature. 2018 Mar 22;555(7697):469-474. doi: 10.1038/nature26000. Epub 2018 Mar 14. PMID: 29539639; PMCID: PMC6093218.

Chabner BA, Roberts TG Jr. Timeline: Chemotherapy and the war on cancer. Nat Rev Cancer. 2005 Jan;5(1):65-72. doi: 10.1038/nrc1529. PMID: 15630416.

Chaffer CL, Brueckmann I, Scheel C, Kaestli AJ, Wiggins PA, Rodrigues LO, Brooks M, Reinhardt F, Su Y, Polyak K, Arendt LM, Kuperwasser C, Bierie B, Weinberg RA. Normal and neoplastic nonstem cells can spontaneously convert to a stem-like state. Proc Natl Acad Sci U S A. 2011 May 10;108(19):7950-5. doi: 10.1073/pnas.1102454108. Epub 2011 Apr 15. PMID: 21498687; PMCID: PMC3093533.

Chandra T, Ewels PA, Schoenfelder S, Furlan-Magaril M, Wingett SW, Kirschner K, Thuret JY, Andrews S, Fraser P, Reik W. Global reorganization of the nuclear landscape in senescent cells. Cell Rep. 2015 Feb 3;10(4):471-83. doi: 10.1016/j.celrep.2014.12.055. Epub 2015 Jan 29. PMID: 25640177; PMCID: PMC4542308.

Chaligne R, Gaiti F, Silverbush D, Schiffman JS, Weisman HR, Kluegel L, Gritsch S, Deochand SD, Gonzalez Castro LN, Richman AR, Klughammer J, Biancalani T, Muus C, Sheridan C, Alonso A, Izzo F, Park J, Rozenblatt-Rosen O, Regev A, Suvà ML, Landau DA. Epigenetic encoding, heritability and plasticity of glioma transcriptional cell states. Nat Genet. 2021 Oct;53(10):1469-1479. doi: 10.1038/s41588-021-00927-7. Epub 2021 Sep 30. PMID: 34594037; PMCID: PMC8675181.

Chen B, Chen H, Lu S, Zhu X, Que Y, Zhang Y, Huang J, Zhang L, Zhang Y, Sun F, Wang J, Zhu J, Zhen Z, Zhang Y. KDM5B promotes tumorigenesis of Ewing sarcoma via FBXW7/CCNE1 axis. Cell Death Dis. 2022 Apr 15;13(4):354. doi: 10.1038/s41419-022-04800-1. PMID: 35428764; PMCID: PMC9012801.

Chen J, Li Y, Yu TS, McKay RM, Burns DK, Kernie SG, Parada LF. A restricted cell population propagates glioblastoma growth after chemotherapy. Nature. 2012 Aug 23;488(7412):522-6. doi: 10.1038/nature11287. PMID: 22854781; PMCID: PMC3427400.

Chen R, Nishimura MC, Bumbaca SM, Kharbanda S, Forrest WF, Kasman IM, Greve JM, Soriano RH, Gilmour LL, Rivers CS, Modrusan Z, Nacu S, Guerrero S, Edgar KA, Wallin JJ, Lamszus K, Westphal M, Heim S, James CD, VandenBerg SR, Costello JF, Moorefield S, Cowdrey CJ, Prados M, Phillips HS. A hierarchy of self-renewing tumor-initiating cell types in glioblastoma. Cancer Cell. 2010 Apr 13;17(4):362-75. doi: 10.1016/j.ccr.2009.12.049. PMID: 20385361.

Chowell D, Napier J, Gupta R, Anderson KS, Maley CC, Sayres MAW. Modeling the Subclonal Evolution of Cancer Cell Populations. Cancer Res. 2018 Feb 1;78(3):830-839. doi: 10.1158/0008-5472.CAN-17-1229. Epub 2017 Nov 29. PMID: 29187407; PMCID: PMC5811390.

Colardo M, Segatto M, Di Bartolomeo S. Targeting RTK-PI3K-mTOR Axis in Gliomas: An Update. Int J Mol Sci. 2021 May 5;22(9):4899. doi: 10.3390/ijms22094899. PMID: 34063168; PMCID: PMC8124221.

Corsello SM, Nagari RT, Spangler RD, Rossen J, Kocak M, Bryan JG, Humeidi R, Peck D, Wu X, Tang AA, Wang VM, Bender SA, Lemire E, Narayan R, Montgomery P, Ben-David U, Garvie CW, Chen Y, Rees MG, Lyons NJ, McFarland JM, Wong BT, Wang L, Dumont N, O'Hearn PJ, Stefan E, Doench JG, Harrington CN, Greulich H, Meyerson M, Vazquez F, Subramanian A, Roth JA, Bittker JA, Boehm JS, Mader CC, Tsherniak A, Golub TR. Discovering the anti-cancer potential of non-oncology drugs by systematic viability profiling. Nat Cancer. 2020 Feb;1(2):235-248. doi: 10.1038/s43018-019-0018-6. Epub 2020 Jan 20. PMID: 32613204; PMCID: PMC7328899.

Crane CA, Ahn BJ, Han SJ, Parsa AT. Soluble factors secreted by glioblastoma cell lines facilitate recruitment, survival, and expansion of regulatory T cells: implications for immunotherapy. Neuro Oncol. 2012 May;14(5):584-95. doi: 10.1093/neuonc/nos014. Epub 2012 Mar 9. PMID: 22406925; PMCID: PMC3337302.

Criscione SW, De Cecco M, Siranosian B, Zhang Y, Kreiling JA, Sedivy JM, Neretti N. Reorganization of chromosome architecture in replicative cellular senescence. Sci Adv. 2016 Feb 5;2(2):e1500882. doi: 10.1126/sciadv.1500882. PMID: 26989773; PMCID: PMC4788486.

Curt GA, Clendeninn NJ, Chabner BA. Drug resistance in cancer. Cancer Treat Rep. 1984 Jan;68(1):87-99. PMID: 6198082.

Dai B, Hu Z, Huang H, Zhu G, Xiao Z, Wan W, Zhang P, Jia W, Zhang L. Overexpressed KDM5B is associated with the progression of glioma and promotes glioma cell growth via downregulating p21. Biochem Biophys Res Commun. 2014 Nov 7;454(1):221-7. doi: 10.1016/j.bbrc.2014.10.078. Epub 2014 Oct 22. PMID: 25450384.

D'Asti E, Chennakrishnaiah S, Lee TH, Rak J. Extracellular Vesicles in Brain Tumor Progression. Cell Mol Neurobiol. 2016 Apr;36(3):383-407. doi: 10.1007/s10571-015-0296-1. Epub 2016 Mar 18. PMID: 26993504.

De Sousa, A. (2019). Disulfiram: Side Effects and Toxicity. In: Disulfiram. Springer, Singapore. https://doi.org/10.1007/978-981-32-9876-7_7

Devita VT Jr, Serpick AA, Carbone PP. Combination chemotherapy in the treatment of advanced Hodgkin's disease. Ann Intern Med. 1970 Dec;73(6):881-95. doi: 10.7326/0003-4819-73-6-881. PMID: 5525541.

Ding L, Ley TJ, Larson DE, Miller CA, Koboldt DC, Welch JS, Ritchey JK, Young MA, Lamprecht T, McLellan MD, McMichael JF, Wallis JW, Lu C, Shen D, Harris CC,

Dooling DJ, Fulton RS, Fulton LL, Chen K, Schmidt H, Kalicki-Veizer J, Magrini VJ, Cook L, McGrath SD, Vickery TL, Wendl MC, Heath S, Watson MA, Link DC, Tomasson MH, Shannon WD, Payton JE, Kulkarni S, Westervelt P, Walter MJ, Graubert TA, Mardis ER, Wilson RK, DiPersio JF. Clonal evolution in relapsed acute myeloid leukaemia revealed by whole-genome sequencing. Nature. 2012 Jan 11;481(7382):506-10. doi: 10.1038/nature10738. PMID: 22237025; PMCID: PMC3267864.

Dono A, Mitra S, Shah M, Takayasu T, Zhu JJ, Tandon N, Patel CB, Esquenazi Y, Ballester LY. PTEN mutations predict benefit from tumor treating fields (TTFields) therapy in patients with recurrent glioblastoma. J Neurooncol. 2021 May;153(1):153-160. doi: 10.1007/s11060-021-03755-1. Epub 2021 Apr 21. PMID: 33881725; PMCID: PMC8363068.

Draaisma K, Chatzipli A, Taphoorn M, Kerkhof M, Weyerbrock A, Sanson M, Hoeben A, Lukacova S, Lombardi G, Leenstra S, Hanse M, Fleischeuer R, Watts C, McAbee J, Angelopoulos N, Gorlia T, Golfinopoulos V, Kros JM, Verhaak RGW, Bours V, van den Bent MJ, McDermott U, Robe PA, French PJ. Molecular Evolution of IDH Wild-Type Glioblastomas Treated With Standard of Care Affects Survival and Design of Precision Medicine Trials: A Report From the EORTC 1542 Study. J Clin Oncol. 2020 Jan 1;38(1):81-99. doi: 10.1200/JCO.19.00367. Epub 2019 Nov 19. PMID: 31743054.

Drost J, Clevers H. Organoids in cancer research. Nat Rev Cancer. 2018 Jul;18(7):407-418. doi: 10.1038/s41568-018-0007-6. PMID: 29692415.

Eyler CE, Matsunaga H, Hovestadt V, Vantine SJ, van Galen P, Bernstein BE. Single-cell lineage analysis reveals genetic and epigenetic interplay in glioblastoma drug resistance. Genome Biol. 2020 Jul 15;21(1):174. doi: 10.1186/s13059-020-02085-1. PMID: 32669109; PMCID: PMC7364565.

Facompre ND, Harmeyer KM, Sole X, Kabraji S, Belden Z, Sahu V, Whelan K, Tanaka K, Weinstein GS, Montone KT, Roesch A, Gimotty PA, Herlyn M, Rustgi AK, Nakagawa H, Ramaswamy S, Basu D. JARID1B Enables Transit between Distinct States of the Stem-like Cell Population in Oral Cancers. Cancer Res. 2016 Sep 15;76(18):5538-49. doi: 10.1158/0008-5472.CAN-15-3377. Epub 2016 Aug 3. Erratum in: Cancer Res. 2017 Dec 15;77(24):7136. PMID: 27488530; PMCID: PMC5026599.

Facompre ND, Harmeyer KH, Basu D. Regulation of oncogenic PI3-kinase signaling by JARID1B. Oncotarget. 2017 Jan 31;8(5):7218-7219. doi: 10.18632/oncotarget.14790. PMID: 28122362; PMCID: PMC5352311.

Fang L, Zhao J, Wang D, Zhu L, Wang J, Jiang K. Jumonji AT-rich interactive domain 1B overexpression is associated with the development and progression of glioma. Int J Mol Med. 2016 Jul;38(1):172-82. doi: 10.3892/ijmm.2016.2614. Epub 2016 May 30. Erratum in: Int J Mol Med. 2016 Sep;38(3):976. PMID: 27246838; PMCID: PMC4899035.

Franke TF, Hornik CP, Segev L, Shostak GA, Sugimoto C. PI3K/Akt and apoptosis: size matters. Oncogene. 2003 Dec 8;22(56):8983-98. doi: 10.1038/sj.onc.1207115. PMID: 14663477.

Franzen J, Georgomanolis T, Selich A, Kuo CC, Stöger R, Brant L, Mulabdić MS, Fernandez-Rebollo E, Grezella C, Ostrowska A, Begemann M, Nikolić M, Rath B, Ho AD, Rothe M, Schambach A, Papantonis A, Wagner W. DNA methylation changes during long-term in vitro cell culture are caused by epigenetic drift. Commun Biol. 2021 May 19;4(1):598. doi: 10.1038/s42003-021-02116-y. PMID: 34011964; PMCID: PMC8134454.

Fu YD, Huang MJ, Guo JW, You YZ, Liu HM, Huang LH, Yu B. Targeting histone demethylase KDM5B for cancer treatment. Eur J Med Chem. 2020 Dec 15;208:112760. doi: 10.1016/j.ejmech.2020.112760. Epub 2020 Aug 21. PMID: 32883639.

Gimple RC, Yang K, Halbert ME, Agnihotri S, Rich JN. Brain cancer stem cells: resilience through adaptive plasticity and hierarchical heterogeneity. Nat Rev Cancer. 2022 Sep;22(9):497-514. doi: 10.1038/s41568-022-00486-x. Epub 2022 Jun 16. PMID: 35710946.

Gilman A, Philips FS. The Biological Actions and Therapeutic Applications of the B-Chloroethyl Amines and Sulfides. Science. 1946 Apr 5;103(2675):409-36. doi: 10.1126/science.103.2675.409. PMID: 17751251.

GILMAN A. The initial clinical trial of nitrogen mustard. Am J Surg. 1963 May;105:574-8. doi: 10.1016/0002-9610(63)90232-0. PMID: 13947966.

Glas M, Rath BH, Simon M, Reinartz R, Schramme A, Trageser D, Eisenreich R, Leinhaas A, Keller M, Schildhaus HU, Garbe S, Steinfarz B, Pietsch T, Steindler DA, Schramm J, Herrlinger U, Brüstle O, Scheffler B. Residual tumor cells are unique cellular targets in glioblastoma. Ann Neurol. 2010 Aug;68(2):264-9. doi: 10.1002/ana.22036. PMID: 20695020; PMCID: PMC4445859.

Gupta PB, Pastushenko I, Skibinski A, Blanpain C, Kuperwasser C. Phenotypic Plasticity: Driver of Cancer Initiation, Progression, and Therapy Resistance. Cell Stem Cell. 2019 Jan 3;24(1):65-78. doi: 10.1016/j.stem.2018.11.011. Epub 2018 Dec 13. PMID: 30554963; PMCID: PMC7297507.

Hanahan D. Hallmarks of Cancer: New Dimensions. Cancer Discov. 2022 Jan;12(1):31-46. doi: 10.1158/2159-8290.CD-21-1059. PMID: 35022204.

Hata AN, Niederst MJ, Archibald HL, Gomez-Caraballo M, Siddiqui FM, Mulvey HE, Maruvka YE, Ji F, Bhang HE, Krishnamurthy Radhakrishna V, Siravegna G, Hu H, Raoof S, Lockerman E, Kalsy A, Lee D, Keating CL, Ruddy DA, Damon LJ, Crystal AS, Costa C, Piotrowska Z, Bardelli A, Iafrate AJ, Sadreyev RI, Stegmeier F, Getz G, Sequist LV, Faber AC, Engelman JA. Tumor cells can follow distinct evolutionary paths to become resistant to epidermal growth factor receptor inhibition. Nat Med. 2016 Mar;22(3):262-9. doi: 10.1038/nm.4040.

Hegi ME, Diserens AC, Gorlia T, Hamou MF, de Tribolet N, Weller M, Kros JM, Hainfellner JA, Mason W, Mariani L, Bromberg JE, Hau P, Mirimanoff RO, Cairncross JG, Janzer RC, Stupp R. MGMT gene silencing and benefit from temozolomide in glioblastoma. N Engl J Med. 2005 Mar 10;352(10):997-1003. doi: 10.1056/NEJMoa043331. PMID: 15758010.

Hegi ME, Liu L, Herman JG, Stupp R, Wick W, Weller M, Mehta MP, Gilbert MR. Correlation of O6-methylguanine methyltransferase (MGMT) promoter methylation with clinical outcomes in glioblastoma and clinical strategies to modulate MGMT activity. J Clin Oncol. 2008 Sep 1;26(25):4189-99. doi: 10.1200/JCO.2007.11.5964. PMID: 18757334.

Hinohara K, Wu HJ, Vigneau S, McDonald TO, Igarashi KJ, Yamamoto KN, Madsen T, Fassl A, Egri SB, Papanastasiou M, Ding L, Peluffo G, Cohen O, Kales SC, Lal-Nag M, Rai G, Maloney DJ, Jadhav A, Simeonov A, Wagle N, Brown M, Meissner A, Sicinski P, Jaffe JD, Jeselsohn R, Gimelbrant AA, Michor F, Polyak K. KDM5 Histone Demethylase Activity Links Cellular Transcriptomic Heterogeneity to Therapeutic Resistance. Cancer Cell. 2018 Dec 10;34(6):939-953.e9. doi: 10.1016/j.ccell.2018.10.014. Epub 2018 Nov 21. Erratum in: Cancer Cell. 2019 Feb 11;35(2):330-332. PMID: 30472020; PMCID: PMC6310147.

Huang D, Xiao F, Hao H, Hua F, Luo Z, Huang Z, Li Q, Chen S, Cheng X, Zhang X, Fang W, Hu X, Liu F. JARID1B promotes colorectal cancer proliferation and Wnt/β-catenin signaling via decreasing CDX2 level. Cell Commun Signal. 2020 Oct 27;18(1):169. doi: 10.1186/s12964-020-00660-4. PMID: 33109187; PMCID: PMC7590656.

Huang YQ, Zou Y, Zheng RJ, Ma XD. Down-regulation of JARID1B expression inhibits cell proliferation, induces apoptosis and blocks cell cycle in human acute lymphoblastic leukemia cells. Eur Rev Med Pharmacol Sci. 2018 Mar;22(5):1366-1373. doi: 10.26355/eurrev_201803_14480. PMID: 29565495.

Janku F, Yap TA, Meric-Bernstam F. Targeting the PI3K pathway in cancer: are we making headway? Nat Rev Clin Oncol. 2018 May;15(5):273-291. doi: 10.1038/nrclinonc.2018.28. Epub 2018 Mar 6. PMID: 29508857.

Johnson BE, Mazor T, Hong C, Barnes M, Aihara K, McLean CY, Fouse SD, Yamamoto S, Ueda H, Tatsuno K, Asthana S, Jalbert LE, Nelson SJ, Bollen AW, Gustafson WC, Charron E, Weiss WA, Smirnov IV, Song JS, Olshen AB, Cha S, Zhao Y, Moore RA, Mungall AJ, Jones SJM, Hirst M, Marra MA, Saito N, Aburatani H, Mukasa A, Berger MS, Chang SM, Taylor BS, Costello JF. Mutational analysis reveals the origin and therapy-driven evolution of recurrent glioma. Science. 2014 Jan 10;343(6167):189-193. doi: 10.1126/science.1239947. Epub 2013 Dec 12. PMID: 24336570; PMCID: PMC3998672.

Kaley TJ, Panageas KS, Mellinghoff IK, Nolan C, Gavrilovic IT, DeAngelis LM, Abrey LE, Holland EC, Lassman AB. Phase II trial of an AKT inhibitor (perifosine) for recurrent glioblastoma. J Neurooncol. 2019 Sep;144(2):403-407. doi: 10.1007/s11060-019-03243-7. Epub 2019 Jul 19. PMID: 31325145; PMCID: PMC7493746.

Kaley TJ, Panageas KS, Pentsova EI, Mellinghoff IK, Nolan C, Gavrilovic I, DeAngelis LM, Abrey LE, Holland EC, Omuro A, Lacouture ME, Ludwig E, Lassman AB. Phase I clinical trial of temsirolimus and perifosine for recurrent glioblastoma. Ann Clin Transl Neurol. 2020 Apr;7(4):429-436. doi: 10.1002/acn3.51009. Epub 2020 Apr 15. PMID: 32293798; PMCID: PMC7187704.

Kebir S, Ullrich V, Berger P, Dobersalske C, Langer S, Rauschenbach L, Trageser D, Till A, Lorbeer FK, Wieland A, Wilhelm-Buchstab T, Ahmad A, Fröhlich H, Cima I, Prasad S, Matschke J, Jendrossek V, Remke M, Grüner BM, Roesch A, Siveke JT, Herold-Mende C, Blau T, Keyvani K, van Landeghem FKH, Pietsch T, Felsberg J, Reifenberger G, Weller M, Sure U, Brüstle O, Simon M, Glas M, Scheffler B. A Sequential Targeting Strategy Interrupts AKT-Driven Subclone-Mediated Progression in Glioblastoma. Clin Cancer Res. 2023 Jan 17;29(2):488-500. doi: 10.1158/1078-0432.CCR-22-0611. PMID: 36239995; PMCID: PMC9843437

Keller PJ, Arendt LM, Skibinski A, Logvinenko T, Klebba I, Dong S, Smith AE, Prat A, Perou CM, Gilmore H, Schnitt S, Naber SP, Garlick JA, Kuperwasser C. Defining the cellular precursors to human breast cancer. Proc Natl Acad Sci U S A. 2012 Feb 21;109(8):2772-7. doi: 10.1073/pnas.1017626108. Epub 2011 Sep 21. PMID: 21940501; PMCID: PMC3286919.

Kidder BL, Hu G, Zhao K. KDM5B focuses H3K4 methylation near promoters and enhancers during embryonic stem cell self-renewal and differentiation. Genome Biol. 2014 Feb 4;15(2):R32. doi: 10.1186/gb-2014-15-2-r32. PMID: 24495580; PMCID: PMC4053761.

Kim C, Gao R, Sei E, Brandt R, Hartman J, Hatschek T, Crosetto N, Foukakis T, Navin NE. Chemoresistance Evolution in Triple-Negative Breast Cancer Delineated by Single-Cell Sequencing. Cell. 2018 May 3;173(4):879-893.e13. doi: 10.1016/j.cell.2018.03.041. Epub 2018 Apr 19. PMID: 29681456; PMCID: PMC6132060.

Kim J, Lee IH, Cho HJ, Park CK, Jung YS, Kim Y, Nam SH, Kim BS, Johnson MD, Kong DS, Seol HJ, Lee JI, Joo KM, Yoon Y, Park WY, Lee J, Park PJ, Nam DH. Spatiotemporal Evolution of the Primary Glioblastoma Genome. Cancer Cell. 2015 Sep 14;28(3):318-28. doi: 10.1016/j.ccell.2015.07.013. PMID: 26373279.

Klughammer J, Kiesel B, Roetzer T, Fortelny N, Nemc A, Nenning KH, Furtner J, Sheffield NC, Datlinger P, Peter N, Nowosielski M, Augustin M, Mischkulnig M, Ströbel T, Alpar D, Ergüner B, Senekowitsch M, Moser P, Freyschlag CF, Kerschbaumer J, Thomé C, Grams AE, Stockhammer G, Kitzwoegerer M, Oberndorfer S, Marhold F, Weis S, Trenkler J, Buchroithner J, Pichler J, Haybaeck J, Krassnig S, Mahdy Ali K, von Campe G, Payer F, Sherif C, Preiser J, Hauser T, Winkler PA, Kleindienst W, Würtz F, Brandner-Kokalj T, Stultschnig M, Schweiger S, Dieckmann K, Preusser M, Langs G, Baumann B, Knosp E, Widhalm G, Marosi C, Hainfellner JA, Woehrer A, Bock C. The DNA methylation landscape of glioblastoma disease progression shows extensive heterogeneity in time and space. Nat Med. 2018 Oct;24(10):1611-1624. doi: 10.1038/s41591-018-0156-x. Epub 2018 Aug 27. PMID: 30150718; PMCID: PMC6181207.

Körber V, Yang J, Barah P, Wu Y, Stichel D, Gu Z, Fletcher MNC, Jones D, Hentschel B, Lamszus K, Tonn JC, Schackert G, Sabel M, Felsberg J, Zacher A, Kaulich K, Hübschmann D, Herold-Mende C, von Deimling A, Weller M, Radlwimmer B, Schlesner M, Reifenberger G, Höfer T, Lichter P. Evolutionary Trajectories of IDHWT Glioblastomas Reveal a Common Path of Early Tumorigenesis Instigated Years ahead of Initial Diagnosis. Cancer Cell. 2019 Apr 15;35(4):692-704.e12. doi: 10.1016/j.ccell.2019.02.007. Epub 2019 Mar 21. PMID: 30905762.

Kuo KT, Huang WC, Bamodu OA, Lee WH, Wang CH, Hsiao M, Wang LS, Yeh CT. Histone demethylase JARID1B/KDM5B promotes aggressiveness of non-small cell lung cancer and serves as a good prognostic predictor. Clin Epigenetics. 2018 Aug 9;10(1):107. doi: 10.1186/s13148-018-0533-9. PMID: 30092824; PMCID: PMC6085612.

Lan X, Jörg DJ, Cavalli FMG, Richards LM, Nguyen LV, Vanner RJ, Guilhamon P, Lee L, Kushida MM, Pellacani D, Park NI, Coutinho FJ, Whetstone H, Selvadurai HJ, Che C, Luu B, Carles A, Moksa M, Rastegar N, Head R, Dolma S, Prinos P, Cusimano MD, Das S, Bernstein M, Arrowsmith CH, Mungall AJ, Moore RA, Ma Y, Gallo M, Lupien M, Pugh TJ, Taylor MD, Hirst M, Eaves CJ, Simons BD, Dirks PB. Fate mapping of human glioblastoma reveals an invariant stem cell hierarchy. Nature. 2017 Sep 14;549(7671):227-232. doi: 10.1038/nature23666. Epub 2017 Aug 30. PMID: 28854171; PMCID: PMC5608080.

Landau DA, Carter SL, Stojanov P, McKenna A, Stevenson K, Lawrence MS, Sougnez C, Stewart C, Sivachenko A, Wang L, Wan Y, Zhang W, Shukla SA, Vartanov A, Fernandes SM, Saksena G, Cibulskis K, Tesar B, Gabriel S, Hacohen N, Meyerson M, Lander ES, Neuberg D, Brown JR, Getz G, Wu CJ. Evolution and impact of subclonal mutations in chronic lymphocytic leukemia. Cell. 2013 Feb 14;152(4):714-26. doi: 10.1016/j.cell.2013.01.019. PMID: 23415222; PMCID: PMC3575604.

Lathia JD, Mack SC, Mulkearns-Hubert EE, Valentim CL, Rich JN. Cancer stem cells in glioblastoma. Genes Dev. 2015 Jun 15;29(12):1203-17. doi: 10.1101/gad.261982.115. PMID: 26109046; PMCID: PMC4495393.
Lee J, Kotliarova S, Kotliarov Y, Li A, Su Q, Donin NM, Pastorino S, Purow BW, Christopher N, Zhang W, Park JK, Fine HA. Tumor stem cells derived from glioblastomas cultured in bFGF and EGF more closely mirror the phenotype and genotype of primary tumors than do serum-cultured cell lines. Cancer Cell. 2006 May;9(5):391-403. doi: 10.1016/j.ccr.2006.03.030. PMID: 16697959.

Lazaridis L, Schmidt T, Oster C, Blau T, Pierscianek D, Siveke JT, Bauer S, Schildhaus HU, Sure U, Keyvani K, Kleinschnitz C, Stuschke M, Herrmann K, Deuschl C, Scheffler B, Kebir S, Glas M. Precision neuro-oncology: a pilot analysis of personalized treatment in recurrent glioma. J Cancer Res Clin Oncol. 2022 Aug 12. doi: 10.1007/s00432-022-04050-w. Epub ahead of print. PMID: 35953681.

Liau BB, Sievers C, Donohue LK, Gillespie SM, Flavahan WA, Miller TE, Venteicher AS, Hebert CH, Carey CD, Rodig SJ, Shareef SJ, Najm FJ, van Galen P, Wakimoto H, Cahill DP, Rich JN, Aster JC, Suvà ML, Patel AP, Bernstein BE. Adaptive Chromatin Remodeling Drives Glioblastoma Stem Cell Plasticity and Drug Tolerance. Cell Stem Cell. 2017 Feb 2;20(2):233-246.e7. doi: 10.1016/j.stem.2016.11.003. Epub 2016 Dec 15. PMID: 27989769; PMCID: PMC5291795.

Li G, Kanagasabai T, Lu W, Zou MR, Zhang SM, Celada SI, Izban MG, Liu Q, Lu T, Ballard BR, Zhou X, Adunyah SE, Matusik RJ, Yan Q, Chen Z. KDM5B Is Essential for the Hyperactivation of PI3K/AKT Signaling in Prostate Tumorigenesis. Cancer Res. 2020 Nov 1;80(21):4633-4643. doi: 10.1158/0008-5472.CAN-20-0505. Epub 2020 Aug 31. PMID: 32868382; PMCID: PMC8034842.

LI MC, HERTZ R, BERGENSTAL DM. Therapy of choriocarcinoma and related trophoblastic tumors with folic acid and purine antagonists. N Engl J Med. 1958 Jul 10;259(2):66-74. doi: 10.1056/NEJM195807102590204. PMID: 13566422.
Moxley JH 3rd, De Vita VT, Brace K, Frei E 3rd. Intensive combination chemotherapy and X-irradiation in Hodgkin's disease. Cancer Res. 1967 Jul;27(7):1258-63. PMID: 4952914.

Li Q, Shi L, Gui B, Yu W, Wang J, Zhang D, Han X, Yao Z, Shang Y. Binding of the JmjC demethylase JARID1B to LSD1/NuRD suppresses angiogenesis and metastasis in breast cancer cells by repressing chemokine CCL14. Cancer Res. 2011 Nov 1;71(21):6899-908. doi: 10.1158/0008-5472.CAN-11-1523. Epub 2011 Sep 21. PMID: 21937684.

Li X, Liu L, Yang S, Song N, Zhou X, Gao J, Yu N, Shan L, Wang Q, Liang J, Xuan C, Wang Y, Shang Y, Shi L. Histone demethylase KDM5B is a key regulator of genome stability. Proc Natl Acad Sci U S A. 2014 May 13;111(19):7096-101. doi: 10.1073/pnas.1324036111. Epub 2014 Apr 28. PMID: 24778210; PMCID: PMC4024858.

Li Y, Han J, Zhang Y, Cao F, Liu Z, Li S, Wu J, Hu C, Wang Y, Shuai J, Chen J, Cao L, Li D, Shi P, Tian C, Zhang J, Dou Y, Li G, Chen Y, Lei M. Structural basis for activity regulation of MLL family methyltransferases. Nature. 2016 Feb 25;530(7591):447-52. doi: 10.1038/nature16952. Epub 2016 Feb 17. PMID: 26886794; PMCID: PMC5125619.

Liu G, Yuan X, Zeng Z, Tunici P, Ng H, Abdulkadir IR, Lu L, Irvin D, Black KL, Yu JS. Analysis of gene expression and chemoresistance of CD133+ cancer stem cells in glioblastoma. Mol Cancer. 2006 Dec 2;5:67. doi: 10.1186/1476-4598-5-67. PMID: 17140455; PMCID: PMC1697823.

Louis DN, Perry A, Wesseling P, Brat DJ, Cree IA, Figarella-Branger D, Hawkins C, Ng HK, Pfister SM, Reifenberger G, Soffietti R, von Deimling A, Ellison DW. The 2021 WHO Classification of Tumors of the Central Nervous System: a summary. Neuro Oncol. 2021 Aug 2;23(8):1231-1251. doi: 10.1093/neuonc/noab106. PMID: 34185076; PMCID: PMC8328013.

Manning BD, Toker A. AKT/PKB Signaling: Navigating the Network. Cell. 2017 Apr 20;169(3):381-405. doi: 10.1016/j.cell.2017.04.001. PMID: 28431241; PMCID: PMC5546324.

Marine JC, Dawson SJ, Dawson MA. Non-genetic mechanisms of therapeutic resistance in cancer. Nat Rev Cancer. 2020 Dec;20(12):743-756. doi: 10.1038/s41568-020-00302-4. Epub 2020 Oct 8. PMID: 33033407.

Marin-Bejar O, Rogiers A, Dewaele M, Femel J, Karras P, Pozniak J, Bervoets G, Van Raemdonck N, Pedri D, Swings T, Demeulemeester J, Borght SV, Lehnert S, Bosisio F, van den Oord JJ, Bempt IV, Lambrechts D, Voet T, Bechter O, Rizos H, Levesque MP, Leucci E, Lund AW, Rambow F, Marine JC. Evolutionary predictability of genetic versus nongenetic resistance to anticancer drugs in melanoma. Cancer Cell. 2021 Aug 9;39(8):1135-1149.e8. doi: 10.1016/j.ccell.2021.05.015. Epub 2021 Jun 17. PMID: 34143978.

McGranahan T, Therkelsen KE, Ahmad S, Nagpal S. Current State of Immunotherapy for Treatment of Glioblastoma. Curr Treat Options Oncol. 2019 Feb 21;20(3):24. doi: 10.1007/s11864-019-0619-4. PMID: 30790064; PMCID: PMC6394457.

Meacham CE, Morrison SJ. Tumour heterogeneity and cancer cell plasticity. Nature. 2013 Sep 19;501(7467):328-37. doi: 10.1038/nature12624. PMID: 24048065; PMCID: PMC4521623.

Meyer M, Reimand J, Lan X, Head R, Zhu X, Kushida M, Bayani J, Pressey JC, Lionel AC, Clarke ID, Cusimano M, Squire JA, Scherer SW, Bernstein M, Woodin MA, Bader GD, Dirks PB. Single cell-derived clonal analysis of human glioblastoma links functional and genomic heterogeneity. Proc Natl Acad Sci U S A. 2015 Jan 20;112(3):851-6. doi: 10.1073/pnas.1320611111. Epub 2015 Jan 5. PMID: 25561528; PMCID: PMC4311802.

Mitra D, Das PM, Huynh FC, Jones FE. Jumonji/ARID1 B (JARID1B) protein promotes breast tumor cell cycle progression through epigenetic repression of microRNA let-7e. J Biol Chem. 2011 Nov 25;286(47):40531-5. doi: 10.1074/jbc.M111.304865. Epub 2011 Oct 3. PMID: 21969366; PMCID: PMC3220509.

Mroz EA, Tward AD, Hammon RJ, Ren Y, Rocco JW. Intra-tumor genetic heterogeneity and mortality in head and neck cancer: analysis of data from the Cancer Genome Atlas. PLoS Med. 2015 Feb 10;12(2):e1001786. doi: 10.1371/journal.pmed.1001786. Erratum in: PLoS Med. 2015 Mar;12(3):e1001818. Tward, Aaron M [corrected to Tward, Aaron D]. Erratum in: PLoS Med. 2015 Jun;12(6):e1001844. PMID: 25668320; PMCID: PMC4323109.

NCCN Clinical Practice Guidelines in Oncology (NCCN Guidelines®). Central Nervus System Cancers. Version 3.2019-October 18, 2019. NCCN; 2019. NCCN.org.

Neftel C, Laffy J, Filbin MG, Hara T, Shore ME, Rahme GJ, Richman AR, Silverbush D, Shaw ML, Hebert CM, Dewitt J, Gritsch S, Perez EM, Gonzalez Castro LN, Lan X, Druck N, Rodman C, Dionne D, Kaplan A, Bertalan MS, Small J, Pelton K, Becker S, Bonal D, Nguyen QD, Servis RL, Fung JM, Mylvaganam R, Mayr L, Gojo J, Haberler C, Geyeregger R, Czech T, Slavc I, Nahed BV, Curry WT, Carter BS, Wakimoto H, Brastianos PK, Batchelor TT, Stemmer-Rachamimov A, Martinez-Lage M, Frosch MP, Stamenkovic I, Riggi N, Rheinbay E, Monje M, Rozenblatt-Rosen O, Cahill DP, Patel AP, Hunter T, Verma IM, Ligon KL, Louis DN, Regev A, Bernstein BE, Tirosh I, Suvà ML. An Integrative Model of Cellular States, Plasticity, and Genetics for Glioblastoma. Cell. 2019 Aug 8;178(4):835-849.e21. doi: 10.1016/j.cell.2019.06.024. Epub 2019 Jul 18. PMID: 31327527; PMCID: PMC6703186.

Ohta K, Haraguchi N, Kano Y, Kagawa Y, Konno M, Nishikawa S, Hamabe A, Hasegawa S, Ogawa H, Fukusumi T, Uemura M, Nishimura J, Hata T, Takemasa I, Mizushima T, Noguchi Y, Ozaki M, Kudo T, Sakai D, Satoh T, Fukami M, Ishii M, Yamamoto H, Doki Y, Mori M, Ishii H. Depletion of JARID1B induces cellular senescence in human colorectal cancer. Int J Oncol. 2013 Apr;42(4):1212-8. doi: 10.3892/ijo.2013.1799. Epub 2013 Jan 25. PMID: 23354547.

Ostrom QT, Cioffi G, Gittleman H, Patil N, Waite K, Kruchko C, Barnholtz-Sloan JS. CBTRUS Statistical Report: Primary Brain and Other Central Nervous System Tumors Diagnosed in the United States in 2012-2016. Neuro Oncol. 2019 Nov 1;21(Suppl 5):v1-v100. doi: 10.1093/neuonc/noz150. PMID: 31675094; PMCID: PMC6823730.

Patel AP, Tirosh I, Trombetta JJ, Shalek AK, Gillespie SM, Wakimoto H, Cahill DP, Nahed BV, Curry WT, Martuza RL, Louis DN, Rozenblatt-Rosen O, Suvà ML, Regev A, Bernstein BE. Single-cell RNA-seq highlights intratumoral heterogeneity in primary glioblastoma. Science. 2014 Jun 20;344(6190):1396-401. doi: 10.1126/science.1254257. Epub 2014 Jun 12. PMID: 24925914; PMCID: PMC4123637.

Pearson JRD, Regad T. Targeting cellular pathways in glioblastoma multiforme. Signal Transduct Target Ther. 2017 Sep 29;2:17040. doi: 10.1038/sigtrans.2017.40. PMID: 29263927; PMCID: PMC5661637.

Pepe MS, Etzioni R, Feng Z, Potter JD, Thompson ML, Thornquist M, Winget M, Yasui Y. Phases of biomarker development for early detection of cancer. J Natl Cancer Inst. 2001 Jul 18;93(14):1054-61. doi: 10.1093/jnci/93.14.1054. PMID: 11459866.

Raha D, Wilson TR, Peng J, Peterson D, Yue P, Evangelista M, Wilson C, Merchant M, Settleman J. The cancer stem cell marker aldehyde dehydrogenase is required to maintain a drug-tolerant tumor cell subpopulation. Cancer Res. 2014 Jul 1;74(13):3579-90. doi: 10.1158/0008-5472.CAN-13-3456. Epub 2014 May 8. PMID: 24812274.

Rambow F, Rogiers A, Marin-Bejar O, Aibar S, Femel J, Dewaele M, Karras P, Brown D, Chang YH, Debiec-Rychter M, Adriaens C, Radaelli E, Wolter P, Bechter O, Dummer R, Levesque M, Piris A, Frederick DT, Boland G, Flaherty KT, van den Oord J, Voet T, Aerts S, Lund AW, Marine JC. Toward Minimal Residual Disease-Directed Therapy in Melanoma. Cell. 2018 Aug 9;174(4):843-855.e19. doi: 10.1016/j.cell.2018.06.025. Epub 2018 Jul 12. PMID: 30017245.

Ramirez M, Rajaram S, Steininger RJ, Osipchuk D, Roth MA, Morinishi LS, Evans L, Ji W, Hsu CH, Thurley K, Wei S, Zhou A, Koduru PR, Posner BA, Wu LF, Altschuler SJ. Diverse drug-resistance mechanisms can emerge from drug-tolerant cancer persister cells. Nat Commun. 2016 Feb 19;7:10690. doi: 10.1038/ncomms10690. PMID: 26891683; PMCID: PMC4762880.

Rea S, Eisenhaber F, O'Carroll D, Strahl BD, Sun ZW, Schmid M, Opravil S, Mechtler K, Ponting CP, Allis CD, Jenuwein T. Regulation of chromatin structure by site-specific histone H3 methyltransferases. Nature. 2000 Aug 10;406(6796):593-9. doi: 10.1038/35020506. PMID: 10949293.

Reifenberger G, Wirsching HG, Knobbe-Thomsen CB, Weller M. Advances in the molecular genetics of gliomas - implications for classification and therapy. Nat Rev Clin Oncol. 2017 Jul;14(7):434-452. doi: 10.1038/nrclinonc.2016.204. Epub 2016 Dec 29. PMID: 28031556.

Reinartz R, Wang S, Kebir S, Silver DJ, Wieland A, Zheng T, Küpper M, Rauschenbach L, Fimmers R, Shepherd TM, Trageser D, Till A, Schäfer N, Glas M, Hillmer AM, Cichon S, Smith AA, Pietsch T, Liu Y, Reynolds BA, Yachnis A, Pincus DW, Simon M, Brüstle O, Steindler DA, Scheffler B. Functional Subclone Profiling for Prediction of Treatment-Induced Intratumor Population Shifts and Discovery of Rational Drug Combinations in Human Glioblastoma. Clin Cancer Res. 2017 Jan 15;23(2):562-574. doi: 10.1158/1078-0432.CCR-15-2089. Epub 2016 Aug 12. PMID: 27521447; PMCID: PMC5241221.

Reya T, Morrison SJ, Clarke MF, Weissman IL. Stem cells, cancer, and cancer stem cells. Nature. 2001 Nov 1;414(6859):105-11. doi: 10.1038/35102167. PMID: 11689955.

Roesch A, Fukunaga-Kalabis M, Schmidt EC, Zabierowski SE, Brafford PA, Vultur A, Basu D, Gimotty P, Vogt T, Herlyn M. A temporarily distinct subpopulation of slow-cycling melanoma cells is required for continuous tumor growth. Cell. 2010 May 14;141(4):583-94. doi: 10.1016/j.cell.2010.04.020. PMID: 20478252; PMCID: PMC2882693.

Roesch A, Vultur A, Bogeski I, Wang H, Zimmermann KM, Speicher D, Körbel C, Laschke MW, Gimotty PA, Philipp SE, Krause E, Pätzold S, Villanueva J, Krepler C, Fukunaga-Kalabis M, Hoth M, Bastian BC, Vogt T, Herlyn M. Overcoming intrinsic multidrug resistance in melanoma by blocking the mitochondrial respiratory chain of slow-cycling JARID1B(high) cells. Cancer Cell. 2013 Jun 10;23(6):811-25. doi: 10.1016/j.ccr.2013.05.003. PMID: 23764003; PMCID: PMC3810180.

Rosivatz E, Matthews JG, McDonald NQ, Mulet X, Ho KK, Lossi N, Schmid AC, Mirabelli M, Pomeranz KM, Erneux C, Lam EW, Vilar R, Woscholski R. A small molecule inhibitor for phosphatase and tensin homologue deleted on chromosome 10 (PTEN). ACS Chem Biol. 2006 Dec 15;1(12):780-90. doi: 10.1021/cb600352f. PMID: 17240976.

Scorsetti M, Navarria P, Pessina F, Ascolese AM, D'Agostino G, Tomatis S, De Rose F, Villa E, Maggi G, Simonelli M, Clerici E, Soffietti R, Santoro A, Cozzi L, Bello L. Multimodality therapy approaches, local and systemic treatment, compared with chemotherapy alone in recurrent glioblastoma. BMC Cancer. 2015 Jun 30;15:486. doi: 10.1186/s12885-015-1488-2. PMID: 26118437; PMCID: PMC4484625.

Schäfer A, Teufel J, Ringel F, Bettstetter M, Hoepner I, Rasper M, Gempt J, Koeritzer J, Schmidt-Graf F, Meyer B, Beier CP, Schlegel J. Aldehyde dehydrogenase 1A1--a new mediator of resistance to temozolomide in glioblastoma. Neuro Oncol. 2012 Dec;14(12):1452-64. doi: 10.1093/neuonc/nos270. Epub 2012 Nov 6. PMID: 23132408; PMCID: PMC3499020.

Shaffer SM, Dunagin MC, Torborg SR, Torre EA, Emert B, Krepler C, Beqiri M, Sproesser K, Brafford PA, Xiao M, Eggan E, Anastopoulos IN, Vargas-Garcia CA, Singh A, Nathanson KL, Herlyn M, Raj A. Rare cell variability and drug-induced reprogramming as a mode of cancer drug resistance. Nature. 2017 Jun 15;546(7658):431-435. doi: 10.1038/nature22794. Epub 2017 Jun 7. Erratum in: Nature. 2018 Feb 21;: PMID: 28607484; PMCID: PMC5542814.

Sharma SV, Lee DY, Li B, Quinlan MP, Takahashi F, Maheswaran S, McDermott U, Azizian N, Zou L, Fischbach MA, Wong KK, Brandstetter K, Wittner B, Ramaswamy S, Classon M, Settleman J. A chromatin-mediated reversible drug-tolerant state in cancer cell subpopulations. Cell. 2010 Apr 2;141(1):69-80. doi: 10.1016/j.cell.2010.02.027. PMID: 20371346; PMCID: PMC2851638.

Shen S, Faouzi S, Bastide A, Martineau S, Malka-Mahieu H, Fu Y, Sun X, Mateus C, Routier E, Roy S, Desaubry L, André F, Eggermont A, David A, Scoazec JY, Vagner S, Robert C. An epitranscriptomic mechanism underlies selective mRNA translation remodelling in melanoma persister cells. Nat Commun. 2019 Dec 16;10(1):5713. doi: 10.1038/s41467-019-13360-6. PMID: 31844050; PMCID: PMC6915789.

Shen S, Vagner S, Robert C. Persistent Cancer Cells: The Deadly Survivors. Cell. 2020 Nov 12;183(4):860-874. doi: 10.1016/j.cell.2020.10.027. PMID: 33186528.

Shergalis A, Bankhead A 3rd, Luesakul U, Muangsin N, Neamati N. Current Challenges and Opportunities in Treating Glioblastoma. Pharmacol Rev. 2018 Jul;70(3):412-445. doi: 10.1124/pr.117.014944. PMID: 29669750; PMCID: PMC5907910.

Shibue T, Weinberg RA. EMT, CSCs, and drug resistance: the mechanistic link and clinical implications. Nat Rev Clin Oncol. 2017 Oct;14(10):611-629. doi: 10.1038/nrclinonc.2017.44. Epub 2017 Apr 11. PMID: 28397828; PMCID: PMC5720366.

Singh N, Miner A, Hennis L, Mittal S. Mechanisms of temozolomide resistance in glioblastoma - a comprehensive review. Cancer Drug Resist. 2021;4(1):17-43. doi: 10.20517/cdr.2020.79. Epub 2021 Mar 19. PMID: 34337348; PMCID: PMC8319838.

Singh SK, Clarke ID, Terasaki M, Bonn VE, Hawkins C, Squire J, Dirks PB. Identification of a cancer stem cell in human brain tumors. Cancer Res. 2003 Sep 15;63(18):5821-8. PMID: 14522905.

Sood D, Tang-Schomer M, Pouli D, Mizzoni C, Raia N, Tai A, Arkun K, Wu J, Black LD 3rd, Scheffler B, Georgakoudi I, Steindler DA, Kaplan DL. 3D extracellular matrix microenvironment in bioengineered tissue models of primary pediatric and adult brain tumors. Nat Commun. 2019 Oct 4;10(1):4529. doi: 10.1038/s41467-019-12420-1. PMID: 31586101; PMCID: PMC6778192.

Stoller RG, Hande KR, Jacobs SA, Rosenberg SA, Chabner BA. Use of plasma pharmacokinetics to predict and prevent methotrexate toxicity. N Engl J Med. 1977 Sep 22;297(12):630-4. doi: 10.1056/NEJM197709222971203. PMID: 302412

Strahl BD, Allis CD. The language of covalent histone modifications. Nature. 2000 Jan 6;403(6765):41-5. doi: 10.1038/47412. PMID: 10638745.

Stupp R, Mason WP, van den Bent MJ, Weller M, Fisher B, Taphoorn MJ, Belanger K, Brandes AA, Marosi C, Bogdahn U, Curschmann J, Janzer RC, Ludwin SK, Gorlia T, Allgeier A, Lacombe D, Cairncross JG, Eisenhauer E, Mirimanoff RO; European Organisation for Research and Treatment of Cancer Brain Tumor and Radiotherapy Groups; National Cancer Institute of Canada Clinical Trials Group. Radiotherapy plus

concomitant and adjuvant temozolomide for glioblastoma. N Engl J Med. 2005 Mar 10;352(10):987-96. doi: 10.1056/NEJMoa043330. PMID: 15758009.

Stupp R, Taillibert S, Kanner AA, Kesari S, Steinberg DM, Toms SA, Taylor LP, Lieberman F, Silvani A, Fink KL, Barnett GH, Zhu JJ, Henson JW, Engelhard HH, Chen TC, Tran DD, Sroubek J, Tran ND, Hottinger AF, Landolfi J, Desai R, Caroli M, Kew Y, Honnorat J, Idbaih A, Kirson ED, Weinberg U, Palti Y, Hegi ME, Ram Z. Maintenance Therapy With Tumor-Treating Fields Plus Temozolomide vs Temozolomide Alone for Glioblastoma: A Randomized Clinical Trial. JAMA. 2015 Dec 15;314(23):2535-43. doi: 10.1001/jama.2015.16669. PMID: 26670971.

Stupp R, Taillibert S, Kanner A, Read W, Steinberg D, Lhermitte B, Toms S, Idbaih A, Ahluwalia MS, Fink K, Di Meco F, Lieberman F, Zhu JJ, Stragliotto G, Tran D, Brem S, Hottinger A, Kirson ED, Lavy-Shahaf G, Weinberg U, Kim CY, Paek SH, Nicholas G, Bruna J, Hirte H, Weller M, Palti Y, Hegi ME, Ram Z. Effect of Tumor-Treating Fields Plus Maintenance Temozolomide vs Maintenance Temozolomide Alone on Survival in Patients With Glioblastoma: A Randomized Clinical Trial. JAMA. 2017 Dec 19;318(23):2306-2316. doi: 10.1001/jama.2017.18718. Erratum in: JAMA. 2018 May 1;319(17):1824. PMID: 29260225; PMCID: PMC5820703.

Sui X, Chen R, Wang Z, Huang Z, Kong N, Zhang M, Han W, Lou F, Yang J, Zhang Q, Wang X, He C, Pan H. Autophagy and chemotherapy resistance: a promising therapeutic target for cancer treatment. Cell Death Dis. 2013 Oct 10;4(10):e838. doi: 10.1038/cddis.2013.350. PMID: 24113172; PMCID: PMC3824660.

Tang B, Qi G, Tang F, Yuan S, Wang Z, Liang X, Li B, Yu S, Liu J, Huang Q, Wei Y, Zhai R, Lei B, Yu H, Jiao X, He S. JARID1B promotes metastasis and epithelial-mesenchymal transition via PTEN/AKT signaling in hepatocellular carcinoma cells. Oncotarget. 2015 May 20;6(14):12723-39. doi: 10.18632/oncotarget.3713. Erratum in: Oncotarget. 2020 May 12;11(19):1797-1798. PMID: 25909289; PMCID: PMC4494969.

Tarabichi M, Salcedo A, Deshwar AG, Ni Leathlobhair M, Wintersinger J, Wedge DC, Van Loo P, Morris QD, Boutros PC. A practical guide to cancer subclonal reconstruction from DNA sequencing. Nat Methods. 2021 Feb;18(2):144-155. doi: 10.1038/s41592-020-01013-2. Epub 2021 Jan 4. PMID: 33398189; PMCID: PMC7867630.

Thorpe LM, Yuzugullu H, Zhao JJ. PI3K in cancer: divergent roles of isoforms, modes of activation and therapeutic targeting. Nat Rev Cancer. 2015 Jan;15(1):7-24. doi: 10.1038/nrc3860. PMID: 25533673; PMCID: PMC4384662.

Umkehrer C, Holstein F, Formenti L, Jude J, Froussios K, Neumann T, Cronin SM, Haas L, Lipp JJ, Burkard TR, Fellner M, Wiesner T, Zuber J, Obenauf AC. Isolating live cell clones from barcoded populations using CRISPRa-inducible reporters. Nat Biotechnol. 2021 Feb;39(2):174-178. doi: 10.1038/s41587-020-0614-0. Epub 2020 Jul 27. PMID: 32719478.

van den Bent MJ, Tesileanu CMS, Wick W, Sanson M, Brandes AA, Clement PM, Erridge S, Vogelbaum MA, Nowak AK, Baurain JF, Mason WP, Wheeler H, Chinot OL, Gill S, Griffin M, Rogers L, Taal W, Rudà R, Weller M, McBain C, Reijneveld J, Enting RH, Caparrotti F, Lesimple T, Clenton S, Gijtenbeek A, Lim E, Herrlinger U,

Hau P, Dhermain F, de Heer I, Aldape K, Jenkins RB, Dubbink HJ, Kros JM, Wesseling P, Nuyens S, Golfinopoulos V, Gorlia T, French P, Baumert BG. Adjuvant and concurrent temozolomide for 1p/19q non-co-deleted anaplastic glioma (CATNON; EORTC study 26053-22054): second interim analysis of a randomised, open-label, phase 3 study. Lancet Oncol. 2021 Jun;22(6):813-823. doi: 10.1016/S1470-2045(21)00090-5. Epub 2021 May 14. PMID: 34000245; PMCID: PMC8191233.

Verhaak RG, Hoadley KA, Purdom E, Wang V, Qi Y, Wilkerson MD, Miller CR, Ding L, Golub T, Mesirov JP, Alexe G, Lawrence M, O'Kelly M, Tamayo P, Weir BA, Gabriel S, Winckler W, Gupta S, Jakkula L, Feiler HS, Hodgson JG, James CD, Sarkaria JN, Brennan C, Kahn A, Spellman PT, Wilson RK, Speed TP, Gray JW, Meyerson M, Getz G, Perou CM, Hayes DN; Cancer Genome Atlas Research Network. Integrated genomic analysis identifies clinically relevant subtypes of glioblastoma characterized by abnormalities in PDGFRA, IDH1, EGFR, and NF1. Cancer Cell. 2010 Jan 19;17(1):98-110. doi: 10.1016/j.ccr.2009.12.020. PMID: 20129251; PMCID: PMC2818769.

Voabil P, de Bruijn M, Roelofsen LM, Hendriks SH, Brokamp S, van den Braber M, Broeks A, Sanders J, Herzig P, Zippelius A, Blank CU, Hartemink KJ, Monkhorst K, Haanen JBAG, Schumacher TN, Thommen DS. An ex vivo tumor fragment platform to dissect response to PD-1 blockade in cancer. Nat Med. 2021 Jul;27(7):1250-1261. doi: 10.1038/s41591-021-01398-3. Epub 2021 Jul 8. PMID: 34239134.

Vogel FCE, Bordag N, Zügner E, Trajkovic-Arsic M, Chauvistré H, Shannan B, Váraljai R, Horn S, Magnes C, Thomas Siveke J, Schadendorf D, Roesch A. Targeting the H3K4 Demethylase KDM5B Reprograms the Metabolome and Phenotype of Melanoma Cells. J Invest Dermatol. 2019 Dec;139(12):2506-2516.e10. doi: 10.1016/j.jid.2019.06.124. Epub 2019 Jun 21. PMID: 31229500.

Wang D, Han S, Peng R, Jiao C, Wang X, Yang X, Yang R, Li X. Depletion of histone demethylase KDM5B inhibits cell proliferation of hepatocellular carcinoma by regulation of cell cycle checkpoint proteins p15 and p27. J Exp Clin Cancer Res. 2016 Feb 25;35:37. doi: 10.1186/s13046-016-0311-5. PMID: 26911146; PMCID: PMC4766611.

Wang EJ, Chen JS, Jain S, Morshed RA, Haddad AF, Gill S, Beniwal AS, Aghi MK. Immunotherapy Resistance in Glioblastoma. Front Genet. 2021 Dec 17;12:750675. doi: 10.3389/fgene.2021.750675. PMID: 34976006; PMCID: PMC8718605.

Wang J, Cazzato E, Ladewig E, Frattini V, Rosenbloom DI, Zairis S, Abate F, Liu Z, Elliott O, Shin YJ, Lee JK, Lee IH, Park WY, Eoli M, Blumberg AJ, Lasorella A, Nam DH, Finocchiaro G, Iavarone A, Rabadan R. Clonal evolution of glioblastoma under therapy. Nat Genet. 2016 Jul;48(7):768-76. doi: 10.1038/ng.3590. Epub 2016 Jun 6. PMID: 27270107; PMCID: PMC5627776.

Wang X, Gu M, Ju Y, Zhou J. Overcoming radio-resistance in esophageal squamous cell carcinoma via hypermethylation of PIK3C3 promoter region mediated by KDM5B loss. J Radiat Res. 2022 May 18;63(3):331-341. doi: 10.1093/jrr/rrac004. PMID: 35333349; PMCID: PMC9124615.

Wang Z, Tang F, Qi G, Yuan S, Zhang G, Tang B, He S. KDM5B is overexpressed in gastric cancer and is required for gastric cancer cell proliferation and metastasis. Am J Cancer Res. 2014 Dec 15;5(1):87-100. PMID: 25628922; PMCID: PMC4300698.

Weller M, van den Bent M, Preusser M, Le Rhun E, Tonn JC, Minniti G, Bendszus M, Balana C, Chinot O, Dirven L, French P, Hegi ME, Jakola AS, Platten M, Roth P, Rudà R, Short S, Smits M, Taphoorn MJB, von Deimling A, Westphal M, Soffietti R, Reifenberger G, Wick W. EANO guidelines on the diagnosis and treatment of diffuse gliomas of adulthood. Nat Rev Clin Oncol. 2021 Mar;18(3):170-186. doi: 10.1038/s41571-020-00447-z. Epub 2020 Dec 8. Erratum in: Nat Rev Clin Oncol. 2022 May;19(5):357-358. PMID: 33293629; PMCID: PMC7904519.

Weinstein IB. Cancer. Addiction to oncogenes--the Achilles heal of cancer. Science. 2002 Jul 5;297(5578):63-4. doi: 10.1126/science.1073096. PMID: 12098689.

Weinstein IB, Joe A. Oncogene addiction. Cancer Res. 2008 May 1;68(9):3077-80; discussion 3080. doi: 10.1158/0008-5472.CAN-07-3293. PMID: 18451130.

Wen PY, Weller M, Lee EQ, Alexander BM, Barnholtz-Sloan JS, Barthel FP, Batchelor TT, Bindra RS, Chang SM, Chiocca EA, Cloughesy TF, DeGroot JF, Galanis E, Gilbert MR, Hegi ME, Horbinski C, Huang RY, Lassman AB, Le Rhun E, Lim M, Mehta MP, Mellinghoff IK, Minniti G, Nathanson D, Platten M, Preusser M, Roth P, Sanson M, Schiff D, Short SC, Taphoorn MJB, Tonn JC, Tsang J, Verhaak RGW, von Deimling A, Wick W, Zadeh G, Reardon DA, Aldape KD, van den Bent MJ. Glioblastoma in adults: a Society for Neuro-Oncology (SNO) and European Society of Neuro-Oncology (EANO) consensus review on current management and future directions. Neuro Oncol. 2020 Aug 17;22(8):1073-1113. doi: 10.1093/neuonc/noaa106. PMID: 32328653; PMCID: PMC7594557.

Wick W, Gorlia T, Bendszus M, Taphoorn M, Sahm F, Harting I, Brandes AA, Taal W, Domont J, Idbaih A, Campone M, Clement PM, Stupp R, Fabbro M, Le Rhun E, Dubois F, Weller M, von Deimling A, Golfinopoulos V, Bromberg JC, Platten M, Klein M, van den Bent MJ. Lomustine and Bevacizumab in Progressive Glioblastoma. N Engl J Med. 2017 Nov 16;377(20):1954-1963. doi: 10.1056/NEJMoa1707358. PMID: 29141164.

Wong SH, Goode DL, Iwasaki M, Wei MC, Kuo HP, Zhu L, Schneidawind D, Duque-Afonso J, Weng Z, Cleary ML. The H3K4-Methyl Epigenome Regulates Leukemia Stem Cell Oncogenic Potential. Cancer Cell. 2015 Aug 10;28(2):198-209. doi: 10.1016/j.ccell.2015.06.003. Epub 2015 Jul 16. PMID: 26190263; PMCID: PMC4536132.

Wu A, Wei J, Kong LY, Wang Y, Priebe W, Qiao W, Sawaya R, Heimberger AB. Glioma cancer stem cells induce immunosuppressive macrophages/microglia. Neuro Oncol. 2010 Nov;12(11):1113-25. doi: 10.1093/neuonc/noq082. Epub 2010 Jul 28. PMID: 20667896; PMCID: PMC3098021.

Wu L, Qu X. Cancer biomarker detection: recent achievements and challenges. Chem Soc Rev. 2015 May 21;44(10):2963-97. doi: 10.1039/c4cs00370e. Epub 2015 Mar 5. PMID: 25739971.

Xie L, Pelz C, Wang W, Bashar A, Varlamova O, Shadle S, Impey S. KDM5B regulates embryonic stem cell self-renewal and represses cryptic intragenic transcription. EMBO J. 2011 Apr 20;30(8):1473-84. doi: 10.1038/emboj.2011.91. Epub 2011 Mar 29. PMID: 21448134; PMCID: PMC3102288.

Yabo YA, Niclou SP, Golebiewska A. Cancer cell heterogeneity and plasticity: A paradigm shift in glioblastoma. Neuro Oncol. 2022 May 4;24(5):669-682. doi: 10.1093/neuonc/noab269. Erratum in: Neuro Oncol. 2022 May 27;: PMID: 34932099; PMCID: PMC9071273.

Yamane K, Tateishi K, Klose RJ, Fang J, Fabrizio LA, Erdjument-Bromage H, Taylor-Papadimitriou J, Tempst P, Zhang Y. PLU-1 is an H3K4 demethylase involved in transcriptional repression and breast cancer cell proliferation. Mol Cell. 2007 Mar 23;25(6):801-12. doi: 10.1016/j.molcel.2007.03.001. Epub 2007 Mar 15. PMID: 17363312.

Yue H, Hu Z, Hu R, Guo Z, Zheng Y, Wang Y, Zhou Y. ALDH1A1 in Cancers: Bidirectional Function, Drug Resistance, and Regulatory Mechanism. Front Oncol. 2022 Jun 22;12:918778. doi: 10.3389/fonc.2022.918778. PMID: 35814382; PMCID: PMC9256994.

Zhang SM, Cai WL, Liu X, Thakral D, Luo J, Chan LH, McGeary MK, Song E, Blenman KRM, Micevic G, Jessel S, Zhang Y, Yin M, Booth CJ, Jilaveanu LB, Damsky W, Sznol M, Kluger HM, Iwasaki A, Bosenberg MW, Yan Q. KDM5B promotes immune evasion by recruiting SETDB1 to silence retroelements. Nature. 2021 Oct;598(7882):682-687. doi: 10.1038/s41586-021-03994-2. Epub 2021 Oct 20. PMID: 34671158; PMCID: PMC8555464.

Zhang Y, Liang J, Li Q. Coordinated regulation of retinoic acid signaling pathway by KDM5B and polycomb repressive complex 2. J Cell Biochem. 2014 Sep;115(9):1528-38. doi: 10.1002/jcb.24807. PMID: 24619877.

Zhang Z, Zhou L, Xie N, Nice EC, Zhang T, Cui Y, Huang C. Overcoming cancer therapeutic bottleneck by drug repurposing. Signal Transduct Target Ther. 2020 Jul 2;5(1):113. doi: 10.1038/s41392-020-00213-8. PMID: 32616710; PMCID: PMC7331117.

5. Methods

5.1. Research samples

Short-term expanded vital cell populations were obtained from collected tumor tissue of *IDH*-wt glioblastoma patients at the University Bonn Medical Center (sample IDs: BN; n=6 patients; Table 1) and at the University Hospital Essen (sample IDs: E; n=2 patients; Table 1). As previously described (Kebir et al. Clin Cancer Res. 2022), studies were conducted in accordance with recognized ethical guidelines (Declaration of Helsinki). Respective local ethics committees (institutional review boards) approved the studies and all patients provided informed written consent. The Bonn Cohort of samples (University of Bonn Medical Center, Ethics Committee approval: #182/08), was established 2008-2014. The collection of samples for the Essen Cohort (University of Duisburg-Essen, Medical Faculty Ethics Committee approval: 18-8308-BO; West German Biobank (WBE) approval: 18_WBE_059), started in June 2019 and is still ongoing. Tumor classification relied on the World Health Organization guidelines from 2021 (Louis et al., Neuro Oncol 2021). The IDH mutation status and the O6-methylguanine DNA methyltransferase (MGMT) promoter methylation status of the samples was determined by routine neuropathological methods. Patient cell samples were tested negative for mycoplasma regularly using polymerase chain reaction (PCR). Authentication of samples was conducted by STR analysis.

Paired research samples included treatment-naive (^{naive}) cells from newly diagnosed glioblastoma patients (primary disease) and clinical relapse (^{cR}) cells from the relapse tumor tissue of the same patient. In addition, experimental relapse ($^{TMZ\rightarrow eR}$) cells were generated by serial *in vitro* exposure of temozolomide (500 µM) to (^{naive})cells for 16 days. Furthermore, experimental relapse cells were derived from (^{naive})cells serially exposed to 2 Gy ionizing irradiation *in vitro* every day for 12 days ($^{RT\rightarrow eR}$ cells).

Stable ALDH1A1-overexpressing (ALDH1A1 Ovx) as well as stable shRNA ALDH1A knockdown (shALDH1A1) cells were generated by former members of the lab. ALDH1A1 Ovx and the corresponding GFP control (GFP Ctrl) cells were produced by lentiviral transduction of a pLenti6.2/V5-DEST Gateway Vector (Life Technologies), into which coding sequences of ALDH1A1 or control-GFP were cloned into ^{naive}BN46 cells. shALDH1A1 and the corresponding shRNA non-targeting control (shNT) cells were produced using a MISSION short hairpin RNA plasmid against ALDH1A1 and a non-targeting control (both Sigma-Aldrich) by lentiviral transduction into ^{naive}BN46 cells.

All transduced cells were selected with blasticidin (5 mg/ mL; Santa Cruz Biotechnology). Stable expression and knockdown was confirmed by qPCR using standard protocols and primers for ALDH1A1 and the constitutive expressed housekeeper gene RPL37A as a reference gene.

Table 1: Cohort of vital patient cells (from Ullrich et al., in revision 2023).

Patient ID	Neuropathology: Glioblastoma, IDH wild type, CNS WHO grade 4	MGMT in primary tissue	Sex	Age	Extent of resection	KPS	Relapse surgery	PFS (months)	Primary therapy	Vital cell samples	MGMT in cells
BN46	yes	um	m	76	partial	100	No	NA	R, TMZ	^{naive}BN46	um
										TMZ->^{eR}BN46	um
BN78	yes	um	m	52	gross total	80	No	3,1	R, RT/TMZ, 2xTMZ(5/28)	^{naive}BN78	um
										TMZ->^{eR}BN78	um
BN91	yes	um	m	52	gross total	90	Yes	7,2	R, RT/TMZ, 4xTMZ(5/28)	^{naive}BN91	um
										^{cR}BN91	um
BN118	yes	um	m	63	gross total	90	Yes	7,3	R, RT/TMZ, 4xTMZ(5/28)	^{naive}BN118	um
										^{cR}BN118	um
BN123	yes	meth	m	58	gross total	70	Yes	26,2	R, RT/TMZ, 6xTMZ (5/28)	^{naive}BN123	meth
										^{cR}BN123	meth
BN132	yes	um	m	76	gross total	70	Yes	9,8	R, RT/TMZ, 4xTMZ(5/28)	^{naive}BN132	um
										^{cR}BN132	um
E049	yes	um	f	53	gross total	90	Yes	3,3	R, RT/TMZ	^{naive}E049	um
										^{cR}E049	um
E056	yes	um	f	67	gross total	90	Yes	3,7	R, RT/TMZ	^{naive}E056	um
										^{cR}E056	um

Legend:

"Age, patient's age at primary surgery; cR, cell sample isolated from clinical relapse tissue; IDH, isocitrate dehydrogenase; KPS, Karnofsky Performance Score before primary surgery; m, male; meth, methylated; MGMT in primary tissue, O6-methylguanine DNA methyltransferase promoter measured on primary tissue; MGMT in cells, O6-methylguanine DNA methyltransferase promoter measured on cells; NA, not assessable; naive, cell sample isolated from primary surgery tissue; Neuropathology, classification based on the 2021 WHO guidelines (Louis et al. Neuro Oncol 2021); PFS, progression-free survival (defined as the time from primary surgery to relapse surgery); R, resection; RT/TMZ, concomitant radiotherapy and temozolomide; TMZ (5/28), one course of maintenance temozolomide at days 1-5 of 28 days; RTx+CTx, concomitant radiotherapy and temozolomide; TMZ, temozolomide; TMZ->eR, experimental relapse cell sample generated in vitro from TMZ-exposed naive cells; um, unmethylated; WT, wild-type. Compare Kebir et al., Clin Cancer Res. 2023)." (Ullrich et al., in revision 2023)."

5.2. Sample preparation and cell culture

To derive vital cells from surgical tissue, samples were minced with a scalpel to small pieces and gently dissociated using trypsin at 37°C for 5-15 min. The single cell suspension was centrifuged for 5 min at 400g, the pellet resuspended in prewarmed

medium and the cells were seeded into poly-L-ornithine (PO) coated plasticware. The cells were maintained in Neurobasal-media supplemented with 1 % L-Glutamin, 1 % B-27 Supplement, 1 % Antibiotic-Antimycotic (ABX), 0,5 % N-2 Supplement and 1 µg/mL Laminin at 37°C and 5 % CO_2. Cells were supplemented every 48 hours with 10 ng/mL EGF and bFGF (Basic fibroblast growth factor), provided in Dulbecco's modified eagle medium (DMEM)-F12 carrier solution containing 10 % Fetal Bovine Serum (FBS) and 1 % Antibiotic-Antimycotic and cell culture media was exchanged after 7 days. Cell culture media, reagents, and analytical compounds were obtained from Life Technologies (Carlsbad, CA, USA) or Sigma-Aldrich (St. Louis, MO, USA). At a cell confluence between 60-90% cells were washed with PBS and trypsinized at 37°C until cells were detached. Serum was added to stop trypsinization and the single cell suspension was centrifuged and reseeded in a new dish in diluations of 1:2 or 1:3 for further culturing. In order to seed specific cell numbers, 100 µL of single-cell suspension were diluted 1:1 beforehand with trypan blue and counted using a Neubauer counting chamber. Cells could be cryoconserved for future analysis at any time, by using same parts of DF10 and freeze media and stored at -140°C for long-term storage. For all experiments of this thesis work, cell samples were used at cell culture passages 5-18.

The commercially available LN229 glioblastoma cell line was grown adherently in DMEM-F12, supplemented with 10 % FBS and 1 % ABX.

5.3 KDM5B-promoter-EGFP-reporter construct cells

A KDM5B promoter-EGFP-reporter construct (pLU-JARID1Bprom-EGFP-BLAST; Roesch et al., Cell 2010), was stably integrated into naive BN46, BN118, E049, E056 patient cell samples, as well as into TMZ-exposed $^{TMZ\rightarrow eR}$BN46 and ^{cR}BN118 patient cell samples at cell culture passages 4-13 via lentiviral infection. A four-plasmid system was used, consisting of the packaging plasmids pRRE (containing Gag and Pol) and pRSV-Rev (containing Rev), the envelope plasmid pMD2G that expresses vesicular stomatitis virus G glycoprotein (VSV-G) and the transfer plasmid pLU-JARID1Bprom-EGFP-BLAST. Gag is a precursor product containing the viral capsid and nucleocapsid components, while Pol is needed for the Reverse Transcriptase, transcribing the viral RNA into complementary DNA, as well as for Integrase components. The Regulator of expression of virion proteins (Rev) binds to the Rev Response Element (RRE) in order to facilitate the nuclear export of unspliced RNA transcripts. The VSV-G, enables the

entrance to the host cell by fusion of the viral with the host cell membrane. The transfer plasmid contains the construct, the viral long terminal repeats (LTRs) and the psi packaging signal, as well as a blasticidin resistance cassette for the selection of successfully transduced cells.

For future reference, a standard nomenclature was used for the respectively transduced cell populations; treatment-naive cell samples: $^{naive}BN46^{KDM5B\text{-}EGFP}$, $^{naive}BN118^{KDM5B\text{-}EGFP}$, $^{naive}E049^{KDM5B\text{-}EGFP}$ and $^{naive}E056^{KDM5B\text{-}EGFP}$ and experimental/clinical relapse cell samples: $^{TMZ\rightarrow eR}BN46^{KDM5B\text{-}EGFP}$ and $^{cR}BN118^{KDM5B\text{-}EGFP}$.

5.3.1. Chemical transformation of competent cells

The used plasmids were amplified by chemical transformation of competent cells (stable 3). The competent cells were thawed on wet ice and gently mixed. 1 µL Plasmid was incubated with 25 µL competent cells for 30 min on ice, before being heat-shocked for 45 seconds in a 42°C water bath and placed on ice again for 3 minutes. 0.9 mL S.O.C. media was added and the suspension was shacked for 1 hour at 225 rpm and 37°C. Per Ampicillin Plate 100 - 150 µL solution were distributed and incubated overnight at 37°C. Colonies were picked and incubated in 150 mL LB media supplemented with Ampicillin (1/1000) overnight at 37°C. Afterwards Maxipreps were conducted using a Plasmid Maxi Kit (Qiagen) following the manufactures instructions and the plasmids were finally eluted in water before stored at -20°C for further use.

5.3.2. Lenti-virus production

The lentivirus carrying the construct was produced in Human embryonic kidney (HEK) 293T cells (commercially available). One day before the transfection, $5*10^5$ HEK293T cells were seeded with prewarmed DMEM-F12 media, supplemented with 10% FBS and 1% antibiotics (Penicillin-Streptomycin) into 10 cm dishes. The next day the media was changed to one with 10% FBS and without antibiotics at least 4 hours before the plasmids were added to 300 µL OPTIMEM. The following plasmids were used: 2.5 µg Lenti (pLU-JARID1Bprom-EGFP-BLAST; from[9]), 2.5 µg pMDLg/pRRE (Addgene, Watertown, MA, USA #12251), 2.5 µg pRSV-Rev (Addgene #12253) and 2.5 µg pMD2.G (Addgene #12259). 16 µL TransIT-TKO transfection reagent (Mirus), a cationic polymer/lipid transfection reagent was added to 400 µL Opti-MEM™ reduced-serum medium (Thermo Fisher Scientific) in a separate tube. After 5 min incubation the Mirus-mix was added dropwise to the plasmid-mix and the mixture was incubated

for 20 min at RT, before added dropwise to the HEK cells. After 24 hours the media is changed to DMEM supplemented with 10 % FBS and 1% P/S. After co-transfection of HEK 293T-cells with the three plasmids the HEK293T cells produced the different virus components that assemble to a virus, so that infectious virus particles, so-called nucleocapsides, were released into the media and can be collected after additional 48 hours, filtered using 0.45 µm filters (Sigma-Aldrich) and frozen at -80°C for the later infection of patient cells.

5.3.3. Transduction and Selection of glioblastoma patient cells

The day before the transduction $1*10^6$ patient cells were seeded in a 6 cm cell culture dish. The thawed virus was added dropwise to the media. After 48 hours the cells were washed with PBS, trypsinized and pelleted at 400 rcf for 5 min before the pellet was resuspended in PBS. The percentage of EGFP+ cells was detected using flow cytometry. Afterwards selection of transduced cells was achieved by addition of blasticidin (Invivogen) for 4 days 8 µg/mL onto adherent cells. Successful selection (90-100 % EGFP+ cells) was confirmed using flow cytometry. Then the stably transduced cells were expanded and used for experiments. Treatment was performed following the indicated treatment schemes and the readout of EGFP intensities was performed via flow cytometry.

5.4. Cellular assays

5.4.1. In vitro drug exposure

Vital cells were seeded 24 h before drug exposure onto laminin/poly-L-ornithine coated cell culture dishes. Compounds were provided as a single dose or every other day (TMZ, 500 µM, Sigma-Aldrich; MK2206, 5 µM, Selleckchem; CPI-455, 12 µM, Selleckchem; SF167, 10 nM; Selleckchem). Treatment schemes for each experiment are presented above the corresponding plots. For all paradigms, DMSO was applied in corresponding concentrations as a control. The effect of drug exposure was evaluated by multiple readouts (e.g., via cell confluence, cell viability, qPCR, flow cytometry).

5.4.2. Knockdown studies

To specifically knockdown the expression of the target genes ALDH1A1 or KDM5B, RNA interference with small interfering RNAs was performed. 10,000 cells/cm^2 were

seeded in ABX-free media one day prior to siRNA transfection. The siRNA stocks were dissolved in 1x siRNA buffer (Horizon Discovery), that was produced by dilution of 5x siRNA buffer with Ribonuclease (RNAse) free water and applied at a concentration of 20 µM. The transfection was performed using Lipofectamine™ RNAiMAX Transfection Reagent (Thermo Fischer) and Opti-MEM™ Reduced Serum Medium (Thermo Fischer). The siRNA Opti-MEM™ mix and the Lipofectamine™ Opti-MEM™ mix were incubated separately for 10 min at RT, before they were mixed, incubated for another 20 min at RT and added into the media. Before readout was performed, successful knockdown of ALDH1A1 respectively KDM5B was verified after 6 days by qPCR using primers for ALDH1A1 or KDM5B and the constitutive expressed housekeeper gene RPL37A as a reference gene (Table “6.6. Primers qPCR”). The effect of the siRNA-mediated knockdown was either investigated for changes in downstream protein expression changes via Western blot or flow cytometry, for effects on cell viability using AlamarBlue™ or for the influence on clonogenicity via the neurosphere assay.

5.5. Experimental readout

5.5.1 Cell Confluence measurement

The cell confluence was measured via using software-based cell recognition using the Nyone, a fully automated cell imager (image cytometry). It enables determination of cell confluence non-invasively using brightfield imaging over longer time periods. The first measurement was performed before the first drug treatment (day 0). For all subsequent measurements each well was normalized to day 0 of the corresponding well.

5.5.2. Cell viability assessment

As an indicator for cell viability AlamarBlue™ (Life Technologies, Carlsbad, CA, USA) was used, which is a quantitative and highly sensitive method for the measurement of the viability of cells. It is based on the reduction of Resazurin to Resorufin whereby a color change from the blue non-fluorescent Resazurin, to the pink fluorescent Resorufin takes place. The fluorescence intensity is proportional to the amount of living metabolically active cells. The AlamarBlue reagent was added at a final concentration of 10% to the cell culture media and incubated at 37°C and 5 % CO_2 for 5 hours. Fluorescence intensity was measured using the Tecan Infinite F200 instrument (TECAN) at an emission wavelength of 580- 610 nm. All measured values were normalized to corresponding DMSO controls.

5.5.3. Quantitative polymerase chain reaction (qPCR)

To evaluate differences in gene expression in paired patient samples, RNA of short-term expanded cells was isolated using the TRIzol™ Reagent (Invitrogen) as instructed by the manufacturer. RNA was stored at -80°C for long-term storage. The complementary deoxyribonucleic acid (cDNA) synthesis was performed using Oligo(dT)20 Primer (Invitrogen), SuperScript IV Reverse Transcriptase (including buffer + DTT) (Invitrogen), dNTPs (Genecraft) and Random Hexamers dN6 (Thermo Fischer) on a PCR Mastercycler nexus GX2 (Eppendorf). cDNA was stored at -20°C for long-term storage. The qPCR was done using the Luminoct® SYBR Green qPCR Ready Mix (Sigma-Aldrich) and primers for the genes of interest (Table "6.6. Primers qPCR") on a CFX96 Touch real-time 20 cycler (BioRad). As a reference gene I used the constitutive expressed housekeeper gene *RPL37A*. Relative gene expression was calculated the by ΔCt method. Firstly, I calculated the ΔCt by normalizing the detected Ct values of the analyzed genes to the Ct (Cycle threshold) values of the housekeeper gene RPL37A using the following formula: ΔCT = CT (gene of interest) - CT (housekeeper). Afterwards, I converted the ΔCT values to relative expression using the formula: Relative expression = $2^{-\Delta CT}$.

For the correlation analysis I aimed to measure the amount of linear association/the strength of relationship between two variables, from triplicate qPCR data of 6 paired patient samples. I determined the R squared value (R^2), the square of the Pearson correlation coefficient, which stands for the coefficient of determination. The lowest possible value of R^2, is 0 and the highest possible value is 1. If it is equal to 1, all of the data points fit perfectly on the regression line, indicating a low extent of variation and a high correlation between the investigated values. The linear regression line was inserted as well as the calculation of R squared performed using GraphPad Prism software (v8).

5.5.4. Flow cytometric analysis

Flow cytometry is a technique used to analyze characteristics of a population of cells simultaneously. The cells are suspended in a fluid and injected into the flow cytometer, where they pass as single cells in a continuous suspension stream a laser beam. Detection of the forward scatter of the light (FSC) indicates the cell size, with larger cells having a stronger forward scatter signal and depending on the granularity of the cell, the angle of the scattered light changes (side scattered light (SSC)). Gating is

used to select for specific cells or a subpopulation to analyze it in more detail or to disclose it from further analysis. In addition to this, cells can be labeled with fluorescence-tagged antibodies or carry an integrated fluorescent protein. These fluorescence-labeled cells emit fluorescent light when excited by the respective laser. The fluorescent dyes are excited and emitted at a specific wavelength. If the peak emission wavelengths are far enough apart from each other, so that each signal can be detected by a separated detector, multiple antibodies can be used in the same sample to discriminate subpopulations or to investigate potential overlap between two markers. The fluorescent pattern of each subpopulation can be used to investigate relative percentages. To check if spillover from one channel into the other channel takes place single labels for each specific dye were performed. To avoid detection of unspecific binding, isotype controls were included.

For antibody labeling, I dissociated 2.5 $x10^5$ - $5x10^5$ with trypsin into a single cell suspension, provided them with 10% FBS to stop trypsinization and centrifuged at 400 rcf for 5 min after which the supernatant was discarded. The pellet was resuspended in FACS buffer (2 mM EDTA, 0.1 % BSA in 1x PBS), and incubated with human Fc Block (1:100; BD Biosciences) for 15 min at RT to reduce unspecific antibody-binding. In order to fix and permeabilize the cells for intracellular antibody staining the BD Cytofix/Cytoperm Fixation/Permeabilization Kit was used (BD Biosciences) according to the manufacturer instructions. All washing steps were conducted at 4 °C and 400 rcf for 5 min using wash buffer included in the kit. Cells were stained for KDM5B, ALDH1A1 and pAKT using the following antibodies: ALDH1A1 (FITC, Abcam (1:5)) and ALDH1A1 (unconjugated, rabbit, Abcam (1:100)); p-AKT (Ser473) (Alexa488, BD Biosciences (1:2.5)) and p-AKT (Ser473) (PE, BD Biosciences (1:2.5)); KDM5B (unconjugated, rabbit, Novus (1:25)). The unconjugated antibodies against ALDH1A1 and KDM5B were combined with an Alexa-Fluor 555 coupled secondary antibody (goat anti-rabbit IgG, Life Technologies #A21428 (1:200)). Incubation of antibodies was performed for 30 min on ice. Prior to the FACS analysis, cells were washed twice and resuspended in FACS buffer.

For the analysis of apoptosis, cell suspensions were assayed for active Caspase-3. Caspase 3 is part of the cysteine-aspartic acid protease family and exists as an inactive proenzyme and in its active (proteolytically cleaved) state. It can activate further caspases initiating apoptosis. Active Caspase-3 levels revealing early apoptotic events were analyzed using flow-cytometry via a FITC-conjugated active Caspase 3

antibody (BD Bioscience). Cells were prepared as described above before being incubated with the active Caspase-3 (FITC, BD Bioscience #559341 (1:5)) via incubation with the antibody for 30 min on ice. Prior to analysis, cells were washed and resuspended in FACS buffer.

To asses proliferation, CellTracer dyes can be added to the cells, which are diluted which each cell division, leading to decreased fluorescent intensity in cycling cells, whereas less or non-cycling cells show a higher fluorescent intensity. For proliferation analysis CellTrace™ Far Red (Thermo Fischer) was added onto adherently growing cells carrying the KDM5Bpromoter-EGFP-reporter construct. The CellTrace™ Far Red DMSO stock was diluted in pre-warmed PBS to a concentration of 5 µM. The cells were washed twice with PBS, before they were incubated with the CellTrace™ Far Red suspension for 30 min at RT on a shaker. Afterwards the suspension was washed away twice with culture medium before pre-warmed culture medium was added. After incubation of the cells at 37°C and 5 % CO_2 for 1h TMZ was added to a final concentration of 500 µM. The readout via flow cytometry was taken on a flow cytometer 5 days later.

The 7-AAD Viability Staining Solution (eBioscience) (Thermo Fischer) was applied to trypsinized KDM5Bpromoter-EGFP-reporter construct-carrying cells after they were exposed to DMSO (0.05%) or TMZ (500 µM). 7-Aminoactinomycin D (7-AAD) is excluded from viable cells, but can penetrate cell membranes of non-viable cells. The cells were trypsinized, pelleted and resuspended in PBS before 0.25 µg 7-AAD Staining Solution were added per $1x10^6$ cells 10 minutes prior to flow cytometric analysis.

All samples were assayed on a FACSCelesta™ flow cytometer (BD Biosciences) using a FACSDiva™ software version v8.0.1.1 (BD Biosciences). The data analysis was performed using the FlowJo software version v10.5.3 (BD Biosciences). The percental increase of an antibody-labeled marker (e.g. ALDH1A1, pAKT) was calculated by normalization of its mean fluorescence intensity to the corresponding isotype controls using the formula (MFI(marker)-MFI(Isotype))/MFI(Isotype) multiplied by 100. In the case of siRNA treated samples, a similar calculation was used (MFI(siRNA)-MFI(siNT))/MFI(siNT) multiplied by 100. The mean fold change of MFIs was calculated by mean MFI(relapse)/mean MFI(naive) or mean MFI(siRNA)/mean MFI(siNT). The gating strategy for double-positive cell

determination in experiments with two labeled markers (e.g. ALDH1A1+/pAKT+), included gating of the control sample (DMSO) to 5 % double positive cells and projecting this gate on each treated sample. The gating strategy for the detection of KDM5B^{high} cells, was to take the 5% highest fluorescence intensity (of the KDM5B-promoter-EGFP-reporter or antibody-based) in the respective control sample (naive cells or DMSO) as a threshold. This control gate was projected onto each treated sample to determine the frequency of cells reaching the set threshold. These cells were defined as KDM5B^{high} subpopulation.

5.5.5. Protein expression studies

Western blotting was use to analyze protein expression after siRNA-mediated knockdown. The adherent cells were washed once with ice cold PBS before the lysis buffer Pierce™ RIPA Buffer (Life Technologies) supplemented with cOmplete™ Protease Inhibitor Cocktail (Roche) and PhosSTOP™ (Sigma-Aldrich) was added onto the dish. The cells were collected with a cell scraper and centrifuged at 4°C and 12000 x g for ten minutes. After transferring the clear supernatant to new Protein LoBind Eppendorf tubes, the Thermo Scientific Pierce Bicinchoninic Acid (BCA) Protein Assay (Thermo Fischer) is performed according to the standard protocol (Thermo Fisher) to determine the protein concentration using a Tecan Infinite F200 instrument. Subsequently, 5x Laemmli with 10 % ß-Mercaptoethanol is added to each of the samples. The samples are vortexed, before they are heated at 95°C for 5min and stored at -20°C for further use. The protein was separated by SDS-PAGE on 4–15% Mini-PROTEAN® TGXTM Precast Protein Gels (BioRad) and afterwards transferred onto a nitrocellulose membrane (Trans-Blot® Turbo™ Mini Nitrocellulose Transfer Packs; Biorad) by electroblotting on a Trans Blot Turbo Transfer System (Biorad). The membranes were blocked in 5 % milk powder (Carl Roth) dissolved in PBS (Thermo Fischer) with 0.05 % TWEEN®-20 (Sigma-Aldrich) (PBST) for 1 hour. After blocking the membranes were separately incubated with the following primary antibodies: KDM5B (1:250 Sigma-Aldrich); PTEN XP® (1:1000, Cell signaling); phospho-AKT (Ser473) XP® (1:2000, Cell signaling); phospho-GSK-3ß (Ser9) (1:1000, Cell signaling); phospho-mTOR (Ser2448) XP® (1:1000, Cell signaling) and Cyclin D3 (1:1000, Cell signaling) overnight at 4°C in 5 % milk in PBST. A β-actin antibody (1:5000, Sigma-Aldrich) was used as a loading control and was applied for 1 hour at room temperature. After three 10 min washing steps in PBST, the horseradish peroxidase (HRP)-coupled secondary antibodies (Anti-rabbit IgG, HRP-linked.

(1:2000, Cell signaling); Anti-mouse IgG, HRP-linked (1:2000, Cell signaling)) were incubated in 5 % milk in PBST at RT for 1 h, before they could be detected via ClarityTM Western ECL Substrate (Biorad) and a ChemiDoc System (Biorad). If needed, stripping was performed for 45 min at 42°C on a shaker with a stripping buffer containing 0.05 M Tris-HCL, 2 % SDS and 0.1 M ß-Mercaptoethanol. Then blocking in 5 % milk powder and the incubation with additional antibodes was performed as described above. The intensity of bands was quantified using Image Lab^{TM} software version 6.0.1 (Biorad). The obtained values were first normalized to the ß-actin loading control, before siRNA-mediated knockdown samples were visualized as percentage of the corresponding siNT control samples.

5.5.6. Limiting dilution analysis

In order to analyze the clonogenic potential of cells, a limiting dilution analysis was performed. ALDH1A1 overexpression cells and the corresponding GFP-control cells as well as shALDH1A1 cells and the corresponding shNT control cells were seeded with a density of 0.5 cells per well into five 96-well plates with a total volume of 150 µL per well. Distribution of single cells/well was confirmed 24 h after plating using the NyOne, to distinguish if evolving colonies had a mono- or polyclonal origin. Only wells with single cells were further evaluated. Colony formation was photodocumented via the Nyone on day 16 of the assay. The amount of monoclonal colonies and the number of cells per monoclonal colony was determined. Based on the assumption of exponential growth, the number of completed cell divisions during the expansion period was calculated. Using this number and the assay duration, the approximate doubling time of the cells was estimated.

5.5.7. Neurosphere assay

To analyze stem-cell characteristics, a neurosphere assay was applied. $0.5x10^4$ cells/cm^2 harboring an ALDH1A1 knockdown (and the respective GFP-control) or ALDH1A1 overexpression (and the respective shNT control), were taken into equal parts of 2x DF and Methylcellulose (Sigma-Aldrich), substituted with 10 ng/mL EGF/bFGF and seeded into non-coated ultra-low adhesion flat bottom plates. 10 ng/mL EGF/bFGF was added every other day. The 1º generation of neurospheres was cultured for 12 days, photo-documented using an automated cell imager (Nyone) and counted. In order to transfer the neurospheres into the 2º generation PBS was added

and the suspension was centrifuged for 10 min at 400 rcf. After discarding the supernatant, the pellet was resuspended in 3 mL Trypsin and incubated for 10 min at 37 °C. Trypsinization was stopped by addition of 10% FBS before the neurospheres were dissociated using a pipette. The cells were counted and $0.5x10^4$ cells per cm^2 were spinned down and seeded into equal parts of 2x DF and Methylcellulose as described for the first generation. Secondary neurospheres were documented and counted using Nyone 12 days later. The fold change from the 1º to the 2º generation of neurospheres illustrates the cells self-renewal capacity. To investigate the generation of neuronal and glial phenotypes, a fraction of 2º neurospheres were transferred into PO pre-coated cell culture dishes and FC+L cell culture medium was provided. The neurospheres were photo-documented via a Zeiss inverted microscope after 3 h and 24 h of growth. Individual plated neurospheres were allowed to grow and differentiate without 10 ng/mL EGF/bFGF for 2 weeks before the plates were washed with PBS and fixed using 4 % paraformaldehyde (ROTI®Histofix; Carl Roth) for 10 min at RT. After three washing steps of 10 min the cells were covered in blocking buffer, consisting of 10 % FBS, 2 % normal goat serum (NGS) and 0.1 % Triton-X in PBS. Subsequently the cells were washed again in PBS for 10 min and incubated with the primary antibodies diluted in buffer against glial fibrillary acidic protein (GFAP) to label glial cells and β3-tubulin to label neuronal cells at 4°C overnight. The next day, three 10 min washing steps using PBS were completed, before secondary Alexa-Fluor linked antibodies were added to the cells in antibody-buffer and incubated for 1.5 hours at RT in the dark. After additional washing steps in PBS, nuclei staining was performed using DAPI contained in Aqueous Fluoroshield mounting medium (Abcam). Fluorescent images were taken using a Zeiss inverted microscope.

For siRNA-mediated knockdown in the neurosphere-assay, cells were plated 5 days prior the seeding of neurospheres in ABX-free medium. The next day cells were transfected with a small interfering RNA (siRNA) pool targeting ALDH1A1 (Dharmacon) or a non-targeting (siNT) control pool (Dharmacon) for 4 days. Lipofectamine was used as a control. An additional siRNA knockdown was performed by addition of siALDH1A1 or siNT pools to the 1º generation of neurospheres upon seeding into the media.

5.6. DNA Barcoding

One million individual patient cells from the cases ^{naive}BN46 and ^{naive}BN118 were DNA-barcoded with the Clontracer System (Bhang et al. Nat Med. 2015) via lentiviral infection. The ClonTracer library (Addgene #67267) consists of semi-random 30 basepair (bp) long DNA barcodes with 15 repeats of alternating weak (G or C) and strong bases (A or T) and a flanking primer pair for PCR-based amplification of the barcodes. It was cloned into the lentiviral vector backbone pRSI9-U6-(sh)-UbiC-TagRFP-2A-Puro (Cellecta), containing a puromycin resistance cassette and RFP as a fluorescent marker. For the ClonTracer library, a 3-plasmid system is used, consisting of the packaging plasmid delta8.2, containing Gag, Pol and Rev genes, the envelope plasmid VSV-G, which encodes the Env gene and the transfer plasmid. The functions of Gag, Pol, Rev and VSV-G are described in Methods chapter “5.3 KDM5B-promoter-EGFP-reporter construct cells”. The transfer plasmid contains the ClonTracer construct, the viral long terminal repeats (LTRs), the Rev Response Element and the psi packaging signal. The 30 bp barcodes has been cloned into the lentiviral backbone pRSI9-U6-(sh)-UbiC- TagRFP-2A-Puro (Cellecta) at the ClaI-XhoI site. Moreover, the transfer plasmid encodes for RFP in order to detect infected and therefore barcoded cells via flow cytometry analysis and the puromycin resistance gene for the selection of successfully barcoded cells.

5.6.1. Chemical Transformation of competent cells

The plasmids were amplified by Chemical Transformation of competent cells, similar as described for the KDM5B-promoter-EGFP-reporter construct. Stable 3 cells for the packaging as well as the envelope plasmid and DH10b for the ClonTracer plasmid were thawn on wet ice and gently mixed before 20 uL were aliquoted into chilled tubes. 1-10 ng plasmid was added to the cells and incubated on ice for 30 min. The mixture was heat-shocked for 30 seconds in a 42°C water bath and placed on ice for 3 minutes afterwards. 0,2 mL of room temperature S.O.C. medium was added and the solution was shaked at 225 rpm and 37°C for 1 h. For the packaging as well as the envelope plasmid 450 µL of the mixture was added to ampicillin plates and incubated overnight at 37°C, before colonies were picked and incubated in 150 mL LB media with ampicillin (1/1000) overnight at 37°C. For the ClonTracer plasmid the mixture was not incubated on Ampicillin plate, but directly added to LB media containing 100 µg/mL ampicillin and incubated overnight at 37°C on a shaker, before a Maxiprep was performed following

the manufacturer's instructions Plasmids were eluted in water and stored at -20°C for further use.

5.6.2. Virus production in HEK293T cells

A lenti-viral pool was produced by transfection via a 3-plasmid system into HEK293T cells. The transfection was performed, as described for the KDM5B-promoter-EGFP-reporter (see Methods chapter "5.3.2. Lenti-virus production") in HEK293T cells using the TransIT-TKO® transfection reagent Mirus (Mirus Bio), Opti-MEMTM Reduced Serum Medium (Thermo Fisher Scientific) and the following plasmids: 2.4µg ClonTracer Barcoding Library (containing barcodes, RFP and puromycin resistance cassette, Addgene #67267), 2.4µg pCMV delta R8.2 (Addgene #12263), 1.2µg pCMV-VSV-G (Addgene #8454). After 48 hours the virus was collected from the media, filtered using 0.45 µm filters (Sigma-Aldrich) and stored at -80°C for infection of patient cells.

5.6.3. Transduction and Selection of glioblastoma patient cells

For the transduction of glioblastoma cells, $10*10^6$ cells were seeded in a 15 cm cell culture dish one day before the virus is added dropwise into the media. 48 hours after the transduction, the percentage of RFP+ cells was determined using flow cytometry, revealing successfully barcoded cells. Therefore, the cells were washed with PBS, trypsinized and pelleted at 400 rcf for 5 min. The supernatant was removed and the pellet was resuspended in PBS containing the dye 4,6-diamidin-2-phenylindoldihydrochlorid (DAPI) (5 µg/mL). The uptake of DAPI enables the separation and exclusion of dead cells in flow cytometry. To ensure that each cell is marked by just a single barcode and to avoid the same barcode being integrated into several different cells, a low transduction efficiency is anticipated. To achieve the transduction efficiency of 10-30%, (RFP-based flow cytometry), different virus concentrations were tested during the DNA barcoding technology establishment. Selection of barcoded cells was performed using puromycin (Thermo Fisher Scientific). Different puromycin concentrations between 0,5 µg/mL and 3 µg/mL were tested. The chosen concentration was 4 µg/mL every other day for 4-8 days. Afterwards, the media was changed to one without Puromycin and successful selection of 95% to 100 % RFP positive cells was validated by flow cytometry.

5.6.4. Treatment and sample collection of barcoded patient cells

From this Prepool the cells were expanded *in vitro* to generate n=8 replicates (Naive). The cells were exposed to DMSO (0.5%) as a control (^{DMSO}CTRL) or treated with TMZ (500 µM, Sigma-Aldrich), for 16 days every other day. The DTP samples were harvested after 16 days TMZ-on phase. The other replicates were kept in culture until clonal expansion of $^{TMZ→eR}$cells (DTEPs). Representative samples were derived from each time point. For harvesting the adherent cells were washed with PBS, trypsinized and pelleted. The supernatant was removed and the pellet was frozen at -80°C. To assess barcode presentation the DNA of all harvested samples was extracted using Gentra Puregene Precipitation Kit (Quiagen) following the manufactures instructions. The pellet was dissolved in nuclease free water by incubation at 65°C for 1 h followed by incubation at RT overnight with gentle shaking. DNA amount was measured using TECAN reader and the amount of PCR reactions needed the transcribed the whole samples was calculated, due to the limits of 2 µg DNA and 25 µl total volume per reaction.

5.6.5. Sample preparation and sequencing of barcoded patient cells

In order to enrich the barcode region and to add unique indices for the later sequencing, PCR reactions were performed using the KAPA HiFi HotStart ReadyMix (Roche) with the same forward primer and different reverse index primer in each sample (Table “6.7. Primers Barcoding” and “6.8. Indices of Barcoding Primers”). Adding of unique indices to each sample (TruSeq Small RNA Indices A - Sequences 1–12; TruSeq Small RNA Libary Prep Reference Guide), enabled multiplexing and sequencing of all samples as a pooled library. The PCR-amplified products were purified using an 2 % Agarose gel with TAE buffer. A 100 bp DNA ladder (Fermentas or Cleaver) and a DNA Loading Dye 6x (Thermo Fischer Scientific) were used. The products of 173 bp length, shown in Supplementary Figure 16 were cut out under UV light in an Imaging System ChemiDoc Touch (Biorad). Gelextraction was performed using QIAquick Gel Extraction Kit (Qiagen) as instructed by the manufacturer. Elution of DNA was achieved in water prewarmed to 50°C before the DNA was measured in a TECAN reader and the amount of each sample needed for a 10-14 nM pooled multiplex was calculated.

For the sorting experiment, a barcoded sample at the treatment-naive timepoint was sorted for KDM5B^{high} cells using fluorescence-activated cell sorting (FACS). FACS

provides the possibility to sort single cells out of a heterogeneous mixture of cells, into separated collection tubes for further analysis. The stream of cells is separated into individual droplets, in a way that ideally not more than one cell is distributed into one droplet. For this procedure the cells were stained using a KDM5B antibody KDM5B (rabbit Novus (1:25)) and a secondary antibody (Alexa-Fluor 555 coupled, goat anti-rabbit IgG, Life Technologies (1:200)), as described in Methods chapter "5.5.4. Flow cytometric analysis", so that the cells can be sorted, based on the fluorescent characteristics chosen (top 5 % highest fluorescent intensity = $KDM5B^{high}$ cells). From the sorted $KDM5B^{high}$ sample, DNA isolation, PCR amplification of the barcode region, purification and gelextraction was performed as described above.

All samples were pooled and send for sequencing on a Illumina HiSeq 2000 v4 single-read 50bp platform or a NextSeq 550 Single-read 75bp using the Multiplex Index Type Illumina TruSeq. A custom primer to sequence the product (Table "6.7. Primers Barcoding") and Illumina Primers for sequencing the Index sequence of the pooled samples were needed. Biorinformatic analyses was performed as described in Ullrich et al., in revision:

> *"The Illumina bcl2fastq 2.20.0.422 Conversion Software was used to demultiplex sequencing data and convert base call (BCL) files into FASTQ files. Quality control of the sequencing data was performed using the FastQC Reports. The barcode representation for each sample (reads per barcode per sample) was extracted from the FASTQ files from the barcode-sequencing runs, using a custom-written Python script (version 3.9.9) according to the Clontracer System (Bhang et al. Nat Med. 2015). Only the 30N barcodes, which consisted of alternating weak and strong base pairs and were flanked by a specific sequence, were further analyzed. Barcode reads were normalized by dividing reads per barcode by total read count of the sample."*

The relative abundance of the barcodes above (or equal to) a threshold of 1% in at least one sample, were depicted using Bubble plots, that were generated in R (version 4.1.2) by using the ggplot2 package (version 3.3.6). The stacked plots, showing thenTOP50 barcodes of each sample, stacked to 100%, were generated using R (software version 4.2.2).

5.7. Chromatin Immunoprecipitation Sequencing (CHIP-Seq)

To localize and quantify the binding of proteins as for example histone demethylases onto the DNA, Chromatin Immunoprecipitation Sequencing (CHIP-Seq) can be performed. For this purpose, a cross-linking of histone and non-histone proteins to the DNA is implemented. The cross-linked chromatin is fragmented using a nuclease featuring endonuclease activity (micrococcal nuclease) and sonication, before the actual immunoprecipitation (IP) is carried out. The used antibodies, to which magnetic beads are coupled, enable to isolate the protein of interest and co-precipitate the chromatin fragments bound to it. After isolation, the chromatin-protein cross-link is resolved and the DNA is purified. The purified DNA can then be analyzed using qPCR for a previously suspected specific region or via next generation sequencing (NGS) for a broad overview of binding regions. In this thesis the binding of a histone demethylase to specific genomic regions was not detected directly using a KDM5B antibody, but rather indirectly via the analysis of the amount of the histone modification H3K4trimethylation, that is removed by KDM5B.

For the CHIP-Seq using a H3K4me3 antibody the SimpleChIP® Enzymatic Chromatin IP Kit (Magnetic Beads) (Cell signaling) was used according to the manufacturer's instructions. Cells were seeded into a 15cm dish 24 hours prior to a siRNA-mediated KDM5B knockdown. The knockdown was implemented using the SMARTpool: ON-TARGETplus KDM5B siRNA pool and the corresponding ON-TARGETplus Non-targeting Pool control (Horizon Discovery) as described in Methods chapter "5.4.2. Knockdown studies" and validated via qPCR. 37 % formaldehyde was given directly into the media in order to crosslink the cells after 6 days. Then, 10x glycine was added for 5 min at RT prior to media removal and washing with ice-cold PBS. Afterwards, cells could be scraped into ice-cold PBS, that contained a protease inhibitor cocktail. Chromatin was digested and nuclei preparation was done using a Micrococcal Nuclease, included in the SimpleChIP® Enzymatic Chromatin IP Kit (Magnetic Beads) kit and sonication with an Utrasonic Homogenizer mini 20 (Bandelin). Before the final experiment could be performed, the optimal amount of nuclease as well as the optimum sonication duration were determined empirically. The condition of the nuclei was examined under a microscope and the fragment sizes (aimed fragment size: 150-900 bp) were validated via Agarose gelelectrophoresis. The amount of the Micrococcal Nuclease finally used was 2.5 µl and the most successful sonication was approximately 3 times 20 seconds. After DNA purification the chromatin

immunoprecipitation could be performed using the Anti-Histone H3 (tri methyl K4) antibody - ChIP Grade (Abcam) and magnetic beads, which were included in the SimpleChIP® Enzymatic Chromatin IP Kit. For each sample a 2 % Input sample was preserved as a background signal control in the later sequencing. Besides the antibody against the methylation of interest a positive control (Histone H3 (D2B12) XP® Rabbit mAb) and a negative control (Normal Rabbit IgG) were included. The chromatin was eluted from the magnetic beads, the cross-links were reversed using a Proteinase and the DNA was purified again following the manufactures instructions. The successful CHIP was validated through the positive and negative antibody control samples in a qPCR with primers for the ribosomal housekeeper gene RPL30 (included in the SimpleChIP® Enzymatic Chromatin IP Kit). As described in Ullrich et al., in revision:

> *"EMBL Genomics Core Facilities 30 (Heidelberg, Germany) prepared the barcoded ChIP-Seq libraries for all samples along with their corresponding inputs. Also, the deep uni-directional sequencing of prepared barcoded ChIP-Seq libraries with a read-length of 85 bases was performed on an Illumina NextSeq200 in a P3-50se run. Samples were prepared with a NEB Ultra II DNA library prep kit and the fragment size of final libraries was ~250bp including adapters. TruSeq adapters were used. 35 Overall bioinformatic analysis of sequencing was performed by Diagenode Epigenomic Services (Seraing, Belgium). This included trimming of the adaptors with cutadapt, followed by a quality control of the trimmed reads using FastQC. Trimmed reads were aligned to the reference genome (hg38) using BWA software v.0.7.17. Samples were filtered for regions blacklisted by the ENCODE project. PCR duplicates and multimapping reads were removed 40 using samtools. Alignment coordinates were converted to BED format using BEDTools v.2.17 and peak calling was performed using epic2 with optimized parameters for H3K4me3 and KDM5B."*

The signal intensities/peaks of H3K4me3 at the specific gene loci of the PI3K pathway were visualized using the Integrative Genomic Viewer (IGV) Software (Version 2.11).

5.8. Statistical analysis

Unless otherwise specified, data are presented as mean ± SD. For each set of data the used statistical methods are described in the figure legends. The significance threshold was set to 0.05.

The R software (The R Foundation for Statistical Computing, v4.1.3) and GraphPad Prism software (v8) were used for data analysis and visualization.

6. Material

6.1. Commercially available cells

LN229 = human glioblastoma cells (female; 60 year old; surgically extracted 1979)

HEK293T = human embryonic kidney cells (epithelial-like)

Competent E. coli cells: Stable 3 and DH10b

6.2. Devices

Table 2: Devices

Appliance	**Manufacturer**
Agarose gel power supply Consort EV2310	Cleaver Scientific (Rugby, Warwickshire, United Kingdom)
Bench steril Maxisafe 2020	Thermo Fischer Scientific (Waltham, USA)
Centrifuge (5804R, 5424R,5702R, 5430)	Eppendorf (Hamburg, Germany)
CFX96 Touch real-time cycler	BioRad (Hercules, USA)
ChemiDoc System	BioRad (Hercules, USA)
Eppendorf ThermoMixer®	Eppendorf (Hamburg, Germany)
FACS Celesta flow cytometer	BD Biosciences (Franklin Lakes, USA)
FACS Aria III cell sorter	BD Biosciences (Franklin Lakes, USA)
Freezer (-20 °C)	Liebherr Medline (Ochsenhausen, Germany)
Freezer (-80 °C)	BioRad (Hercules, USA)
Freezer (-150 °C)	Panasonic (Kadoma, Osaka, Japan)
Fridge (4 °C)	Liebherr Medline (Ochsenhausen, Germany)
Imaging System ChemiDoc Touch	BioRad (Hercules, USA)
Incubator Heracell 150i	Thermo Fischer Scientific (Waltham, USA)
Mastercycler® nexus X2	Eppendorf (Hamburg, Germany)
Microscope Axio Vert.A1	Zeiss (Oberkochen, Germany)
Microwave	Sharp (Montvale, New Jersey, USA)
NyOne®	Synentec (Elmshorn, Germany)
Orbital Shaker-Incubator ES-20	Grant-bio (Shepreth, Cambridgeshire, United Kingdom)
PCR Mastercycler nexus GX2	Eppendorf (Hamburg, Germany)
Qubit Fluorometer	Thermo Fischer Scientific (Waltham, USA)
Sterile bench	Thermo Fischer Scientific (Waltham, USA)

Tecan Infinite F200	Tecan (Männedorf, Switzerland)
Trans Blot Turbo Transfer System	BioRad (Hercules, USA)
Utrasonic Homogenizer mini 20	Bandelin (Berlin, Germany)
Vortex Genie 2	Carl Roth (Karlsruhe, Germany)
Water bath	Memmert (Schwabach, Germany)
Weighing scale Entris Sartorius	Thermo Fischer Scientific (Waltham, USA)

6.3. Consumables

Table 3: Consumables

Product	**Manufacturer**
Cell Scraper TPE-blade 20 mm	Avantor (Radnor, USA)
Costar 6-/12-/24-/96-well plate	Corning (Corning, NY, USA)
Cover Glasses 20 x 20 mm	Marienfeld (Lauda-Königshofen, Germany)
Dishes, TC treated (6 cm, 10cm, 15cm)	Corning (Corning, NY, USA), Greiner (Kremsmünster, Austria), Thermo Scientific (Waltham, USA)
DNA LoBind Tubes (0.5mL, 1mL, 1.5mL)	Eppendorf (Hamburg, Germany)
Falcon 5 ml round bottom polystyrene test tube, with cell strainer snap cap	Corning (Corning, NY, USA)
Filters 0.45 µm Minisart Sartorius Stedim biotech	Sigma-Aldrich (St. Louis, USA)
Flat bottom, ultra-low attachment surface plates	Corning (Corning, NY, USA)
Glass Pasteur pipettes	Thermo Scientific (Waltham, USA)
Neubauer Counting Chamber	Marienfeld (Lauda-Königshofen, Germany)
Pipette tips	Greiner (Kremsmünster, Austria)
Protein LoBind Tubes	Eppendorf (Hamburg, Germany)
qPCR 96-well plates	Sarstedt (Nümbrecht, Germany)
Reaction tubes (500 µL, 1.5 mL, 2 mL)	Eppendorf (Hamburg, Germany)
Serological pipettes	Sarstedt (Nümbrecht, Germany), Greiner (Kremsmünster, Austria)
Trans-Blot® TurboTM Mini Nitrocellulose Transfer Packs	BioRad (Hercules, USA)
4–15% Mini-PROTEAN® TGXTM Precast Protein Gels	BioRad (Hercules, USA)
6 cm cell culture dishes (TC-treated)	Eppendorf (Hamburg, Germany)
6-Well / 12-Well / 24-Well / 96-Well TC-treated, Multiple Well Plates	Corning (Corning, NY, USA)
15 mL/50 mL Falcon tubes	Corning (Corning, USA)

6.4. Buffers and chemicals

Table 4: Buffers and chemicals

Product	Manufacturer
Agarose	Carl Roth (Karlsruhe, Germany)
AlamarBlue™ Cell Viability Reagent	Thermo Fischer Scientific (Waltham, USA)
Ampicillin	Carl Roth (Karlsruhe, Germany)
Antibiotic-Antimycotic agent (ABX)	Life-Technologies (Darmstadt, Germany)
Antibody buffer immunhistochemistry	
10 % FBS	GE Healthcare Lifesciences (Chicago, USA)
0.1 % Triton-X	Sigma-Aldrich (St. Louis, USA)
DPBS	Thermo Fischer Scientific (Waltham, USA)
Aqueous Fluoroshield mounting medium with DAPI	Abcam (Cambride, UK)
B-27™ Supplement (50X), serum free	Thermo Fischer Scientific (Waltham, USA)
Basic fibroblast growth factor (bFGF)	R&D Systems (Wiesbaden, Germany)
Blasticidin	Invivogen (San Diego, California, USA)
Blocking buffer	
10 % FBS	GE Healthcare Lifesciences (Chicago, USA)
0.1 % Triton-X	Sigma-Aldrich (St. Louis, USA)
2 % Normal Goat Serum	Sigma-Aldrich (St. Louis, USA)
DPBS	Thermo Fischer Scientific (Waltham, USA)
CellTrace™ Far Red	Thermo Fischer Scientific (Waltham, USA)
Characterized Fetal Bovine Serum, US Origin	Thermo Fischer Scientific (Waltham, USA)
ClarityTM Western ECL Substrate	BioRad (Hercules, USA)
CPI-455	Selleckchem (Munich, Germany)
dNTPs: dATP, dCTP, dGTP, dTTP (100 mM)	Genecraft (Manchester, UK)
DAPI	Thermo Fischer Scientific (Waltham, USA)
2xDF	
47.5 mL DMEM/F-12	Thermo Fischer Scientific (Waltham, USA)
1 mL B27	Thermo Fischer Scientific (Waltham, USA)

0.5 mL N2 supplement	Thermo Fischer Scientific (Waltham, USA)
1 mL ABX	Life-Technologies (Darmstadt, Germany)
Dimethyl sulfoxide (DMSO)	Sigma-Aldrich (Taufenkirchen, Germany)
DNA ladder Generuler 100 bp	Fermentas (Waltham, USA)
DNA Ladder CSL-MDNA-100BP	Cleaver (Rugby, United Kingdom)
DNA Loading Dye 6x	Thermo Fischer Scientific (Waltham, USA)
Dithiothreitol (DTT)	Invitrogen (Carlsbad, CA, USA)
Dulbecco's Phopshate-Buffered Saline (DPBS)	Thermo Fischer Scientific (Waltham, USA)
Dulbecco's Modified Eagle Medium/Nutrient Mixture F-12 (DMEM/F-12)	Thermo Fischer Scientific (Waltham, USA)
Epidermal growth factor (EGF)	R&D Systems (Wiesbaden, Germany)
Ethanol	Carl Roth (Karlsruhe, Germany)
FACS Buffer	
2mM EDTA	Sigma-Aldrich (Taufenkirchen, Germany)
0.1% Bovine serum albumin fraction V (BSA)	Carl Roth (Karlsruhe, Germany)
DPBS	Thermo Fischer Scientific (Waltham, USA)
Gel red, DNA stain G	Serva (Catoosa, Oklahoma, USA)
HyClone Fetal Bovine Serum (FBS)	GE Healthcare Lifesciences (Chicago, USA)
KAPA HiFi HotStart ReadyMix	Roche (Basel, Switzerland)
Laemmli loading buffer (5x)	
0.004% Bromphenol blue	Sigma-Aldrich (St. Louis, USA)
10% beta-mercaptoethanol	Carl Roth (Karlsruhe, Germany)
20% Glycerol	Sigma-Aldrich (St. Louis, USA)
4 % Natriumdodecylsulfat (SDS)	Sigma-Aldrich (St. Louis, USA)
0.125 M Tris-Hydrochlorid (HCL)	Sigma-Aldrich (St. Louis, USA)
Laminin Mouse Protein, Natural-1 mg	Thermo Fischer Scientific (Waltham, USA)
LB-medium	Carl Roth (Karlsruhe, Germany)
L-glutamine	Thermo Fischer Scientific (Waltham, USA)
Lipofectamine™ RNAiMAX Transfection Reagent	Thermo Fischer Scientific (Waltham, USA)
LuminoCt SYBR Green qPCR Ready Mix	Sigma-Aldrich (St. Louis, USA)

Methanol	Carl Roth (Karlsruhe, Germany)
Methylcellulose (total volume = 200 mL, pH = 7.3)	
2.4 g DMEM powder	Sigma-Aldrich (St. Louis, USA)
0.48 g $NaHCO_3$	Sigma-Aldrich (St. Louis, USA)
4 g Methylcellulose	Sigma-Aldrich (St. Louis, USA)
Milk powder	Carl Roth (Karlsruhe, Germany)
MK2206-HCl	Selleckchem (Munich, Germany)
N-2 supplement	Thermo Fischer Scientific (Waltham, USA)
Neurobasal medium	Thermo Fischer Scientific (Waltham, USA)
Oligo(dT)20 Primer	Invitrogen (Carlsbad, CA, USA)
Opti-MEM™ Reduced Serum Medium	Thermo Fischer Scientific (Waltham, USA)
Page ruler™, prestained protein ladder	Thermo Fischer Scientific (Waltham, USA)
Penicillin-Streptomycin Gibco™	Thermo Fischer Scientific (Waltham, USA)
Pierce BCA Protein Assay	Thermo Fischer Scientific (Waltham, USA)
Poly-L-Ornithine Hydrobromide (PO)	Sigma-Aldrich (St. Louis, Germany)
Propidium iodide (PI)	Thermo Fischer Scientific (Waltham, USA)
Protein Lysis Buffer	
Pierce™ RIPA Buffer	Thermo Fischer Scientific (Waltham, USA)
cOmplete™ Protease Inhibitor Cocktail	Roche (Basel, Switzerland)
PhosSTOP™	Sigma-Aldrich (St. Louis, Germany)
Puromycin	Thermo Fischer Scientific (Waltham, USA)
Random Hexamer dN6 (50 µM)	Invitrogen (Carlsbad, CA, USA)
RNase A (100mg/mL) Pure Link	Invitrogen (Carlsbad, CA, USA)
ROTI®Histofix 4 %	Carl Roth (Karlsruhe, Germany)
Roti-Safe GelStain	Carl Roth (Karlsruhe, Germany)
SDS Running Buffer	BioRad (Hercules, USA)
SF167	Selleckchem (Munich, Germany)
siRNA buffer 5x	Horizon Discovery Biosciences Limited (Waterbeach, UK)
SSIV Buffer	Invitrogen (Carlsbad, CA, USA)
Stripping Buffer (total volume = 20mL)	
0.05 M Tris-Hydrochlorid (HCL) (stock 0.5 M, pH 6.8)	Sigma-Aldrich (St. Louis, USA)

2% Natriumdodecylsulfat (SDS) (stock 10%)	Sigma-Aldrich (St. Louis, USA)
0.1 M beta-mercaptoethanol (stock 14,3 M)	Carl Roth (Karlsruhe, Germany)
ddH_20	
S.O.C.-Medium	Thermo Fischer Scientific (Waltham, USA)
SuperScript™ IV Reverse Transcriptase	Invitrogen (Carlsbad, CA, USA)
50x TAE Buffer	
242 g Tris-HCL	Sigma-Aldrich (St. Louis, USA)
57.1 mL acetic assid	Carl Roth (Karlsruhe, Germany)
100 mL 0.5M EDTA	Sigma-Aldrich (St. Louis, USA)
Temozolomide	Sigma-Aldrich (St. Louis, USA)
TransIT-TKO® Transfection Reagent (Mirus)	MIRUS (Madison, WI, USA)
TRIzol	Thermo Fischer Scientific (Waltham, USA)
Trypanblue	Thermo Fischer Scientific (Waltham, USA)
Trypsin (total volume = 1 L, pH = 7.3)	
5 g trypsin	Thermo Fischer Scientific (Waltham, USA)
2 mL phenol red (0.5 %)	Sigma-Aldrich (St. Louis, USA)
20 mL ABX	Life-Technologies (Darmstadt, Germany)
(Ready-to-use) trypsin for cell culture	
1/5 Versene-buffer 5X	
2/5 TD-buffer 2X	
2/5 Trypsin	
2x TD buffer (total volume = 1 L, pH = 7.5)	
16 g sodium chloride	Sigma-Aldrich (St. Louis, USA)
0.76 g potassium chloride	Sigma-Aldrich (St. Louis, USA)
0.2 g disodium hydrogen phosphate	Sigma-Aldrich (St. Louis, USA)
6 g Sigma 7-9 (pH = 7.5)	Sigma-Aldrich (St. Louis, USA)
Tween®-20	Sigma-Aldrich (St. Louis, USA)
5x Versene buffer (total volume = 1 L, pH = 7.3-7.4)	
0.2 g EDTA	Sigma-Aldrich (St. Louis, USA)
8 g sodium chloride	Sigma-Aldrich (St. Louis, USA)
0.2 g potassium chloride	Sigma-Aldrich (St. Louis, USA)
1.19 g disodium hydrogen phosphate	Sigma-Aldrich (St. Louis, USA)

0.18 g potassium hydrogen phosphate	Sigma-Aldrich (St. Louis, USA)
7-AAD Viability Staining Solution (eBioscience)	Thermo Fischer Scientific (Waltham, USA)

6.5. Kits

Table 5: Kits

Kit	**Manufacturer**
All Prep DNA/RNA Mini Kit	Quiagen (Hilden, Germany)
BD Cytofix/Cytoperm Fixation/Permeabilization Kit	BD Biosciences (Franklin Lakes, USA)
DNeasy Blood and Tissue Kit	Quiagen (Hilden, Germany)
Gentra Puregene Precipitation Kit	Quiagen (Hilden, Germany)
Plasmid Maxi Kit	Quiagen (Hilden, Germany)
SimpleChIP® Enzymatic Chromatin IP Kit (Magnetic Beads)	Cell signaling (Danvers, MA, USA)
QIAquick Gel Extraction Kit	Quiagen (Hilden, Germany)

6.6. Primers qPCR

Table 6: Primers qPCR

Target and sequence	**Distributor**
ALDH1A1 Fw: GCACGCCAGACTTACCTGTC Rv: CCTCCTCAGTTGCAGGATTAAAG	Integrated DNA technologies (Coralville, USA)
KDM5A Fw: GTCACCTGGAGCTAAGGCAC Rv: CCGTTTCCGTTTCTTCTCTG	Integrated DNA technologies (Coralville, USA)
KDM5B Fw: AGTGGGCTCACATATCAGAGG Rv: CAAACACCTTAGGCTGTCTCC	Integrated DNA technologies (Coralville, USA)
KDM6A Fw: TACAGGCTCAGTTGTGTAACCT Rv: CTGCGGGAATTGGTAGGCTC	Integrated DNA technologies (Coralville, USA)
RPL37A Fw: GACGTACAATACCACTTCCGC Rv: GGAGCGTCTACTGGTCTTTCA	Integrated DNA technologies (Coralville, USA)

6.7. Primers Barcoding

Table 7: Primers Barcoding

Target and sequence	Distributor
PCR Primer Forward AATGATACGGCGACCACCGAGATCTACACACT GACTGCAGTCTGAGTCTGACAG	Eurofins (Luxembourg)
PCR Primer Reverse CAAGCAGAAGACGGCATACGAGAT - (index of 6 bases) - GTGACTGGAGTTCAGACGTGTGCTCTTCCGATCTCT AGCATAGAGTGCGTAGCTCTGCT	Eurofins (Luxembourg)
Custom Primer Illumina Sequencing ACACACTGACTGCAGTCTGAGTCTGACA	Eurofins (Luxembourg)

6.8. Indices of Barcoding Primers

Table 8: Indices of Barcoding Primers

Name	Sequence	Distributor
Index1	ATCACG	Eurofins (Luxembourg)
Index2	CGATGT	Eurofins (Luxembourg)
Index3	TTAGGC	Eurofins (Luxembourg)
Index4	TGACCA	Eurofins (Luxembourg)
Index5	ACAGTG	Eurofins (Luxembourg)
Index6	GCCAAT	Eurofins (Luxembourg)
Index7	CAGATC	Eurofins (Luxembourg)
Index8	ACTTGA	Eurofins (Luxembourg)
Index9	GATCAG	Eurofins (Luxembourg)
Index10	TAGCTT	Eurofins (Luxembourg)
Index11	GGCTAC	Eurofins (Luxembourg)
Index12	CTTGTA	Eurofins (Luxembourg)

6.9. Antibodies used for flow cytometry analyses

Table 9: Antibodies used for flow cytometry analyses

Antibody	Conjugation	Company	RRID	Clone	Dilution
Active Caspase-3	FITC	BD Biosciences (Franklin Lakes, USA)	AB_397234	C92-605	1:5
ALDH1A1	FITC	Abcam (Cambride, UK)	N/A Cat No. #ab275646	03	1:5

ALDH1A1	-	Abcam (Cambride, UK)	AB_867566	EP1933Y	1:100
Human Fc Block	-	BD Biosciences (Franklin Lakes, USA)	AB_2869554	Fc1.3216	1:100
KDM5B	-	Novus (St. Louis, Missouri, USA)	AB_1291176	polyclonal	1:25
p-AKT (Ser473)	Alexa Fluor 488	BD Biosciences (Franklin Lakes, USA)	AB_1645342	M89-61	1:2.5
p-AKT (Ser473)	PE	BD Biosciences (Franklin Lakes, USA)	AB_1645328	M89-61	1:2.5
Human IgG1 Isotype Control	FITC	BioLegend (San Diego, USA)	AB_2847831	QA16A12	1:25
Mouse IgG1, κ Isotype Control	PE	BioLegend (San Diego, USA)	AB_326435	MOPC- 21	1:500
Sec. antibody goat anti-rabbit IgG	Alexa Fluor 555	Life Technologies (Carlsbad, USA)	AB_2535849	polyclonal	1:200

6.10. Antibodies used for immunofluorescence

Table 10: Antibodies used for immunofluorescence

Antibody	**Conjugation**	**Company**	**RRID**	**Clone**	**Host**	**Dilution**
Glial Fibrillary Acidic Protein (GFAP)	-	Agilent Technologies /DAKO (Santa Clara, USA)	AB_10013382		rabbit	1:400
Tubulin β 3 (TUBB3)	-	BioLegend (San Diego, USA)	AB_2313773	TUJ1	mouse	1:1000

Sec. antibody anti-rabbit IgG	Alexa Fluor™ 555	Thermo Fisher Scientific (Waltham, USA)	AB_2535849		goat	1:800
Sec. antibody anti-mouse IgG	Alexa Fluor™ 488	Thermo Fisher Scientific (Waltham, USA)	AB_2534069		goat	1:800

6.11. Antibodies used for Western Blots

Table 11: Antibodies used for Western Blots

Antibody	Company	RRID	Clone	Host	Dilution
ALDH1A1	Abcam (Cambride, UK)	AB_867566	EP1933Y	rabbit	1:2000
Cyclin D3	Cell signaling (Danvers, MA, USA)		DCS22	mouse	1:1000
KDM5B	Sigma-Aldrich (St. Louis, USA)	AB_1851987		rabbit	1:250
p-AKT (Ser473) XP®	Cell signaling (Danvers, MA, USA)	AB_2315049	D9E	rabbit	1:2000
p-GSK3ß (Ser9)	Cell signaling (Danvers, MA, USA)	AB_10013750	D85E12	rabbit	1:1000
p-mTOR (Ser2448) XP®	Cell signaling (Danvers, MA, USA)	AB_10691552	D9C2	rabbit	1:1000
PTEN XP®	Cell signaling (Danvers, MA, USA)	AB_2253290	D4.3	rabbit	1:1000
ß-Actin	Sigma-Aldrich (St. Louis, USA)	AB_476744	AC-15	mouse	1:5000
Anti-mouse IgG, HRP-linked	Cell signaling (Danvers, MA, USA)	AB_330924		goat	1:2000
Anti-rabbit IgG, HRP-linked	Cell signaling (Danvers, MA, USA)	AB_2099233		goat	1:2000

6.12. Antibodies used for CHIP-Seq

Anti-Histone H3 (tri methyl K4) antibody - ChIP Grade (Abcam #ab8580; RRID:AB_306649)

6.13. siRNA pools

Table 12: siRNA Pools

Name	Distributor
ON-TARGETplus Non-targeting Pool (5 nmol)	Horizon Discovery Biosciences Limited (Waterbeach, UK)
ON-TARGETplus Human ALDH1A1 (216) siRNA – SMARTpool (5 nmol)	Horizon Discovery Biosciences Limited (Waterbeach, UK)
ON-TARGETplus KDM5B siRNA (5 nmol)	Horizon Discovery Biosciences Limited (Waterbeach, UK)

6.14. Plasmids

Table 13: Plasmids

Name	Source / Distributor
ClonTracer library	Addgene #67267
pCMV delta R8.2	Addgene #12263
pCMV-VSV-G	Addgene #8454
pLU-JARID1Bprom-EGFP-BLAST	Roesch et al., Cell 2010
pMD2.G	Addgene #12259
pMDLg/pRRE	Addgene #12251
pRSV-Rev	Addgene #12253

6.15. Software

Table 14: Software

Software	Developer
Affinity Designer v1.10.6	Serif (West Bridgford, UK)
FACS Diva software version v8.0.1.1	BD Biosciences (Franklin Lakes, USA)
FlowJo software v10.5.3	BD Biosciences (Franklin Lakes, USA)
GraphPad Prism v8	GraphPad Software Inc. (California, USA)
Image LabTM software v6.0.1	BioRad (Hercules, USA)
Python v3.9.9	Python Software Foundation (PSF)
R software v4.2.2	Posit PBC
ZEN	Zeiss (Oberkochen, Germany)

6.16. External Services

Diagenode Epigenomic Services (Seraing, Belgium)

DKFZ-Sequencing Unit (Heidelberg, Germany)

EMBL Genomics Core Facilities (Heidelberg, Germany)

7. Supplementary Figures

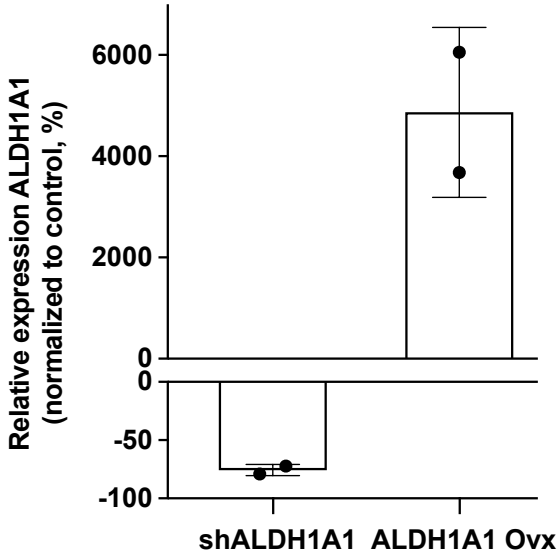

Supplementary Figure 1: "Relative ALDH1A1 expression in -knockdown (shALDH1A1) and -overexpression (Ovx) BN46 cells […]. Data shown as mean ± SD, normalized to their respective controls (ALDH1A1 Ovx to GFP Ctrl | shALDH1A1 to shNT Ctrl)." (adapted from Kebir et al., Clin Cancer Res 2023)

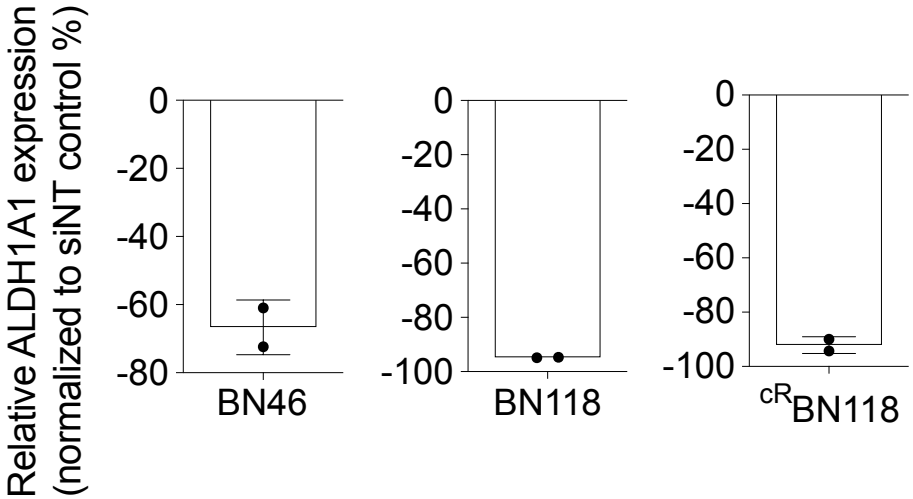

Supplementary Figure 2: "Exemplary qRT-PCR data presenting knockdown efficacy of the siRNA approach in respective cells, normalized to siNT control. Mean of duplicates ± SD." (adapted from Kebir et al., Clin Cancer Res 2023)

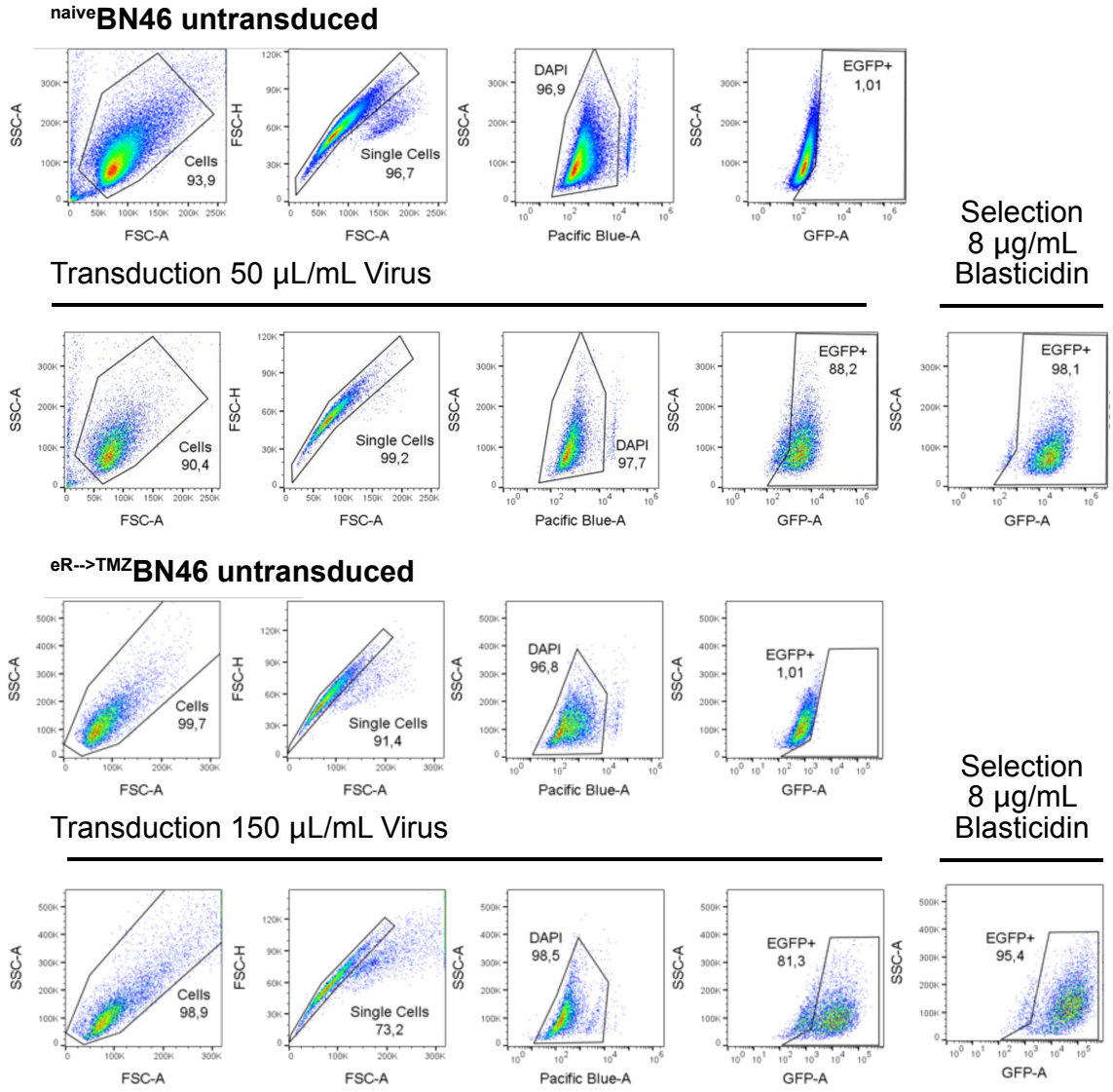

Supplementary Figure 3: Exemplary flow cytometry profiles for KDM5B-promoter-EGFP-reporter construct transduction and selection for ^{naive}BN46 and $^{TMZ \rightarrow eR}$BN46; detected via EGFP fluorescence intensity.

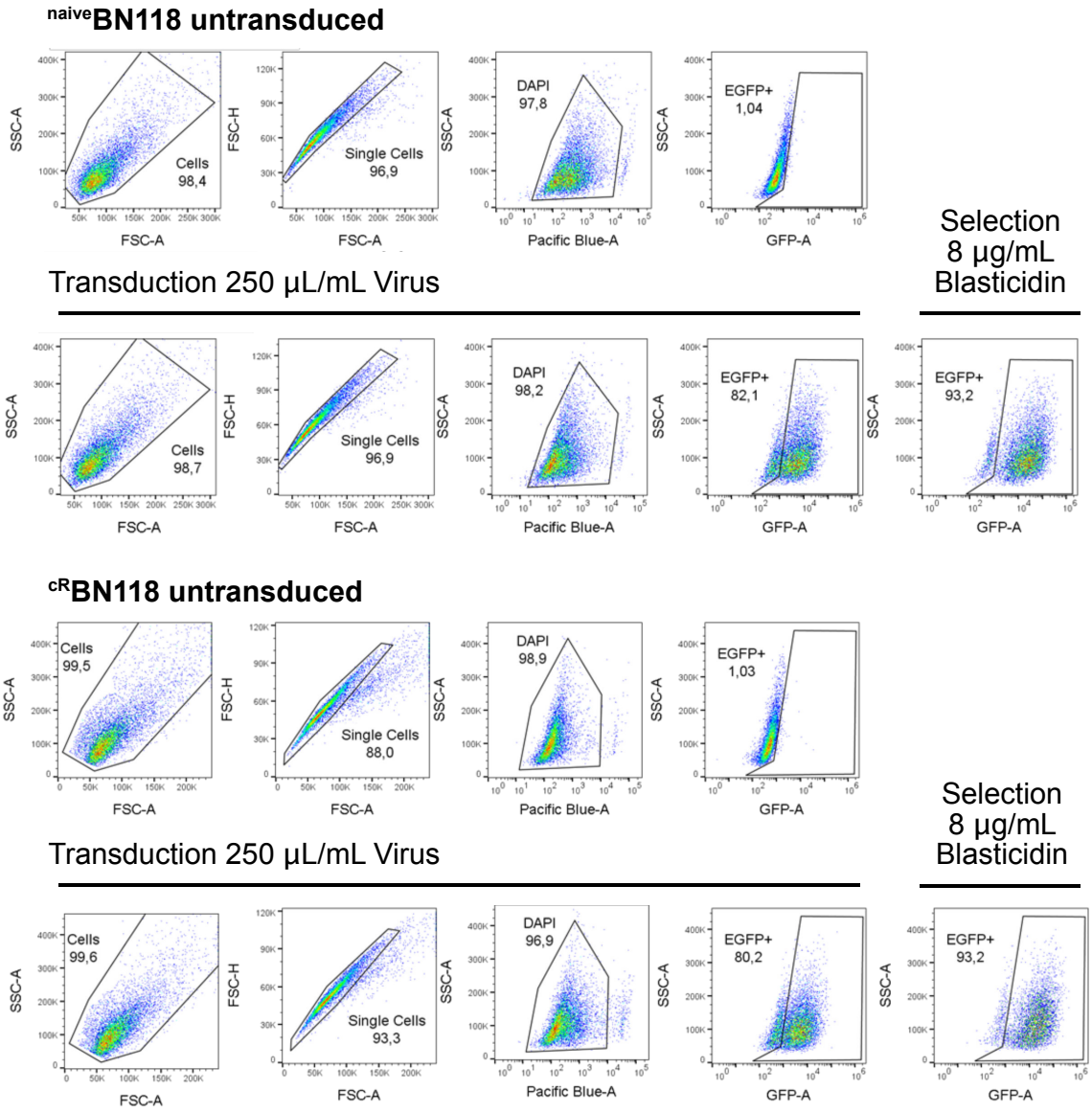

Supplementary Figure 4: Exemplary flow cytometry profiles for KDM5B-promoter-EGFP-reporter construct transduction and selection for naiveBN118 and cRBN118; detected via EGFP fluorescence intensity.

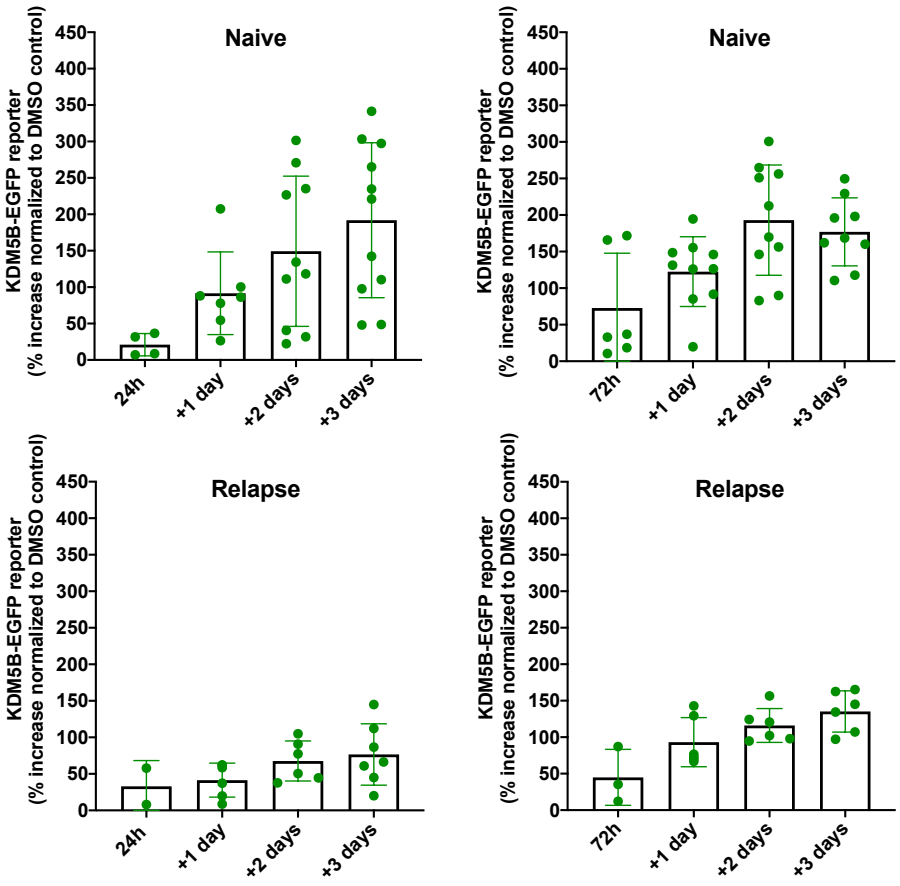

Supplementary Figure 5: Bar plots depicting the increase of KDM5B^{high} subpopulations in reporter construct-bearing naive (BN46$^{KDM5B\text{-}EGFP}$, BN118$^{KDM5B\text{-}EGFP}$, E049$^{KDM5B\text{-}EGFP}$, E056$^{KDM5B\text{-}EGFP}$) and relapse ($^{TMZ\rightarrow eR}$BN46$^{KDM5B\text{-}EGFP}$, ^{cR}BN118$^{KDM5B\text{-}EGFP}$) patient cell samples. Time points of TMZ (500µM) -on/-off schedule as indicated. Presented are more condensed (24h TMZ-on + 1/2/3 days TMZ-off) or prolonged (72h TMZ-on + 1/2/3 days TMZ-off) schedules. Values normalized to corresponding (0.5%) DMSO controls and shown as mean ± SD.

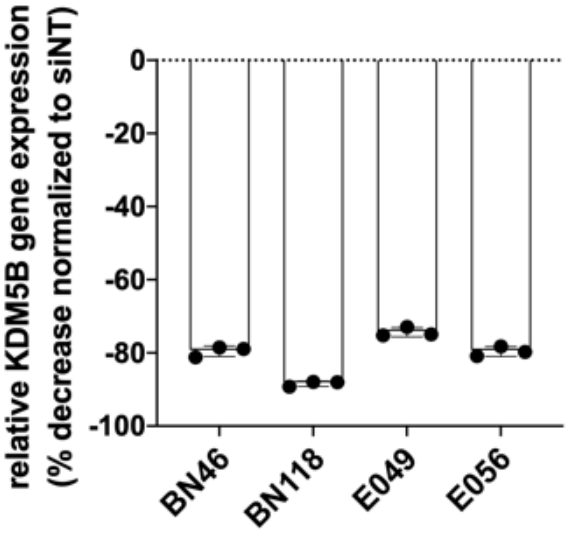

Supplementary Figure 6: "Validation of KDM5B expression subsequent to siRNA- knockdown; qPCR analysis, patient IDs indicated.", Mean of triplicates ± SD (adapted from Ullrich et al., in review 2023)

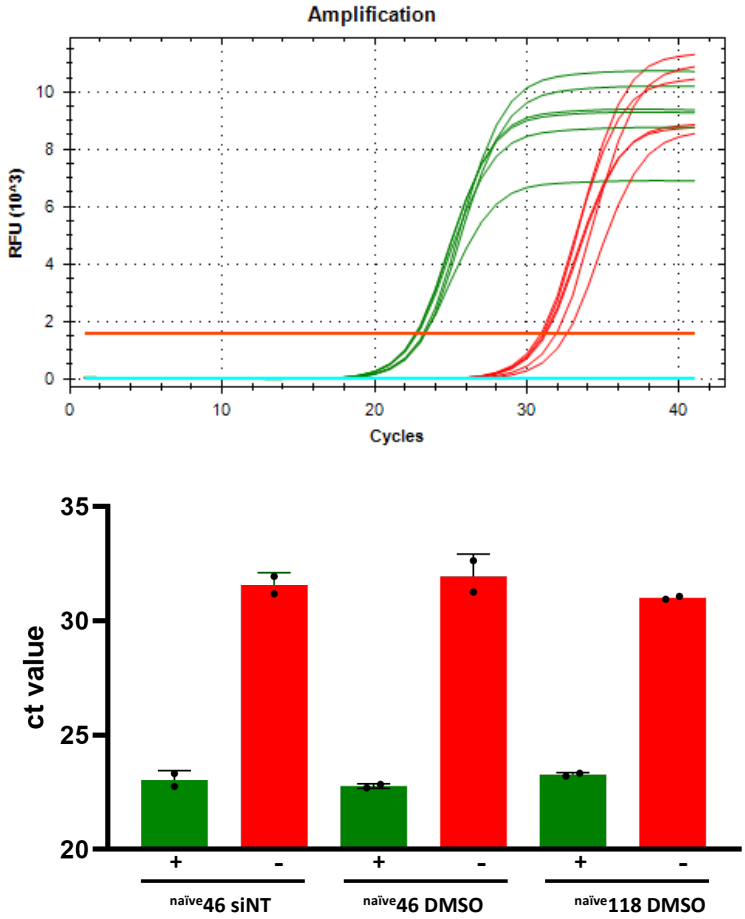

Supplementary Figure 7: Exemplary qPCR analysis for positive and negative controls of ChIP-seq using primers of ribosomal housekeeper gene RPL30; Upper panel: amplification curve, lower panel: absolute CT-values; green: positive control → low ct value → enrichment of RPL30, red: negative control → high ct value → no enrichment of RPL30

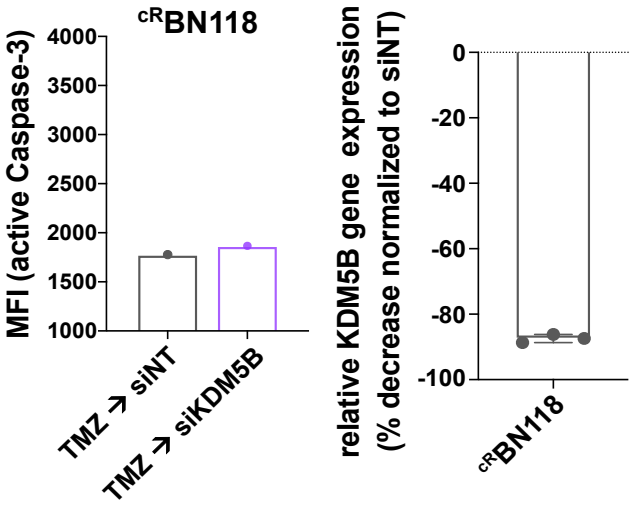

Supplementary Figure 8: Left: Bar chart showing MFI of active Caspase-3 in glioblastoma relapse sample cRBN118; sample was TMZ pretreated for 4 days before siNT or siKDM5B knockdown was performed for 6 days; Right: Knockdown efficiency normalized to siNT control. Mean of triplicates ± SD.

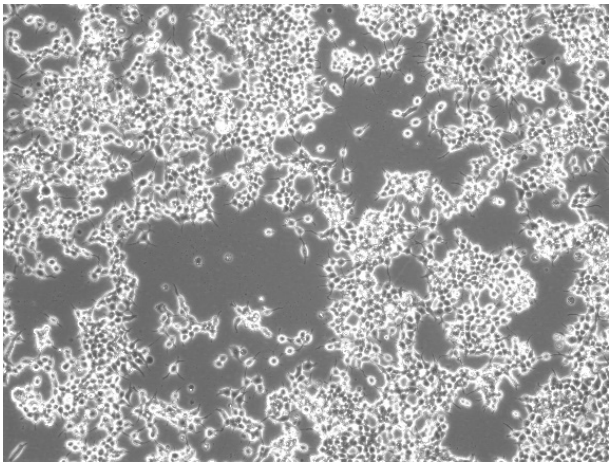

Supplementary Figure 9: Exemplary brightfield image of HEK293T cells after transfection; Microscope Axio Vert.A1 (Zeiss), 10x magnification

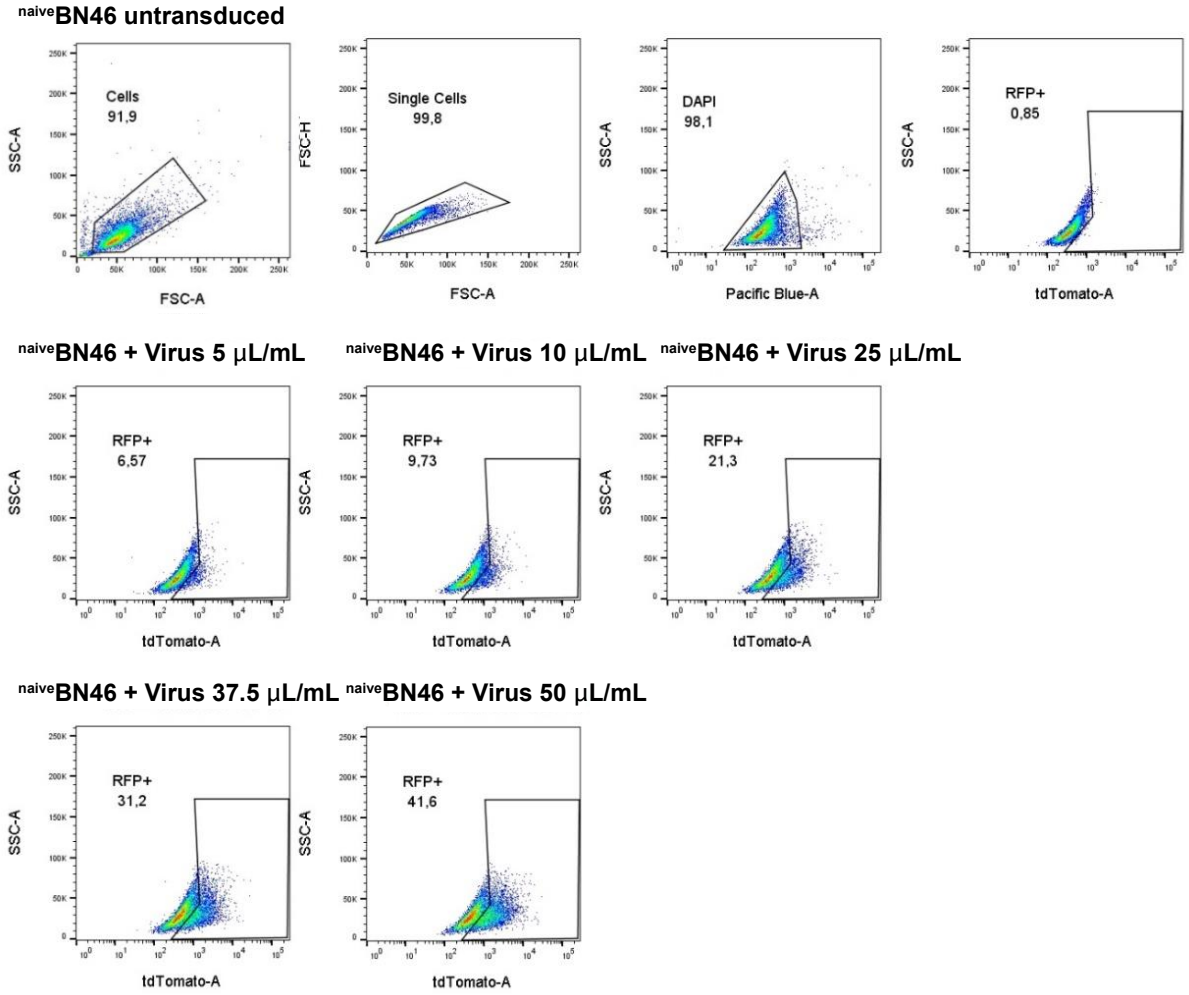

Supplementary Figure 10: Exemplary flow cytometry profiles of ClonTracer barcoding experiment; transduction of naiveBN46 with different concentrations of the virus; detected via RFP fluorescence intensity.

naiveBN118 untransduced

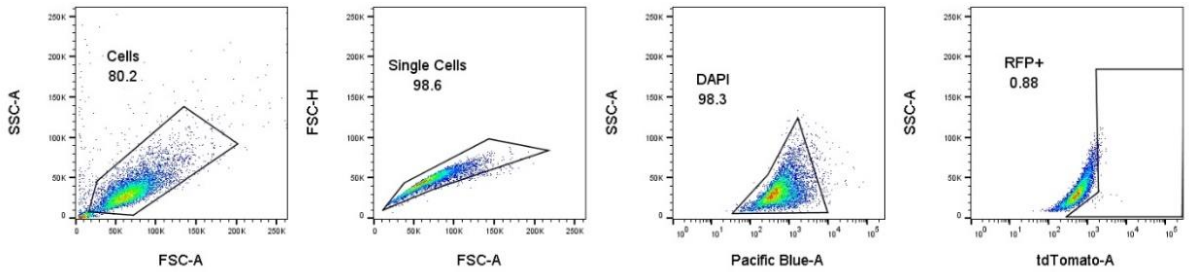

naiveBN118 + Virus 5 µL/mL **naiveBN118 + Virus 10 µL/mL** **naiveBN118 + Virus 25 µL/mL**

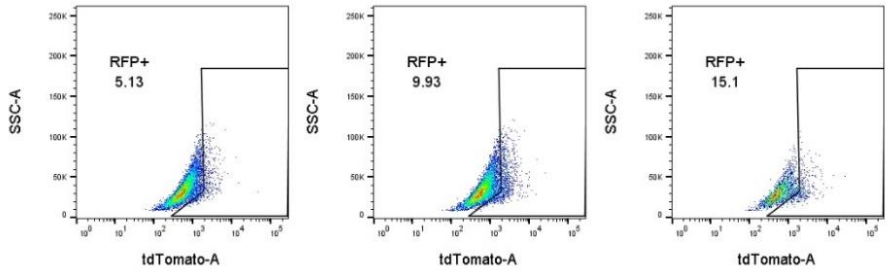

naiveBN118 + Virus 37.5 µL/mL **naiveBN118 + Virus 50 µL/mL**

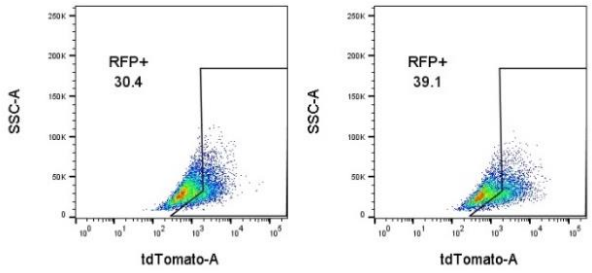

Supplementary Figure 11: Exemplary flow cytometry profiles of ClonTracer barcoding experiment; transduction of naiveBN118 with different concentrations of the virus; detected via RFP fluorescence intensity.

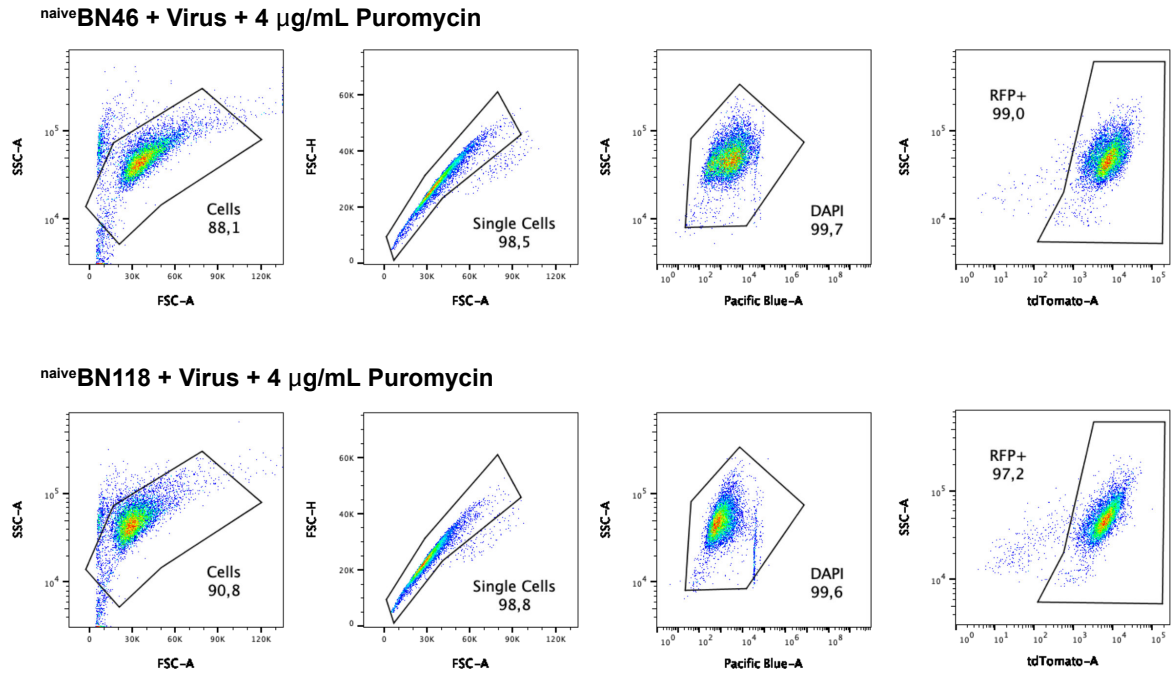

Supplementary Figure 12: Exemplary flow cytometry profiles of ClonTracer barcoding experiment; selection of naiveBN46 and naiveBN118 with Puromycin, detected via RFP fluorescence intensity.

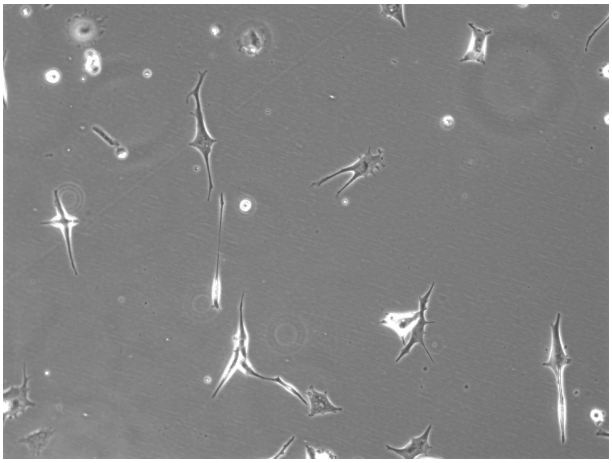

Supplementary Figure 13: Exemplary brightfield image of barcoded DTP sample of naiveBN46 after 16 days TMZ exposure; image taken with Microscope Axio Vert.A1 (Zeiss), 10x magnification.

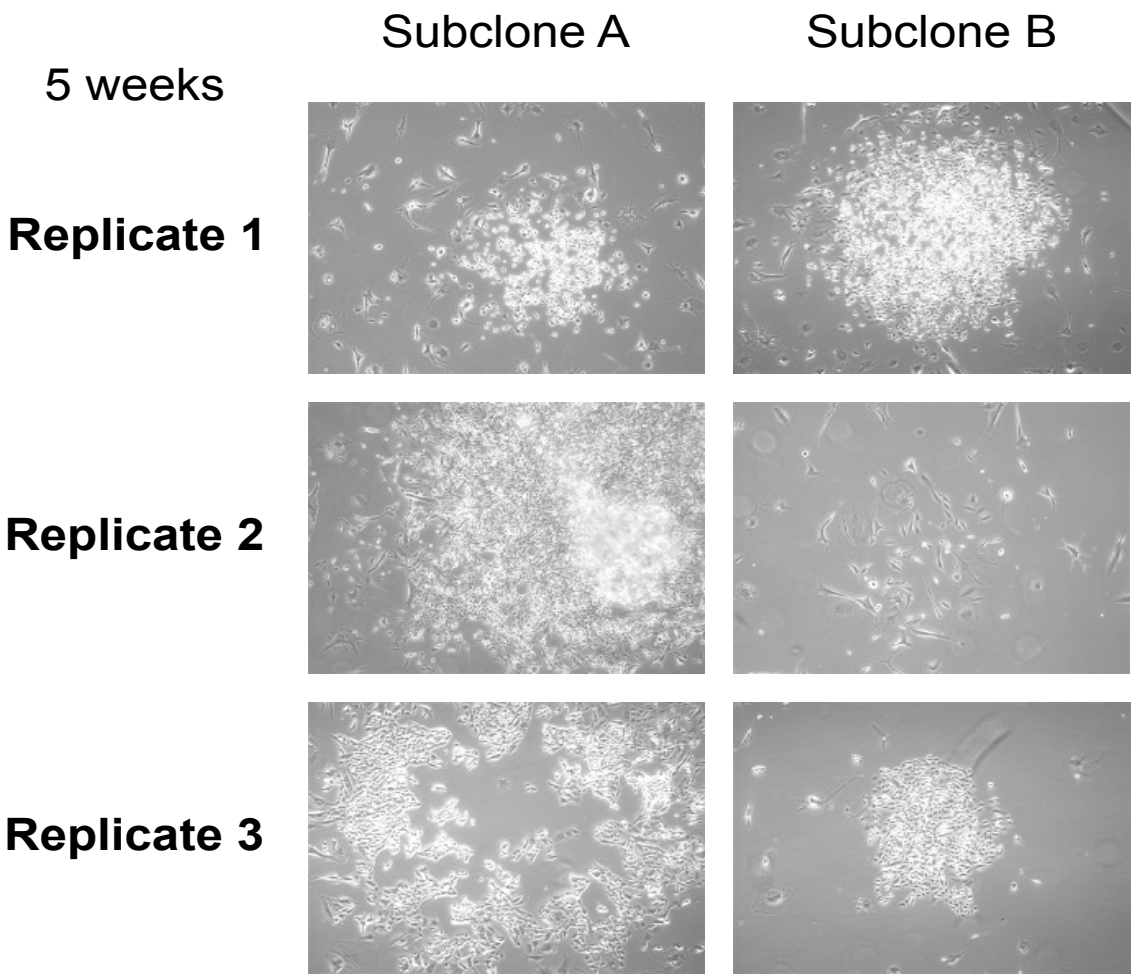

Supplementary Figure 14: Exemplary brightfield images of barcoded DTEP samples of ^{naive}BN46; microscopically distinguishable subclones are shown; images taken with Microscope Axio Vert.A1 (Zeiss), 5x magnification.

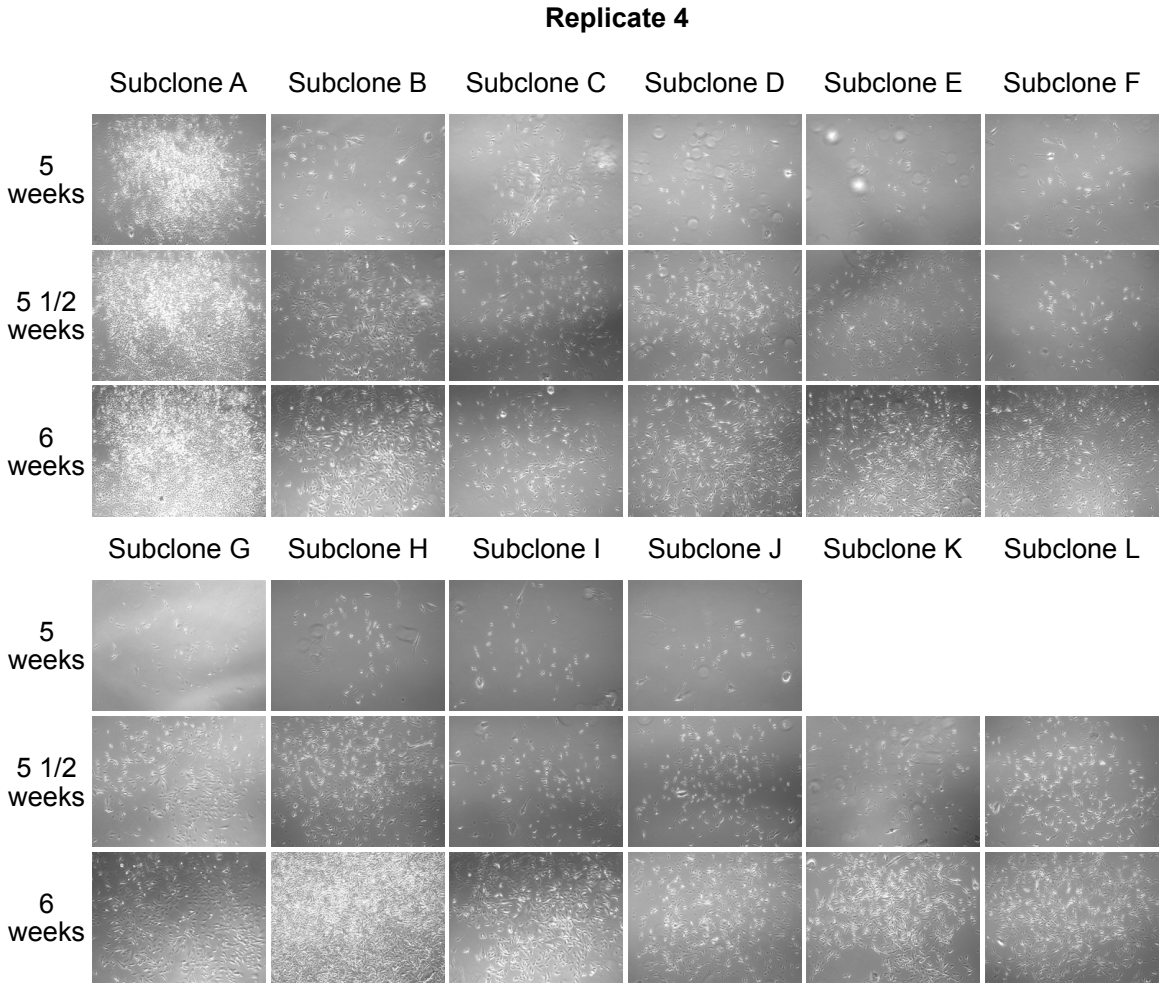

Supplementary Figure 15: Exemplary brightfield image of barcoded DTEP samples of ^{naive}BN46; microscopically distinguishable subclones are shown; images taken with Microscope Axio Vert.A1 (Zeiss), 5x magnification.

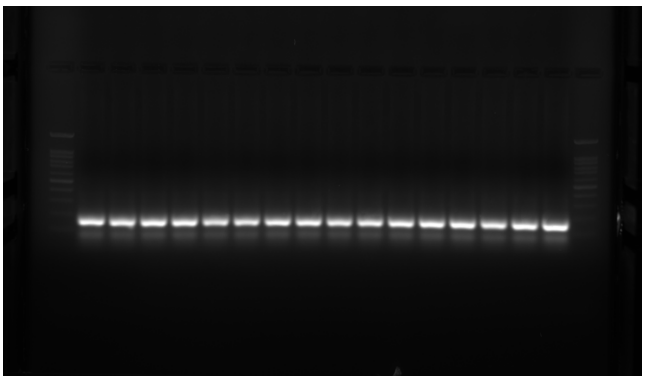

Supplementary Figure 16: Exemplary image of gelelectrophoresis of PCR-amplified barcode region in ^{naive}BN118; length of expected product = 173 bp

8. List of Abbreviations

ABX	Antibiotic-Antimycotic
(p)AKT	(phosphorylated) protein kinase B
ALDH1A1	Aldehyde Dehydrogenase 1 Family Member A1
ATP	Adenosintriphosphat
BCA	Bicinchoninic Acid
bFGF	Basic fibroblast growth factor
bp	base pair
BRCA1	Breast cancer type 1
BSA	Bovine serum albumin
CaTCH	CRISPRa tracing of clones in heterogeneous cell populations
CDK4	cyclin-dependent kinase 4
CDKN2A/B	cyclin-dependent kinase inhibitor 2A/B
cDNA	complementary deoxyribonucleic acid
CNS	central nervous system
CO_2	carbon dioxide
cR	Clinical Relapse
CRISPR	Clustered Regularly Interspaced Short Palindromic Repeats
CSC	Cancer stem cell
CT	Cycle threshold
CT	ClonTracer
DAPI	4,6-diamidin-2- phenylindoldihydrochlorid
DMEM	Dulbecco's Modified Eagle Medium
DMSO	Dimethyl sulfoxide
DNA	Desoxyribonucleic acid
DPBS	Dulbecco's Phosphate Buffered Saline
DTEP	Drug tolerant expanded persisters
DTP	Drug tolerant persisters
DTT	Dithiothreitol
EDTA	Ethylenediaminetetraacetate
e.g.	exempli gratia
EGF	Epidermal growth factor
EGFP	Enhanced green fluorescent protein
EGFR	Epidermal Growth Factor Receptor
eR	Experimental Relapse
EMT	Epithelial-to-mesenchymal transition
FACS	Fluorescence activated cell sorting
FBS	Fetal Bovine Serum
FFPE	Formalin-fixed paraffin-embedded
FITC	Fluorescein isothiocyanate
FSC	Forward scatter
FSC-A	Forward Scatter-Area
FSC-H	Forward Scatter-Width
GFP	Green Fluorescent Protein
GSC	Glioblastoma stem cell
GSEA	Gene set enrichment analysis
GSK3β	Glycogen synthase kinase-3 beta
H3K4 / H3K9 / H3K27	Histone 3 lysine 4/9/27
H&E	Hematoxylin and eosin
HEK	Human Embryonic Kidney

IDH	Isocitrate dehydrogenase
i.e.,	id est
IgG	Immunoglobulin G
IL-10	Interleukin 10
KDMs	Histone demethylases
LDA	limiting dilution analysis
LSD1	Lysine-specific histone demethylase 1
LTR	long terminal repeats
MFI	Mean fluorescence intensity
MGMT	O6-Methylguanine-DNA-Methyltransferase
mL	Mililiter
mOS	median overall survival
MTIC	5-(3-methyltriazen-1-yl)imidazole-4-carboxamide
(p)mTOR	(phosphorylated) mammalian target of rapamycin
ng	Nanogramm
NGS	Next generation sequencing
NF1	neurofibromatosis type 1
NSCLC	non-small cell lung cancer
NT	Non-Targeting
NuRD	Nucleosome Remodeling and Deacetylase complex
Ovx	Overexpression
p53	Tumor protein P532
PBS	Phosphate buffered saline
PBST	Phosphate buffered saline with Tween
PCR	Polymerase Chain Reaction
PDX	Patient derived xenografts
PD-L1	Programmed death-ligand 1
PDGFRA	platelet-derived growth factor receptor alpha
PFS	Progression-free survival
PI3K	Phosphatidylinositol-3-kinase
PIP2	phosphatidylinositol-4, 5-bisphosphate
PIP3	phosphatidylinositol-3, 4, 5-triphosphate
PO	Poly-L-Ornithin
PPS	Post-progression survival
PRC2	Polycomb Repressive Complex 2
PTEN	Phosphatase and Tensin Homolog
qPCR	quantitative Polymerase Chain Reaction
rcf	Relative centrifugal force
REV	Regulator of expression of virion proteins
RNase	Ribonuclease
RFP	Red Fluorescent Protein
RNA	Ribonucleic acid
RPL37A	60S ribosomal protein L37a
RPL30	60S ribosomal protein L30
RRE	Rev response element
RT	Radiotherapy
RT	Room Temperature
RTK	Receptor Tyrosine Kinase
SD	Standard deviation
SDS-Page	Sodium Dodecyl Sulfate Polyacrylamide gel electrophoresis

SETDB1	SET domain bifurcated histone lysine methyltransferase 1
shRNA	short hairpin RNA
siRNA	small interfering RNA
SSC	Side Scatter
SSC-A	Side Scatter-Area
TAR	Trans-activation response element
TERT	Telomerase Reverse Transcriptase
TGF-ß	Transforming growth factor beta
TMZ	Temozolomide
TTFields	Tumor-treating fields
VSVG	Vesicular stomatitis virus glycoprotein
WHO	*World Health Organization*
WT	wildtype
°C	Degrees Celsius
7-AAD	7-aminoactinmycin-D
µL	Microliter
µM	Micromole

9. List of Figures

10. List of Supplementary Figures

11. List of Tables

Danksagung

An dieser Stelle möchte ich all denjenigen meinen größten Dank aussprechen, die mich während meiner Promotion begleitet haben. Ohne die Unterstützung der folgenden Menschen wäre das Erstellen dieser Arbeit nicht möglich gewesen:

Mein besonderer Dank gilt meinem Doktorvater Prof. Dr. Björn Scheffler, für seine hervorragende Betreuung, die enorme Unterstützung, seine vielen Ideen sowie seine konstruktive Kritik. Er hat immer an meine Arbeit geglaubt und letztendlich eine bessere Wissenschaftlerin aus mir gemacht. Herzlichen Dank für alles.

Ebenso möchte ich mich bei meiner Zweitgutachterin Prof. Dr. Verena Jendrossek bedanken, sowie bei Prof. Dr. Alexander Rösch und Prof. Dr. Barbara Grüner, die mich seit dem ersten Tag meines Doktors begleitet und mit ihrer Unterstützung und ihren Ideen meine Arbeit sehr vorangebracht haben.

Außerdem möchte ich meinen Arbeitskollegen der DKFZ-Abteilung für Translationale Neuroonkologie danken, die mir zu jeder Zeit mit fachlichem Feedback geholfen, aber mich vor allem auch mit aufmunternden Gesprächen und vielen lieben Worten durch diese Doktorarbeit begleitet haben. Eine schönere Arbeitsatmosphäre, ob während oder außerhalb der Arbeit, hätte ich mir nicht wünschen können und ohne euch alle, wäre es nicht eine so wunderbare Zeit geworden: Celia Dobersalske, Sarah Ertmer, Sarah Langer, Pia Berger, Anna Baginska, Mihaela Keller, Anita Steinbach, Loona Meyer, Dr. Hanah Gull, Dr. Igor Cima, Dr. Shruthi Prasad und Sandra Hartmann.

Besonders hervorheben möchte ich noch einmal Sarah Ertmer, Sarah Langer und Loona Meyer, die während ihrer Bachelor- bzw. Masterarbeiten mit viel Enthusiasmus und Begeisterung an meinem Projekt mitgearbeitet haben. Ich bin euch so dankbar für die tolle Zusammenarbeit. Ohne euer Engagement und euren Fleiß wäre diese Arbeit nicht in dieser Form möglich gewesen. Einen gesonderten Dank auch an Anna Baginska, Hanah Gull und Igor Cima, die ebenfalls intensiv an den Projekten dieser Doktorarbeit mitgearbeitet haben. Ebenso möchte ich im Besonderen Mihaela Keller erwähnen, die mir vor allem in meinen Anfängen alles über Patienten - Zellkultur beigebracht hat und mir auch später oft noch mit Rat oder Unterstützung zur Seite gestanden hat.

Eine besondere Rolle hat die Interaktion mit der Klinik gespielt: vielen Dank an alle Kollegen aus der Abteilung für Klinische Neuroonkologie für die Zusammenarbeit.
Insbesondere danke ich Dr. Sied Kebir dafür, dass ich Teil des von ihm begonnenen, spannenden Projekts sein durfte, auf das meine weitere Doktorarbeit aufgebaut hat.
Ebenso danke ich den Kollegen der Neurochirurgie, vor allem Prof. Dr. Ulrich Sure, Dr. Laurèl Rauschenbach und erneut Dr. Hanah Gull, die uns unermüdlich klinische Proben liefern, ohne die unsere Forschung nicht möglich wäre.

Des weiteren möchte ich den mit uns kollaborierenden Gruppen von Prof. Dr. Barbara Grüner, Prof. Dr. Jens Siveke, Prof. Dr. Alexander Schramm und Prof. Dr. Alexander Rösch danken, die ihr Fachwissen, ihre Erfahrungen oder ihre Laborausstattung mit uns geteilt haben und das Projekt mit ihren Anregungen zu dem gemacht haben was es nun ist. Ich möchte einzelne Mitglieder dieser Arbeitsgruppen besonders hervorheben: Anna Baginska (die wir schon vollkommen als Teil unseres Labors ansehen), sowie Philip Dujardin, Dr. Madeleine Dorsch und Stefanie Egetemaier, die mir zu jeder Zeit mit ihrem fachlichen Rat und ihren Ideen weitergeholfen haben, die aber auch durch emotionalen Beistand oder viele unterhaltsame Gespräche die letzten vier Jahre zu einer unvergesslichen Zeit gemacht haben!

Für die finanzielle Unterstützung während meiner Dissertation danke ich dem Universitätsklinikum Essen, sowie der DFG, für die Anstellung als wissenschaftliche Mitarbeiterin im Rahmen der DFG-geförderten Klinischen Forschergruppe 337 “Phenotypic Therapy and Immune Escape in Cancer”.

Und schließlich möchte ich mich bei den wichtigsten Menschen in meinem Leben bedanken!
Vielen Dank für die unglaubliche Unterstützung an meine Eltern, an meinen Freund, und auch an meine besten Freunde. Ihr habt mich immer unterstützt, mir Rückhalt und Kraft gegeben, hattet Geduld und Verständnis für all die Abende, Wochenenden und Feiertage die ich im Labor verbracht habe. Und vor allem danke ich euch dafür, dass ihr mich stets ermutigt und immer an mich geglaubt habt. Ohne euch hätte ich das nicht geschafft! Danke!

"Der Lebenslauf ist in der Online-Version aus Gründen des Datenschutzes nicht enthalten."

"Der Lebenslauf ist in der Online-Version aus Gründen des Datenschutzes nicht enthalten."

Erklärung:

Hiermit erkläre ich, gem. § 6 Abs. (2) g) der Promotionsordnung der Fakultät für Biologie zur Erlangung der Dr. rer. nat., dass ich das Arbeitsgebiet, dem das Thema ***„Targeting clonally expanding drug-resistant tumor cells in recurrent glioblastoma“*** zuzuordnen ist, in Forschung und Lehre vertrete und den Antrag von ***Vivien Ullrich*** befürworte und die Betreuung auch im Falle eines Weggangs, wenn nicht wichtige Gründe dem entgegenstehen, weiterführen werde.

Essen, den _____ _____ _____

Name des Betreuers an der Universität Duisburg-Essen

Unterschrift

Erklärung:

Hiermit erkläre ich, gem. § 7 Abs. (2) d) + f) der Promotionsordnung der Fakultät für Biologie zur Erlangung des Dr. rer. nat., dass ich die vorliegende Dissertation selbständig verfasst und mich keiner anderen als der angegebenen Hilfsmittel bedient, bei der Abfassung der Dissertation nur die angegeben Hilfsmittel benutzt und alle wörtlich oder inhaltlich übernommenen Stellen als solche gekennzeichnet habe.

Essen, den _____ _____

Unterschrift des/r Doktoranden/in

Erklärung:

Hiermit erkläre ich, gem. § 7 Abs. (2) e) + g) der Promotionsordnung der Fakultät für Biologie zur Erlangung des Dr. rer. nat., dass ich keine anderen Promotionen bzw. Promotionsversuche in der Vergangenheit durchgeführt habe und dass diese Arbeit von keiner anderen Fakultät/Fachbereich abgelehnt worden ist.

Essen, den _____ _____

Unterschrift des/r Doktoranden/in

DOI: 10.17185/duepublico/79218
URN: urn:nbn:de:hbz:465-20250107-083954-3